Development of Graphene Oxide Coated Long Period Grating based Fibre Optic Sensors

by

Kasun Prabuddha Wasantha Dissanayake

Thesis submitted for the degree of Doctor of Philosophy

Supervised by

Professor Kenneth T.V. Grattan OBE

Professor Tong Sun OBE

City, University of London

School of Mathematics, Computer Science and Engineering

EC1V 0HB, London, UK

July 2020

Table of Contents

Table of Contents i
Table of Figures iv
Table of Tables xvi
Acknowledgements xvii
Copyright Declaration xviii
Abstract xix
Glossary of Symbols, Abbreviations and Chemicals xxi
Chapter 1 : Introduction and Background
1.1 Introduction 1
1.2 Aims and Objectives 3
1.3 Structure of the Thesis 4
1.4 Summary 6
1.5 References 6
Chapter 2 : Coated Long Period Gratings (LPGs) for Fibre Optic Sensor Applications
2.1 Introduction 7
2.2 Mode Coupling in Optical Fibres 7
2.3 Properties of Fibre Gratings 10
2.3.1 Fibre Bragg Gratings (FBG) 10
2.3.2 Long Period Gratings (LPG) 12
2.4 Fabrication of LPGs 15
2.5 Comparison between LPG & FBG based Fibre Optic Sensors 20
2.6 Sensing Characteristics of LPGs 21
2.6.1 Strain Sensitivity 23
2.6.2 Temperature Sensitivity 23
2.6.3 External Refractive Index Sensitivity 25
2.7 Coated LPG Sensors – Essential Theory 28
2.7.1 Effect of Overlay Thickness 29
2.7.2. Mode Guiding in an Overlay 31
2.8 Coated LPG based Fibre Optic Sensors 35
2.9 Summary 45
2.10 References 46
Chapter 3 : Graphene Nanomaterials-based Fibre Optic Sensors
3.1 Introduction 52

3.2 Graphene and its Derivatives 52
3.2.1 Graphene 52
3.2.2 Graphene Oxide (GO) 55
3.3 Synthesis Methods of Graphene Nanomaterials 57
3.3.1 Synthesis of Graphene 57
3.3.2 Synthesis of Graphene Oxide 60
3.4 Optical Properties of Graphene Nanomaterials 62
3.4.1 Optical Properties of Graphene 62
3.4.2 Optical and Colloidal Properties of Graphene Oxide 66
3.5 Graphene Nanomaterials based Fibre Optic Sensors 71
3.6 Summary 81
3.7 References 82
Chapter 4 : Development and Characterisation of a GO coated LPG based External RI Sensor System
4.1 Introduction 89
4.2 Sensing Principle 90
4.3 GO Synthesis Process 92
4.3.1 Materials 92
4.3.2 GO Synthesis – Modified Hummer's Method 93
4.4 GO Material Characterisation 96
4.4.1 UV/Visible Spectrum 97
4.4.2 Fourier-Transform Infrared (FTIR) spectrum 98
4.4.3 Energy Dispersive X-ray Analysis (EDAX) Analysis 99
4.4.4 GO Particle Size 100
4.4.5 GO Surface Potential 100
4.5 LPG: Theoretical Analysis and Fabrication 101
4.5.1 Theoretical Analysis 101
4.5.2 LPG Fabrication 102
4.6 GO Deposition on the Optical Fibre Surface 103
4.7 Experimental Setup for Evaluating External RI Changes 107
4.8 Experimental Results and Analysis 108
4.9 Summary 116
4.10 References 117
Chapter 5 : Graphene oxide-coated LPG-based Relative Humidity Sensor
5.1 Introduction 120

5.2 GO based Humidity Sensors 121
5.2.1 GO based Electrical Humidity Sensors 122
5.2.3 GO based Optical Humidity Sensors 125
5.3 Sensing Principle 128
5.4 Fabrication of the Sensor Probe 129
5.5 Experimental Setup for Evaluating the Humidity Sensitivity 131
5.6 Experimental Results and Analysis 132
5.6.1 Humidity Response 132
5.5.2 Temperature Response 136
5.6 Summary 139
5.7 References 139

Chapter 6 : GO Functionalised LPG for Label-Free Measurement of Bovine Serum Albumin (BSA) Concentration

6.1 Introduction 143
6.2 Importance of GO and Optical Fibre Sensors in Biosensing 144
6.3 Dual Peak Resonance of LPGs 150
6.4 Fabrication of the Sensor Probes 154
6.5 Experimental Setup 159
6.6 Performance Analysis of GO-DLPG Biosensor 160
6.7 Summary 171
6.8 References 171

Chapter 7 : Conclusions and Future Work

7.1 Conclusions of the work carried out 175
7.2 Proposal for Future Work 177

List of Publications 180

Table of Figures

Fig 2. 1 Propagating constants of the forward and reverse-propagating guided modes in an optical fibre [2-3]. 8

Fig 2. 2 Propagation constant distribution of cladding modes in an optical fibre [2-3]. 9

Fig 2. 3 Mode coupling mechanism in FBGs [2-3]. 11

Fig 2. 4 Principle of operation of a FBG [2-6]. 12

Fig 2. 5 Mode coupling between two forward propagating guided modes [2-3]. 12

Fig 2. 6 Mode coupling in LPGs [2-3]. 13

Fig 2. 7 Typical transmission spectrum of a LPG [2-3]. 14

Fig 2. 8 Phase mask FBG writing scheme [2-36]. 16

Fig 2. 9 Setup used to fabricate LPGs using an amplitude mask and an excimer laser [2-3]. . 17

Fig 2. 10 Excimer laser-based LPG fabrication setup at City, University of London. 18

Fig 2. 11 Transmission spectra of a LPG before and after annealing at 120 ℃ for 3 hours. .. 19

Fig 2. 12 Wavelength shift (with respect to that at 31.2 °C) with temperature for various resonance bands of a long-period grating. The dashed line (E) is the shift for a Bragg grating at 1550 nm with a temperature coefficient 1.3 nm/100 °C [2-43]. 25

Fig 2. 13 (a) Broad-band transmission spectrum of Λ = 275 μm LPG for n_{sur} ranging 1 to 1.45. (b) Broad-band transmission spectrum for n_{sur} ranging from 1.46 to 1.72. Dotted lines indicate attenuation band wavelengths at n_{sur} = 1 [2-48]. 26

Fig 2. 14 Experimentally measured centre wavelength and the attenuation of the longest wavelength attenuation band in the Λ = 275 μm LPG as a function of surrounding RI [2-49]. 27

Fig 2. 15 Transverse and longitudinal sections of a LPG structure, showing deposition of an overlay upon the cladding [2-57]. 28

Fig 2. 16 Experimental shift in the central wavelengths of the attenuation bands plotted as a function of the thickness of the tricosenoic acid overlay. Filled circles: attenuation band corresponding to coupling to the 5^{th} cladding mode, filled squares: attenuation band corresponding to coupling to the 6th cladding mode [2-57].....30

Fig 2. 17 (a) Illustrative schematic of LPG with an nm-thick thin-film coating (b) Index profile of the thin-film coated LPG, n_1 is index of fibre core, n_2 is index of fibre cladding, n_3 is index of the thin-film, n_{air} is index of air, and $n_3>n_1>n_2>n_{air}$. Thickness d of the film is denoted d=b-a [2-58].....31

Fig 2. 18 Effective index as a function of the overlay thickness of (a) the first 15 cladding modes and (b) the core mode and the first six cladding modes [2-60].....31

Fig 2. 19 Shift in resonance wavelength caused by coupling between the core mode and the seventh (LP07) and the eighth (LP08) cladding modes of the structure as a function of the thickness of the overlay. Open square, experimental values; solid curves, theoretical values [2-57].....33

Fig 2. 20 Transmission spectrum showing the $EH_{1,17}$,$HE_{1,16}$,$EH_{1,15}$, and $HE_{1,14}$ mode resonances for four overlay thickness values: 0, 255, 289, and 335 nm. The overlay refractive index is 1.62, and the ambient index is 1 [2-60].....33

Fig 2. 21 $HE_{1,16}$ resonance wavelength as a function of the overlay thickness. The overlay refractive indices are 1.55 and 1.8, and the ambient index is 1 [2-60].....34

Fig 2. 22 Spectral change seen when the coated LPG is exposed to various humidity levels ranging from 33% to 97%, with PVA coating thicknesses of (a) 4 μm and (b) 800 nm [2-61].....36

Fig 2. 23 (a) Chemical structures of the composite materials. Polyvinyl alcohol is on the left, polyethylene glycol is on the right (b) schematic configuration of the long-period fibre grating (LPFG) RH sensor coated with a PEG/PVA composite film [2-62].....37

Fig 2. 24 (a) A comparison of different materials for relative humidity sensing (b) Humidity sensing characteristics of the LPFGs coated by the films with different PEG proportions in the humidity range from 50% to 95% RH [2-62].....37

Fig 2. 25 Schematic figure and photos of the gas monitoring system [2-63]. 38

Fig 2. 26 (a) Single ended aPS coated LPG based gas sensor (b) Wavelength shift of the LP_{07} band during the exposure to different butane concentrations [2-63]. 38

Fig 2. 27 Schematic diagram of the hydrogel coated LPG based salinity sensor and its resonance wavelength response against different salinity concentrations [2-64]. 39

Fig 2. 28 Schematic of the coated LPG based toluene sensor [2-65]. 39

Fig 2. 29 Dilution curve of Toluene and Ethanol solution and their response of thecalix[4]res C11 coated LPG sensor [2-65].....40

Fig 2. 30 Schematic of a LPG modified with a thin HRI overlay (a) transversal cross section of the device, (b) a zoom on the surface where a biomolecular recognition process is taking place [2-73].....40

Fig 2. 31 LPG sensorgram reporting the wavelength shift of the 5th order cladding mode attenuation band (a) during the multiple biomolecular interactions, steps I-III and (b) the IgG binding and subsequent affinity assay with anti-IgG, steps IV-VIII. Inset: sketch of coated LPG surface with the different biological entities used in the experiment [2-69]. 41

Fig 2. 32 Variation of (a) the spectral shift of the resonance wavelength prior to and after the E. coli incubation on the LPFG, and (b) the spectral shift of the resonance wavelength as a function of the E. coli concentration in the PBS buffer [2-70]. 42

Fig 2. 33 Schematic representation of the fibre surface modification steps leading to phage detection [2-71]. 43

Fig 2. 34 (a) Schematic representation of the LPG fibre sensor probe (b) Immobilization of enzyme to create the bio-recognition layer on the optical fibre probe [2-72]. 44

Fig 2. 35 Transmission spectrum at different concentrations of triacylglyceride (TGs) at room temperature and 37 °C, corresponding shift in resonance wavelength vs. concentrations of triacylglyceride along with standard deviation in the inset [2-72]. 44

Fig 3. 1 Carbon allotropes and related materials [3-13]. 53

Fig 3. 2 Graphene (a) geometry (b) bonding [3-14]. 53

Fig 3. 3 One-atom-thick single crystals (a**)** Graphene visualized by atomic force microscopy. The folded region exhibiting a relative height of ≈4 Å (0.4 nm) clearly indicates that it is a single layer. (b**)** A graphene sheet freely suspended on a micrometre-size metallic scaffold. (c**)** Scanning electron micrograph of a relatively large graphene crystal, which shows that most of the crystal's faces are zigzag and armchair edges as indicated by blue and red lines and illustrated in the inset. 1D transport along zigzag edges and edge-related magnetism attract significant attention [3-15].....54

Fig 3. 4 Summary of older models illustrating the chemical structure of GO [3-26].....56

Fig 3. 5 Variations of the Lerf-Klinowski model indicating ambiguity regarding the presence (top) or absence (bottom) of carboxylic acids on the periphery of the basal plane of the graphitic platelets of GO [3-25] 57

Fig 3. 6 Sketch showing the different ways nanotubes could be unzipped to yield graphene nanoribbons (GNRs): (a) chemical route, involving acid reactions that start to break carbon-carbon bonds (e.g., H_2SO_4 and $KMnO_4$ as oxidizing agents) (b) intercalation-exfoliation of MWCNTs, involving treatments in liquid NH_3 and Li, and subsequent exfoliation using HCl and heat treatments (c) catalytic approach, in which metal nanoparticles "cut" the nanotube longitudinally like a pair of scissors (d) physicochemical method, by embedding the tubes in a polymer matrix followed by Ar plasma treatment and (e) the electrical method, by passing an electric current through a nanotube. The resulting structures are either (f) GNRs or (g) graphene sheets [3-31].....58

Fig 3. 7 Schematic chemical structures of graphene, GO, and reduced GO (b) Route of graphite to reduce GO [3-33].....59

Fig 3. 8 Summary of the main graphene synthesis methods [3-40].....60

Fig 3. 9 Schematic illustration of graphene oxide synthesis by chemical oxidation using Brodie's, Staudenmaier's, and Hummer's methods [3-44]. 61

Fig 3. 10 (a) White light absorption of graphene [3-46] (b) theoretical transparency of graphene [3-47].....62

Fig 3. 11 Optical constants of graphene n (solid line) and k (dashed line). Inset: χ_{red} as a function of the thickness fit parameter; a unique minimum is found for 3.4 Å [3-49]. 63

Fig 3. 12 (a) Extinction spectra of graphene and gold biosensors covered with a protein layer. The thick curves are the measured spectra and the thin curves are the fittings for bare graphene and gold biosensors. (b) Field confinement percentage as a function of the distance from the biosensor surface for both graphene and gold. The inset is the enlarged version in the small distance d regime [3-58]. 65

Fig 3. 13 (a) Representative PL Emission, PL spectra, and luminescent photograph of GQDs (b) Emission images of different kinds of GQDs under excitation of a 365 nm UV lamp [3-61]. 66

Fig 3. 14 UV–vis absorption spectra of GO in water as a function of elapsed time during chemical reduction by hydrazine [3-64]. 66

Fig 3. 15 (a) PL spectra of a GO suspension in water (l-GO) and a GO film on a substrate (s-GO), excited at 500 nm [3-67] (b) PL emission spectrum for excitation at 325nm and excitation spectrum for emission at 388nm for a GO thin film reduced by hydrazine for 3 min [3-66]..67

Fig 3. 16 Optical constants of GO flakes as a function of wavelength [3-69].....68

Fig 3. 17 Digital pictures of as-prepared graphite oxide dispersed in water and 13 organic solvents through bath ultrasonication (1 h). Top: dispersions immediately after sonication. Bottom: dispersions 3 weeks after sonication. The yellow colour of the o-xylene sample is due to the solvent itself [3-70].....69

Fig 3. 18 Raman spectra of a monolayer of GO, rGO, and mechanically exfoliated graphene on SiO_2/Si substrates normalized to the G-peak intensity [3-74]. 70

Fig 3. 19 (a) Setup of the GMHW-MZI for NH_3 sensing. (b) Schematic diagram of the GMHW [3-76].....71

Fig 3. 20 Sensing performances of the GMHW (red) and the microfiber on MgF_2 without graphene attached (blue) [3-76].....71

Fig 3. 21 (a) Schematic representation of the refractive index sensing element formed by the deposition of a graphene overlay onto an MZI (b) Change in intensity of the interference vs. RI for two separate trials (diamonds and triangles) conducted one week apart [3-77]. 72

Fig 3. 22 Principle of graphene-based fibre optic SPR biosensor and the experimental setup (a) When the traveling p-polarized incident light heats the graphene–core interface, the surface plasmon wave (SPW) is excited at the graphene–analyte interface. The meaningful signals are obtained due to the interaction between SPW and the propagation constant of analyte (b) There are three main parts; optics part, sensing part, and measurement part. LED light source and sort of optics are involved in the first part. The fabricated sensor with analytes is the second part and lastly, the spectrometer and PC are the measurement part [3-78].....73

Fig 3. 23 The SPR probe response to without any analyte state (air), buffer, and various concentrations of DXB and SA, viz. 50, 100, 200, and 400 mM. (a) The SPR peak spectra were obtained by data analysis with Lorentzian fitting. Every spectrum was drawn in arbitrary values of normalized intensity but in same scale. There are minute change for the concentrations for DXB and SA respectively, and noticeable difference between the analytes. (b) The bar chart for SPR wavelengths for each analyte. The SPR peaks appeared at around 524 nm for without analyte and buffer cases, 525.3–529.5 nm for DXB samples, and 539.6–540.8 nm for SA samples [3-78].....73

Fig 3. 24 Schematic illustration of the experimental setup used to evaluate the performance of the GO and rGO polymer optical fibre sensors (a) Schematic representation for fabrication of one-headed POF sensor with (b) GO, (c) rGO and (d) GO-rGO (e) Schematic representation for fabrication processes of GO-rGO POF sensor by converting GO into rGO with sunlight [3-80]. 74

Fig 3. 25 Comparative plots of the sensing responses to eight different vapours at a 500 ppb concentration level [3-80]. 75

Fig 3. 26 Schematic diagram for (a) the experimental setup and sensing scheme used and (b) the U-bent sensing probe (c) The guiding mechanism of light in the U-bent optical fibre [3-81]. 76

Fig 3. 27 (a) shows the principle of the graphene based ‘FRET on fiber’ (b) Schematically demonstrates the detection system containing two channels. One is for fluorescence detection, and the other is for all-fibre interference phase measurement (c) Illustrates the probe structure in detail. rGO film (black hexagons) is deposited around the etched MMF section. In the interferometer, interference between HE_{11} and HE_{12} mode occurs, while the HE_{12} mode is

enhanced in the rGO-coated area (simulated by FEM method, COMSOL). (d) The SEM image, in which the dark film is the rGO film. (e) The zoom-in of (d) [3-82].....77

Fig 3. 28 (a) Schematic diagram of GO coated TFBG (b) intensity of four different cladding modes under different RH conditions changing from 10% to 80% [3-83].....78

Fig 3. 29 (a) Schematic diagram of the rGO coated eFBG gas sensor (b) Shift in Bragg wavelength as a function of time for different concentrations of NO_2 gas. The inset shows one complete adsorption and desorption cycle for 3 ppm NO_2 gas exposure [3-84]. 78

Fig 3. 30 Transmission spectra of the GO coated LGP at different sugar concentration [3-85]. 79

Fig 4. 1 (a) Ice bath used (b) Reflux system used (c) Resultant brown coloured mixture. 93

Fig 4. 2 (a) Bright yellow coloured solution obtained (b) Settled particles after a 24-hour undisturbed time period (c) Filtering process used.....94

Fig 4. 3 (a),(b) GO flakes synthesised (c) SEM image of the GO flakes synthesised. 94

Fig 4. 4 GO aqueous dispersion after centrifugation process. 95

Fig 4. 5 (a) Optical microscopic image of the supernatant (b) Optical microscopic image of the precipitant (c) SEM image of the supernatant (d) SEM image of the precipitant. 95

Fig 4. 6 UV/Vis spectrum of the prepared GO aqueous dispersion before and after centrifugation. 96

Fig 4. 7 Absorbance of different concentrations of GO [4-14].....97

Fig 4. 8 FTIR spectrum of synthesised GO flakes.....98

Fig 4. 9 (a) EDAX Image showing C and O sites on GO flakes (b) EDAX spectrum of the squared. Region.....99

Fig 4. 10 (a) Size distribution of GO supernatant and precipitant (b) Malvern ZetaSizer Nano CS.....100

Fig 4. 11 Surface Zeta potential of GO flakes synthesised.....100

Fig 4. 12 Simulated attenuation bands over the operating wavelength range. 102

Fig 4. 13 Transmission spectra of the fabricated LPG with an amplitude mask of 250 μm. 103

Fig 4. 14 (a) supernatant taken from the GO dispersion (b) 2 mL of the supernatant diluted with 3 mL of DI water (c) 2 mL of the supernatant diluted with 8mL of DI water.....104

Fig 4. 15 EDAX spectrum of the GO-coated fibre surface of Sensor A. Inset shows the zoomed SEM image of the coated GO layer on Sensor A and the respective red boxed area on the GO coated fibre surface selected to obtain the EDAX analysis. 105

Fig 4. 16 SEM images of GO coated fibre surface of Sensors A (91 nm GO overlay), B (166 nm GO overlay), C (269 nm GO overlay) and D (394 nm GO overlay). 105

Fig 4. 17 SEM image taken of the cross section of the coated fibre surface of Sensor D to measure the GO coating thickness. 106

Fig 4. 18 Experimental arrangement used for external RI sensing measurements. 107

Fig 4. 19 RI of NaCl solutions with varying NaCl concentrations. 108

Fig 4. 20 Transmission spectra of Sensor A (a), B (b), C (c) and D (d) with increasing value of the surrounding RI. 110

Fig 4. 21 Centre wavelength shift of the LP08 resonance loss band of GO-coated LPG sensors and of a bare, uncoated LPG. 112

Fig 4. 22 (a) Swelling of GO in the presence of water molecules (b) Change of d-spacing in GO in the presence of NaCl [4-21]. 113

Fig 4. 23 Minimum intensity change of the LP08 resonance loss band of GO coated LPG sensors and of a bare, uncoated LPG. 114

Fig 4. 24 Centre wavelength shift sensitivity of the LP08 resonance loss band of GO- coated LPG sensors and of a bare, uncoated LPG. 115

Fig 5. 1 Characterization of the sensor and humidity testing system (a) Digital photographs of the device (Reference is a 1 Dime US coin) (b) SEM image of the area set off by a red dashed line (c) SEM image of the interdigitated electrodes without GO (d) SEM image of interdigitated

electrodes covered with G-O films. (e) Schematic diagram of the humidity testing system [5-9]. 122

Fig 5. 2 Capacitance and sensitivity versus RH at 100 Hz, 1 kHz, and 10 kHz (a) Output capacitances of sensors as a function of RH (b) Defined sensitivity as a function of RH [5-9]. 123

Fig 5. 3 (a) Schematic image of capacitive humidity sensor where GO coated SF has been implemented. The average diameter of SF is 0.17 cm (b) The capacitance and its derivative curve of the sensor when the humidity changed between 20% RH and 90% RH. The dot represents the intact silk between the two Cu plates (c) Schematic image of H_2O absorption (RH 90%) and desorption (RH 20%) characteristics on GO coated SF [5-10]. 123

Fig 5. 4 (a) Optical image of sensor array on a flexible PI substrate. (b) Schematic illustration of as-fabricated sensor prototype [5-11]. 124

Fig 5. 5 Capacitance response of the SnO_2/RGO hybrid composite sensor under switching RH at 10 kHz [5-11]. 124

Fig 5. 6 Colorimetric GO based humidity sensor [5-6]. 125

Fig 5. 7 GO coated SU8 polymer waveguide in a humidity measurement setup [5-14]. 126

Fig 5. 8 Piezoelectric inkjet technology used to coat the fibre with GO [5-15]. 126

Fig 5. 9 Schematic diagram of the experimental setup (a) structure of the waist-enlarged taper, and (b) the partially enlarged drawing of the sensing head [5-16]. 127

Fig 5. 10 Transmission spectrum of the LPG inscribed with an amplitude mask of 400 μm129

Fig 5. 11 Microscopic image of GO-coated LPG (right) and a bare, uncoated LPG (left). ..129

Fig 5. 12 Transmission spectra of the LPG before and after coating, in the wavelength region 1584 nm to 1604 nm. 130

Fig 5. 13 (a) Experimental setup used for humidity sensing (b) Humidity Chamber.....131

Fig 5. 14 Spectrum of the LS1 Ocean Optics broadband light source.....131

Fig 5. 15 Humidity response of a bare LPG used for cross-comparison. 132

Fig 5. 16 Transmission spectra of GO coated LPG at different relative humidity levels. 133

Fig 5. 17 Schematic of humidity sensing at GO thin films [5-9].....134

Fig 5. 18 Swelling of GO thin film layers in the presence of water molecules [5-17]. 134

Fig 5. 19 Intensity variations of the resonance band centred at 1592 nm at different RH levels. 135

Fig 5. 20 (a) Transmission spectra of GO coated LPG at different temperatures (b) Centre wavelength of the resonance band as a function of temperature. 136

Fig 6. 1 Sensing applications of GO [6-13]. 145

Fig 6. 2 (a) Sensing principle of the GO/SWCNT coated etched FBG based biosensor (b) Change in the surrounding medium which acts as cladding of the etched FBG as a function of concentration of Con A solution [6-14]. 146

Fig 6. 3 Schematic of the glucose sensing mechanism for etched FBG sensor coated with the APBA-RGO complex [6-15]. 146

Fig 6. 4 Schematic illustration of fibre optic biosensor based on GO-coated DLPG: (a) DLPG silica fibre surface with alkaline treatment (b) Silanization by APTES (c) GO deposition (d) IgG immobilization via EDC/NHS (e) Passivation of unreacted sites by BSA blocking solution (f) Binding interaction between probe bioreceptor (IgG) and target analyte (anti-IgG) [6-17]. 147

Fig 6. 5 Dependence of wavelength shift against anti-IgG concentrations. The red line is the best logistic fitting curve [6-17].....148

Fig 6. 6 Schematic (not at scale) of: (a) single-ended LPG sensor; (b) Sensor surface bio-functionalization and sensing mechanism (in inset the Raman spectrum of GO) [6-24]. 149

Fig 6. 7 Spectrum of LP07 band of sample LPG1 acquired in PBS after the incubation of each concentration of bBSA [6-24].....149

Fig 6. 8 Calculated relationship between resonant wavelengths and grating periods for the first 30 cladding modes in B/Ge co-doped fibre. Open circles, dispersion turning points of the phase curves [6-25]. 151

Fig 6. 9 Measured transmission spectra before and after the transition from the dual-resonance state (solid curves) to the dispersion turning point (dotted curves) (a) ʌ = 202.5 μm (b) ʌ= 175 μm (c) ʌ= 153 μm (d) ʌ= 133 μm (e) ʌ= 120 μm (f) ʌ= 109 μm [6-25].....152

Fig 6. 10 (a) Simulated phase curves of a dual-peak LPG of 160 μm period for reduced cladding radii from 62.5 to 51.5 μm (b) Spectral evolution of a dual-peak LPG with a period of 158 μm under increased (arrow direction) UV exposure [6-26].....153

Fig 6. 11 Transmission spectrum of the Λ = 153 μm grating for different values of the SRI [6-12]. 154

Fig 6. 12 Setup used for the deposition of GO on the fibre surface. 156

Fig 6. 13 SEM images of the fibre surface of (a) bare fibre (b) LPG (c) DLPG. 156

Fig 6. 14 EDAX spectrum of the GO coated fibre surface of the DLPG. Inset shows the zoomed SEM image of the coated GO layer on DLPG and the respective red boxed area selected to obtain the EDAX analysis.....157

Fig 6. 15 Transmission spectra of uncoated and GO coated LPG. 158

Fig 6. 16 Transmission spectra of uncoated and GO coated DLPG. 159

Fig 6. 17 (a) Transmission spectra of bare DLPG measured in different sucrose concentrations (b) Zoomed evolution of LP_{012} mode (c) Zoomed evolution of $LP013blue$peak (d) Zoomed evolution of $LP013red$ peak. 161

Fig 6. 18 (a) Transmission spectra of GO- DLPG measured in different sucrose concentrations (b) Zoomed evolution of LP_{012} mode (c) Zoomed evolution of $LP013blue$peak (d) Zoomed evolution of $LP013red$ peak. 162

Fig 6. 19 Dual peak separation of GO-DLPG and LP_{08} wavelength shift of GO-LPG under varying external RI values. 163

Fig 6. 20 Transmission spectra of GO-LPG biosensor probe under different BSA concentrations. 164

Fig 6. 21 (a) Transmission spectra of bare DLPG measured in different BSA concentrations (b) Zoomed evolution of LP_{012} mode (c) Zoomed evolution of $LP013blue$peak (d) Zoomed evolution of $LP013red$ peak. 165

Fig 6. 22 (a) Transmission spectra of GO coated DLPG measured in different BSA concentrations (b) Zoomed evolution of LP_{012} mode (c) Zoomed evolution of $LP013blue$peak (d) Zoomed evolution of $LP013red$ peak. 166

Fig 6. 23 Wavelength shift of the sensor probes with varying BSA concentrations. 167

Fig 6. 24 FTIR spectra of GO, BSA and GO-BSA [6-31].....168

Table of Tables

Table 3. 1 Summary of the properties and characteristics of graphene nanomaterial-based fibre optic sensors 80

Table 4. 1 Spectral shift of the LPG sensors before and after GO coating.....109

Table 5. 1 Comparison between the responses of optical RH sensors coated with different material 137

Acknowledgements

First and foremost, I would like to express my heartfelt gratitude to my supervisors, Professor Kenneth Grattan, Professor Tong Sun and also Dr. Weiping Wu for their unending help, support and guidance, which helped me immensely in successfully completing this research programme. It was an honour and a privilege to work under such professional and kind-hearted experts in the field.

I would also like to thank Erasmus Mundus Leaders programme for giving me the opportunity to conduct a PhD programme at City, University of London. Special thanks to Professor Hairul Azhar, Professor Azizur Rahman and Anna Hajduk for their continuous help and support extended to me during the application process.

Special thanks to my fellow researchers, Dr. Matthias Fabian, Dr. Miodrag Vidakovic, Dr. Ye Chen, Dr. Hien Nguyen, Dr. Bruno Rente, Rahul Kumar and Dr. Souvik Ghosh for your suggestions, ideas and most importantly, for picking me up whenever I was overwhelmed and exhausted without much progress, which I believe to be a part of every PhD researchers' life. Without your encouraging words and insightful chats, my journey would have been a much longer and a lonely one.

I would also like to thank Dr. Lourdes Alwis and Leonardo Binetti for their continuous support with material characterisation. Special thanks to Caroline Sipos and Brigita Juristic for allowing me to be part of London City Incubator, which helped me immensely in developing my business skills.

Finally, I would like to extend my warmest gratitude to my wife, Dinuka, for putting up with all my tantrums while continuously believing in me and encouraging me to be the best version of myself. Special thanks go to my parents and Nirmanie's parents for everything that they have done in every part of my life. Last but not least, I would like to express my deepest gratitude to my son, Seniya, for being a bundle of joy when the going gets tough and filling my heart with laughter, enthusiasm and hope.

Copyright Declaration

Abstract

Graphene, a “wonder material”, is the world’s thinnest, strongest, and stiffest material, as well as being an excellent conductor of heat and electricity. Graphene oxide (GO), a derivative of graphene with oxygen containing groups at its basal plan and its edges, has gained significant attention as a sensing material in chemical and biochemical sensing due to the extremely rich surface chemistry that it possess in comparison with other graphene nanomaterials. On the other hand, optical fibres have emerged as a major sensing mechanism due to their attractive features such as, ability to provide remote sensing, multiplexing capability, resistant to harsh environments, small size and light weight, biocompatibility and immune to electromagnetic interference. Thus, there lies an opportunity to combine the advantages of fibre optic sensors with unique characteristics of GO to develop novel sensor systems. In this regard, if a thin film overlay of GO is deposited on a Long Period Gratings (LPGs) surface, the Refractive Index (RI) of the coated GO overlay will change with perturbations in the surrounding medium, which will be reflected in the transmission spectrum of the GO coated LPG, forming the basis of a graphene nanomaterial-based fibre optic sensor system. This thesis reports the design and development of a suite of GO coated LPG based external RI sensors in the fields of sodium chloride (NaCl) salinity measurement in water, Relative humidity (RH) measurements in structural health monitoring and Bovine Serum Albumin (BSA) concentration measurement in biosensing, all of which illustrate the versatility of the GO coated LPG sensor approach.

An external RI sensor system which contained GO coated LPG as the basis was developed and its performance was analysed with varying overlay thicknesses of GO to optimise the sensor design. The developed sensor system increased the external RI sensitivity of an uncoated LPG by 83%, which highlighted the enhanced RI sensitivity achieved by GO overlays on fibre gratings. Surrounding RI variations were achieved with the use of NaCl solutions with varying concentrations, which successfully established the NaCl salinity measuring capability of the developed GO coated LPG sensor probes. These promising results indicated that GO coated LPGs provide an efficient and stable basis for the development of more species-specific, highly sensitive chemical and biochemical sensor systems.

A satisfactory linear response of a GO coated LPG based RH sensor probe was achieved in the RH region of 60%RH - 95%RH, reporting a sensitivity of 0.15 dB/%RH at room temperature. Simultaneous measurement of temperature and RH levels was achieved and by this, the GO-coated LPG sensor probe has shown that it has the potential to be developed into a temperature

compensated fibre optic humidity probe by optimising its temperature response in the operational RH range of 60%RH – 95%RH.

A novel but simple method of measuring BSA protein concentration in a label-free manner has been introduced by depositing a thin layer of GO on a Dual Resonance Peak LPG (DLPG) surface. Strong binding affinity of GO with protein molecules was successfully established by analysing the BSA concentration detection performance of the fabricated GO coated DLPG sensor probe. A limit of detection (LOD) of 0.9 µg/mL was achieved, which proved to be 11 times better in sensitivity than that of a GO-coated LPG sensor probe. A highest sensitivity of 22 nm/(g/mL) was achieved by the dual peak separation of the GO coated DLPG sensor probe in the BSA concentration region from 0.2 g/mL to 0.8 g/mL. These promising results indicated that the GO coated DLPG sensor probe developed in this work has the ability to be used as highly sensitive, label-free biosensing platform, which could also be made species-specific by modifying the GO surface with other species-specific functional groups.

The research concludes by considering future directions for the work conducted in this thesis.

Glossary of Symbols, Abbreviations and Chemicals

Abbreviations:

2D	Two Dimensional
3D	Three Dimensional
CCG	Chemically Converted Graphene
CF	Carbon Fibres
CNT	Carbon Nanotubes
CVD	Chemical Vapour Deposition
DI	De-ionized
DLPG	Dual Peak Resonance LPG
DNA	Deoxyribonucleic Acid
DTP	Dispersion Turning Point
EDAX	Energy Dispersive X-ray Analysis
eFBG	Etched Fibre Bragg Grating
ESA	Electrostatic Self Assembly
FBG	Fibre Bragg Grating
FEM	Finite Element Method
FRET	Fluorescent Resonance Energy Transfer
FTIR	Fourier-Transform Infrared
GCNT	Graphene oxide Carbon Nano Tubes
GMHW	Graphene Microfibre Hybrid Waveguide
GO	Graphene oxide
GQD	Graphene Quantum Dots
HRI	High Refractive Index
IR	Infrared
LB	Langmuir-Blodgett
LED	Light Emitting Diode
LOD	Limit of Detection
LPG	Long Period Grating
MMF	Multimode Fibre

MWCNT	Multi-Walled Carbon Nanotubes
MZI	Mach-Zehnder Interferometer
NMR	Nuclear Magnetic Resonance
OOT	Optimum Overlay Thickness
OSA	Optical Spectrum Analyser
PCF	Photonic Crystal Fibre
PL	Photoluminescence
POF	Plastic Optical Fibre
rGO	Reduced Graphene Oxide
RH	Relative Humidity
RI	Refractive Index
SEM	Scanning Electron Microscope
SF	Silk Fibre
SMF	Single Mode Fibre
SPR	Surface Plasmon Resonance
SPW	Surface Plasmon Wave
SWCNT	Single Walled Carbon Nanotubes
TFBG	Tilted Fibre Bragg Grating
UV	Ultraviolet
VOC	Volatile Organic Compound

Symbols:

% wt	Weight to weight percentage
ω	Angular frequency
Λ	Grating period
ξ	Perturbation
β	Propagating constant
Δ	Variation of a particular parameter
ΔC	Local change in analyte concentration
β_{clad}^{m}	Propagating constant of the m^{th} order cladding mode

β_{core}	Propagating constant of the fundamental core mode
K_i	Coupling coefficient of the i^{th} order cladding mode
P_w	Partial water pressure
P_{ws}	Saturation water vapour pressure
T_i	Minimum transmission of the i^{th} cladding mode
n_{GO}	Refractive index of GO overlay
$n_{cladd.m}^{eff}$	Effective refractive index of the m^{th} order cladding mode
n_{core}^{eff}	Effective refractive index of the fundamental core mode
σ_g	Thermo-optic coefficient of graphene
µm	Micro metre
µM	Micro-Mole
Å	Angstrom
aM	Attomole
℃	Celcius
c	Speed of light
cfu	Colony-forming unit
cm	Centi-metre
dB	Decibel
dBm	Decibels with respect to a milliwatt
E	Effectiveness of the interaction between GO and the analyte
EH	Hybrid mode in which TM mode dominates
ε	Axial strain
g	Gram
HE	Hybrid mode in which TE mode dominates
Hz	Hertz
k	Free space propagation constant
K	Kelvin
L	Length
LP	Linearly Polarized
m	Metre

M	Mole
mg	Milli-gram
mJ	Milli-joule
mL	Milli-litre
mm	Milli-metre
mM	Milli-mole
mV	Milli-volt
n	Index of refraction
n_{clad}	Cladding refractive index
n_{core}	Core refractive index
n_{eff}	Effective refractive index
nm	Nanometre
nM	Nano-mole
n_{sur}	Surrounding refractive index
PFU	Plaque-forming unit
pM	Pico-Mole
ppb	Parts per billion
ppm	Parts per million
RIU	Refractive index unit
rpm	Revolutions per minute
s	Seconds
S	Sensitivity
S	Siemens
S_{RI}	Sensitivity to the external RI change
T	Temperature
TE	Transverse Electric mode
TPa	Tera-pascal
W	Watt
δ	Small variation (of a particular parameter)
λ	Wavelength

λ_{Bragg}	Bragg wavelength
λ_{res}	Resonance wavelength
με	Micro strain
π	Pi

Abbreviations of Chemicals:

Al_2O_3	aluminium oxide
APBA	amino phenyl boronic acid
aPS	atactic polystyrene
APTES	(3-Aminopropyl)triethoxysilane
B	boron
bBSA	biotinylated BSA
BSA	Bovine Serum Albumin
C	carbon
Cd^{2+}	cadmium ions
CO_2	carbon dioxide
Con A	concanavalin A protein
CRP	C-reactive protein
Cu	copper
D_2O	dicarbon monoxide
DM	dendrimers
DMF	N, N-dimethylformamide
DXB	double crossover DNA
EDC	1-ethyl-3-(3-dimethylaminopropyl)-carbodiimide
KrF	krypton fluoride
Ge	germanium
H	hydrogen
H_2O_2	hydrogen peroxide
H_2SO_4	sulphuric acid
HbA1c	D-glucose and glycated haemoglobin

HCl	hydrochloric acid
HF	hydrofluoric acid
HNO_3	nitric Acid
IgG	immunoglobulin G
IPA	isopropyl alcohol
$KClO_3$	potassium chlorate
$KMnO_4$	potassium permanganate
Mn_2O_7	diamanganese heptoxide
NaCl	sodium chloride
$NaNO_3$	sodium nitrate
NH_3	ammonia
NHS	N-hydroxysuccinimide
NMP	N-methyl-2-pyrrolidone
NO_2	nitrogen dioxide
O	oxygen
PBS	Phosphate buffered saline
PC	polycarbonate
PDDA	poly(diallyldimethylammonium chloride)
PETIM	poly(propyl ether imine)
PI	polyamide
PMMA	poly(methyl methacrylate)
PVA	polyvinyl alcohol
SA	streptavidin
Si	silica
SiC	silicon carbide
SnO_2	tin oxide
ssDNA	single stranded DNA
TG	triacylglyceride
THF	tetrahydrofuran

Chapter 1

Introduction and Background

1.1 Introduction

Two-dimensional (2D) materials were introduced with the successful isolation of graphene in 2004 by Andre Geim and Konstantin Novoselov [1]. Since then, these special materials, especially graphene, have attracted increasing interest among the scientific community due to the exceptional and often unique properties and characteristics they possess. Scientists are still working on the true potential of their interesting characteristics and for the past decade, graphene, a 2D carbon nanomaterial with one atom thickness, has been making headlines in various scientific fields such as physics, chemistry and material sciences for many reasons. Its outstanding electrical and optical properties make it an ideal candidate for a range of applications, such as flexible and printable electronics, high performance transistors, anti-corrosion paints and coatings, drug delivery and faster Deoxyribonucleic Acid (DNA) sequencing, clean energy devices, efficient solar panels, graphene-polymer nanocomposites, highly sensitive and fast response sensors and many more [2].

However, to have available an effective and easy-to-use method of producing high quality graphene in large quantities is essential to allow the exploitation of the full potential of graphene in many engineering applications. In this regard, the material graphene oxide (GO) produces a useful solution with many other advantages. GO is a mono-layer graphene sheet, with oxygen containing groups such as epoxy and carboxyl groups at its basal plane and its edges. Due to these oxygen containing groups, GO offers a unique set of characteristics such as being easily dispersible in aqueous and organic compounds and the establishment of chemical and physical interactions with diverse chemical species, nanoparticles and biostructures: it can be easily turned into reduced GO (which has similar characteristics to graphene) by chemical or thermal reduction, along with a simple and low-cost bulk synthesis process. Therefore, GO can be used as a good substitute, in many graphene-based applications. Among these applications, graphene and GO have been widely used in the field of sensing during the last decade due to their extremely high surface to volume ratio, low noise and high

electron mobility. There is a wide range of graphene nanomaterial-based electronic, chemical and biochemical sensors exploited in the areas such as environmental monitoring, gas detection and biosensing [3]. Their study is an important part of this thesis.

A further area of study is the use of optical fibres, which were developed mainly as optical waveguides for the benefit of the telecommunication industry, as an alternative to copper wires. Benefitting from the rapid advancements of optical fibre technology stimulated by the increasing demands of the communications sector, optical fibre sensors have become increasingly popular among other sensing technologies in the last few years, especially due to the major advantages they offer over their electronic counterparts. Optical fibre sensors are typically compact, lightweight and small in size. They are biocompatible, immune to electromagnetic interference and they can withstand corrosive and hazardous environments and usually significantly high temperatures. Another major characteristic that optical fibre sensors benefit from is that the optical fibre itself can act both as the transmission medium and the transducer, which enables remote sensing and multiplexing [4]. These features make them highly suitable for some specific applications such as structural health monitoring, chemical sensing and biosensors. One of the major developments in the field of optical fibre sensing is the discovery of photosensitivity in optical fibres by Kenneth Hill in 1978 [5]. This discovery led to the development of the Fibre Bragg Grating (FBG) and the Long Period Grating (LPG), used widely in sensors, exploiting their sensitivity to strain and temperature. The important characteristics and several relevant, important applications of these sensors are discussed in detail in Chapter 2.

With many industries seeking out suitable, innovative technologies to solve measurement problems to tackle ongoing and indeed an increasing range of monitoring challenges, especially in the structural health monitoring, chemical sensing and biosensor fields mentioned above, there lies a significant opportunity to *combine* the unique characteristics of 2D materials (such as graphene and GO) *and* optical fibres to create a type of sensor that exploits the positive characteristic of these two technologies to develop novel, more efficient, highly sensitive and selective sensor systems. However, to date, publications on optical fibre sensors based on graphene materials have been limited (and are discussed in some detail in Chapter 3) where the ‘gaps in this market’ can be seen.

Building on that and the opportunity to develop new sensor systems that take full advantage of the strengths of these technologies in tandem, this research programme has been focused on

exploiting this opportunity, while addressing some of the pressing issues faced by industries and scientists. First, this thesis focuses on solving the problem of measuring NaCl salinity concentration in water, as measuring NaCl salinity concentration in fresh water is very important to tackle current climate changing challenges since many aquatic organisms have varying abilities to survive at different salinity levels as the solubility of oxygen in water decreases as salinity increases. Secondly, the issue of measuring and monitoring of relative humidity and temperature has been addressed. Measuring relative humidity is a significant factor in food storage industry, health and agriculture sectors and also in semiconductor fabrication. Monitoring relative humidity in structural health monitoring is also very important as the moisture level within a structure directly influences the rate of corrosion. Therefore, monitoring the moisture level inside a structure, in real time, enables engineers to monitor the level of corrosion and essentially, estimate the health of the structure. Thirdly, this thesis focuses on Bovine Serum Albumin (BSA) detection and measuring its concentration. Measuring BSA protein concentration is very important in the fields of biochemical, food, disease and drug research and immunology. It is also a very useful marker to follow the bovine disease, mastitis, which causes significant losses in the agricultural industry. This variety of applications has been chosen to be representative of the variety of new applications that have opened up with the development of graphene technology for optical fibre sensors. Thus, it is evident that it would be highly beneficial to be able to develop new sensor systems that could be made available to detect and monitor these, and other important parameters, across a range of engineering applications.

1.2 Aims and Objectives

In light of the discussion above and the gap in the market identified from the combination of these optical fibre and graphene-based technologies, this research has aimed to combine the advantages offered by both graphene-based nanomaterials *and* optical fibre sensors to develop and assess the performance of a suite of such sensors, focusing (as will be discussed later) on GO-coated LPG based sensors, to address better the challenges faced by several, key representative industrial sectors such as structural health monitoring, refractive index (salinity) measurements and protein measurements in biosensing. A series of projects was undertaken to achieve this, and the major objectives of the research work reported in this thesis are as follows.

- To conduct a comprehensive literature review on grating based fibre optic sensors as a background to this research
- To conduct a comprehensive review on graphene nanomaterials-based fibre optic sensors and their applications to understand the potential of the excellent properties of graphene nanomaterials for optical fibre sensors
- Having thus identified the opportunities from the combination of these two technologies, to design and fabricate consistent GO thin film layers that can be coated on an optical fibre surface to develop innovative GO-coated fibre optic sensors and perform material characterisation to quantify the performance of the GO nanomaterials synthesised, overcoming problems identified in consistent fabrication of the devices
- To develop a series of GO-coated LPG based external Refractive Index (RI) sensors to measure NaCl salinity concentrations in water and to investigate the performance of these sensors with regard to different GO overlay thicknesses that can be used
- To create a suite of graphene-based, in-fibre grating sensors for relative humidity measurement and also investigate the respective temperature responses to compare their performance with those using other sensing materials
- To conduct experiments with GO coated in-fibre gratings to measure BSA protein concentrations with the objective of developing and characterising GO-coated LPG-based biosensors
- To draw relevant conclusions on the effectiveness of the graphene nanomaterial-based sensors developed and to propose related future work
- To disseminate the results of the work at major conferences and in the peer reviewed international literature following consideration of the Intellectual Property developed

1.3 Structure of the Thesis

The thesis is structured as follows, encompassing seven chapters which sequentially detail and describe a comprehensive programme of research work carried out in order to achieve the aims and objectives mentioned above.

Chapter 1 begins with a brief introduction to the background to the thesis and to graphene nanomaterials and the unique features they possess due to their two-dimensional nature. This is followed by an introduction to optical fibre sensors describing why they show advantages over their electronic counterparts. The opportunity arising from combining these unique

technologies to solve some pressing industrial problems is identified and described. The chapter concludes with a review of the aims and objectives and the structure of this thesis.

Chapter 2 consists of a detailed overview of current work in grating-based optical fibre sensors, concentrating mainly on sensing mechanism and characteristics of LPG based fibre optic sensors, highlighting their advantages for RI sensing over other optical fibre sensor designs. A number of coated LPG based sensor applications are discussed and, based on the literature, the gaps in the market identified as the basis of the direction of the further work described in subsequent chapters.

Chapter 3 focuses on a comprehensive overview of the graphene nanomaterial-based fibre optic sensor systems available to date. Based on several representative examples identified from the literature, the advantages of combining graphene nanomaterials with fibre optic sensors are highlighted and a direction for the work employing methods of GO synthesis have also been discussed.

Chapter 4 reports the work undertaken to develop a GO-coated LPG based external RI sensor system, whose performance is illustrated here to measure the NaCl salinity concentration in water. GO synthesis methods used throughout this research are discussed in detail while presenting the work done to develop and optimise coating methods to deposit the prepared GO thin films on the optical fibre surface and create a stable, consistent platform for the sensor work, followed by results on GO material characterisation. The performance of a suite of GO-coated LPG-based external RI sensors, each with increasing GO overlay thickness is also described, with a view to the optimisation of the sensor design.

Chapter 5 reports research carried out to develop a temperature-compensated GO-coated LPG-based fibre optic relative humidity and temperature sensor. The performance of the humidity sensor developed in this research has been compared with other graphene nanomaterial-based optical sensors and optical fibre-based humidity sensors using other technologies reported in literature.

Chapter 6 reports the design, fabrication and implementation of a GO-coated LPG-based sensor probe used for measuring BSA concentrations, highlighting how the unique characteristics of GO in an optical fibre context can be exploited in the field of biosensing. The performance of this BSA sensor has been enhanced by using a dual-peak LPG, which utilises highly sensitive higher order cladding modes and the results of this study are presented, in this chapter.

Chapter 7 concludes the thesis with a summary of results obtained through the work carried out in this research programme, highlighting the main achievements with reference to the aims and objectives discussed in Chapter 1. Based on the results obtained and thus the knowledge and experience gained during the course of this research, some interesting future work has been proposed, while pointing out some of the limitations of the technologies identified from this research.

1.4 Summary

In this chapter, a brief introduction to graphene-based nanomaterials and optical fibre sensors has been provided, highlighting the importance of combining these two technologies to develop novel 2D material-based optical fibre sensor systems. The aims and the objectives of this research have been highlighted, followed by the structure of the thesis, outlining the content of each chapter and the path towards reaching conclusions which represent an advance of knowledge in this field through the work done.

1.5 References

[1] Novoselov K S, Geim A K et al., "Electric Field Effect in Atomically Thin Carbon Films," Science, 666-669, 2004.

[2] Mohan V B, Lau K, Hui D, Bhattacharyya D, "Graphene-based materials and their composites: A review on production, applications and product limitations," Composites Part B: Engineering, 142, 200-220, 2018.

[3] Hernaez M, Zamarreño C R, Melendi-Espina S, Bird L R, Mayes A G, Arregui F J, "Optical Fibre Sensors Using Graphene-Based Materials: A Review," Sensors, 17, 155, 2017.

[4] Yeo T L, Sun T, and Grattan K T V, "Fibre-optic sensor technologies for humidity and moisture measurement," Sensors and Actuators A: Physical, 144, 1, 280-295, 2008.

[5] Hill K O, "Photosensitivity in optical fiber waveguides: Application to reflection filter fabrication," Applied Physics Letters, 32, 15, 1978.

Chapter 2

Coated Long Period Gratings (LPGs) for Fibre Optic Sensor Applications

2.1 Introduction

All the GO-coated fibre optic sensors developed in this thesis were based on LPGs and as such, it is essential to have a strong understanding of fundamental theoretical concepts that govern the light propagation in LPGs to understand the sensing mechanisms of the GO based fibre optic sensors discussed in this thesis. LPGs were, in summary, chosen as the basis of this sensor scheme (by comparison to the more familiar FBG-based methods) predominantly due to the fact that LPGs are intrinsically sensitive to perturbations in the surrounding RI, whereas external RI of FBGs must be realised by carrying out clad etching procedures, which involves harmful chemicals such as HF.

In this chapter, given the above, the working principles of a LPG are discussed in detail by focusing on mode coupling in an optical fibre as well as a fibre grating structure. The important fundamentals of FBGs and LPGs (and their comparison) are discussed, while presenting a review (and thus a selection of) the methods used to fabricate such optical fibre grating structures. This is followed by a comparison between typical LPG- and FBG-based fibre optic sensors and a review of the coated LPG-based fibre optic sensors discussed in the literature, emphasizing on the advantages of using LPGs in sensing and their intrinsic characteristics and sensitivities to strain, temperature and external RI sensing. Although a variety of grating structures such as chirped, tilted and tapered have been reported, this chapter and the thesis are focused on uniform grating structures inscribed on single mode fibres because these more complex and difficult to fabricate fibre structures do not offer particular advantages for the application under consideration.

2.2 Mode Coupling in Optical Fibres

A mode in an optical fibre can be defined as a set of electromagnetic waves that participates in propagation of energy in the fibre [1]. There exists a finite number of guided modes travel in a

fibre with discrete propagating constants (β) and the optical characteristics of these modes are governed by the optical source wavelength and fibre parameters. These propagation constants can be realised by the use of Maxwell's equations and electric and magnetic field boundary conditions at the core-cladding interface [1].

The propagation constant β of a mode in an optical fibre can be defined as [2],

$$\beta = nk \tag{2.1}$$

Where, n is the effective RI of the mode and k is the free space propagation constant at wavelength λ $(k = 2\pi/\lambda)$. Therefore, the β values of the guided modes in an optical fibre are confined to $n_2k<|\beta|<n_1k$, where n_1 and n_2 correspond to core and cladding RI, respectively. β can also be illustrated by

$$\beta = \frac{\omega n}{c} \tag{2.2}$$

Where ω is the angular frequency and n is the effective index of refraction $(n_2<n<n_1)$ and c is the speed of light in vacuum. Forward propagating guided modes (β>0) and reverse-propagating guided modes (β<0) of an optical fibre as functions of the optical frequency are presented in Fig. 2.1 below [3].

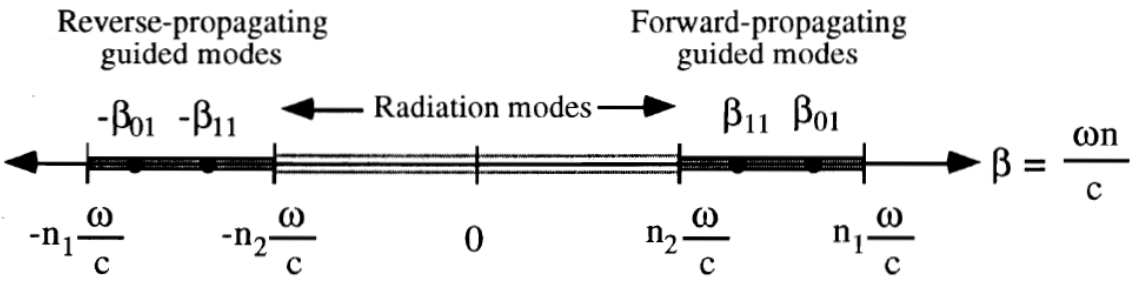

Fig 2. 1 Propagating constants of the forward and reverse-propagating guided modes in an optical fibre [3].

As can be seen in Fig. 2.1, the discrete β values of the guided modes are shaded in black. β_{01} and β_{11} are the propagation constants of the two lowest order forward-propagating guided modes.

Apart from the guided modes, radiation modes also satisfy the Maxwell's electromagnetic equations and boundary values [2]. Radiation modes are not guided by the fibre and they arise mostly due to the presence of waveguide imperfections which lead to a continuous loss of power from the guided modes. As illustrated in Fig. 2.1, there exists an infinite number of

radiation modes in an optical fibre in the region of $0<|\beta|<n_2k$, which possess a continuum of complex β values. When guided modes are analysed, the cladding is considered to be infinite [1] due to the rapidly decaying optical fields of the guided modes outside the core that contain insignificant field values at the outer boundary of the cladding. However, when radiation modes are analysed, the same assumption cannot be applied as radiation modes extend to infinity and are strongly influenced by the cladding-surrounding medium boundary [3]. Moreover, some of the radiation modes are confined to the cladding due to the reflection occurs (based on the RI values of the cladding and the surrounding medium) at the cladding-surrounding medium interface and these modes are termed as cladding modes [2]. The propagation constants of these cladding modes in an optical fibre are bounded by $n_3k<|\beta|<n_2k$, where n_3 is the RI of the medium surrounding the cladding (with air as the ambient index, $n_3=1$). β values corresponding to the cladding modes are illustrated in Fig. 2.2 below [3].

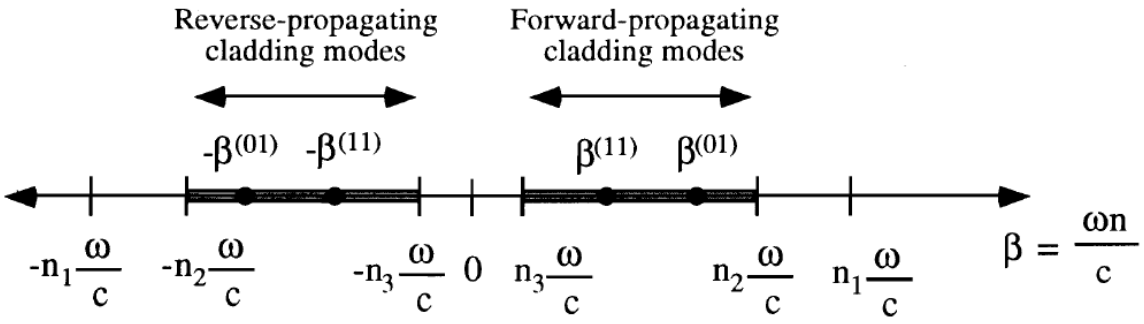

Fig 2. 2 Propagation constant distribution of cladding modes in an optical fibre [3].

As can be seen in Fig. 2.2, cladding modes can travel either in the forward or backward direction, similar to guided modes. Due to their high density, cladding modes almost form a continuum [2]. Cladding modes are affected significantly by the bends in the fibre, scattering and optical absorption caused by the polymer fibre jacket and the coupling of energy from guided modes to discrete cladding modes forms the principle of operation of LPGs.

In 1953, Pierce [4] analysed the transfer of power between two propagating modes in an optical fibre. In such fibre structures, power is transferred in the form of modes. When an ideal scenario is considered, the modes discussed above should propagate through the fibre without losing or gaining any power along the fibre length. However, systems that are used in practical scenarios possess imperfections such as variations in core and cladding diameters along the length of the fibre, inhomogeneous doping that causes changes in the RI of core and the cladding, the presence of another waveguide in close proximity and fibre bending. These variations results in energy coupling between two modes propagating in a fibre waveguide structure.

Coupled mode theory enables us to analyse the interactions and power transfers between two propagating modes in a waveguide structure, such as an optical fibre. Therefore, it can be used to investigate the transfer of optical power between co-propagating and counter-propagating modes in a fibre grating structure, such as a FBG or a LPG, and thus, to realise phase matching conditions that enables significant exchange of optical power between two modes. In a fibre grating structure, usually, a periodic perturbation exists in the core RI. Coupling between two modes is caused by this periodic RI perturbation. If two propagating modes with discrete propagating constants β_1 and β_2 in a fibre grating structure with a periodic core RI perturbation of period Λ and is considered, the difference in their propagating constants Δ can be expressed as [3],

$$\Delta = \beta 1 - \beta 2 - \frac{2\pi}{\Lambda} \tag{2.3}$$

To enable synchronous transfer of optical power between these two modes, the condition $\Delta=0$ needs to be achieved, which is commonly defined as the phase-matching condition. Thus, phase matching condition of a fibre grating structure with a periodic perturbation can be defined as [3],

$$\Delta\beta = \beta 1 - \beta 2 = \frac{2\pi}{\Lambda} \tag{2.4}$$

where $\Delta\beta$ is the differential propagation constant and Λ is the grating period. The propagating constants β_1 and β_2 will be positive for forward propagating modes and negative for reverse propagating modes. In the next subsection, mode coupling and properties of a FBG and a LPG will be discussed in detail based on the phase matching condition defined above.

2.3 Properties of Fibre Gratings

In this section a brief cross-comparison of FBGs and LPGs, in the context of their use in sensor applications, is given.

2.3.1 Fibre Bragg Gratings (FBG)

FBGs were first demonstrated by Hill et al. [5], from the Communications Research Centre in Canada in 1978. In a FBG, power from the forward propagating fundamental core mode couples with its contra-propagating counterpart, which is caused by the spatially modulated index of refraction present in its core. If a FBG with core RI perturbation with a spatial

periodicity Λ is considered, the mode propagating mechanism can be presented by Fig. 2.3 below [3].

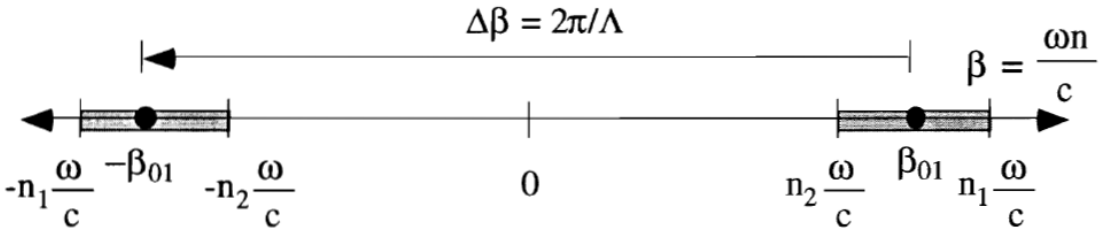

Fig 2. 3 Mode coupling mechanism in FBGs [3].

β_{01} is the propagation constant of the forward propagating fundamental core mode, where,

$$\beta_{01} = \frac{2\pi n_{eff}}{\lambda} \tag{2.5}$$

at wavelength λ. n_{eff} is the effective RI of the fundamental core mode. As mentioned in section 2.2, $n_{clad} < | n_{eff} | < n_{core,}$ where, n_{core} and n_{clad} are RI of the core and the cladding, respectively. The propagation constant of the counter propagating guided mode has the same magnitude as the forward propagating fundamental core mode, but with opposite polarity. Thus, by substituting these values in equation 2.4, phase matching condition of a FBG can be written as,

$$\lambda_{Bragg} = 2n_{eff}\Lambda \tag{2.6}$$

where, λ_{Bragg} is termed the Bragg Wavelength. In a FBG, the forward propagating core mode (LP_{01}) couples with its reverse propagating counterpart at the Bragg Wavelength. Due to this phase matching phenomenon, λ_{Bragg} will be reflected back if a FBG is interrogated by use of a broadband light source. The working principle of a FBG is depicted in Fig. 2.4.

As can be seen from equation 2.6, Bragg wavelength is a function of the grating period (Λ) and the effective RI (n_{eff}) of the LP_{01} mode. Variations of the physical parameters strain and temperature can induce changes in both these parameters and thus, FBGs are intrinsically sensitive to strain and temperature. The wavelength shift caused by this intrinsic sensitivity has been used to develop various types of fibre optic sensors [7]. Further applications of FBGs can be found in [8-11] and the next part of this chapter is focused on the working principles of LPGs and their applications as sensors.

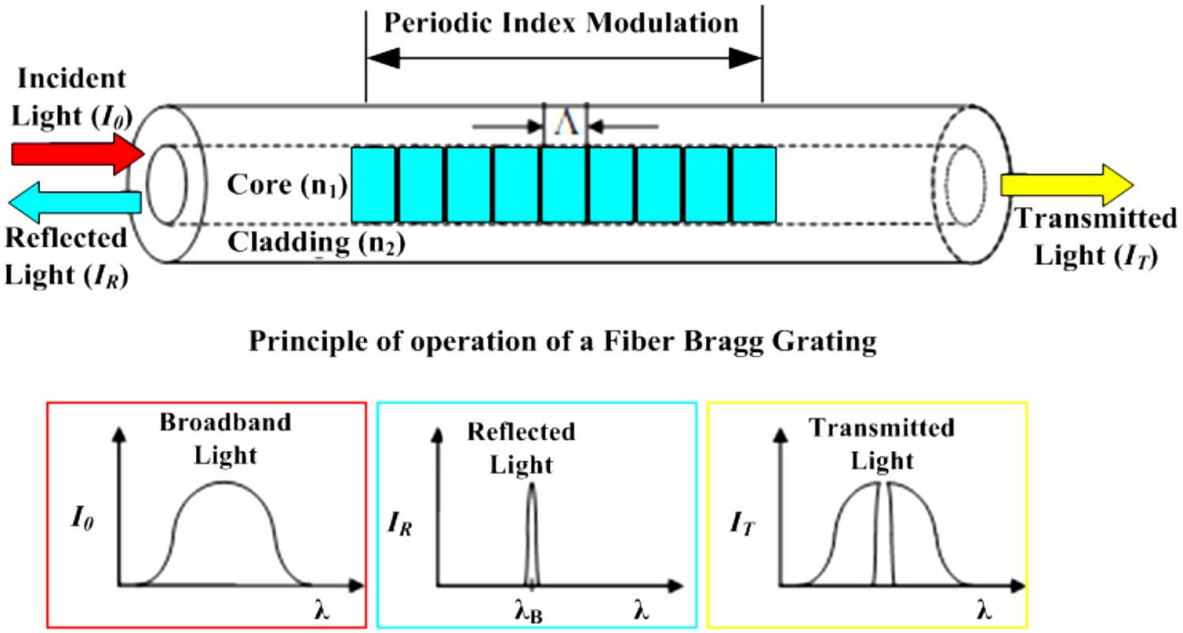

Fig 2. 4 Principle of operation of a FBG [6].

2.3.2 Long Period Gratings (LPG)

As discussed above, the working principle of a FBG is based on the mode coupling between the forward propagating fundamental core mode and its reverse-propagating counterpart. Therefore, as can be seen from Fig. 2.3, the two modes propagating in opposite directions need to overcome a larger modal mismatch to meet the phase matching condition ($\Delta\beta$) and as such, based on the equation 2.4, it is evident that a small value of periodicity (Λ) is required to achieve the phase matching direction.

In some applications, it is required to couple light from the forward propagating fundamental core mode (LP_{01}) to other co-propagating guided modes. Mode coupling between two forward propagating guided modes is illustrated in Fig. 2.5 below [3].

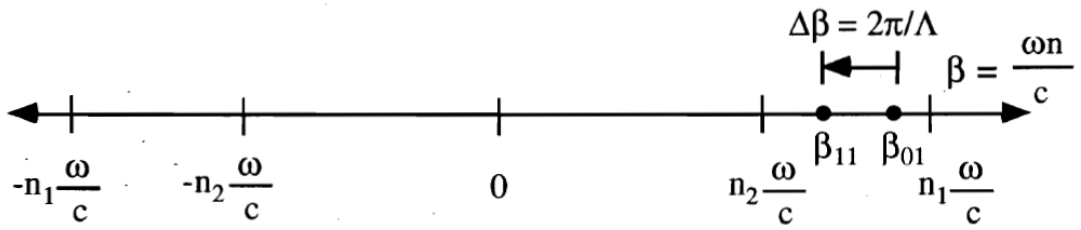

Fig 2. 5 Mode coupling between two forward propagating guided modes [3].

Due to the small differential propagation constant ($\Delta\beta$) that can be seen in Fig. 2.5 in comparison with Fig. 2.3, it is evident that large values of grating periodicity (Λ) are required to meet the phase matching condition in these kinds of grating structures. In practice,

periodicity of the devices that use mode coupling between two modes that propagate in the same direction are hundreds of micrometres (in contrast, periodicity of FBGs are usually less than 1µm) and thus, are called long period gratings. It should be noted that the LPGs discussed above in Fig. 2.5 use mode coupling between two guided modes and this kind of LPGs were first proposed by Hill et al. in [12]. A couple of similar LPG structures that use coupling between two guided modes are depicted in [13] and [14]. Such grating devices, though useful as modal couplers, require modal filters to be used for operational efficiency as such, increase the cost and the complexity of the optical systems [3].

In 1995, Vengsarkar et al. proposed the first LPG structure that coupled light between the fundamental core mode and co-propagating cladding modes [15]. These types of grating structures are usually realised by exposing a B/Ge co-doped fibre core to a UV laser beam with a periodic pattern to form a periodic RI perturbation in the photosensitive core. For the remaining portion of this thesis, unless otherwise specified, LPGs specifically refer to the grating structures that couple light from forward propagating fundamental core mode to the core propagating cladding modes. The working principle of such a LPG structure is depicted in Fig. 2.6.

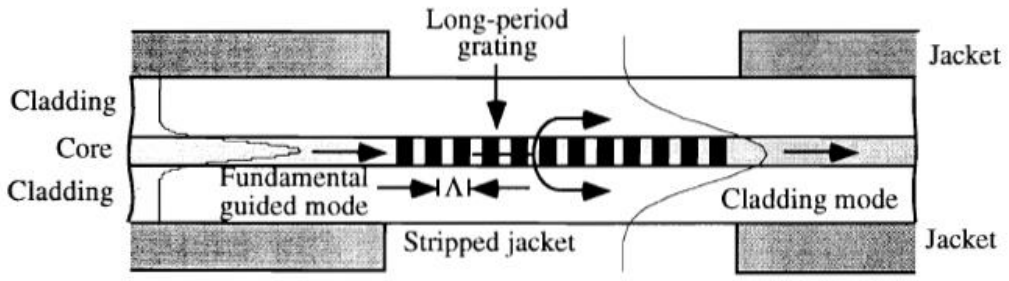

Fig 2. 6 Mode coupling in LPGs [3].

Due to the RI perturbation present in the core, light in the LP_{01} mode couples to the co-propagating LP_{0m} cladding order modes (m= 1,2,3,…..) at discrete wavelength values when the phase matching condition given in equation 2.4 is satisfied, which can be expressed specifically for LPGs as ,

$$\beta_{core} - \beta_{clad}^{m} = \frac{2\pi}{\Lambda} \tag{2.7}$$

where β_{core} is the propagating constant of the fundamental core mode, β_{clad}^{m} is the propagating constant of the m^{th} order cladding mode, and Λ is the grating period. These propagation constants can further be expressed as follows,

$$\beta_{core} = \frac{2\pi}{\lambda} n_{core}^{eff} \tag{2.8}$$

$$\beta_{clad}^{m} = \frac{2\pi}{\lambda} n_{clad,m}^{eff} \tag{2.9}$$

Based on (2.8) and (2.9), the resonance wavelength λ_{res} of an attenuation band caused by the light coupling between the fundamental core mode and the respective co-propagating cladding mode can then be written as:

$$\lambda_{res} = (n_{core}^{eff} - n_{cladd.m}^{eff})\Lambda_{LPG} \tag{2.10}$$

where n_{core}^{eff} and $n_{cladd.m}^{eff}$ are the effective refractive indices of the fundamental core mode and the m^{th} cladding mode, respectively. Λ_{LPG} is the grating period of the LPG.

The phase matched modes (LP_{0m}, m= 1,2,3,…) attenuate heavily due to the cladding absorption and as such, light at these discrete phase matched wavelengths (λ_{res} values corresponding to phase matched cladding modes) is lost from the fibre, resulting in a series of resonance loss bands in the transmission spectrum of a LPG, which can be seen in Fig. 2.7.

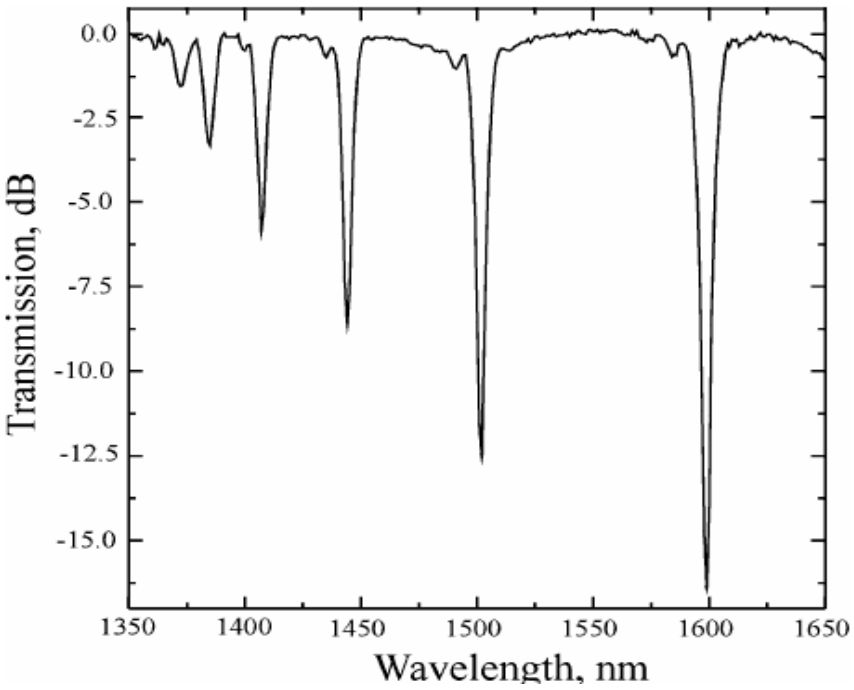

Fig 2. 7 Typical transmission spectrum of a LPG [3].

The resonance bands that can be seen in Fig. 2.7 have different values of intensities and bandwidth, which is a result of dissimilar coupling coefficients that are functions of the modal overlap.

The minimum transmission of loss bands in a LPG is governed by the equation [16],

$$T_i = 1 - sin^2 (K_i L) \quad (2.11)$$

where T_i is the minimum transmission of the i^{th} cladding mode and K_i is the coupling coefficient of the i^{th} cladding mode, which is obtained by the overlap integral of the core and cladding mode, and by the amplitude of the periodic modulation of the mode propagation constants. L is the length of the RI perturbation in the LPG grating structure. Therefore, it is evident that the magnitude of loss and the width of a particular resonance loss band depends on the coupling coefficient of the respective cladding order mode that couples with the fundamental core mode.

It is evident from equation 2.10 that, resonance wavelength (λ_{res}) of these loss bands is a function of the effective RI of the coupled cladding order mode ($n_{cladd.m}^{eff}$) and the grating period of the LPG (Λ_{LPG}). Fibre optic sensors have been developed by the use of this dependency and such sensing characteristics of LPGs will be discussed after the next sub section of this chapter, which focuses on fabrication techniques of LPG structures.

2.4 Fabrication of LPGs

Mode coupling in a fibre grating is achieved by introducing a periodic perturbation in the optical properties of the fibre. This can be realised either by physical deformation of the fibre or by a periodic RI modulation in the core of the fibre. Even though the latter of the two methods is used much more frequently, LPGs fabricated by deforming the core [17] or the cladding [18], micro tapering [19] and mechanically pressing the fibre [20] have been reported. LPGs have also been achieved in Photonic Crystal Fibres (PCFs) by periodically collapsing the holes of the fibre using CO_2 laser treatment [21].

There is a number of techniques available that can be used to achieve a permanent modification of the RI of the core in fabricating in-fibre LPGs. Relaxation of mechanical stress [22], Infrared (IR) irradiation using femtosecond pulses [23], electrical discharges [24], ion implantation [25] and irradiation by the use of a CO_2 laser [26] can be mentioned as examples for such techniques that have been reported in literature. The most common way of achieving a periodic RI modulation in the core is by use of UV exposure, which has been reported in [27-29].

The UV exposed RI modulation in the core is typically realised by use of a photosensitive fibre. Photosensitivity of a silica optical fibre is achieved by doping the core with germanium (Ge) and much higher photosensitivity can be achieved by co-doping the core with boron (B) and

Ge [30] or by hydrogen loading [31]. Typical UV wavelengths used in development of LPGs by UV exposure are in the wavelength region from 193 nm and 266 nm [16]. The periodic RI perturbations in the core are realised by formation of Ge related glass defects in the photosensitive fibres discussed above.

RI modulation in the core of a photosensitive fibre by UV exposure can be realised on a point by point basis [32] or by exposing the entire length of the grating structure simultaneously [33].

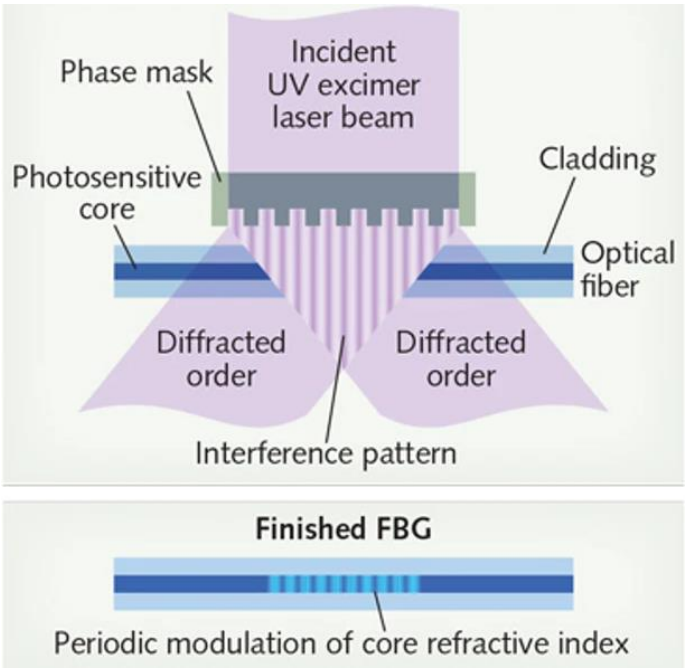

Fig 2. 8 Phase mask FBG writing scheme [36].

A periodic core RI modulation over the entire grating length can be achieved simultaneously by exposing the entire grating length to UV light through a phase mask [33], amplitude mask [15], via a patterned mirror [34] or using a microlens array [35]. Phase mask uses optical diffraction technique to spatially modulate and diffract the incident UV laser beam to realise a permanent periodic RI perturbation in the core of the photosensitive fibre, which is identical to the interference pattern generated by the mask and this method is very commonly used in fabrication of FBGs [33]. A schematic diagram that illustrates a FBG writing scheme that uses phase mask technique is shown in Fig. 2.8.

A typical optical configuration used in fabricating LPGs by exposing the photosensitive core to the UV light through an amplitude mask is shown in Fig. 2.9. Due to high durability and relatively less amount of time required to fabricate LPGs, the amplitude mask technique is one of the most popular methods used in UV inscription of LPGs in photosensitive fibres.

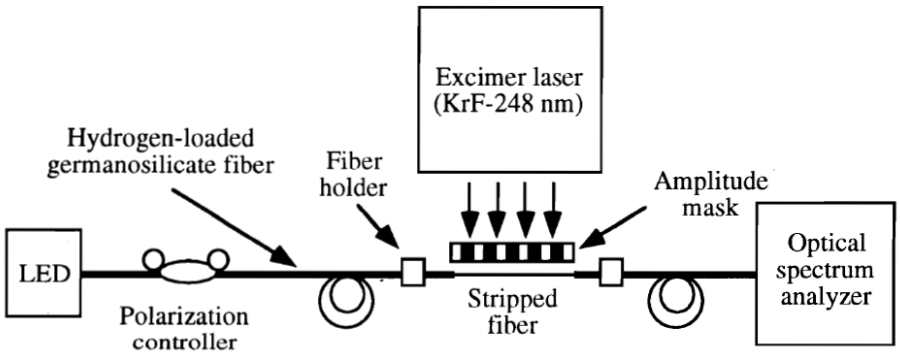

Fig 2. 9 Setup used to fabricate LPGs using an amplitude mask and an excimer laser [3].

As can be seen from Fig. 2.9, UV light from a laser source is used to illuminate the photosensitive core through an amplitude mask of a chosen period, which is usually fabricated with metal, using metal foil [15] or chrome plated silica [37]. The metal amplitude mask allows UV light to fall on the fibre in a periodic manner based on the period of the mask and the RI modulation of the photosensitive core is realised in the form of an intensity modulated pattern of the incident UV laser beam. The main advantage of this fabrication method is that a number of LPGs with same characteristics can be produced with relative ease.

The LPGs used in this thesis have been fabricated by using the above mentioned metal amplitude mask technique. B/Ge co-doped photosensitive fibres purchased from Fibrecore, UK, were exposed to the light from a 248-nm Krypton Fluoride (KrF) excimer laser with a pulse energy of 10 mJ and a pulse frequency of 175 Hz through metal amplitude masks with different grating periods to inscribe the LPG structures used to develop GO coated sensor probes discussed in this thesis. The high doping concentrations of Ge enabled the gratings to be written on these photosensitive fibres without the need of hydrogen loading. The PS1250/1500 photosensitive fibre used consist of a cladding diameter of 125 μm and a numerical aperture of 0.12. The in-house fabrication setup used to realise the LPGs can be seen in Fig. 2.10 below.

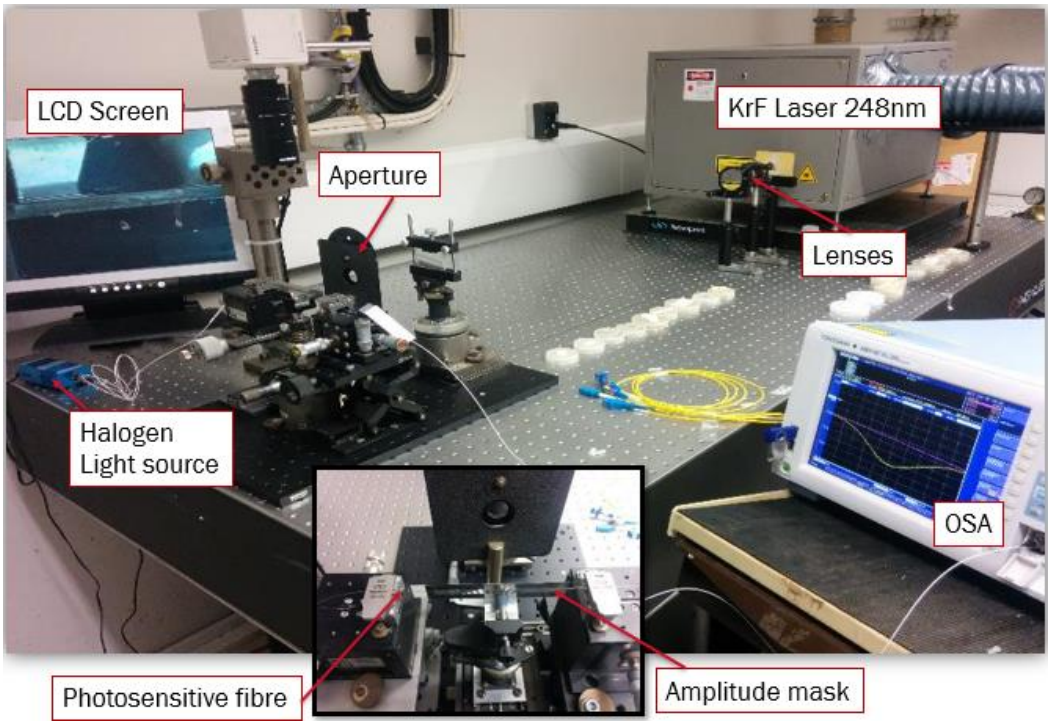

Fig 2. 10 Excimer laser-based LPG fabrication setup at City, University of London.

As can be seen in Fig. 2.10, the transmission spectrum of the LPG is monitored throughout the inscription process to identify the centre wavelength of the resonance loss bands and their respective amplitudes. A lens system has been used to widen the beam from the excimer laser to achieve a beam width of 25-30 mm, which is typically the length of the LPGs that have been fabricated in this thesis. The resonance wavelengths and their respective intensities depends on the dopant concentrations of the photosensitive fibres being used, length of the grating, exposure time and the period of the amplitude mask. Therefore, the choice of the amplitude mask was dependent on the type of photosensitive fibre that was used and the desired wavelength of attenuation that was required by the application. It was also noticed that the resonance loss bands performed a red shift and their intensities were increased gradually with increasing UV exposure time, until saturation occurs. The spectral shift is related to the increased guided mode effective RI while the increase in loss band intensity is attributed to the enhancement of the coupling coefficient [3]. Exposure time should be optimised depending on the characteristics of the photosensitive fibre that is being used, grating length desired and the period of the amplitude mask.

Even though UV exposure via an amplitude mask is a well-established technique in fabrication of LPGs, there are some stability implications of the optical properties that affect the spectral characteristics in LPGs associated with UV irradiation. One such issue is the presence of birefringence which can be resulted in producing polarization splitting in resonance bands in

LPGs fabricated in non-polarization-maintaining fibres [38]. The RI change caused by UV exposure is known to contain an unstable component, which has been reported to cause significant changes in the central wavelength of the resonance loss bands and coupling strength over time [15]. Thermal annealing has been identified as an efficient method in removing this unstable component and thus producing LPGs with consistent optical characteristics, allowing LPGs to be used in many applications. Erdogan et al. [39] have shown that the decay of the induced RI change in FBGs can be accelerated by keeping the fabricated FBGs at high temperatures post-fabrication. As such, thermal annealing is proven to be an essential component in development of in-fibre grating based fibre optic sensors, particularly for the sensors that use fibre gratings for temperature sensing, where reversible optical changes with temperature excursions are critical in obtaining accurate measurement [40]. It has also been reported that noise formed in resonance loss bands of LPGs can also be reduced by thermal annealing [41].

The LPGs used in this thesis have been thermally annealed post-fabrication at a temperature higher than the maximum operating temperature for each of the sensors that will be discussed in Chapter 4, 5 and 6 to ensure the removal of any unstable optical changes in the resonance loss bands that could affect the experimental results. Transmission spectrum of a 25 mm long LPG fabricated using a 380 µm amplitude mask, before and after an annealing process that has been carried out at 120 ℃ for 3 hours can be seen in Fig. 2.11 below.

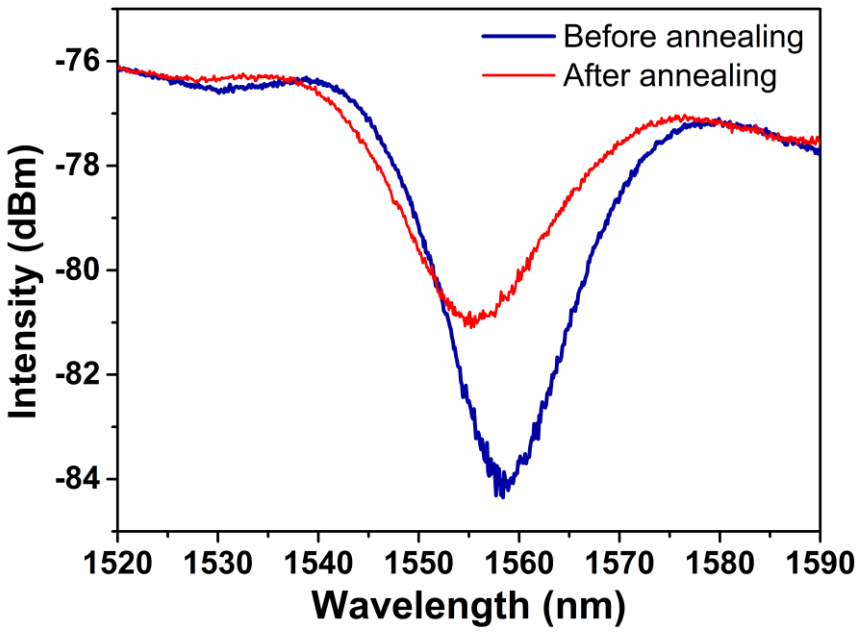

Fig 2. 11 Transmission spectra of a LPG before and after annealing at 120 ℃ for 3 hours.

2.5 Comparison between LPG & FBG based Fibre Optic Sensors

As discussed in detail in section 2.3, there are two major categories of in-fibre gratings based on the period of RI perturbation present in the core of the fibre. FBGs consist of typical grating periods of ~ 1μm, which enables the coupling of fundamental core mode to its counterpart, propagating in the opposite direction to realise a narrow band reflection from the grating, which behaves like a notch filter. The reflected wavelength is termed the Bragg wavelength, which has been defined by the equation 2.6. In contrast, LPGs contain RI modulations of the core with typical grating periods of more than hundreds of micrometres, which results in forming of a series of resonance loss bands as a result of fundamental core mode coupling to the co-propagating cladding modes at discrete wavelengths. These resonance wavelengths values can be realised by the equation 2.10, which was derived in detail in section 2.3.2.

It is evident from the equations 2.6 and 2.10 that resonance wavelengths of FBGs and LPGs are functions of the effective RI of the fundamental core mode and their respective grating period values, which can be perturbed by applying strain and temperature variations on the in-fibre gratings. This allows both these grating structures to be used as strain and temperatures sensors [42]. The major advantage of FBG based sensor systems is that they can be multiplexed to develop distributed sensing measurements [42]. A single interrogating detector can be used to detect the spectral shift from a series of multiplexed FBG strain and temperature sensors. In contrast, LPGs consist of several resonance loss bands in a single grating structure and as such, it is difficult to monitor spectral changes when two or more LPG structures are multiplexed, mainly due to the overlap of resonance loss bands that would cause difficulty in uniquely detecting spectral shift of individual attenuation bands.

One major disadvantage of FBGs is the relatively higher fabrication cost of phase masks, as different phase masks are required to fabricate FBGs with different Bragg wavelengths. On the other hand, LPGs can be fabricated by use of a metal amplitude mask, which reduces the fabrication cost significantly. FBGs have also reported to show limited strain and temperature sensitivities of 1.3 nm wavelength shift for 100 ℃ change in temperature and 11 nm spectral shift for 1% strain variation, which requires the use of high-resolution spectrum analysers to detect and monitor these small optical perturbations [3]. In contrast, LPGs have recorded 3 nm/ 100 ℃ to 10 nm/ 100℃ temperature sensitivities and 2.2 nm/ 1000$\mu\varepsilon^{-1}$ of strain sensitivity [43], which enables the use of relatively less expensive interrogator systems to develop less expensive sensor systems. However, in FBGs, Bragg wavelength shift is measured in reflection

mode, which allows them to be used as sensor probes in their natural state. In contrast, since core mode couples with co-propagating cladding modes, optical changes in resonance loss bands of LPGs are typically monitored in the transmission mode, which limits the flexibility of such sensors to be used as sensor probes in its natural state. Techniques such as coating a silver mirror at the end of the LPG grating to develop Michelson Interferometric LPG sensor probes [44] have been proposed to overcome such limitations of LPGs operating in transmission mode.

FBGs have been proposed as external RI sensors, which requires etching of the fibre clad to expose the evanescent wave of the guided mode to the outward environment [45]. However, etching of the fibre clad reduces the strength and the integrity of the fibre grating, which limits the use of such sensors in harsh environments such as structural health monitoring. Moreover, the etching process uses chemicals such as HF, which is harmful to humans and the environment and as such, there's a limited number of FBG based external RI sensors reported in literature.

In contrast, it is evident from equation 2.10 that resonance wavelength of LPG attenuation bands are a function of effective RI of the cladding, which comprises of both RI of the cladding, as well as the RI of the outward environment. This dependency of the surrounding RI arises from the fact that fundamental core mode of an LPG is couples to higher order cladding modes, which contain longer evanescent tails that penetrates the cladding-surrounding medium to increase the light-matter interaction at the cladding-surrounding medium interface. As such, LPGs are intrinsically sensitive to their surrounding RI, which can be utilized to develop external RI sensors without the need of using expensive and complicated processes such as clad etching.

As mentioned in Chapter 1, aims and objectives of this research consist of development of a series of external RI based chemical sensors and thus, based on the enhanced external RI sensitivity explained above, LPGs were chosen as the basis of the sensors developed in this thesis. Sensing characteristics of LPGs will be discussed in detail in the next subsection of this chapter, followed by an overview of the coated LPG based sensors reported in the literature.

2.6 Sensing Characteristics of LPGs

It has been established in section 2.5 that LPGs are inherently sensitive to strain, temperature and also excursions in the RI of the material that surrounds the cladding. These inherent

sensitivities can be exploited to develop sensors that can be used in various applications and are explored in detail in this sub section.

It was explained in section 2.3.2 that the amount of power transferred between the fundamental core mode and corresponding cladding order modes of a LPG depends on phase matching and the coupling coefficient of these modes. The coupling coefficient value merely changes the amplitude and the width of the resonance loss bands and as such, not that significant in sensing applications that uses wavelength shift as the monitoring mechanism. Therefore, such sensing mechanism can be expressed based on the phase matching condition, which results in a coupling resonance wavelength of λ [3],

$$\lambda = (\delta n_{eff})\Lambda \tag{2.12}$$

Where Λ is the grating period of the LPG and δn_{eff} is the differential effective index between the fundamental core mode and a cladding mode, which can be expressed as,

$$\delta n_{eff} = n_{eff}^{core} - n_{eff}^{clad} \tag{2.13}$$

Where n_{eff}^{core} and n_{eff}^{clad} are the effective RI values of the fundamental core mode and the coupled cladding mode, respectively. On the basis of these equations, it is evident that the principle operating mechanism of a LPG based sensor depends on the modulation of effective RI values of the core and the cladding modes and/or the grating period by any external perturbation. If an external perturbation ξ (such as strain or temperature) acts on the grating region of an optical fibre with a grating periodicity of Λ, wavelength shift per unit perturbation $d\lambda/d\xi$ can be derived by using the chain rule derivatives in equation 2.12. Thus, $d\lambda/d\xi$ can be expressed as,

$$\frac{d\lambda}{d\xi} = \frac{d\lambda}{d(\delta n_{eff})}\frac{d(\delta n_{eff})}{d\xi} + \frac{d\lambda}{d\Lambda}\frac{d\Lambda}{d\xi} \tag{2.14}$$

It is evident that wavelength shift is a function of the change in the differential effective index per unit perturbation $d(\delta n_{eff})/\, d\xi$, and also the change in the grating period per unit perturbation $d\Lambda/d\xi$. The factor $d\lambda/d\Lambda$ is dependent on the grating period, fibre parameters, order of the resonance band and the writing and annealing conditions. On the other hand, a change in differential effective index usually arises from the modulation of materials properties of the fibre such as the core and the cladding RI values. Therefore, the spectral shift of a LPG can be divided into two categories. The first part of the right-hand side of the equation can be

described as the material contribution and the second part can be described as the waveguide contribution. As such, it is evident that the overall spectral shift per unit perturbation of a LPG is dependent on the cumulative effect of relative magnitudes and the polarities of the material and waveguide contributions.

2.6.1 Strain Sensitivity

Axial strain applied on a fibre changes the core and cladding radii as well as their respective RI values. These strain induced changes will result in a spectral shift according to equation 2.14. If an axial strain of $\Delta\varepsilon$ is applied on a LPG with a grating periodicity of Λ, equation 2.14. can be modified with $\xi=\varepsilon$ to obtain,

$$\frac{d\lambda}{d\varepsilon} = \frac{d\lambda}{d(\delta n_{eff})} \frac{d(\delta n_{eff})}{d\varepsilon} + \frac{d\lambda}{d\Lambda} \frac{d\Lambda}{d\varepsilon} \tag{2.15}$$

Where $\Delta\varepsilon$ is defined as the ratio of change in grating length and the original length ($\Delta\varepsilon=\Delta L/L$). Therefore, $\Delta\varepsilon$ can be written as,

$$\Delta\varepsilon = \frac{dL}{L} = \frac{d\Lambda}{\Lambda} \tag{2.16}$$

By substituting equations 2.16 and 2.13, equation 2.15 can be modified to,

$$\frac{d\lambda}{d\varepsilon} = \frac{d\lambda}{d(\delta n_{eff})} \left(\frac{d(n_{eff}^{core})}{d\varepsilon} - \frac{d(n_{eff}^{clad})}{d\varepsilon} \right) + \Lambda \frac{d\lambda}{d\Lambda} \tag{2.17}$$

Therefore, it is evident that the spectral shift caused by applying an axial strain on a LPG is dependent upon both material and waveguide effects, as mentioned under the discussion of equation 2.14. Based on the equation 2.17, it can be seen that the waveguide contribution for strain sensitivity of a LPG depends solely on the grating period and the order of the cladding mode in a given fibre. It has also been recorded that strain induced perturbations in the core and cladding dimensions contribute significantly to the material effect of LPG strain sensitivity, which is caused by the Poisson's effect [46].

2.6.2 Temperature Sensitivity

Spectral shift of a LPG caused by temperature perturbations can be expressed in a similar way to axial strain sensitivity above, by considering a temperature change of ΔT and modifying the equation 2.33 with $\xi=T$ to obtain,

$$\frac{d\lambda}{dT} = \frac{d\lambda}{d(\delta n_{eff})}\frac{d(\delta n_{eff})}{dT} + \frac{d\lambda}{d\Lambda}\frac{d\Lambda}{dT} \tag{2.18}$$

As can be seen from equation 2.18, the material effect of temperature induced wavelength shift on a LPG is a function of the change in differential effective RI with temperature while waveguide effect is dominated by the perturbations in the grating period caused by varying temperature. Substituting equation 2.13 in 2.18, it is possible to derive,

$$\frac{d\lambda}{dT} = \frac{d\lambda}{d(\delta n_{eff})}\left(\frac{d(n_{eff}^{core})}{dT} - \frac{d(n_{eff}^{clad})}{dT}\right) + \Lambda\frac{d\lambda}{d\Lambda}\frac{1}{L}\frac{dL}{dT} \tag{2.19}$$

Where length of the LPG is denoted by L with ($d\Lambda/\Lambda dT = dL/LdT$).

Temperature sensitivity of a LPG is strongly dependent on the variations in the effective RI values of the fundamental core mode and the coupled cladding order modes. These effective RI values are also a function of operating wavelength λ for the corresponding cladding mode. Therefore, the material contribution is strongly dependent upon the thermo-optic coefficients of the core and cladding of the fibre and thus, is a function of the fibre composition. It has also been reported that for resonance loss bands corresponding to lower order cladding modes (for Λ>100μm), the material contribution dominates and for resonance loss bands corresponding to higher order cladding modes (for Λ<100μm), the material effect for germanosilicate fibres can be negligible [47]. Therefore, for standard LPGs inscribed with grating periodicities above hundreds of micrometres, the material contribution supersedes the waveguide contribution in temperature sensing. The waveguide contribution is dependent on the thermal sensitivity of the grating periodicity and based on the characteristics of the respective cladding mode that is being coupled, the waveguide term in equation 2.19 can be negative or positive [37]. When the light propagating in the core mode is coupled to lower order cladding modes, $d\lambda/d\Lambda$ is positive, while for the coupling to higher order cladding modes, it is negative.

Bhatia et al. have demonstrated the temperature sensitivity of different resonance loss bands of a LPG in [43]. The LPG has been fabricated with a periodicity of 280 μm in a Corning SMF-28 fibre. The temperature response of four resonance loss bands in comparison with the temperature response of a FBG is presented in Fig. 2.12 below.

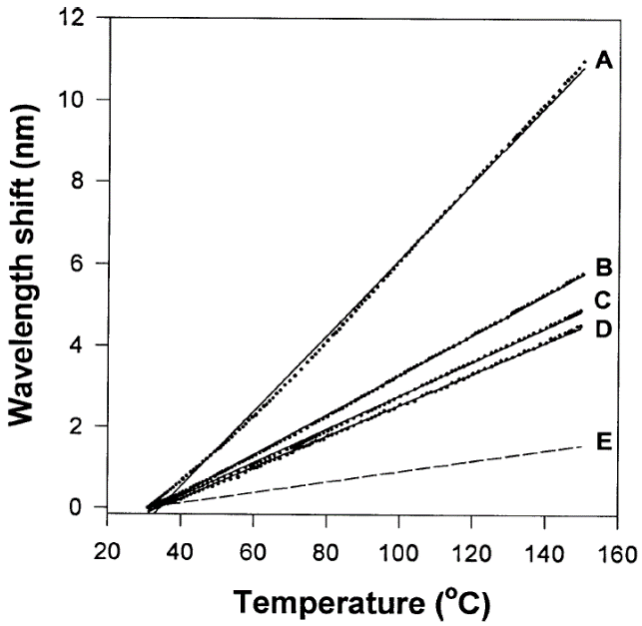

Fig 2. 12 Wavelength shift (with respect to that at 31.2 °C) with temperature for various resonance bands of a long-period grating. The dashed line (E) is the shift for a Bragg grating at 1550 nm with a temperature coefficient 1.3 nm/100 °C [43].

It is evident from Fig. 2.12 that temperature response of LPG resonance loss bands are significantly higher in comparison with the response of a FBG. A highest temperature sensitivity of 0.093nm/°C has been recorded for the resonance loss band corresponds to the A curve, which is almost an order or magnitude higher than the sensitivity observed in a FBG.

2.6.3 External Refractive Index Sensitivity

As discussed previously in this chapter, the external RI sensitivity of a LPG arises from its dependency of effective RI of the cladding in achieving phase-matching conditions between fundamental core mode and co-propagating cladding modes. This external RI sensitivity can be analysed with the help of equation 2.14, which can be re-written as follows considering a surrounding RI value of n_{sur}.

$$\frac{d\lambda}{dn_{sur}} = \frac{d\lambda}{d(\delta n_{eff})}\frac{d(\delta n_{eff})}{dn_{sur}} + \frac{d\lambda}{d\Lambda}\frac{d\Lambda}{dn_{sur}} \tag{2.20}$$

Considering the fact that there would be no waveguide contribution with changes in the surrounding index, the second part on the right-hand side of the equation 2.20, which corresponds to waveguide effect would be null and the equation would simplify to,

$$\frac{d\lambda}{dn_{sur}} = \frac{d\lambda}{d(\delta n_{eff})}\left(\frac{d(n_{eff}^{core})}{dn_{sur}} - \frac{d(n_{eff}^{clad})}{dn_{sur}}\right) \tag{2.21}$$

However, perturbations in the surrounding RI will only affect the effective RI of the cladding and thus, external RI sensitivity of a LPG can be expressed as,

$$\frac{d\lambda}{dn_{sur}} = \frac{d\lambda}{d(n_{eff}^{clad})} \frac{d(n_{eff}^{clad})}{dn_{sur}} \tag{2.22}$$

Therefore, it is evident that the effective RI values of the cladding modes are dependent upon the difference between the RI of the cladding and that of the medium surrounding the cladding, which results in resonance wavelength of LPG attenuation bands being a function of surrounding RI, forming the working principle of LPG based external RI sensors.

Patrick et al. have recorded the transmission spectra of a LPG that contains seven distinct resonance loss bands against a series of surrounding RI values from 1 to 1.72 [48]. A grating periodicity of 275 μm and a grating length of 25 mm have been used in fabrication of the LPG that was used in the experiment. The recorded transmission spectra against varying surrounding RI values can be seen in Fig. 2.13.

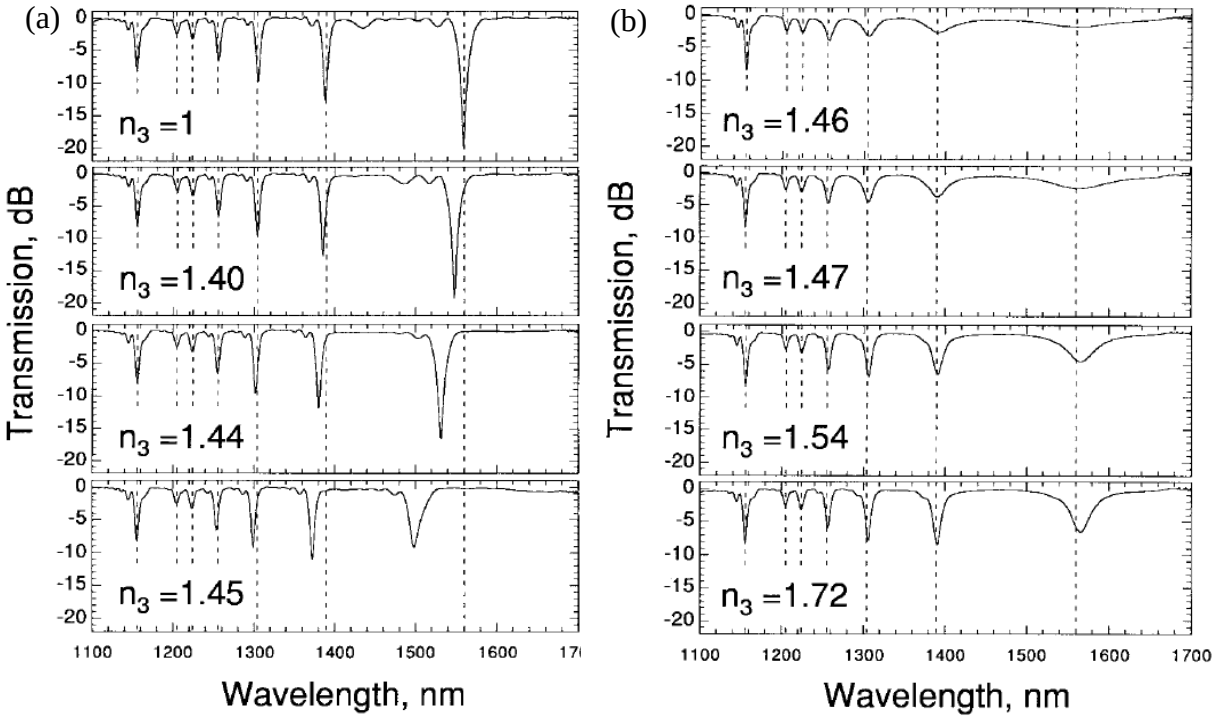

Fig 2. 13 (a) Broad-band transmission spectrum of Λ = 275 μm LPG for n_{sur} ranging 1 to 1.45. (b) Broad-band transmission spectrum for n_{sur} ranging from 1.46 to 1.72. Dotted lines indicate attenuation band wavelengths at n_{sur} = 1 [48].

It is noticeable that the main spectral change occurred when surrounding RI value is lower than that of the cladding (from 1 to 1.44) is a blue shift of the centre wavelength of the resonance loss bands, particularly significant in the attenuation bands corresponding to higher order

cladding modes. In another work, the same group has shown that higher order resonance loss bands are most sensitive to perturbations in the surrounding RI values and performed large wavelength shifts compared with the resonance loss bands corresponding to lower order modes [49]. This enhanced sensitivity of higher order cladding modes has been achieved as evanescent field of these modes extend further into the external medium. The highest sensitivity has been observed when the external RI value is approaching that of the cladding in the region of 1.40 to 1.45.

When the surrounding RI matches the RI of the cladding, an "infinite" cladding is seen by the fibre core, and the cladding no longer supports any discrete cladding modes, which results in no distinct attenuation bands being observed in the transmission spectrum of the LPG. This is caused by the broadband radiation mode coupling losses that are present at this specific surrounding RI value.

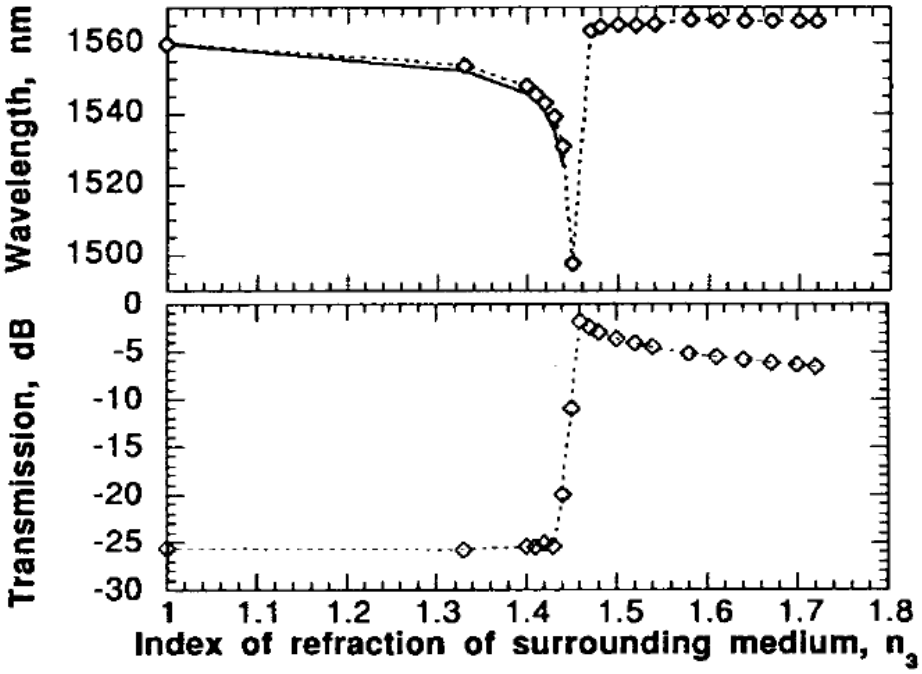

Fig 2. 14 Experimentally measured centre wavelength and the attenuation of the longest wavelength attenuation band in the Λ = 275 μm LPG as a function of surrounding RI [49].

When the external RI is higher than that of the cladding, the phase matching conditions discussed earlier in this chapter will no longer be satisfied. The cladding-surrounding medium interface will lose its total internal reflection condition, and thus guided modes in the cladding will act as radiation modes or leaky cladding modes and the fundamental core mode will couple with these radiation modes [50]. These resonance loss bands present when the cladding no longer acts as a waveguide are attributed to the Fresnel reflection, rather than the total internal

reflection in the cladding-surrounding medium interface [51]. Under these conditions, the change in the intensity of resonance loss bands, which is affected by the amount of light reflected back at the cladding-surrounding medium interface, will supersede the change in the wavelength shift. The above discussed spectral changes with varying surrounding RI values are further illustrated in the Fig. 2.14.

Based on the intrinsic external RI sensitivity discussed above, LPG based fibre optic sensors have been developed in measuring chemical concentrations such as sodium chloride [52], calcium chloride[52] and ethylene glycol [49]. RI sensitivity of LPGs has also been exploited in liquid level monitoring [53], rebar corrosion monitoring [54], petroleum hydrocarbon detection [55] and development of an optical viscometer [56] as well. Based on these examples, it is evident that LPGs are proven to be an effective and attractive sensing mechanism in developing external RI based chemical sensors.

2.7 Coated LPG Sensors – Essential Theory

All the external RI sensing examples mentioned above involve bulk immersion of LPG into a solution without any modifications applied to the LPG structure. One major disadvantage of developing external RI sensors based on this approach is that the wavelength shift of the resonance loss bands would be sensitive to any perturbation of surrounding RI that is in reach of its evanescent field and thus, the sensing will not be specific to the analyte under investigation. In this regard, deposition of an analyte-specific coating that exhibits variations in its RI against perturbations in the local environment proves to be an interesting solution to overcome the external RI sensing limitation of LPGs mentioned above. A schematic diagram illustrating the design of such a coated LPG based external RI sensor with four layers is shown in Fig. 2.15 below.

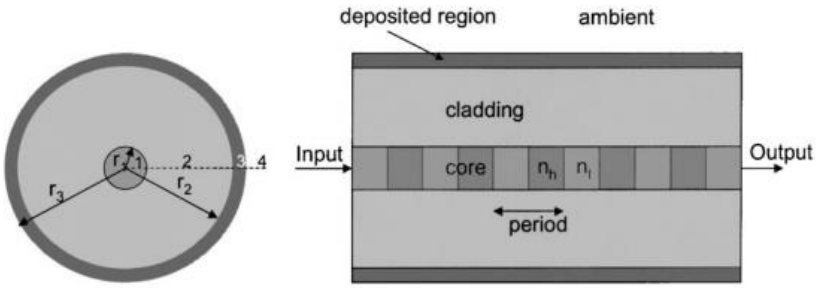

Fig 2. 15 Transverse and longitudinal sections of a LPG structure, showing deposition of an overlay upon the cladding [57].

It was discussed in section 2.6.3 that when the surrounding RI value is lower than that of the cladding, a prominent wavelength shift is observed and when it is higher than that of the

cladding, a prominent intensity shift is observed. As such, when an analyte-specific material is coated on a LPG, which changes its RI based on the variations of the target analyte, either a wavelength shift or an intensity shift could be achieved, forming the basis of coated LPG based external RI sensor designs. In a situation like this, the analyte-specific material acts as the active sensing element and the RI of the coated material and the coating thickness of the overlay should be chosen carefully in order to optimise the external RI sensitivity of the coated LPG to target analyte. The effect of overlay thickness and the mode guiding mechanism of such deposited overlays will be discussed next.

2.7.1 Effect of Overlay Thickness

Rees et al. have investigated the effect of overlay thickness upon the LPG response for the first time by depositing thin layers of tricosenoic acid using Langmuir-Blodgett (LB) method, which enables extremely high resolution of thin film deposition on a nanometre scale [57]. The LPG under investigation has been fabricated on a B-Ge co-doped photosensitive fibre with a grating period of 400 μm and a grating length of 40 mm. The RI of the coating material, tricosenoic acid, has been measured to be 1.57, which is higher than that of the cladding. It has been observed that, when a few hundred nanometre thick thin film coating of a material that has a higher RI than that of the cladding has been deposited over the entire grating length of a LPG, centre wavelength of the resonance loss bands performed a considerable shift. This phenomenon is quite distinct from the LPG behaviour under thick coatings or bulk immersion, in which spectral shift of attenuation bands were observed to be very minimal under high indexed materials (materials that have a RI higher than that of the cladding) as shown in Fig. 2.14. Therefore, the experiment conducted by Rees et al. has shown a strong dependence of resonance loss band centre wavelength with coating thickness of high indexed materials, which is clearly evident in the results illustrated in Fig. 2.16.

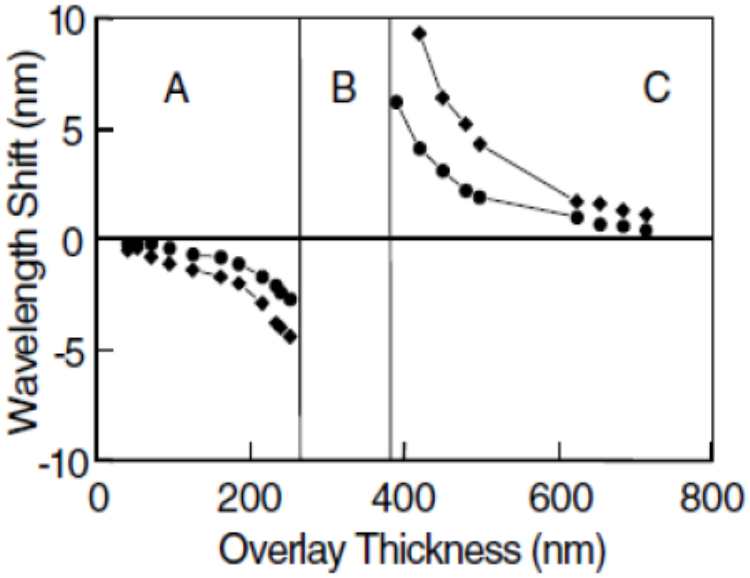

Fig 2. 16 Experimental shift in the central wavelengths of the attenuation bands plotted as a function of the thickness of the tricosenoic acid overlay. Filled circles: attenuation band corresponding to coupling to the 5th cladding mode, filled squares: attenuation band corresponding to coupling to the 6th cladding mode [57].

Fig. 2.16 depicts the central wavelength shift of the resonance loss bands corresponding to 5th and the 6th order cladding modes against increasing overlay thickness of a high indexed material. As can be seen from the figure, there are three distinct regions of spectral response. In region A (below 250 nm), at first, only the RI of the air affects the effective RI of the cladding modes. When the overlay thickness increases, effective RI of the cladding modes increase as RI of both the overlay and air affects the cladding modes, which results in a negative shift in the centre wavelength of the attenuation bands. In region B, the effective RI of the cladding modes are approximately equal to that of the cladding and as such, no guided modes are supported by the cladding, which leads to no attenuation bands present in the transmission spectrum. When the overlay thickness increased above 380 nm (region C), attenuation bands reappeared at a wavelength that is much higher than the wavelength observed when there was no overlay deposited on the grating surface. As the overlay thickness increased further, the centre wavelength values of attenuation bands returned to their original values, which would be observed for an overlay of infinite thickness. Based on these results, it is evident that the centre wavelength response of attenuation bands can be tuned by depositing a thin overlay of a material that has a higher RI value than that of the cladding, providing a basis for the development of species-specific and more efficient external RI sensors based on LPGs.

2.7.2. Mode Guiding in an Overlay

A schematic diagram illustrating the high indexed thin film coated LPG and its RI profile is depicted in Fig. 2.17 below.

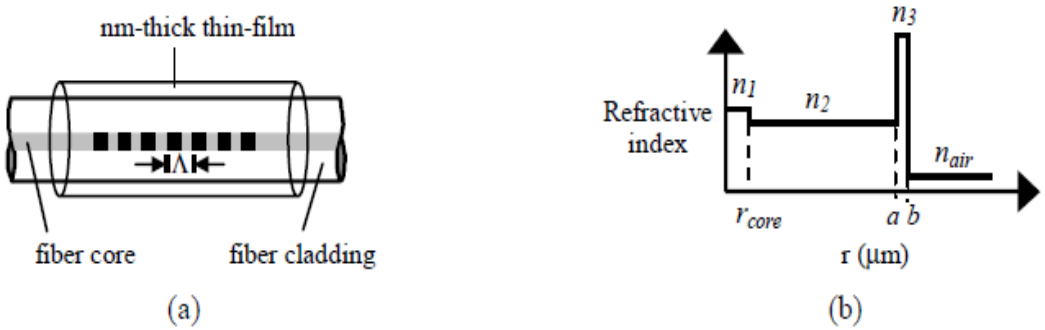

Fig 2. 17 (a) Illustrative schematic of LPG with an nm-thick thin-film coating (b) Index profile of the thin-film coated LPG, n_1 is index of fibre core, n_2 is index of fibre cladding, n_3 is index of the thin-film, n_{air} is index of air, and $n_3>n_1>n_2>n_{air}$. Thickness d of the film is denoted d=b-a [58].

Under the conditions illustrated in Fig. 2.17, when a high indexed thin film layer is coated on a LPG grating surface, the effective RI of the cladding modes is affected by the properties of the deposited overlay (such as RI and thickness) and thus, determines the distribution of cladding mode power in the core, cladding and the deposited overlay. The refraction-reflection that takes place at the cladding-thin film interface decreases the amount of power carried by cladding modes bounded within the core and cladding layers by transferring some of it to be radiated through the high indexed thin film overlay. Under these conditions, the evanescent field of the LPG stretches more to the surrounding medium and thus, increases the effective index of the cladding order modes [59].

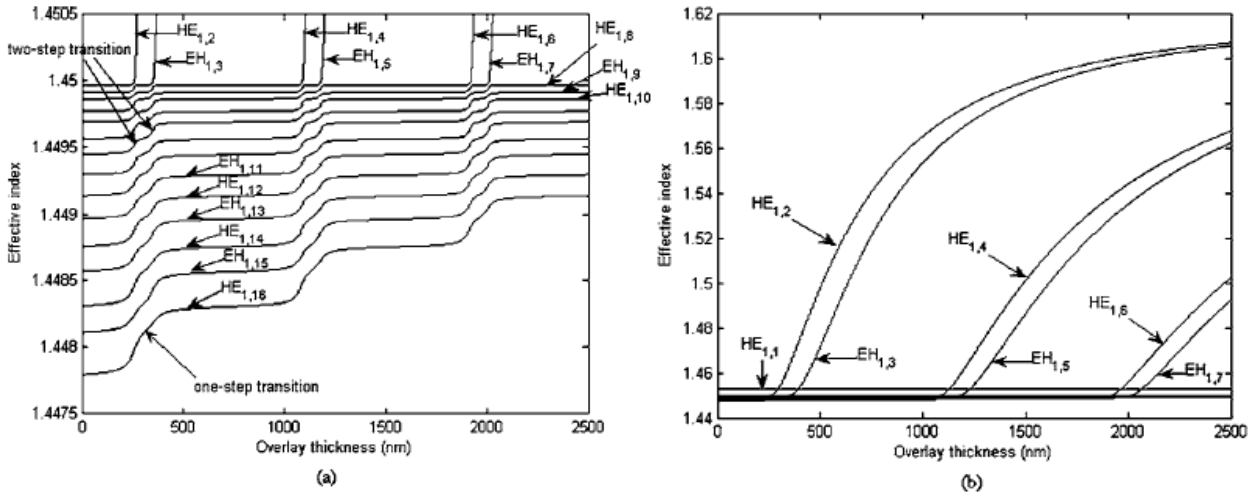

Fig 2. 18 Effective index as a function of the overlay thickness of (a) the first 15 cladding modes and (b) the core mode and the first six cladding modes [60].

As the thickness of the high indexed overlay increases, effective indices of the cladding modes move towards higher values. At one point, when there's enough high indexed material has been deposited on the grating surface, one of the cladding modes is guided by the overlay and thus, deposited overlay becomes a waveguide itself [60].

This critical point is dependent upon the RI of the material and the coating thickness. This phenomenon causes a reorganisation of the effective indices of the rest of the cladding modes. Del Villar et al. have demonstrated this effect by conducting a theoretical simulation and the results are illustrated in Fig. 2.18.

They have demonstrated the shift of the effective indices of cladding modes under increasing overlay thickness of a high indexed material by modelling a fibre with a core RI of 1.4573, cladding RI of 1.45 and the overlay RI of 1.62 considering a polymer material, [PDDA+/PolyR-478−] at an operating wavelength of 1200 nm. As mentioned above, when the thickness of the overlay increases, at one point, the overlay starts guiding a mode. It is always the mode with the highest effective index or the lowest order mode that starts propagating in the overlay. If the thickness of the overlay is increased further, more modes start to be guided in the overlay. It is always the mode with the highest effective index (or the lowest order mode from the group of modes that are not guided in the overlay) that transfers to the overlay. At these transition points, a significant change in the effective RI of the other modes take place and after the transition, the effective RI of each mode is equal to that of the corresponding lower order cladding mode before the transition. This effect is highlighted in the Fig. 2.18 above. The HE_{12}, HE_{14} and HE_{16} corresponding to LP_{02}, LP_{03} and LP_{04} modes start guiding in the overlay at a thickness of about 260 nm, 1090 nm and 1920 nm, respectively. It is also observed in Fig. 2.18 (b) that, when the overlay thickness is further increased, the effective RI of these modes seem to reach the RI value of the overlay (1.62), which suggests that the modes are more confined in the overlay region.

A study conducted by the same group (experiment conducted with same parameters as [60]) have illustrated this effective index transition even further in the results shown in Fig. 2.19 [57].

At the transition points mentioned above, the mode with the highest effective index starts guiding in the overlay and a reorganisation of the rest of the modes take place by a sudden change in the corresponding effective index values. This is highlighted in Fig. 2.19.

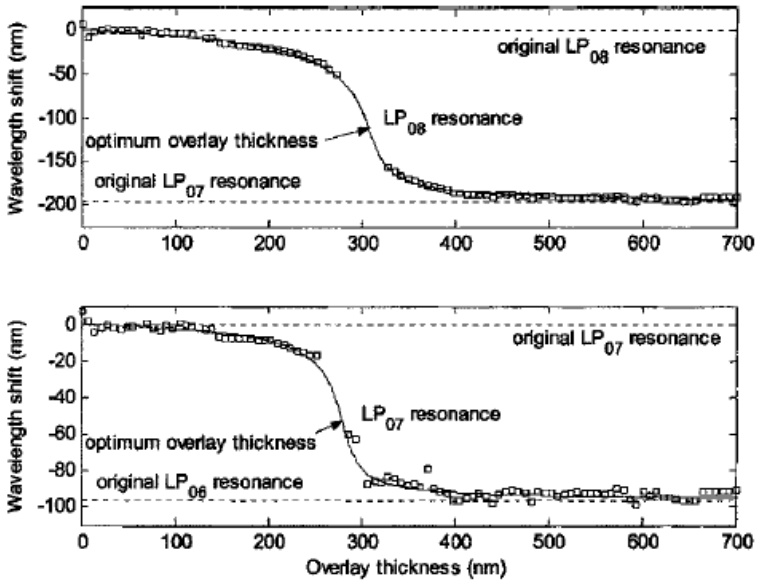

Fig 2. 19 Shift in resonance wavelength caused by coupling between the core mode and the seventh (LP_{07}) and the eighth (LP_{08}) cladding modes of the structure as a function of the thickness of the overlay. Open square, experimental values; solid curves, theoretical values [57].

When the thickness of the overlay increases, after the transition point that corresponds to an overlay thickness of ~300 nm occurs, the effective RI of the LP_{08} mode will be that of the LP_{07} mode and the effective RI of the LP_{07} mode will be that of the LP_{06} mode and so forth. The same trend can be related to centre wavelength values of corresponding attenuation bands of the LPG transmission spectrum as well [57].

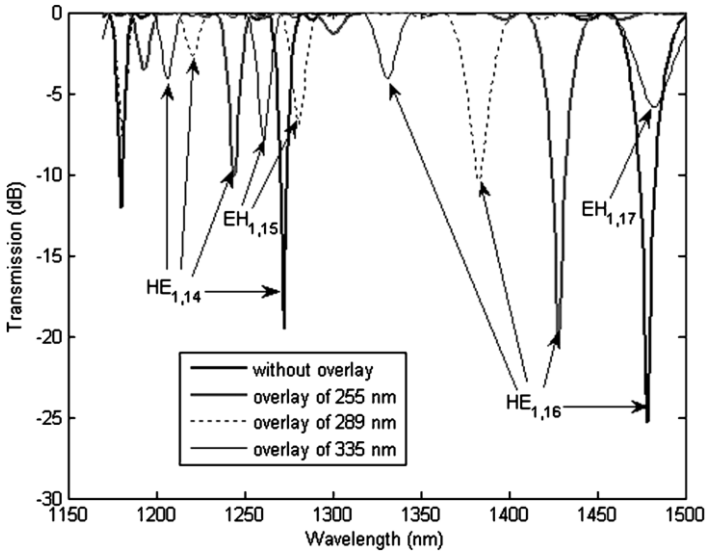

Fig 2. 20 Transmission spectrum showing the $EH_{1,17}$,$HE_{1,16}$,$EH_{1,15}$, and $HE_{1,14}$ mode resonances for four overlay thickness values: 0, 255, 289, and 335 nm. The overlay refractive index is 1.62, and the ambient index is 1 [60].

The centre wavelength of the resonance loss band corresponding to LP_{08} mode will shift its centre wavelength to that of resonance loss band corresponding to LP_{07} mode and centre wavelength of the resonance loss band corresponding to LP_{07} mode will shift its centre wavelength to that of the resonance loss band corresponding to LP_{06} mode and so forth. This wavelength shift effect is illustrated in the Fig. 2.20 above.

It is evident from Fig. 2.19 that there is a sharp change in the effective index of a cladding mode at the transition points that occur when the overlay thickness is increased and thus, there is a fast change in the centre wavelength of the corresponding attenuation bands as well. It is also evident from Fig. 2.19 that the shift is maximum when the effective RI of the mode is halfway between the original effective RI of the corresponding cladding mode and the original effective RI of the corresponding lower order cladding mode before deposition. It has been reported that the LPG external RI sensitivity could be enhanced by more than one order of magnitude if the overlay deposition were stopped at this particular thickness value [57]. Therefore, there exists an optimum overlay thickness (OOT) value which corresponds to the highest external RI sensitivity of an external RI sensor based on a coated LPG with a material that has a higher RI than that of the cladding.

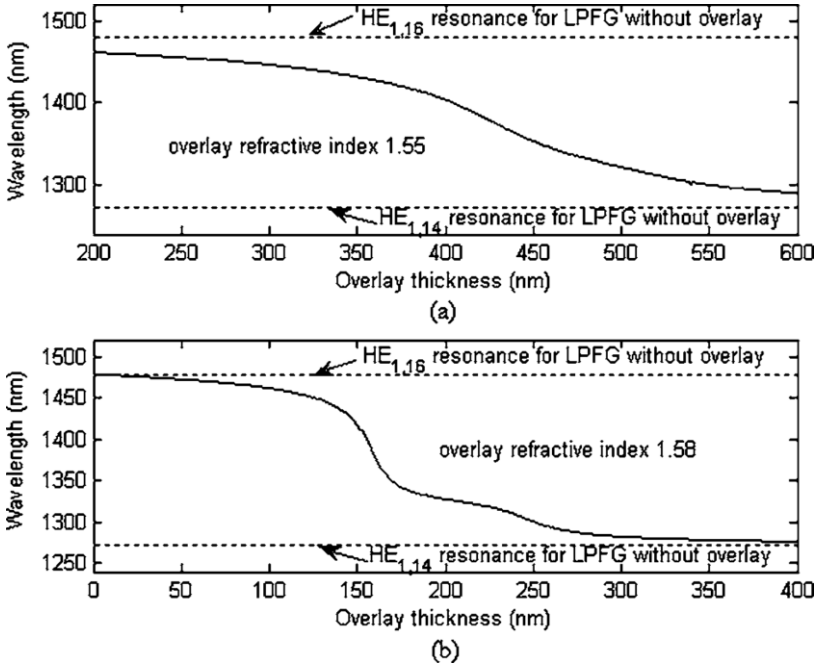

Fig 2. 21 $HE_{1,16}$ resonance wavelength as a function of the overlay thickness. The overlay refractive indices are 1.55 and 1.8, and the ambient index is 1 [60].

Fig. 2.21 depicts the centre wavelength of a resonance loss band corresponding to $HE_{1,16}$ cladding mode as a function of the overlay thickness for two high indexed materials that have been used as the overlay [60]. It can be noticed in Fig. 2.21 that for the material with a relatively

low index (1.55), a weak overlay guidance condition is met whereas for the material with a relatively high index (1.8), the two transition points are very clear. Therefore, it is evident that OOT is a function of the RI of the coated material. For example, if the coating thickness is fixed at about 150 nm, the RI of the coated material should be closer to 1.8 as the transition point that caused highest effective index change occurs in that region of overlay thickness. This means that the same spectral shift could be achieved if the coating thickness and the ambient RI is fixed and the RI of the coated material varies. OOT also depends upon the thickness of the deposited overlay. If the RI of the coating material (overlay) is fixed, the OOT can be reached by changing the overlay thickness. If a material with a relatively high RI is used, OOT can be achieved with a minimum thickness, which reduces the amount of material required. Another important parameter that affects the OOT is the ambient RI (RI of the material that surrounds the thin film overlay).

Based on these simulation and experimental results, it is evident that the external RI sensitivity of a LPG can be enhanced by depositing a thin film coating of a material that has a higher RI than that of the cladding. It was also discussed that the RI sensitivity of a coated LPG depends upon the overlay thickness and there exists an OOT, which can be achieved by changing the overlay thickness for a given coating material or by choosing the right material with a suitable RI for a given overlay thickness. The most interesting feature associated with the dependency of the centre wavelength shift of resonance loss bands of a LPG with overlay thickness and the RI of the coated material is that, it is independent of the cladding RI, which has caused limitations in designing external RI sensors based on LPGs. In the next section, some fibre optic sensors that have been developed using a coated LPG approach to detect and monitor changes in the surrounding RI will be discussed in detail.

2.8 Coated LPG based Fibre Optic Sensors

In this subsection, some of the coated LPG based fibre optic sensors reported in the literature will be discussed in detail. Venugopalan et al. have developed a RH sensor by coating a thin layer of polyvinyl alcohol (PVA), which has a RI higher than that of the cladding, on a LPG surface [61]. After coating the LPG surface with PVA using a dip coating technique, they have recorded the transmission spectra of the PVA coated LPG sensor probe under four different humidity conditions, 33%RH, 53%RH, 75%RH and 97%RH by use of different salt solutions. When the coated PVA layer interacts with varying humidity conditions, the RI of the PVA layer changes and thus, a centre wavelength shift of the attenuation bands is observed.

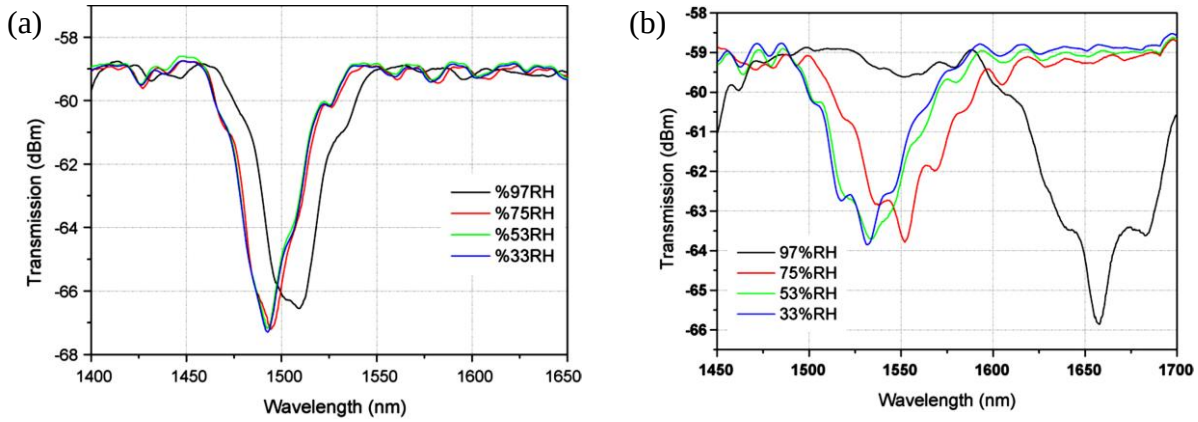

Fig 2. 22 Spectral change seen when the coated LPG is exposed to various humidity levels ranging from 33% to 97%, with PVA coating thicknesses of (a) 4 μm and (b) 800 nm [61].

Another interesting characteristic has been observed in this work when RH sensitivity was investigated under two different PVA coating thicknesses. It has been reported that for a PVA thickness of 4 μm (thick coating), poor humidity sensitivity has been observed while a higher humidity sensitivity has been observed for a thin PVA coating of 800 nm. These reported results are illustrated in Fig. 2.22 above.

Wang et al. have very recently reported another polymer composite coated LPG based highly sensitive humidity sensor [62]. They have used a polymer composite film containing PVA and polyethylene glycol (PEG) as the active sensing layer of the proposed LPG based sensor probe. It was discussed in section 2.7 that a highest RI sensitivity of a LPG is observed when the surrounding RI is closer to that of the cladding. In this work, they have used PEG to reduce the average RI of the PEG/PVA composite film to match the RI of the cladding at certain humidity levels to achieve a much higher RH sensitivity. RI of the PEG/PVA composite film changes as a function of the surrounding humidity level and as a result, the RI of the composite film decreases due to the absorption of water molecules by the polymer composite layer. Under certain humidity changes, the effective RI of the composite layer falls below that of the cladding and thus, the centre wavelength shift of the LPG attenuation bands can be adopted as the sensing mechanism. This particular RH range has been observed to be from 50%RH to 95%RH for a PEG/PVA composite film thickness of 900 nm and the schematic diagram of the developed LPG based sensor probe and its humidity response are illustrated in Fig. 2.23 and 2.24, respectively. A highest sensitivity of 2.485 nm/%RH has been achieved in the RH range of 50 – 75%RH.

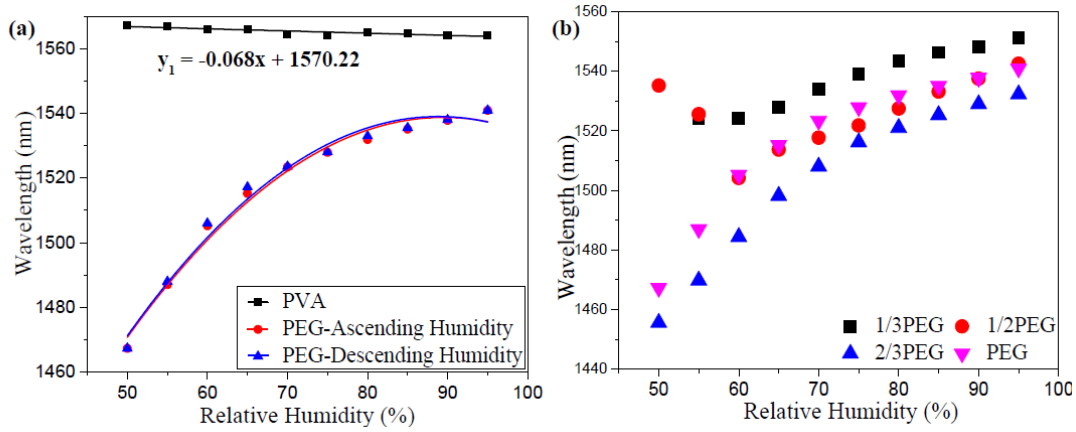

Fig 2. 23 (a) A comparison of different materials for relative humidity sensing (b) Humidity sensing characteristics of the LPFGs coated by the films with different PEG proportions in the humidity range from 50% to 95% RH [62].

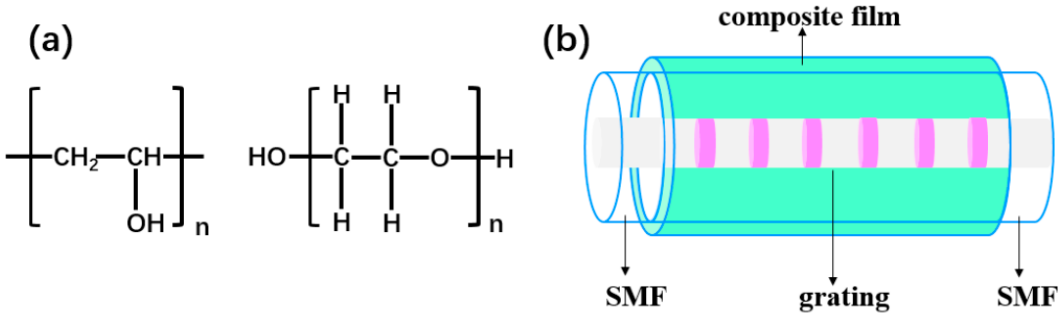

Fig 2. 24 (a) Chemical structures of the composite materials. Polyvinyl alcohol is on the left, polyethylene glycol is on the right (b) schematic configuration of the long-period fibre grating (LPFG) RH sensor coated with a PEG/PVA composite film [62].

A liquefied petroleum gas monitoring system based on a polystyrene coated LPG has been reported by Esposito et al. in [63]. A LPG coated with a thin film of atactic polystyrene (aPS) has been employed as a gas sensor to detect and measure butane concentrations in liquefied petroleum gas. aPS has a RI of 1.55, which is higher than the silica cladding and thus, its thickness can be controlled to achieve the mode transition points of the LPG attenuation bands to realise high RI sensitivities. aPS has been chosen due to its chemical affinity between olefin chains it possess and hydrocarbon molecules. An aPS coating thickness of 320-380 nm has been chosen to achieve the mode transition point of the LP_{07} loss band and a dip coating technique has been used to deposit the aPS thin film layer on the fibre surface.

The developed sensor probe has been used in the reflection mode by depositing a silver mirror at the end of the LPG sensing area and significantly, the developed sensor system has been deployed in a railway tunnel, highlighting the advantages of fibre optic sensors in applications related to harsh environments. A schematic diagram of the developed LPG based gas monitoring system is illustrated in Fig. 2.25.

A schematic diagram showing the aPS coated LPG gas sensor and its response (centre wavelength shift of LP_{07} resonance loss band) as a function of different butane concentrations are shown in Fig. 2.26 below.

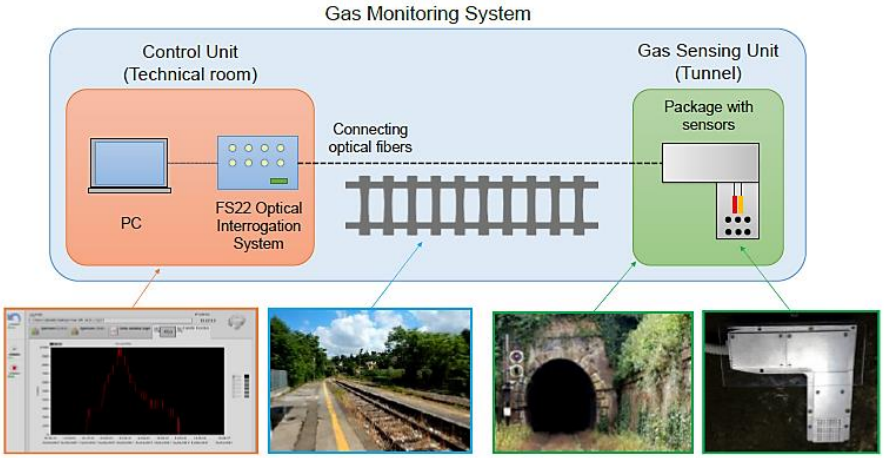

Fig 2. 25 Schematic figure and photos of the gas monitoring system [63].

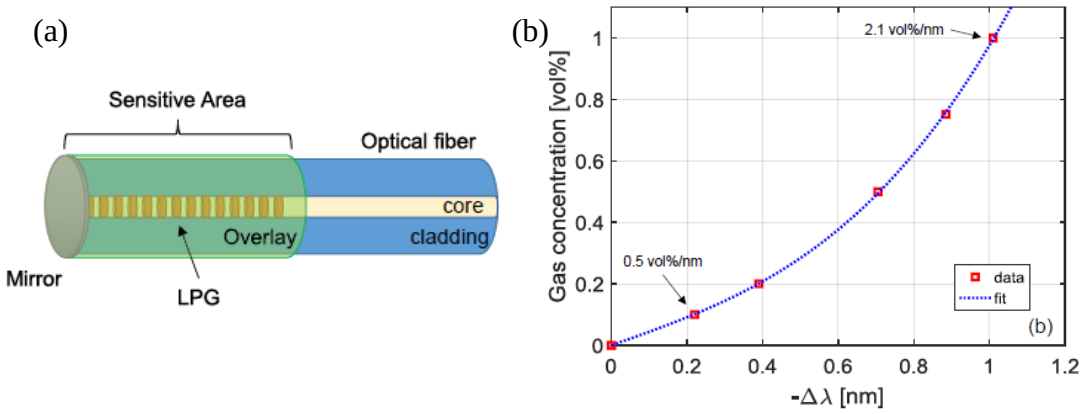

Fig 2. 26 (a) Single ended aPS coated LPG based gas sensor (b) Wavelength shift of the LP_{07} band during the exposure to different butane concentrations [63].

Recently, Yang et al. have reported a hydrogel coated LPG based highly sensitive and fast responding sensor to measure ocean salinity [64]. The RI of seawater varies as a function of marine salinity as thus, LPG based external RI sensors can be used as highly effective salinity sensors. A submicron thick hydrogel layer has been deposited on a LPG surface by use of a layer-by-layer electrostatic self-assembly technique. For a salinity concentration range of 0.4 M to 0.8 M (22.8 – 44.7 g/kg) around 8.1 pH value, a centre wavelength shift of 7 nm/M has been achieved by the developed hydrogel coated LPG based salinity sensor.

With varying salinity levels, swelling and deswelling processes occur in the coated hydrogel layer, which induces large changes in the RI of the hydrogel, leading to centre wavelength

shifts of the LPG resonance loss bands. A schematic diagram showing the sensing mechanism of the developed salinity sensor and its centre wavelength shift against varying salinity conditions are illustrated in Fig. 2.27.

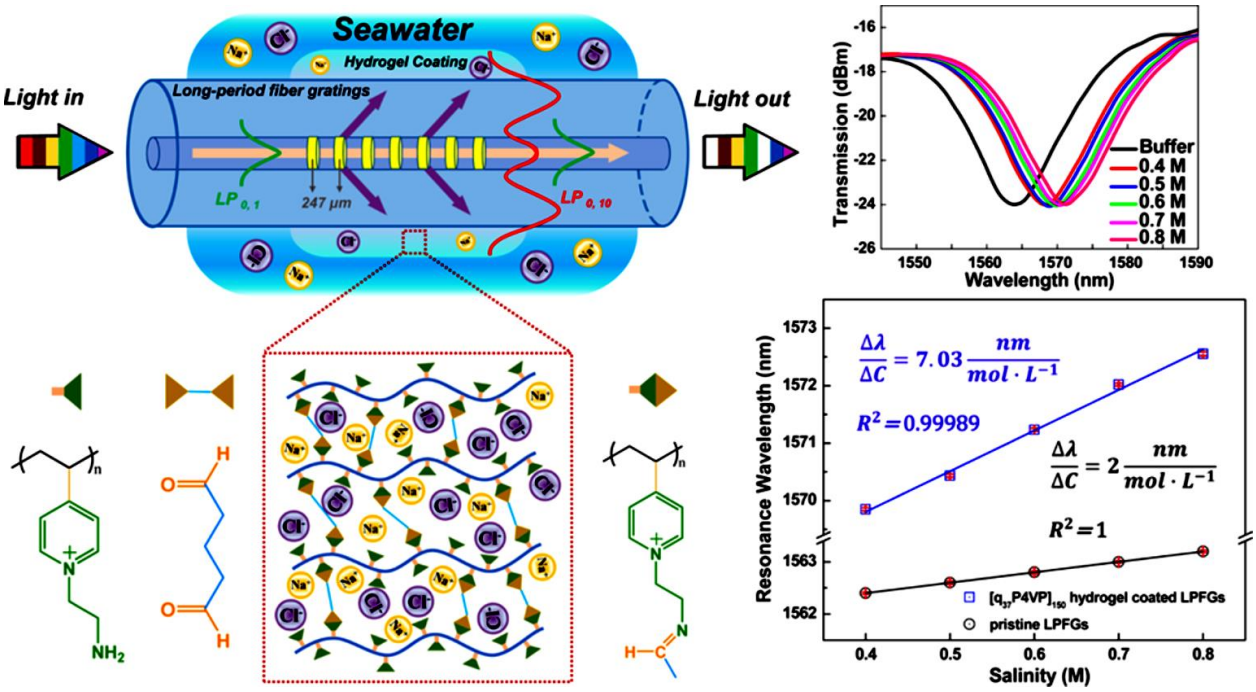

Fig 2. 27 Schematic diagram of the hydrogel coated LPG based salinity sensor and its resonance wavelength response against different salinity concentrations [64].

Partridge et al. have reported a calix[4]resorcinarene coated LPG sensor for the detection of toluene in water as a way of water quality monitoring in both domestic use and industrial sites [65]. calix[4]resorcinarene has been chosen as the sensing material due to its specific sensitivity to aromatic hydrocarbons. When toluene molecules interact with calix[4]resorcinarene coating, RI of the coated layer changes and thus, a shift in LPG resonance loss bands is observed. A schematic diagram of the developed LPG based sensor is shown in Fig. 2.28 below.

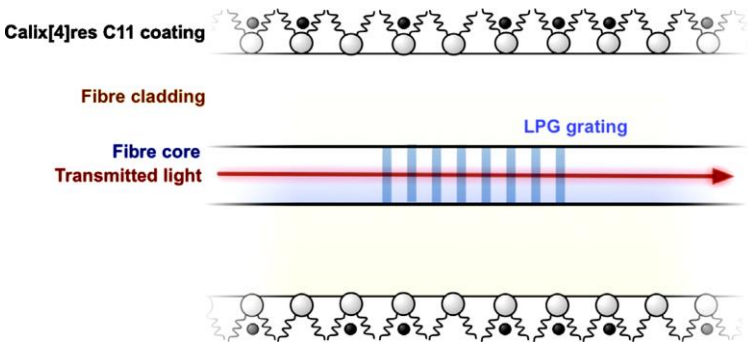

Fig 2. 28 Schematic of the coated LPG based toluene sensor [65].

A limit of detection (LOD) of ~ 100 ppm has been reported for this sensor and its selective wavelength response to toluene in aqueous conditions in comparison with other non-aromatic hydrocarbons is illustrated in Fig. 2.29, showing the dilution curve of the developed calix[4]resorcinarene coated LPG sensor against different toluene and ethanol solutions.

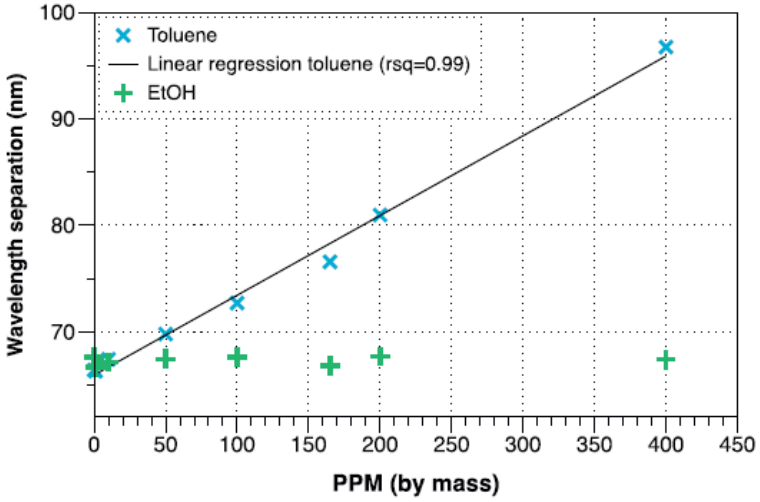

Fig 2. 29 Dilution curve of Toluene and Ethanol solution and their response of thecalix[4]res C11 coated LPG sensor [65].

Coated LPG approach has also been used in the development of species-specific biosensing as well. Conventional optical biosensing techniques rely on luminescence or absorption of light by the target biomolecules [66-67] but coated LPG approach proves to be advantageous in situations where the target biomolecules do not contain optical characteristics (RI change or absorption of light) when in contact with biorecognition elements present in biosensor systems as it relies on the wavelength shift caused by optical changes that occur in the coated biorecognition layer [68]. The external RI sensitivity of a LPG can be exploited to develop biosensors by functionalising the grating surface with a biorecognition element capable of binding the target biomolecule. Therefore, highly selective biosensors can be developed based on the affinity between the biorecognition element used to functionalise the LPG surface and

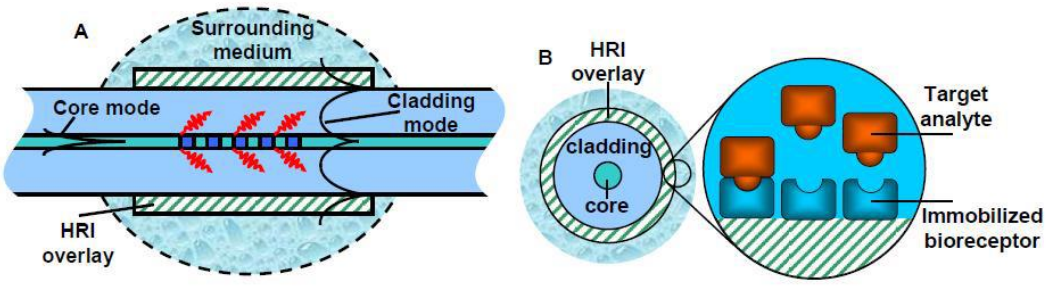

Fig 2. 30 Schematic of a LPG modified with a thin HRI overlay (a) transversal cross section of the device, (b) a zoom on the surface where a biomolecular recognition process is taking place [73].

the target analyte. A schematic diagram that illustrates the above discussed design of a coated LPG based biosensor is shown in Fig. 2.30.

Coated LPG based biosensors allow the detection and measurement of biomolecules in a label-free manner, which allows the bioreceptive element to measure the interaction with the analyte directly and in real time, which increases the efficiency and the response time of the fibre optic biosensors in comparison with conventional luminescent or light absorption based biosensing techniques [69].

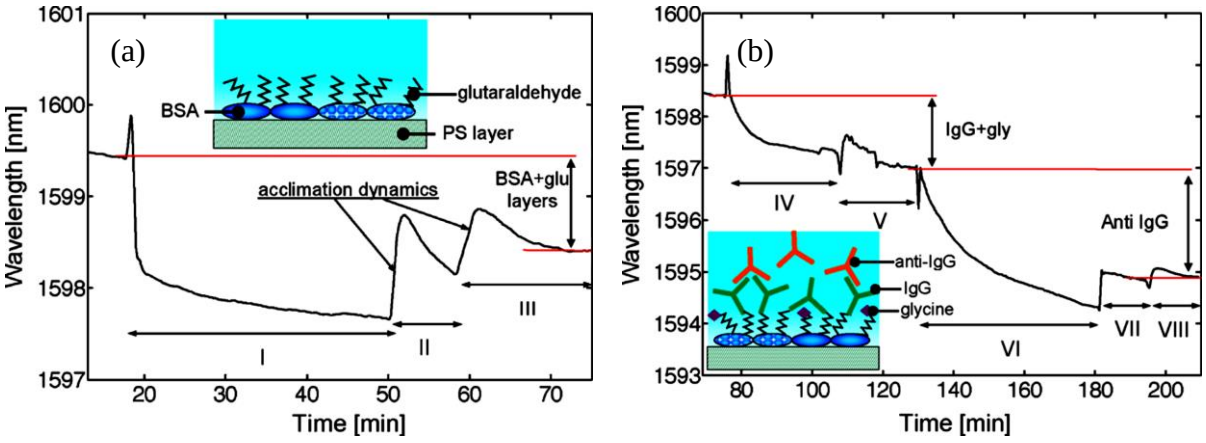

Fig 2. 31 LPG sensorgram reporting the wavelength shift of the 5th order cladding mode attenuation band (a) during the multiple biomolecular interactions, steps I-III and (b) the IgG binding and subsequent affinity assay with anti-IgG, steps IV-VIII. Inset: sketch of coated LPG surface with the different biological entities used in the experiment [69].

Pilla et al. have reported a label-free immunosensor developed by depositing a thin film coating of atactic polystyrene on a LPG surface by use of a dip coating technique [69]. The surface of the polystyrene surface has been functionalised with a BSA layer, which has been further functionalised with a glutaraldehyde conjugation acting as the bioreceptor. The thickness of the high indexed aPS layer has been chosen to tune the LPG, so that it operates around the highly sensitive transition point to achieve the highest sensitivity. To investigate the immunosensing capability of the developed sensor, a human IgG (antibody) has been covalently conjugated to the BSA layer via glutaraldehyde and the specific affinity binding with an anti-human IgG (antigen) has been recorded by monitoring the centre wavelength shift of the resonance loss band corresponding to the fifth order cladding mode. The response of the developed LPG based immunosensor under these multiple biomolecular interactions is illustrated in Fig. 2.31.

Tripathi et al. have reported a label-free biosensor developed to detect E-coli bacteria using a Bacteriophage T4 functionalised LPG sensing probe [70]. When E-coli bacteria is attached to

the Bacteriophage T4 layer on the cladding surface, the local effective RI observed by cladding modes changes and as a result, a shift in the resonance wavelength is observed. They have reported an ultrahigh sensitivity of ~2321 nm/RIU with a detection limit of 10^3 cfu/ml. The response of the developed LPG based bacteria sensor is shown in Fig. 2.32.

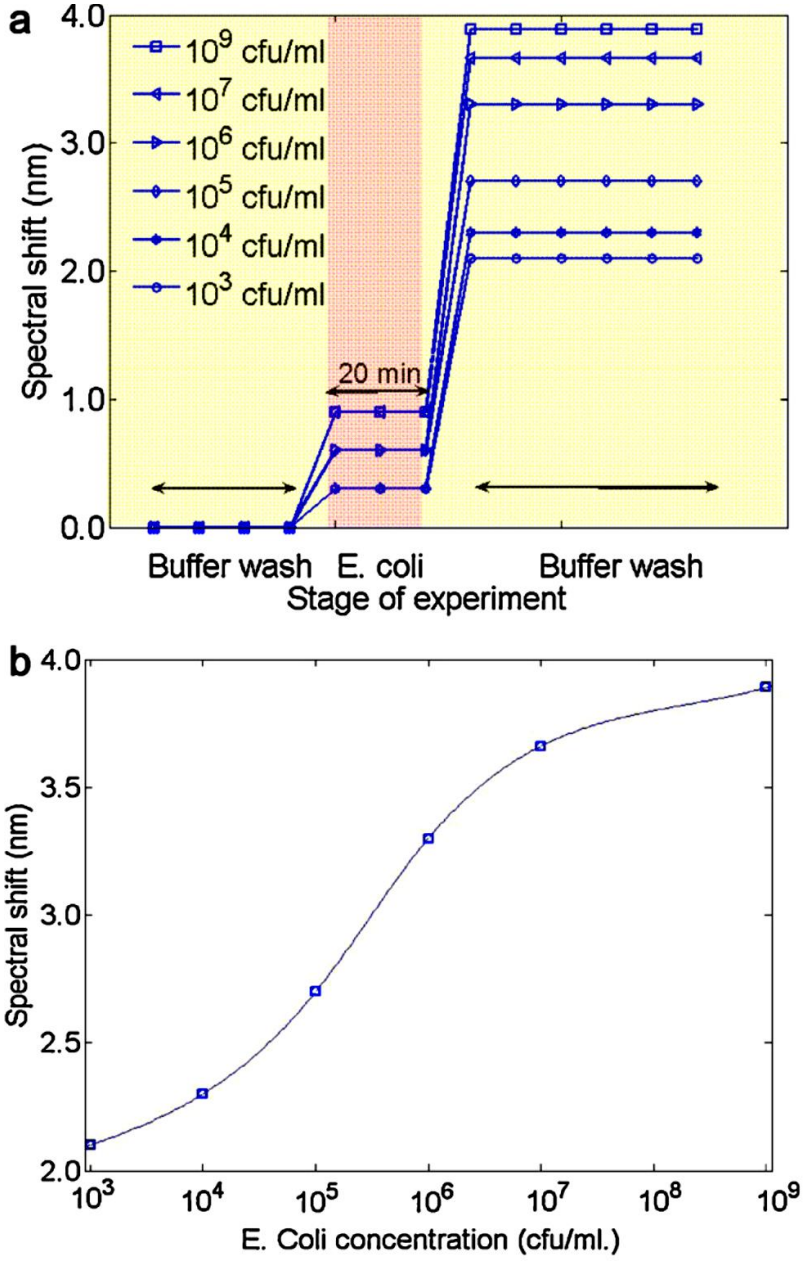

Fig 2. 32 Variation of (a) the spectral shift of the resonance wavelength prior to and after the E. coli incubation on the LPFG, and (b) the spectral shift of the resonance wavelength as a function of the E. coli concentration in the PBS buffer [70].

For the first time, Richter et al. have proposed a virus sensor based on the coated LPG approach for the detection of T7 bacteriophages virus [71]. The proposed LPG sensor probe has been tuned to its highest external RI sensitivity at dispersion turning point and its surface has been modified with T7 antibodies. The fibre surface has been functionalised with 3-

(triethoxysilyl)propylsuccinic anhydride to covalently bind T7 antibodies. The antigen-antibody interaction increases the thickness and the density of the bio-overlay, which results in changing its RI and the T7 phage detection has been made possible by monitoring the resultant resonance wavelength shift induced. A LOD of ~ 5x103 PFU/ml has been reported for this selective coated LPG based virus sensor. Schematic illustration representing the fibre surface modification steps related to each bio-molecular interaction is shown in Fig. 2.33.

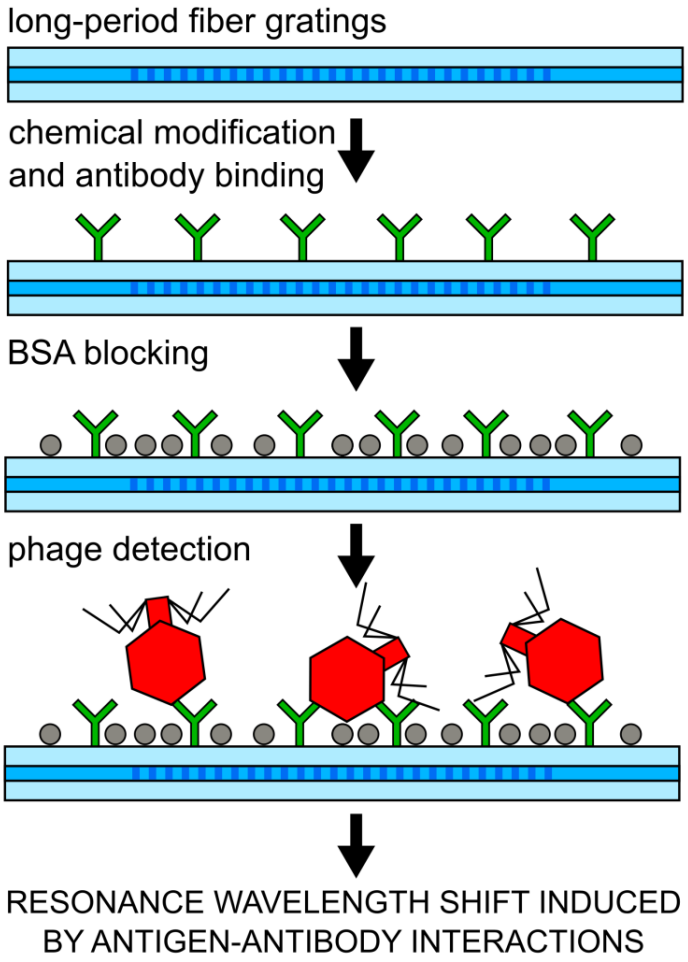

Fig 2. 33 Schematic representation of the fibre surface modification steps leading to phage detection [71].

Baliyan et al. have reported a label-free, enzyme immobilised LPG based biosensor for the detection of triacylglycerides [72]. The enzyme lipase has been immobilised on the LPG surface by using a simple electrostatic self-assembly technique. The sensing mechanism of the developed sensor is based on the resonance wavelength shift of the LPG attenuation bands induced by the interaction of triacylglycerides with the enzyme. The LPG based biosensor probe has reported a sensitivity of 0.5 nm/mM and a low LOD of 17.71 mg/ml for the physiological range of triacylglycerides in human blood.

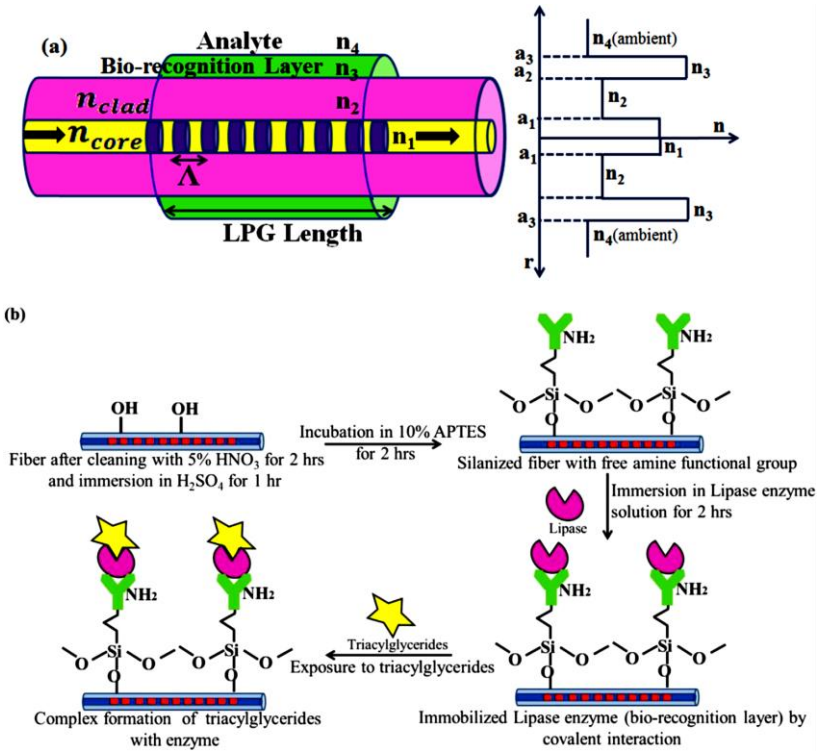

Fig 2. 34 (a) Schematic representation of the LPG fibre sensor probe (b) Immobilization of enzyme to create the bio-recognition layer on the optical fibre probe [72].

A schematic diagram illustrating the developed senor probe and the method carried out during the enzyme immobilisation process is shown in Fig. 2.34 followed by the spectral response at different temperatures in Fig. 2.35.

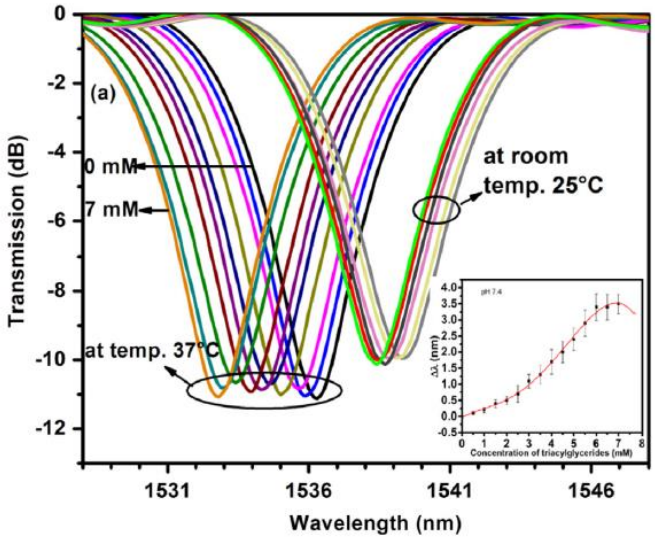

Fig 2. 35 Transmission spectrum at different concentrations of triacylglyceride (TGs) at room temperature and 37 °C, corresponding shift in resonance wavelength vs. concentrations of triacylglyceride along with standard deviation in the inset [72].

Based on the coated LPG sensors discussed above, it is evident that LPG based external RI sensors with a thin film coating of a material that has a high RI than that of the cladding pave the way for development of various chemical sensors used in structural health monitoring, environment monitoring, as well as different kinds label-free biosensors in the field of bio-molecule detection.

2.9 Summary

A detailed overview of the theoretical phenomena governing the characteristics of fibre gratings, contrasting both FBGs and LPGs, has been presented in this chapter. Based on the mode guiding in a grating structure and also the size of the grating period, fibre gratings can be categorised into two main categories, namely, FBGs and LPGs. Mode guiding in both FBGs and LPGs has been discussed in detail, followed by a consideration of the strain, temperature and external RI sensitivity of LPGs, this leading the way to a consideration of the advantages of coated LPG based external RI sensors. If the surrounding RI of a LPG is less than that of the cladding, a wavelength shift in the resonance loss bands is induced and if it matches that of the cladding, no attenuation bands will be observed in the transmission spectrum as no mode is guided in the cladding region. If the surrounding RI is higher than that of the cladding, a limitation in developing external RI sensors exist as intensity shift of resonance loss bands supersedes the wavelength shift in this region of surrounding RI values. The advantageous approach offered by the coated LPG for this application was introduced, providing a satisfactory way of overcoming the problems highlighted with FBG-based methods, while paving the way for more species-specific external RI-based LPG sensors. Finally, a detailed overview of the coated LPG sensors was presented by discussing the performance characteristics of a series of coated LPG sensors reported in the literature in various applications such as gas sensing, chemical sensing and biosensing.

This forms the basis for the approach taken in this work on the use of graphene nanomaterials, showing in the work reported their positive performance as sensing materials. Thus, the focus has been on building on the above in the development of a group of graphene nanomaterial-based fibre optic sensors and an evaluation of their performance using a number of specific tests and evaluations. As such, the next chapter is focused on graphene nanomaterials and their superiority as sensing materials in the development of graphene nanomaterials-based fibre optic sensors.

2.10 References

[1] Keiser G, Optical Fiber Communications, McGraw-Hill, 1983.

[2] Marcuse D, Theory of dielectric optical waveguides, Academic Press, 1991.

[3] Bhatia V, "Properties and sensing applications of long period gratings," PhD Thesis, Virginia Polytechnic Institute and State University, Virginia, 1996.

[4] Pierce J R, "Coupling of modes of propagation," Journal of Applied Physics, 25, 1954.

[5] Hill K O, Fujii Y, Johnson D C, Kawasaki B S, "Photosensitivity in optical fiber waveguides: Application to reflection filter fabrication," Applied Physics Letters, 32, 15, 1978.

[6] Sarkar B, Koley C, Roy N K, Kumbhakar P, "Condition monitoring of high voltage transformers using Fiber Bragg Grating Sensor," Measurement, 74, 255-267, 2015.

[7] Othonos A, and Kalli K, "Fiber Bragg Gratings: Fundamentals and Applications in Telecommunication and Sensing," Artech House, 1999.

[8] Meltz G, Morey W W, Glenn W H, "Formation of Bragg Gratings in Optical Fibers by a Transverse Holographic Method," Optics Letters, 14, 823-825, 1989.

[9] Hill K O, "Photosensitivity in Optical Fiber Waveguides: From Discovery to Commercialisation," IEEE Journal on Selected Topics in Quantum Electronics, 6, 1186-1189, 2000.

[10] Kersey A D, Davis M A, Patrick H J, LeBlanc M, Koo K P, Askin C G, Putnam M A, Friebele E J, "Fiber Grating Sensors," Journal of Lightwave Technology, 15, 1442-1463, 1997.

[11] Hill K O, Malo B, Bilodeau F, Johnson D C, "Photosensitivity in Optical Fibres," Annual Reviews Material Science, 23, 125-157, 1993.

[12] Hill K O, Malo B, Vineberg K A, Bilodeau F, Johnson D C and Skinner I, "Efficient mode conversion in telecommunication fibre using externally written gratings," Electronics Letters, 26, 16, 1270-1272, 1990.

[13] Bilodeau F, Hill, K O, Malo B, Johnson D C and Skinner I M. "Efficient, narrowband LP_{01}-LP_{02} mode convertors fabricated in photosensitive fibre: spectral response," Electronics Letters, 27(8), 682, 1991.

[14] Johnson D C, Bilodeau F, Malo B, Hill K O, Wigley P G J, and Stegeman G I, "Long-length, long-period rocking filters fabricated from conventional monomode telecommunications optical fiber," Optics Letters, 17, 1635-1637, 1992.

[15] Vengsarkar A M, Lemaire P J, Judkins J B, Bhatia V, Sipe J E and Ergodan T E, "Long-period fiber gratings as band-rejection filters," Journal of Lightwave Technology, 14, 58, 1996.

[16] R. Kashyap, "Fibre Bragg Gratings," New York:Academic, 1999.

[17] Narayanan C, Presby H M and Vengsarkar A M, "Band-rejection fibre filter using periodic core deformation," OFC 1996 (San Jose, USA), 267–8, 1996.

[18] Lin C-Y, Chern G-W and Wang L A, "Periodical corrugated structure for forming sampled fibre Bragg grating and long-period fibre grating with tunable coupling strength," Journal of Lightwave Technology, 19 1212–20, 2001.

[19] Kakarantzas G, Dimmick T E, Bricks T A, Le Roux R and Russel P, "Miniature all fiber devices based on CO2 laser microstructuring of tapered fibers," Optics Letters, 26,15, 1137-1139, 2001.

[20] Savin A, Digonnet J F, Kino G S and Shaw H J, "Tunable mechanically induced long period fiber gratings," Optics Letters, 25, 10, 710-712, 2000.

[21] Kakarantzas G, Birks T A and Russell P S, "Structural long-period gratings in photonic crystal fibers," Optics Letters, 271013–15, 2002.

[22] Kim C S, Han Y, Lee B H, Han W-T, Paek U-C and Chung Y, "Induction of the refractive index change in B-doped optical fibers through relaxation of the mechanical stress" Optical Communications, 185, 337–42, 2000.

[23] Kondo Y, Nouchi K, Mitsuyu T, WatanabeM, Kazansky P and Hirao K, "Fabrication of long-period fibre gratings by focused irradiation of infra-red femtosecond laser pulses," Optics Letters, 24, 646–8, 1999.

[24] Rego G, Okhotnikov O, Dianov E and Sulimov V, "High-temperature stability of long-period fibre gratings using an electric arc," Journal of Lightwave Technology, 19, 1574–9, 2001.

[25] Fujumaki M, Ohki Y, Brebner J L and Roorda S, "Fabrication of long-period optical fibre gratings by use of ion implantation," Optics Letters, 25, 88–90, 2000.

[26] Davis D D, Gaylord T K, Glytsis E N, Kosinski S G, Mettler S C and Vengsarkar A M, "Long-period fibre grating fabrication with focused CO_2 laser beams," Electronics Letters, 34, 302–3, 1998.

[27] Bhatia V and Vengsarkar A M, "Optical fibre long-period grating sensors," Optics Letters, 21, 692–4, 1996.

[28] Guan B-Ou, Tam H-Y, Ho S-L, Liu S-Y and Dong X-Y, "Growth of long-period gratings in H_2-loaded fibre after 193 nm UV inscription," IEEE Photonics Technology Letters, 12, 642–4, 2000.

[29] Blows J and Tang D Y, "Gratings written with tripled output of Q-switched Nd:YAG laser," Electronics Letters, 36, 1837–9, 2000.

[30] Williams D L, Ainslie B J, Armitage J R, Kashyap R and Campbell R, "Enhanced UV photosensitivity in boron codoped germanosilicate fibers," Electronics Letters, 29, 45–7, 1993.

[31] Lemaire P J, Atkins R M, Mizrahiu V and Reed W A, "High pressure H_2-loading as a technique for achieving ultrahigh UV photosensitivity and thermal sensitivity in GeO_2 doped optical fibers," Electronics Letters, 29, 1191–3, 1993.

[32] Marshall G D, Williams R J, Jovanovic N, Steel M J, and Withford M J, "Point-by-point written fiber-Bragg gratings and their application in complex grating designs," Optics Express, 18, 19844-19859, 2010.

[33] Yeo T L, "Application of FBG-based sensors in built environment," PhD Thesis, City University London, UK, 2008.

[34] Patrick H J, Askins C G, Mcelhanon R W and Friebele E J, "Amplitude mask patterned on an excimer laser mirror for high intensity writing of long period fibre gratings," Electronics Letters, 33, 1167–8, 1997.

[35] Lu S Y, Tan H Y and Demokan M S, "Low-cost micro lens array for long-period grating fabrication," Electronics Letters, 35, 79–80, 1999.

[36] https://www.laserfocusworld.com/fiber-optics/article/16547082/optics-fabrication-fiber-bragg-grating-fabrication-system-is-automated : Last visited: 11.07.2020

[37] James S W, Tatam R P, "Optical fibre long-period grating sensors: characteristics and application," Measurement Science and Technology, 14, 49-61, 2003.

[38] Duhem O and Douay M, "Effect of UV-induced birefringence on long-period grating coupling characteristics," Electronics Letters, 36, 416–17, 2000.

[39] Erdogan T, Mizrahi V, Lemaire P J, Monroe D, "Decay of ultraviolet-induced fiber Bragg gratings," Journal of Applied Physics, 76, 73, 1994.

[40] Hidayat A, Wang Q, Niay P, Douay M, Poumellec B, Riant I, "Temperature-induced reversible changes in the spectral characteristics of fibre Bragg grating," Applied Optics, 40, 2632-2641, 2002.

[41] Pal S, "Characterisation and high-temperature sensing potential of fibre Bragg gratings in specialised optical fibres," PhD Thesis, City University London, UK, 2004.

[42] Fabian M, Hind D M, Gerada C, Sun T, and Grattan K T V, "Comprehensive Monitoring of Electrical Machine Parameters Using an Integrated Fiber Bragg Grating-Based Sensor System," Journal of Lightwave Technology, 36, 1046-1051, 2018.

[43] Bhatia V, "Applications of long-period gratings to single and multi-parameter sensing," Optics Express, 4, 457–66, 1999.

[44] Alwis L, Grattan K T V, Sun T, "Fibre optic long period grating-based humidity sensor probe using a Michelson interferometric arrangement," Sensors and Actuators B: Chemical, 178, 694-699, 2013.

[45] Sridevi S, Vasu K S, Bhat N, Asokan S, Sood A K, "Ultra sensitive NO_2 gas detection using the reduced graphene oxide coated etched fiber Bragg gratings," Sensors and Actuators B: Chemical, 223, 481-486, 2016.

[46] Huang S, Blake J N, & Kim B Y, "Perturbation effects on mode propagation in highly elliptical core two-mode fibers," Journal of Lightwave Technology, 8, 1, 23-33, 1990.

[47] Bhatia V, Campbell D K, Sherr D, D'Alberto T G, Zabaronick N A, Ten Eyck G A, Murphy K A and Claus R O, "Temperature-insensitive and strain insensitive long-period grating sensors for smart structures," Optical Engineering, 36, 1872–6, 1997.

[48] Patrick H J, Kersey A D, and Bucholtz F, "Analysis of the Response of Long Period Fiber Gratings to External Index of Refraction," Journal of Lightwave Technology, 16, 1606, 1998.

[49] Patrick H J, Kersey A D, Bucholtz F, Ewing K J, Judkins J B, and Vengsarkar A M, "Chemical sensor based on long-period fiber grating response to index of refraction," Proceedings. Conference of Lasers and Electro-Optics, 11, 1997 OSA Technical Digest Series, Optical Society of America, Washington, DC, 420–421, 1997.

[50] Rees N D, James S W, Tatam R P, Ashwell G J, "Optical fiber long-period gratings with Langmuir–Blodgett thin-film overlays," Optics Letters, 27, 9, 686-688, 2002.

[51] Duhem O, Henninot J-F, WarenghemM and Douay M, "Demonstration of long-period grating efficient couplings with an external medium of a refractive index higher than that of silica," Applied Optics, 37, 7223–8, 1998.

[52] Falciai R, Mignani A G and Vannini A, "Long period gratings as solution concentration sensors," Sensors Actuators B, 74, 74–7, 2001.

[53] Khaliq S, James S W and Tatam R P, "Fibre-optic liquid level sensor using a long-period grating" Optics Letters, 26, 1224–6, 2001.

[54] Liu H, Liang D, Zeng J, Jin J, Wu J, Geng J, "Design of a long-period fiber grating sensor for reinforcing bar corrosion in concrete," Journal of Intelligent Material Systems and Structures, 23, 45–51, 2011.

[55] Falate R, Kamikawachi R C, Muller M, Kalinowski H J, Fabris J L, "Fiber optic sensors for hydrocarbon detection," Sensors and Actuators B, 105, 430 – 436, 2005.

[56] Wang J and Tang J, "An optical fiber viscometer based on long-period fiber grating technology and capillary tube mechanism," Sensors, 10, 11174-11188, 2010.

[57] Del Villar I, Matías I R, Arregui F J, and Lalanne P, "Optimization of sensitivity in Long Period Fiber Gratings with overlay deposition," Optics Express, 13, 56-69, 2005.

[58] Gu Z, Shi Y, and Zhang J, "Novel metal coated long period fiber grating liquid sensor based on dual-peak resonance," Optical Engineering, 51(8), 081508, 2012.

[59] Cusano A, Pilla P, Giordano M, Cutolo A, "Modal Transition in Nano-Coated Long Period Fiber Gratings: Principle and Applications to Chemical Sensing," Springer US, 35-75, 2009.

[60] Del Villar I, Matías I R, Arregui F J, "Influence on cladding mode distribution of overlay deposition on long-period fiber gratings," Journal of the Optical Society of America, 23, 651-658, 2006.

[61] Venugopalan, Yeo T L, Sun T, Grattan K V, "LPG-Based PVA Coated Sensor for Relative Humidity Measurement," IEEE Sensors, 8, 1093-1098, 2008.

[62] Wang Y, Liu Y, Zou F, Jiang C, Mou C, Wang T, "Humidity Sensor Based on a Long-Period Fiber Grating Coated with Polymer Composite Film," Sensors (Basel), 19(10):2263, 2019.

[63] Esposito F, Zotti A, Palumbo G, Zuppolini S, Consales M, Cutolo A, Borriello A, Campopiano S, Zarrelli M, Iadicicco A., "Liquefied Petroleum Gas Monitoring System Based on Polystyrene Coated Long Period Grating," Sensors, 18(5):1435, 2018.

[64] Yang F, Hlushko R, Wu D, Sukhishvili S A, Du H, and Tian F, "Ocean Salinity Sensing Using Long-Period Fiber Gratings Functionalized with Layer-by-Layer Hydrogels," ACS Omega,4 (1), 2134-2141, 2019.

[65] Partridge M, Wong R, James S W, Davis F, Higson S P J, Tatam R P, "Long period grating based toluene sensor for use with water contamination," Sensors and Actuators B: Chemical, 203, 621-625, 2014.

[66] Taitt C R, Anderson G P, Ligler F S, "Evanescent wave fluorescence biosensors," Biosensors and Bioelectronics, 20, 2470–2487, 2005.

[67] Luppa P B, Sokoll L J, Chan D W, "Immunosensors—principles and applications to clinical chemistry," Clinica Chimica Acta, 314, 1–26, 2001.

[68] Baldini F, Brenci M, Chiavaioli F, Giannetti A, Trono C, "Optical fibre gratings as tools for chemical and biochemical sensing," Analytical and Bioanalytical Chemistry, 402:109– 116, 2012.

[69] Pilla P, Sandomenico A, Malachovská V, Borriello A, Giordano M, Cutolo A, Ruvo M, Cusano A, "A protein-based bio interfacing route toward label free immunoassays with long period gratings in transition mode," Biosensors and Bioelectronics, 31, 486– 491, 2012.

[70] Tripathi S M, Bock W J, Mikulic P, Chinnappan R, Ng A, Tolba M, Zourob M, "Long period grating based biosensor for the detection of Escherichia coli bacteria," Biosensors and Bioelectronics, 35, 1, 308-312, 2012.

[71] Janczuk-Richter M, Dominik M, Roźniecka E, Koba M, Mikulic P, Bock W J, Łoś M, Śmietana M, Niedziółka-Jönsson J, "Long-period fiber grating sensor for detection of viruses," Sensors and Actuators B: Chemical, 250, 32-38, 2017.

[72] Baliyan A, Sital S, Tiwari U, Gupta R, Sharma E K, "Long period fiber grating based sensor for the detection of triacylglycerides," Biosensors and Bioelectronics, 79, 693-700, 2016.

[73] Alwis S, "Optimization of Polymer Coated Long Period Grating-based Sensors," PhD Thesis, City University London, London, UK, 2013.

Chapter 3

Graphene Nanomaterials-based Fibre Optic Sensors

3.1 Introduction

Two-dimensional materials possess unique and interesting characteristics compared with conventional materials due to their single atom thickness. Since the discovery of graphene, the first ever 2D material discovered, its unique characteristics have been exploited in various applications such as electronics, bioimaging, energy storage, composites, sensors and health. The interest in graphene started to grow even more after the Nobel Prize was awarded for the discovery of graphene in 2010. This chapter is focused on graphene nanomaterials and their unique properties - properties that can be exploited to develop highly sensitive and ultra-efficient sensor systems. First, an introduction to graphene and its derivatives will be presented, followed by an overview of methods used to synthesise graphene-based nanomaterials, following which the properties of graphene and GO will also be discussed in detail. The chapter concludes with a comprehensive review of graphene nanomaterial-based fibre optic sensors that have been reported in literature to date and this provides a direction for the work in discussed in subsequent chapters.

3.2 Graphene and its Derivatives

3.2.1 Graphene

Graphene is a single atom thick, flat monolayer of carbon that contains sp^2 hybridized carbon atoms tightly packed in a honeycomb lattice. It was first discovered accidently by Andre Geim and Konstantin Novoselov in 2004 by using a 'scotch tape' method [1]. Graphene has been termed the 'wonder material' as a result of the unique and interesting characteristics that it possesses due to its 2D nature. These unique properties include high electron mobility of 250,000 cm^2/ Vs [2], high thermal conductivity of 5000 W/m-K [3], the largest surface area of 3000 m^2/g [4], and an exceptional Young's modulus of 1 TPa [5]. Researchers and scientists have paid special attention to graphene due to these exceptional characteristics and graphene

has been used in various engineering applications such as field effect transistors, gas and bio-sensors, transparent electronics and in bio-imaging and energy storage [6].

Carbon (C) is one of the most commonly used elements in day-to-day life. Diamond and graphite are two of the three-dimensional (3D) crystalline forms of carbon. Diamond is formed purely of sp^3 hybridized carbon bonds whereas graphite consists purely of sp^2 hybridized carbon atoms. Due to very strong covalent bonding between sp3 hybridized atoms, diamond shows very strong physical properties in contrast with graphite, which has been reported to have a layered, planar structure [7]. In each of these layers, carbon atoms are tightly packed in a hexagonal lattice with a C-C bond length of 0.142 nm arising from the sp^2 hybridization. The distance between these two layers is 0.335 nm. Therefore, graphene can be identified as the basic structural element of other carbon allotropes [8], which include fullerene [9], carbon nanotubes (CNT) [10] and graphyne [11], carbon fibres (CF), amorphous carbon and charcoal [12]. These carbon allotropes are illustrated in Fig. 3.1 below.

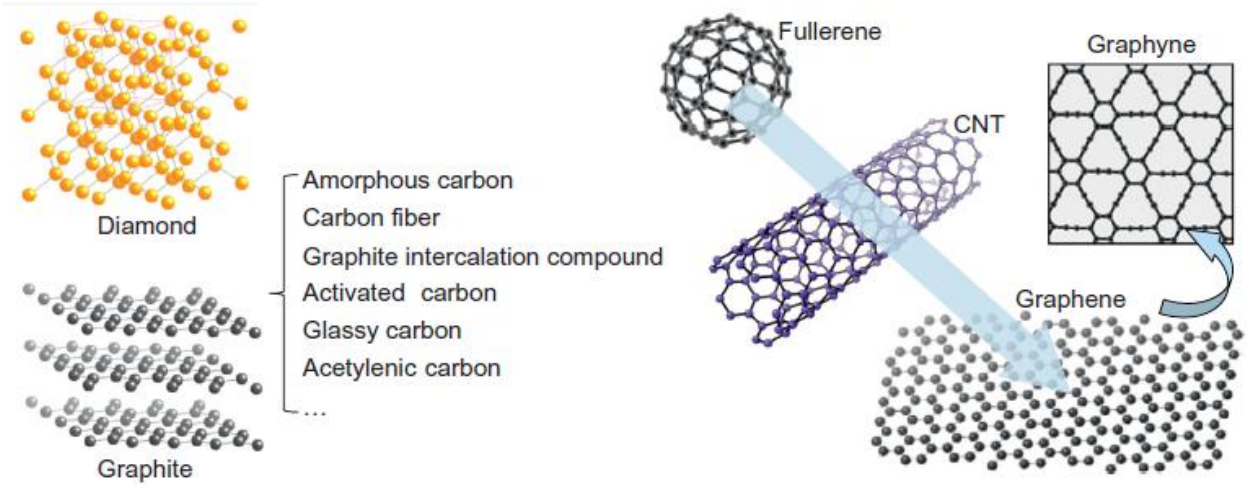

Fig 3. 1 Carbon allotropes and related materials [13].

A schematic diagram illustrating the hexagonal carbon lattice of graphene and the bonding between two carbon atoms is shown in Fig. 3.2.

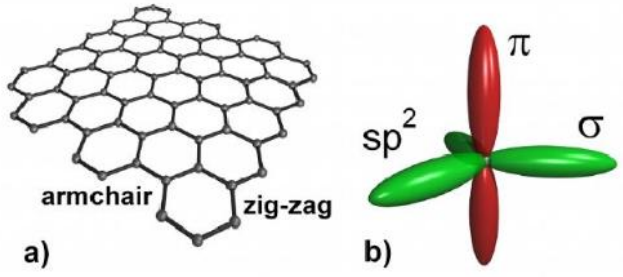

Fig 3. 2 Graphene (a) geometry (b) bonding [14].

As can be seen from Fig. 3.2, three σ bonds exist in each carbon atom, forming a strong hexagonal carbon lattice of graphene. The high stability exhibited by graphene can be attributed to the s, p_x and p_y bonding that forms each of the σ bonds and the tightly packed atomic structure. The high electron mobility resulting in the high conductivity of graphene is mostly attributed to the π bond that exists vertically to the lattice plane, which is formed by the final p_z electron. These bonds hybridize together to form the π and π* bands, which leads to most of the unique electron properties shown by graphene through the half-filled band that allows free-moving electrons [13]. As can be seen from Fig. 3.2 (a), the edge of a graphene sheet can be categorised into 'zigzag' and 'armchair' categories, depending on the type of carbon chain present. These varieties in graphene sheets lead to different conducting behaviours. For example, a graphene nanoribbon with an armchair edge would show conductive characteristics like a metal or a semiconductor whereas a graphene nanoribbon with a zigzag carbon structure would behave like metal [13]. Mechanically exfoliated single layered graphene sheets with zigzag and armchair edges are illustrated in Fig. 3.3 below.

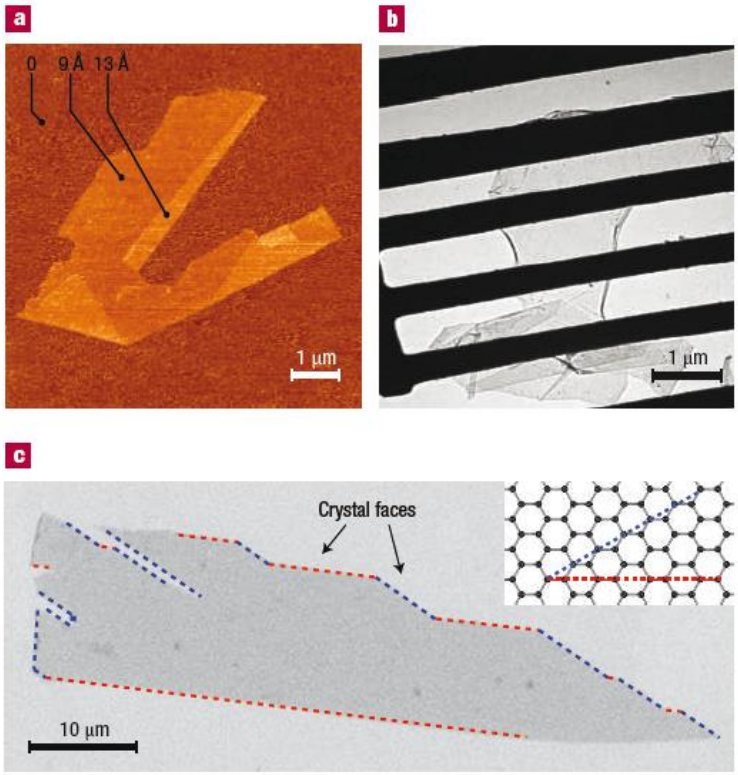

Fig 3. 3 One-atom-thick single crystals (a) Graphene visualized by atomic force microscopy. The folded region exhibiting a relative height of≈4 Å (0.4 nm) clearly indicates that it is a single layer. (b) A graphene sheet freely suspended on a micrometre-size metallic scaffold. (c) Scanning electron micrograph of a relatively large graphene crystal, which shows that most of the crystal's faces are zigzag and armchair edges as indicated by blue and red lines and illustrated in the inset. 1D transport along zigzag edges and edge-related magnetism attract significant attention [15].

3.2.2 Graphene Oxide (GO)

Even though GO has gained significant attention after the discovery of graphene in 2004, it had been synthesised first, one and half centuries earlier by Benjamin Brodie in 1859 [16]. Unfortunately, no one knew about the interesting characteristics of 2D graphene nanomaterials back then and as such, it did not lead to any significant discoveries. In the beginning, GO was regarded as a resultant material of chemical oxidising and exfoliation of graphite crystals [17]. Under these chemical oxidising conditions (which will be discussed in detail in the next part of this chapter), graphite carbon atoms were observed to retain the 2D structure of layers while attaching some oxygen containing groups to both sides of the carbon plane and its edges [18]. Even though this structure was achieved by chemical exfoliation of graphite in the beginning (the 'top down' method), recent research has shown that the same 2D graphene like structures with modified oxygen containing groups can be achieved by bottom-up methods such as hydrothermal treatment of glucose [19] or chemical vapour deposition [20]. Therefore, the general definition of what GO is can be given as 'a single layer carbon sheet that contains oxygen containing functional groups on both sides of its basal plane and its edges'. In a way similar to graphene, GO can have single layer or multilayer structures. GO exhibits characteristics similar to that of graphene in some applications but interestingly, it can also exhibit properties that are far from those of graphene, such as low electron conductance and significantly high surface chemistry, which arise due to its structure that consists of oxygen containing functional groups.

As a result of complexity of the GO material that includes sample-to-sample variability, a nonstoichiometric atomic structure and the lack of techniques or characterisation methods available to investigate such materials, the chemical structure of GO has been under debate over the years and even to date, no specific model that explains the GO atomic structure exists. Even under these difficult circumstances, considerable effort has been focused on determining the chemical structure of GO. The earliest models that illustrated the GO structure have been based on discrete repeat units. The first such structure proposed by Hofmann and Holst revealed epoxy groups present across the basal carbon planes with a net molecular formula of C_2O [21]. Later in 1946, Ruess proposed a model that contained hydroxyl groups attached to the basal plane, which accounted for the hydrogen content of GO [22]. Scholz and Boehm proposed a model in 1969 by completely removing the epoxide and ether groups and substituting regular quinoidal species in a corrugated backbone [23]. Later on, Nakajima and Matsuo suggested a more interesting model by assuming a carbon lattice framework related to a stage two graphite

intercalation compound [24]. These four models illustrating the chemical structure of GO are shown in Fig. 3.4 below.

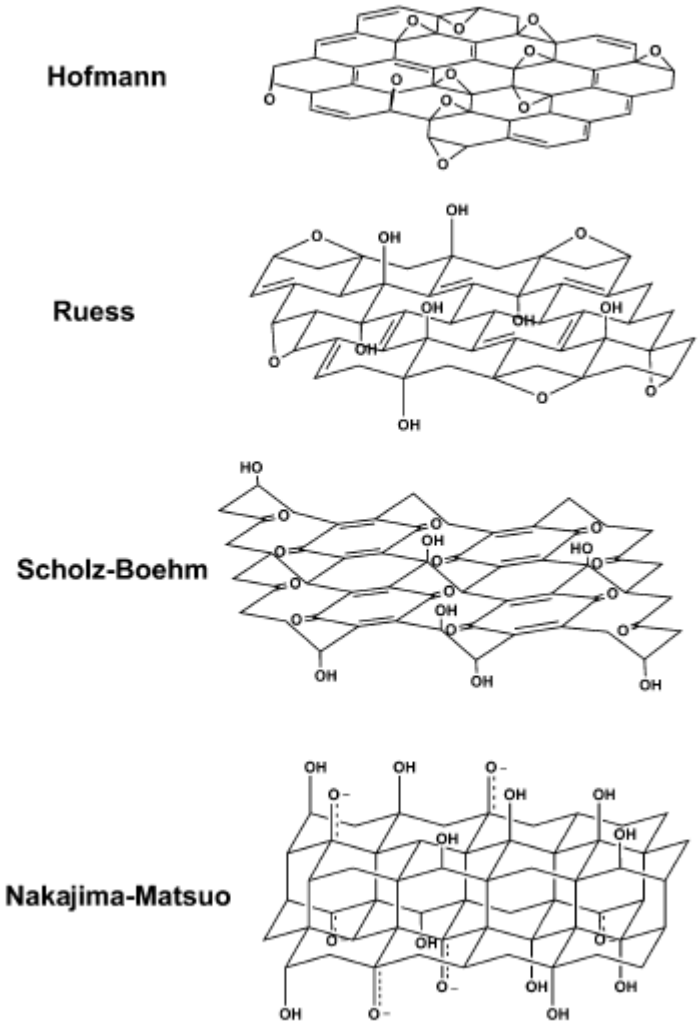

Fig 3. 4 Summary of older models illustrating the chemical structure of GO [26].

Recent models have rejected the lattice-based atomic architecture and have incorporated a nonstoichiometric, amorphous alternative. Anton Lerf and Jacek Klinowski used a solid state nuclear magnetic resonance (NMR) spectroscopy to characterise GO and their model is the most well-known model at the moment, this being illustrated in Fig. 3.5 [25].

Based on the models shown above, it has been established that the chemical structure of GO depends on the degree of oxidation caused by the starting graphite materials and the oxidation protocol used [26]. GO contains functioning oxygen groups such as epoxy, carboxyl, hydroxyl and alcohol groups on its basal planes and its edges but the exact identity and the distribution of these oxide functional groups depend strongly on the extent of the coverage.

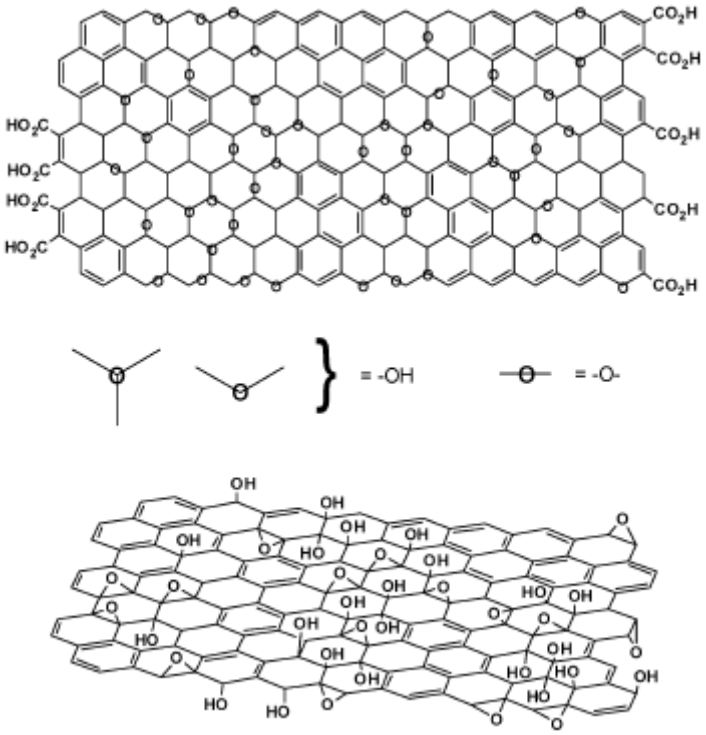

Fig 3. 5 Variations of the Lerf-Klinowski model indicating ambiguity regarding the presence (top) or absence (bottom) of carboxylic acids on the periphery of the basal plane of the graphitic platelets of GO [25]

3.3 Synthesis Methods of Graphene Nanomaterials

3.3.1 Synthesis of Graphene

A number of graphene synthesis processes have been reported, based on the chemical and physical procedures used. The simplest method so far has been reported by Geim et al. in the first publication of the discovery of graphene [1]. They used a mechanical exfoliation method, which can be used to produce high quality sp^2 hybridized graphene sheets up to millimetre size and as such, is an ideal graphene synthesis method for fundamental research and developing prototype graphene devices.

Berger et al. have reported a graphene synthesis method based on epitaxial growth of graphene on a silicon carbide (SiC) substrate which involves a thermal decomposition on a prepared SiC surface in temperatures up to 1450 ℃ for a period of up to 20 minutes [27]. However, due to the high temperatures used, this method is highly energy intensive. Moreover, as a result of strong binding between the deposited graphene layer and the substrate, it is hard to transfer graphene sheets to another surface. Epitaxial growth of graphene has been reported to produce graphene films at a millimetre scale, these being electrically conductive [27].

Chemical vapour deposition (CVD) is another well-known method for producing graphene films. This method involves decomposition of a fluid at a high temperature to deposit a graphene film on a substrate such as silicon wafers or copper foils [28, 29]. High yields of graphene films can be produced with the use of CVD and it has also been reported that the developed graphene films can be transferred to other surfaces relatively easily [30] and as such, this method is much more suitable for applications that require graphene layers deposited on flexible substrates or polymers. The quality of the developed graphene layers depends on the operating temperature and thus, high temperatures must be used to achieve more continuous crystalline structures.

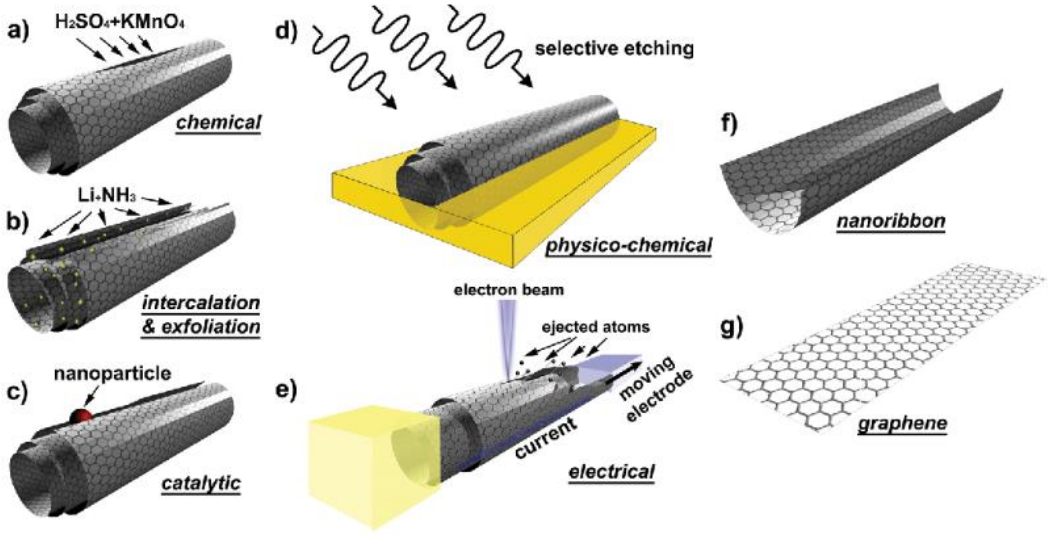

Fig 3. 6 Sketch showing the different ways nanotubes could be unzipped to yield graphene nanoribbons (GNRs): (a) chemical route, involving acid reactions that start to break carbon-carbon bonds (e.g., H_2SO_4 and $KMnO_4$ as oxidizing agents) (b) intercalation-exfoliation of MWCNTs, involving treatments in liquid NH_3 and Li, and subsequent exfoliation using HCl and heat treatments (c) catalytic approach, in which metal nanoparticles "cut" the nanotube longitudinally like a pair of scissors (d) physicochemical method, by embedding the tubes in a polymer matrix followed by Ar plasma treatment and (e) the electrical method, by passing an electric current through a nanotube. The resulting structures are either (f) GNRs or (g) graphene sheets [31].

2D graphene nanoribbons can be produced by unzipping one dimensional CNTs. Various chemical, physico-chemical, mechanical and electrical methods of unzipping single walled CNTs (SWCNTs) and multi-walled CNTs (MWCNTs) have been reported as illustrated in Fig. 3.6 above [31]. Graphene nanoribbons with a width of approximately 10-20 nm can be produced using this method by comparison with continuous sheets produced by other described methods.

Hernandez et al. have reported another synthesis process for graphene, based on liquid phase exfoliation of graphite [32]. Under this method, graphite flakes are dispersed in a solvent and individual graphene layers are separated from multi- and few-layer graphene by use of ultrasonication and centrifugation techniques. The solvent must be selected carefully to minimise the interfacial tension between the graphite flakes and the liquid to minimise the aggregation of single layer graphene sheets.

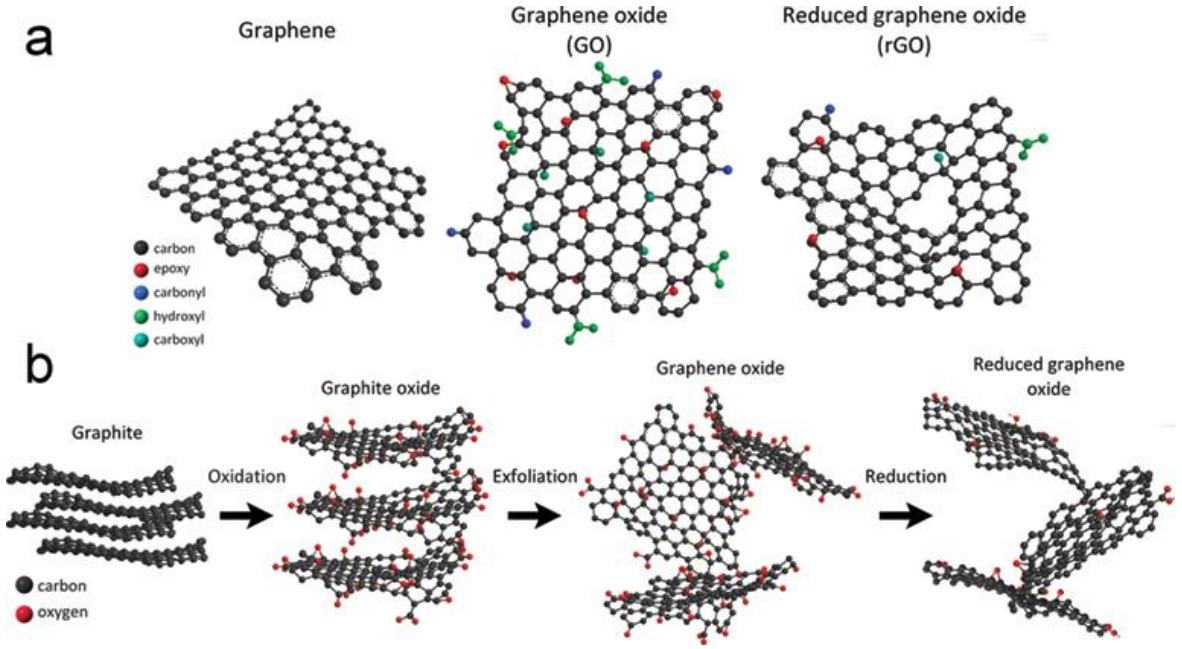

Fig 3. 7 Schematic chemical structures of graphene, GO, and reduced GO (b) Route of graphite to reduce GO [33].

Not all the methods discussed above are suitable for mass production of graphene, which is a disadvantage when it comes real-world commercial applications. However, GO, which is considered as a precursor to graphene, can be produced in large amounts with the use of Hummer's method [34] that involves strong oxidation of graphite by acid (which will be discussed in the next subsection of this chapter). As discussed earlier, GO contains oxygen containing functional groups such as hydroxyl and epoxy groups on its basal planes and carbonyl and carboxyl groups at its edges [35]. The presence of these oxygen containing groups significantly reduces the conductivity of GO in comparison with pristine graphene due to the conjugated π-electron system [36]. These oxygen containing groups can be partially reduced by the use of reduction methods such as thermal [37], chemical [38] and UV exposure [39] and the resultant product is termed reduced Graphene Oxide (rGO) or Chemically Converted Graphene (CCG). The characteristics of rGO will depend upon the reduction method used. A

schematic diagram that illustrates the chemical structure of graphene, GO and rGO is shown in Fig. 3.7 above.

A summary of the above discussed graphene synthesis methods is illustrated in Fig. 3.8 below.

Fig 3. 8 Summary of the main graphene synthesis methods [40].

3.3.2 Synthesis of Graphene Oxide

All the methods used for the synthesis of GO involve the oxidation of graphite flakes with strong oxidizing agents. Graphite is a naturally occurring mineral and thus many localized defects in the π structure are present, which may serve as seed points for oxidation to occur [26]. As mentioned before, the first instance of GO synthesis was reported by the British chemist B. C. Brodie in 1859 [16]. He has used potassium chlorate ($KClO_3$) and fuming nitric acid (HNO_3) to oxidize graphite flakes. Nitric acid is a common oxidizing agent that reacts with aromatic carbon structures and nanotubes to produce oxygen containing groups such as ketones, carboxyls and lactones [41]. $KClO_3$ is also another strong oxidizing agent that produces dioxygen which acts as the reactive species [42]. However, Brodie's method seemed to be time consuming and involved a few hazardous steps. Later on, Staudenmaier improved Brodie's method by adding concentrated sulphuric acid (H_2SO_4) to increase the acidity of the mixture [43], which resulted in the production of highly oxidized GO in a single step process.

The most popular method reported in contemporary literature is the Hummer's method, which has been introduced by Staudenmaier, Hummers and Offeman in 1958 [34]. Hummer's method is based on the graphite flake oxidization by use of concentrated H_2SO_4, potassium permanganate ($KMnO_4$) and sodium nitrate ($NaNO_3$), without the use of HNO_3, followed by filtration and centrifugation. Even though $KMnO_4$ is a natural oxidant, the oxidising agent in Hummer's method is in fact, diamanganese heptoxide (Mn_2O_7), as shown in the reaction below [26].

$$KMnO_4 + 3H_2SO_4 \rightarrow K^+ + MnO_3^+ + H_3O^+ + 3HSO_4^- \quad (3.1)$$

$$MnO_3^+ + MnO_4^- \rightarrow Mn_2O_7 \quad (3.2)$$

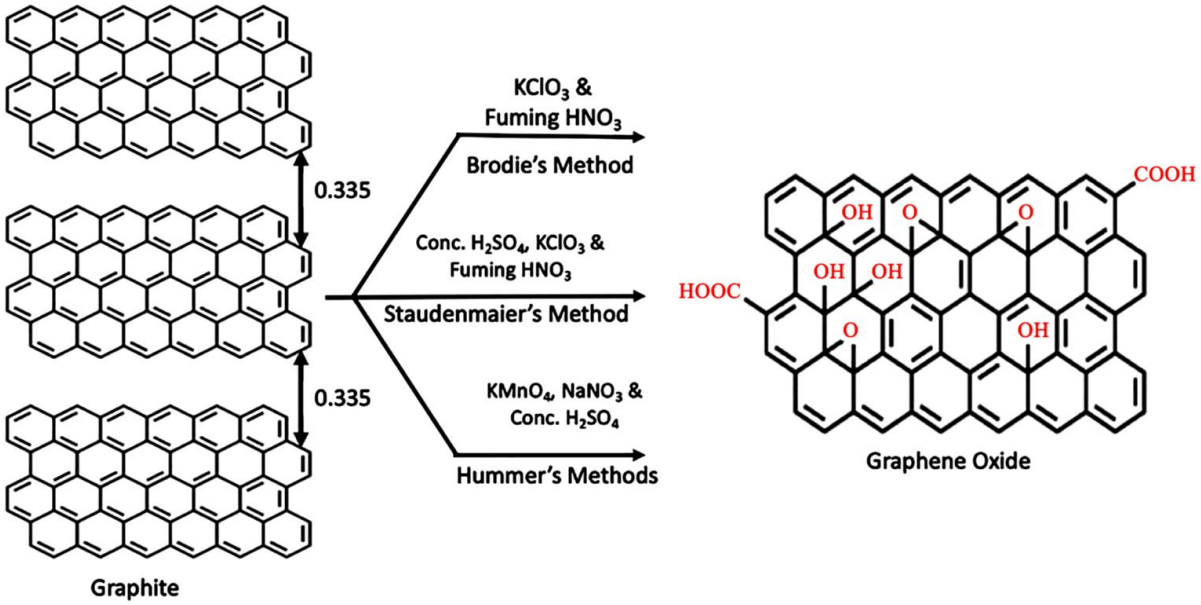

Fig 3. 9 Schematic illustration of graphene oxide synthesis by chemical oxidation using Brodie's, Staudenmaier's, and Hummer's methods [44].

A schematic illustration of the GO synthesis methods discussed above is presented in Fig. 3.9. Hummer's method has proven to be a much safer and quicker way of producing GO in comparison with the other procedures reported. Marcano et al. have reported a modified version of Hummer's method in 2010 by using larger amounts of $KMnO_4$ to increase the level of oxidation [45]. In comparison with the original Hummer's method, this improved version has proved a good way to produce an improved yield of much higher quality GO flakes with high degree of oxidation and thus, it is being widely used today (but with some modifications).

3.4 Optical Properties of Graphene Nanomaterials

3.4.1 Optical Properties of Graphene

Graphene possess many extraordinary and indeed unique characteristics (due to its 2D nature) when it comes to electrical conductivity, thermal conductivity and mechanical strength, that can be exploited in various engineering applications. However, as the work conducted under this thesis is solely based on creating graphene-based optical sensors, the optical properties of graphene are an important focus of this section.

As it consists of just a single layer of carbon atoms, graphene is a super-thin and ultra-light material with a planar density of 0.77 mg/m^2, which is a result of having a hexagonal carbon ring unit structure with an area of 0.052 nm^2 [13]. Graphene also exhibits unique optical transparency characteristics as a result of its single atom thickness. As can be seen from Fig. 3.10, such a thin graphene film absorbs only 2.3% of visible light, leading to a very high transparency of 97.7% [46]. It is also evident from Fig. 3.10 (a) that the light absorption at the interface of substrate-single layer graphene and single layer-bilayer graphene are both 2.3%. The, unique optical transparency characteristic of graphene can be exploited as an indication of the numbers of graphene layers present, an observation which has been validated by the simulations using noninteracting Dirac fermion theory, as depicted in Fig. 3.10 (b) [47].

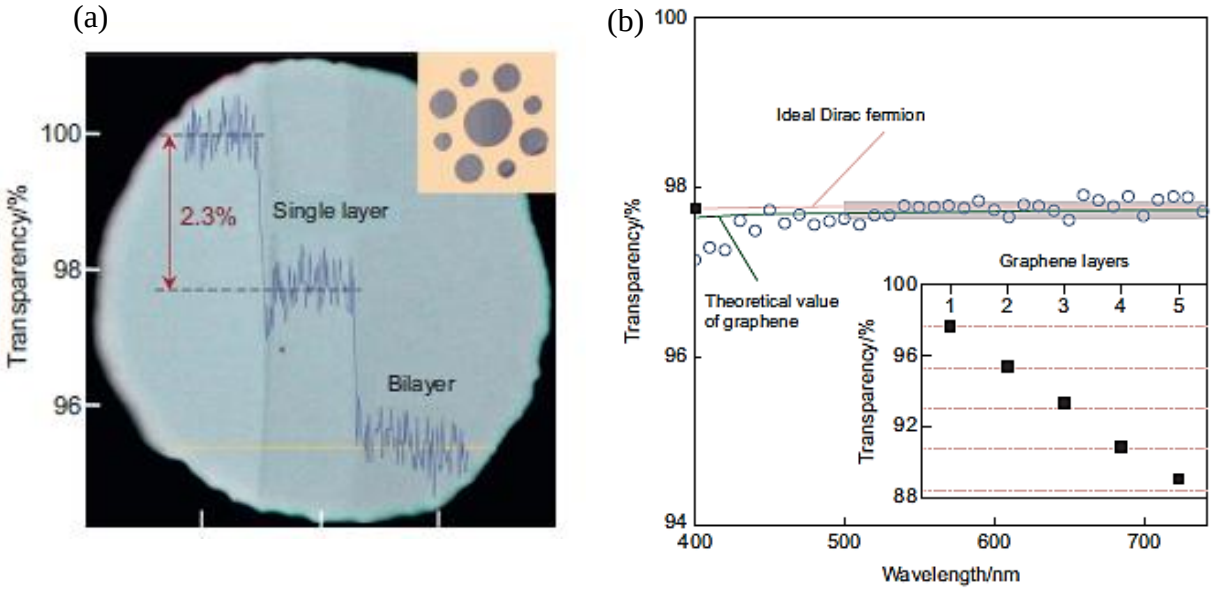

Fig 3. 10 (a) White light absorption of graphene [46] (b) theoretical transparency of graphene [47].

It has also been reported that various graphene layers would exhibit different colours and optical contrasts according to the refraction and interference of light, which is an excellent optical characteristic that could be tuned by altering the thickness of graphene [47]. This unique

optical transparency, combined with the fact that graphene is the most conductive material that has been discovered so far at room temperature, with a conductivity of 10^6 S/m [48], makes graphene a conductive membrane with very rare and unique characteristics that could be used in solar cells, LEDs and many other optoelectronic applications. After reaching a certain critical value of intensity, the light adsorption of graphene would reach a saturation point occurring in the near-infrared region, which is an interesting feature that can be exploited in the development of ultrafast photonic devices such as fibre lasers [13].

Weber et al. have scanned exfoliated graphene flakes with a spectroscopic ellipsometer, and they have used the spectroscopic ellipsometric data with an optical model to determine the refractive index (n) and extinction coefficient (k) of graphene in the wavelength region of 210 nm to 1000 nm and a measured graphene thickness of 3.4 Å (0.34 nm), which can be seen in Fig. 3.11 [49].

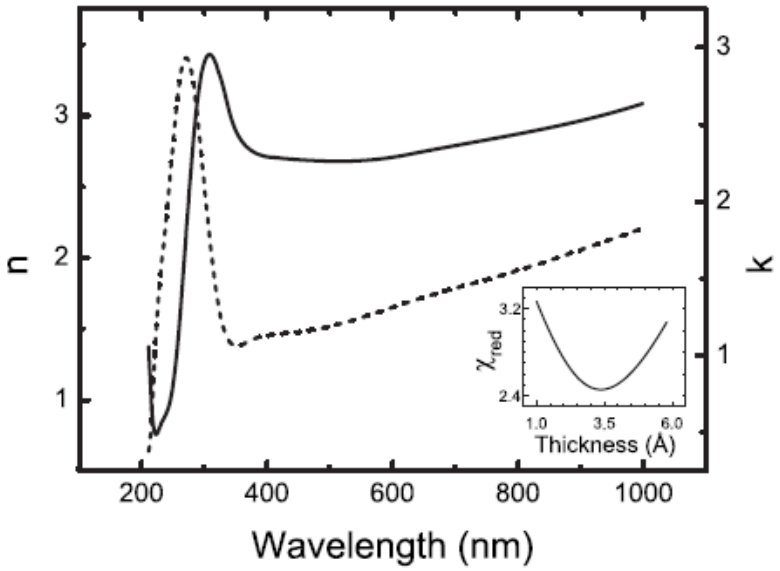

Fig 3. 11 Optical constants of graphene n (solid line) and k (dashed line). Inset: χ_{red} as a function of the thickness fit parameter; a unique minimum is found for 3.4 Å [49].

Cheon et al. have also used two independent methods (SPR angle detection and attenuated total reflection) to calculate the complex RI of graphene at 634 nm, which has found to be 2.65 + 1.27*i* [50].

All carbon allotropes, including graphene, exhibit high thermal conductivities due to C-C covalent bonds that exist and phonon scattering. It has been reported by Sadeghi et al. [51] that graphene exhibits high thermal conductivity without interlayer phonon dispersion and thus, this makes graphene sensitive to external temperature perturbations. The RI of graphene is a

function of the temperature (T), and the relationship can be illustrated by the following equation [52],

$$n_{eff}(T) = n_{eff}(T_0)\left(1 + \sigma_g \Delta T\right) \tag{3.3}$$

where T_0 is the initial temperature, ΔT is temperature change and σ_g is the thermo-optic coefficient of graphene (σ_g=10^{-4}/K). It has also been reported that the structure of graphene is stable at temperatures above 1000 ℃, keeping the thermo-optic properties undisturbed [52]. Highly sensitive temperature sensors based on optical techniques such as interferometry and evanescent wave coupling can be developed by exploiting this thermo-optic relationship [52], but at the same time, graphene's sensitivity to other parameters will be affected by this temperature dependency.

Due to the tightly packed carbon hexagonal ring structure and high charge density, graphene sheets are impermeable to any atom (even the smallest helium atoms) and thus, molecules get adsorbed on the graphene surface [53]. The adsorbed molecules change the local carrier concentration of graphene by one electron at a time [54], which leads to the step-like changes in its resistance, which could be detected due to exceptionally low noise characteristics of graphene. This is a highly attractive feature when it comes to the development of gas sensors. A number of graphene-based gas sensors have been reported by exploiting this feature [55]. These molecule adsorption events also lead to perturbations in the complex RI of graphene, which can be used to develop various types of optical chemical and biochemical sensors.

Surface Plasmon Resonance (SPR) is a widely used optical technique applied to developing highly sensitive optical chemical and biochemical sensors [56]. Recently, Wang et al. have reported excellent transmission characteristics of graphene surface plasmon polaritons in the mid-infrared band, including ultra-compact mode confinement and dynamic tunability, that would help to overcome defects (easy to oxidise under ambient conditions) of noble metals such as gold and silver [57]. The advantages of using graphene in plasmon-based detection of biomolecules in comparison with noble metals have been highlighted in the study conducted by Rodrigo et al. [58]. Due to the superior tunability offered by graphene in comparison with noble metals, sensing frequency range can be tuned in a wide range for a single plasmonic device, which leads to selective sensing [59]. Moreover, due to the very strong energy confinement exhibited by graphene plasmons, sensitivity for detecting a low concentration of molecule is much higher. These advantages are illustrated in Fig. 3.12.

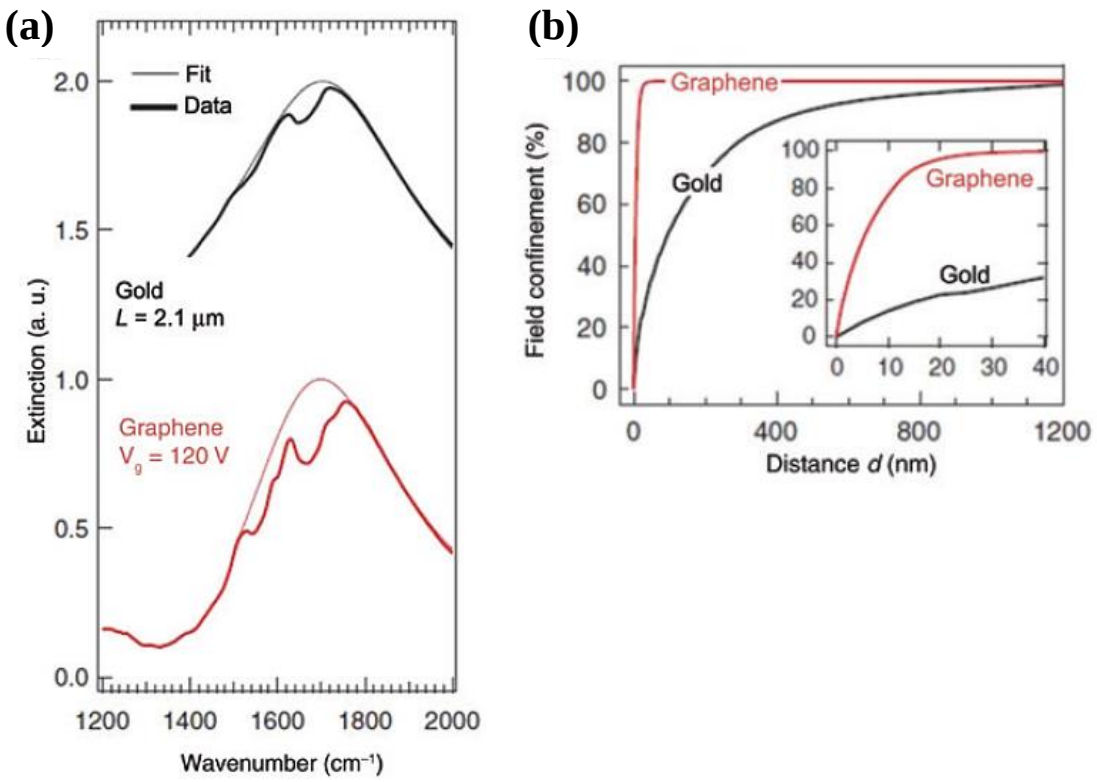

Fig 3. 12 (a) Extinction spectra of graphene and gold biosensors covered with a protein layer. The thick curves are the measured spectra and the thin curves are the fittings for bare graphene and gold biosensors. (b) Field confinement percentage as a function of the distance from the biosensor surface for both graphene and gold. The inset is the enlarged version in the small distance d regime [58].

Fig. 3.12 (a) illustrates the extinction spectra of a protein layer on gold and a graphene nanoribbon antenna. It is evident that the characteristics arising from protein interactions are much more prominent in graphene, in comparison with the graph associated with gold shown. Fig. 3.12 (b) depicts the calculated electrical field spatial distribution curves of gold and graphene nanoribbon antennas, results produced by use of a finite element method (FEM). It is evident that the field confinement in a graphene antenna is much higher than for the gold antenna, which increases its sensitivity at low concentrations of analyte. These highly favourable plasmon characteristics can be used to develop highly sensitive optical SPR based chemical and biochemical sensors.

The photoluminescence (PL) characteristics of graphene have been investigated by the synthesis of graphene quantum dots (GQDs). GQDs are obtained from a graphene sheet cut into 3-20 nm side length and it has been reported to produce a PL effect [60]. PL characteristics of graphene can be tuned, based on the excitation wavelengths and the intensity and the wavelength of the characteristic fluorescence peaks change based on the perturbations in the local environment, which can be used to develop fluorescence-based chemical and biochemical

sensors. Excitation and PL wavelengths of some of the reported GQDs and their emission images under UV light can be seen in Fig. 3.13.

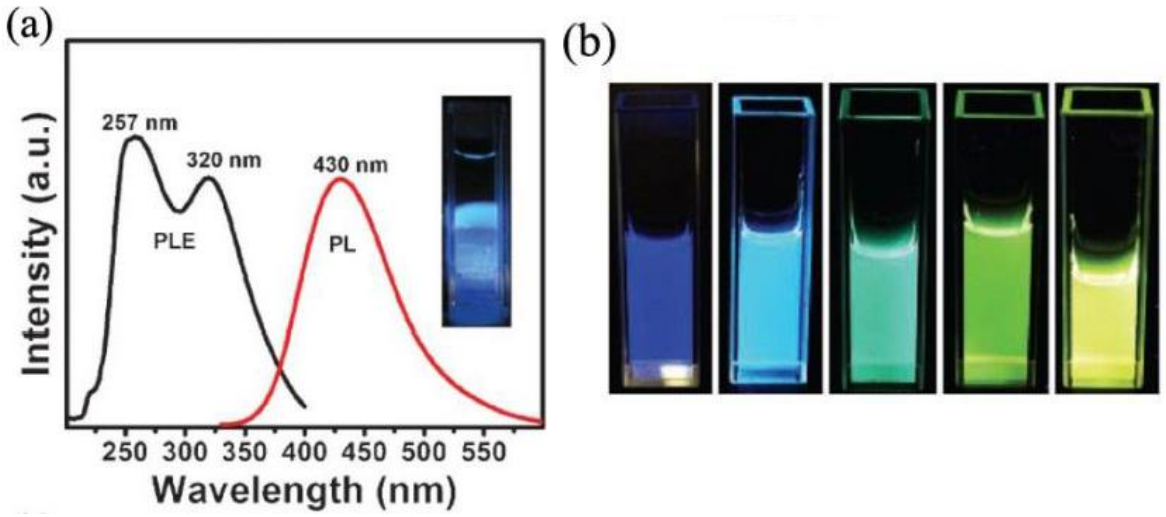

Fig 3. 13 (a) Representative PL Emission, PL spectra, and luminescent photograph of GQDs (b) Emission images of different kinds of GQDs under excitation of a 365 nm UV lamp [61].

3.4.2 Optical and Colloidal Properties of Graphene Oxide

Based on the film thickness, flake size, chemical composition and film morphology, the properties of GO and rGO can be tuned, these being based on the application. GO aqueous dispersions in water are brownish in colour, in contrast with rGO, which appears to be black, indicating differences in the chemical structure [62]. The optical transparency of GO and rGO thin films can be tuned by varying the film thickness or the amount of reduction. Based on the absorption peak seen at wavelengths in the region 225 nm – 275 nm, in UV-Vis-IR spectrum, it is evident that the optical absorption of GO is dominated by the π-π* transitions.

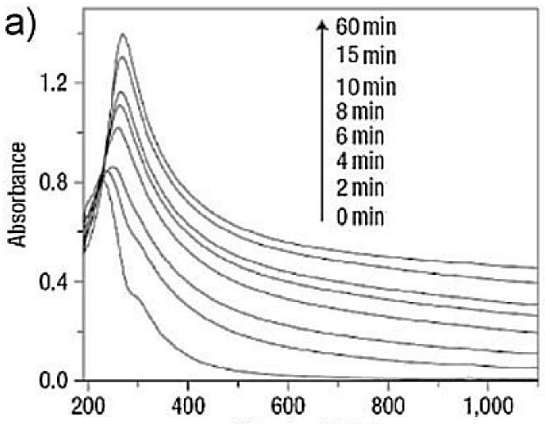

Fig 3. 14 UV–vis absorption spectra of GO in water as a function of elapsed time during chemical reduction by hydrazine [64].

The other noticeable characteristic of GO absorption is a shoulder at around 270 nm, which corresponds to n-π* transitions of C=O bonds [63]. These absorption characteristics of GO are shown in Fig. 3.14 above.

Fig. 3.14 also shows the evolution of the absorption spectra of GO, plotted against an increased reduction time. As can be seen from the figure, no clear absorption peak is observed in the GO spectrum, which suggests that there is no defined bandgap. However, with increased reduction time, the absorption increases to define a much prominent peak, which 'red shifts' to a wavelength ~270 nm. These changes in the plasmonic peak reflect the increased π-electron concentration and the structural ordering [65], which is consistent with the restoration of sp^2 carbon atoms in rGO.

Two distinct types of PL have been reported for GO aqueous dispersions and thin films under illumination by visible and UV light [62]. The first observed PL is a broad PL characteristic around near-RI range (peak intensity observed at around 500-800 nm) and the second is centred in the wavelength region of 390-440 nm, corresponding to a blue emission. It has also been found that PL characteristics of GO are independent of the GO flake size, which suggests that the PL of GO can be attributed to the atomic-scale structure of the material and the size of the GO flake does not define the electron confinement [62]. The PL characteristics of GO under UV light are illustrated in Fig. 3.15 below.

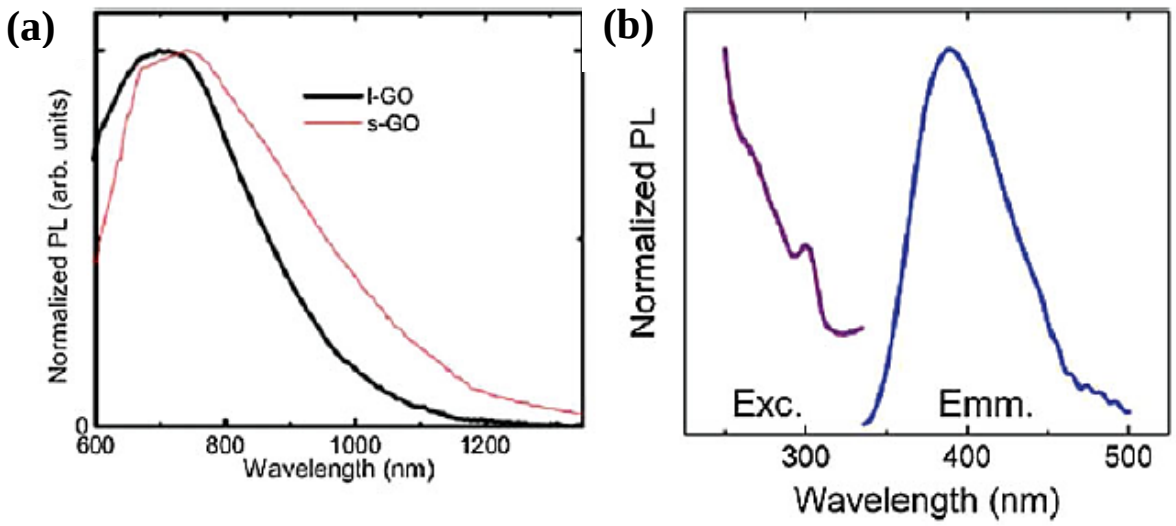

Fig 3. 15 (a) PL spectra of a GO suspension in water (l-GO) and a GO film on a substrate (s-GO), excited at 500 nm [67] (b) PL emission spectrum for excitation at 325nm and excitation spectrum for emission at 388nm for a GO thin film reduced by hydrazine for 3 min [66].

Oxygen containing groups present in GO films lead to sp^3 hybridization of carbon atoms, with the result that GO behaves like a wide-band-gap insulator. sp^2 hybridized pristine graphene

regions on a GO sheet conduct electricity while sp^3 carbon atoms (associated with oxygen functional groups) act like dielectric regions bridging these pristine graphene regions and thus, the conductivity of GO can be tuned based on the amount of reduction achieved. The electrical conductivity of GO has reported to be less than 10^{-10} S cm^{-1} [68].

The wavelength-dependent behaviour of the GO optical constants have been investigated by Kravets et al. [69] in 2015. They have used variable angle spectroscopic ellipsometry on GO flakes assembled on a microfluidic channel to investigate spectrally-dependent refractive indices and extinction coefficients of multilayer GO samples in the wavelength region, 240 nm to 1700 nm.

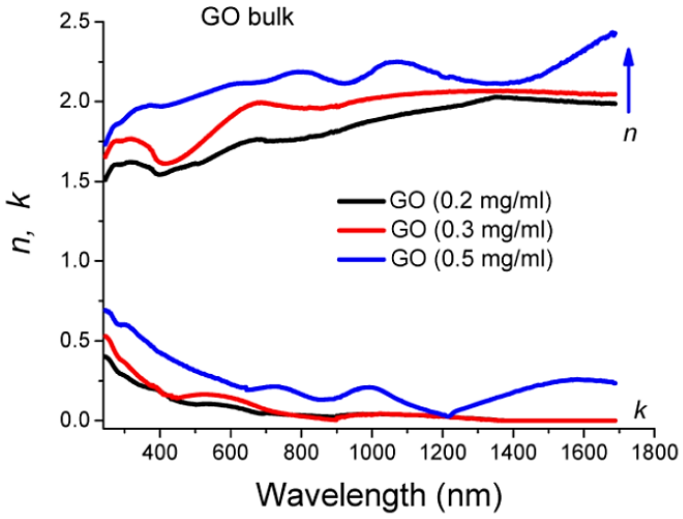

Fig 3. 16 Optical constants of GO flakes as a function of wavelength [69].

Effective RI values (n and k constants referring to real and imaginary parts of the complex RI of GO) for GO thin film thickness of 100 nm are presented in Fig. 3.16. It is evident that both n and k values increase with increasing concentration and thus it is possible to tune the RI of GO by varying the concentration of GO dispersions.

GO is particularly attractive to researchers and scientists due to the oxygen functional groups present on its basal plane (hydroxyl and epoxy groups) and its edges (carboxyl, carbonyl, phenol, lactone and quinone groups) [62]. Due to these oxygen containing groups, GO is hydrophilic, which enables it to be dispersed in many aqueous, organic and inorganic solvents. This enables the production of GO thin films in dispersions, which can be deposited on substrates using techniques such as spin coating, dip coating and drop casting [62]. Paredes et al. have investigated the dispersion behaviour of GO and rGO in different organic solvents and the results are illustrated in Fig. 3.17 [70]. They have prepared 0.5 mg/ml GO dispersions in 13 different organic solvents by bath ultrasonication. The figure shows the stability of these

dispersions one hour after ultrasonication and after keeping them undisturbed for three weeks. As can be seen from the figure, most of the dispersions seem to exhibit short-term stability, except for ethylene glycol, N,N-dimethylformamide (DMF), N-methyl-2-pyrrolidone (NMP) and tetrahydrofuran (THF), which show similar long-term stability as a GO aqueous dispersion of similar concentration. Processing of GO can be manipulated based on these dispersion behaviours for different engineering applications.

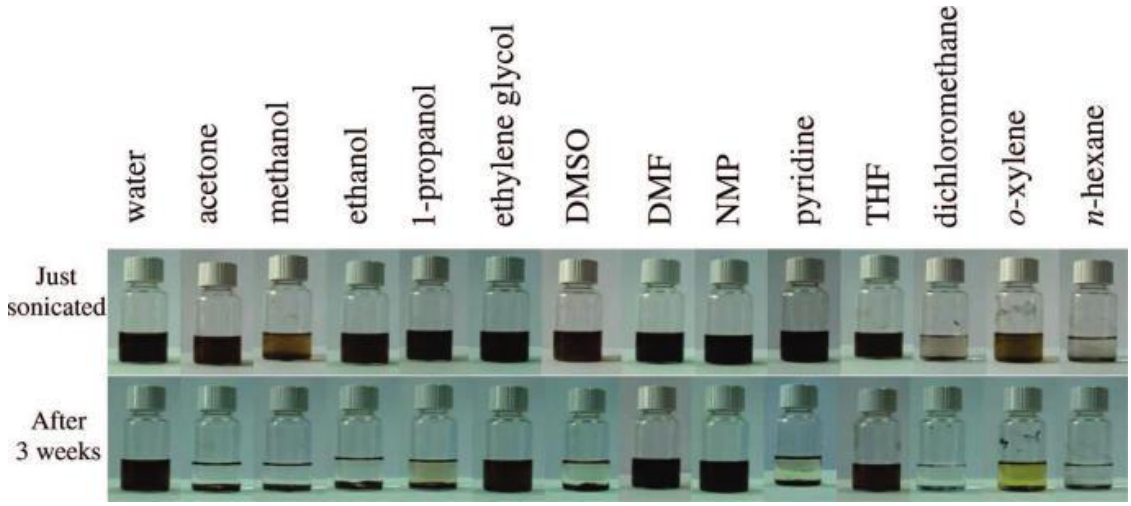

Fig 3. 17 Digital pictures of as-prepared graphite oxide dispersed in water and 13 organic solvents through bath ultrasonication (1 h). Top: dispersions immediately after sonication. Bottom: dispersions 3 weeks after sonication. The yellow colour of the o-xylene sample is due to the solvent itself [70].

The abundance of oxygen-containing groups present in GO gives it very rich surface chemistry, which can be exploited in various applications such as electronics, super capacitors, solar cells, photocatalysts, membranes, lithium batteries, sensors and biomedical applications [71]. However, this unique feature allows GO to undergo various chemical modification as opposed to pristine graphene, that has been highlighted in the review [62]. These modifications include the attachment of other functional groups like amines, formation of polymer composites which are highly desirable in many engineering applications and non-covalent attachment of DNAs and proteins, which makes GO a very attractive material in biosensing applications.

Raman spectroscopy is a widely used non-disruptive characterisation method for carbon materials, which is extremely helpful in obtaining structural information. The main feature of Raman spectrum of a carbon-based materials is the appearance of G and D peaks and their overtones [62]. These D and G peaks are observed at around 1580 and 1350 cm^{-1}, respectively and they appear due to the sp^2 vibrations of the carbon material under investigation.

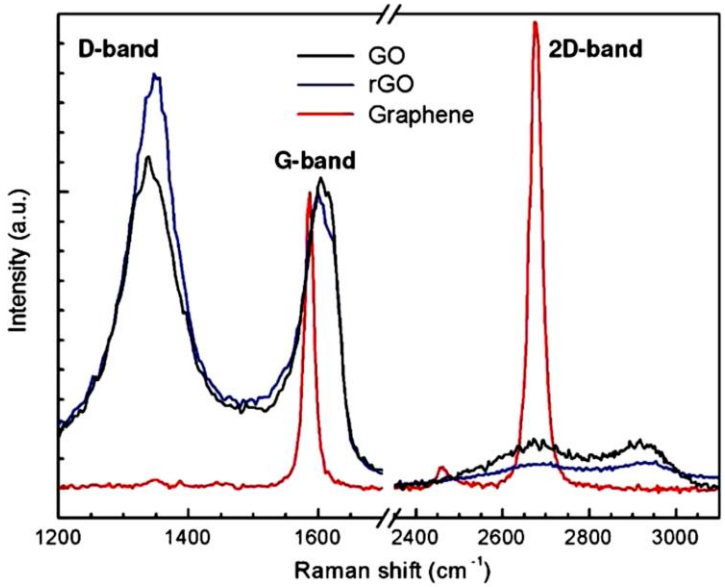

Fig 3. 18 Raman spectra of a monolayer of GO, rGO, and mechanically exfoliated graphene on SiO_2/Si substrates normalized to the G-peak intensity [74].

The G peak can be attributed to the bond stretching of sp^2 carbon pairs in both ring and chain structures while the D peak is associated with breathing mode of aromatic rings that require a defect for its activation [72]. Therefore, the intensity of the D peak can be used as an indication of the number of defects present in the carbon structure. 2D peak (overtone of D peak) is observed at around 2680 cm^{-1} and it is associated with the number of graphene layers [73]. Moreover, the 2D peak is present even when there are no defects in the structure, in contrast with the D peak, which is observed only when defects are present. Fig. 3.18 illustrates the typical Raman spectra of pristine graphene, GO and rGO obtained at an excitation wavelength of 532 nm [74].

These features of the Raman spectra can be observed clearly in the figure above. The D peak related to the defects of the carbon structure can be seen in GO and rGO with a weak and broader 2D peak, which is another indication of the defects present. In contrast, the D peak is absent from the Raman spectrum of the pristine graphene, indicating the absence of defect sites in its structure.

Based on the extraordinary properties and highly attractive features discussed in Section 3.4, which arise from its 2D nature, along with a variety of synthesis methods, graphene nanomaterials are seen to be not only unique but very interesting materials that could be used as a basis for the development of highly sensitive and highly efficient sensors, a number of illustrations of which are discussed next in this chapter.

3.5 Graphene Nanomaterials based Fibre Optic Sensors

As mentioned above, graphene nanomaterials have emerged as promising sensing materials due to the large surface to area ratio (2630 m^2/g) [4], the high signal-to-noise ratio caused by the low intrinsic noise [72], high electron mobility and single molecule detection capability [54]. A variety of graphene nanomaterial-based fibre optic temperature, chemical, gas and biosensors have been reported which exploit some of the unique optical and chemical properties of graphene discussed above [40, 75].

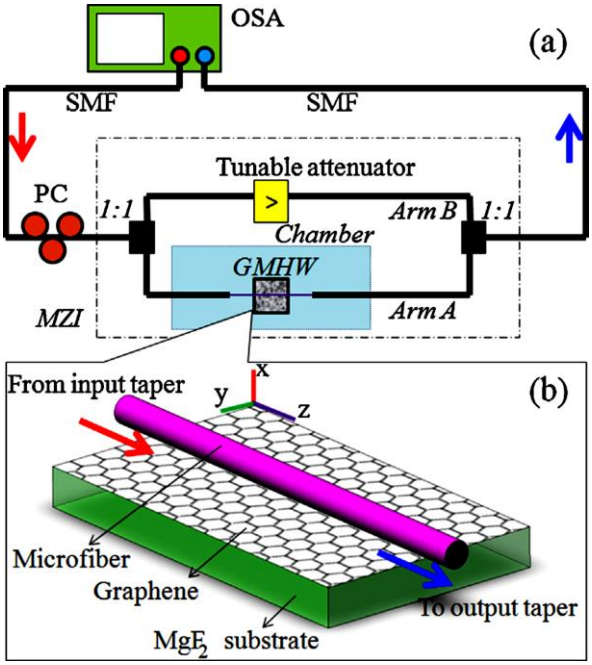

Fig 3. 19 (a) Setup of the GMHW-MZI for NH_3 sensing. (b) Schematic diagram of the GMHW [76].

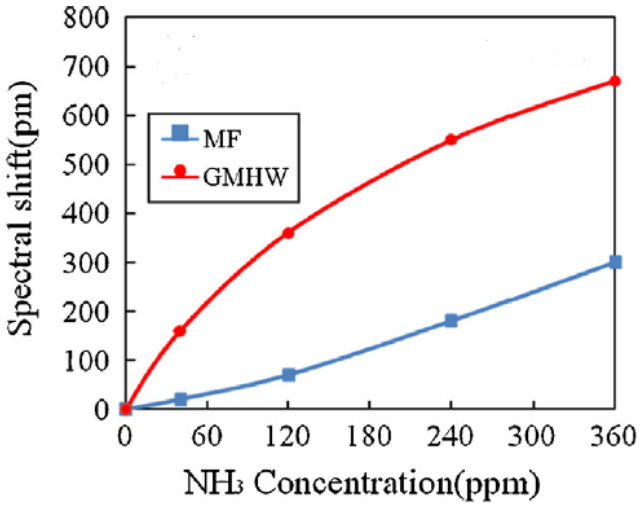

Fig 3. 20 Sensing performances of the GMHW (red) and the microfiber on MgF_2 without graphene attached (blue) [76].

Yao et al. have reported a fibre optic Mach-Zehnder interferometric ammonia (NH_3) sensor based on graphene/microfibre hybrid waveguide (GMHW) [76]. The graphene film has been grown on a Cu foil by CVD method and it has been transferred on to the microfibre/graphene hybrid structure with the help of a PMMA coating. The setup used for NH_3 sensing and the schematic diagram of the graphene/microfibre hybrid waveguide is shown in Fig. 3.19.

A microfibre has been used to launch and collect the light from the graphene waveguide. The sensing mechanism is based on the NH_3 adsorption of graphene film, which changes its conductivity and thus, it's RI, which leads to perturbations in the effective RI of the GMHW. These optical changes can be measured by recording the transmission interference pattern of the Mach-Zehnder Interferometer (MZI). The spectral shift of the GMHW developed is illustrated in Fig. 3.20 and a high sensitivity of ~6 pm/ppm has been achieved by the fabricated graphene-based fibre optic NH_3 sensor.

Tan et al. have reported another graphene-coated MZI based refractometer in [77]. Graphene film has been deposited on to the surface of a PCF using a spray gun. The graphene overlay changes its RI as a function of surrounding RI, resulting in intensity changes of the tranmission interference pattern, which forms the basis of the refractometer developed. External RI sensitivities of 9.4 dB/RIU and 17.5 dB/RIU have been reported for the RI region of 1.33-1.38 and 1.38-1.43, respectively. A schematic diagram illustrating the graphene-coated PCF-based MZI and its intensity response for varying surrounding RI are shown in Fig. 3.21.

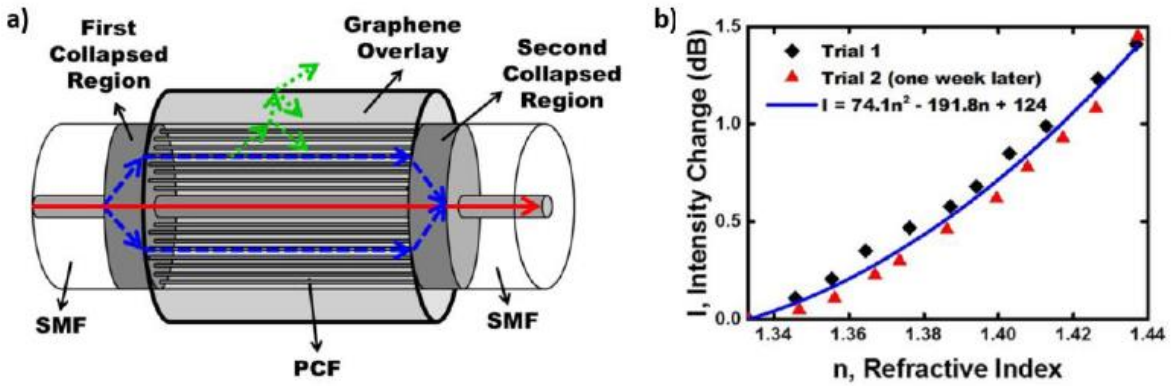

Fig 3. 21 (a) Schematic representation of the refractive index sensing element formed by the deposition of a graphene overlay onto an MZI (b) Change in intensity of the interference vs. RI for two separate trials (diamonds and triangles) conducted one week apart [77].

It was mentioned earlier that unique plasmon properties of graphene allow it to be used as a replacement materials for gold and silver, which forms the basis of conventional fibre optic SPR biosensors. Kim et al. have reported a graphene coated SPR biosensor in the detection of

Biotinylated Double Crossover DNA (DXB) and protein Streptavidin (SA) [78]. A graphene thin film synthesised by the use of a thermal CVD method has been transferred on to a sensing area of the plastic optical fibre (POF) and the schematic diagram explaining the sensing mechanism and the experimental setup used are shown in Fig. 3. 22. The surface plasmon wave (SPW) induced by the deposited graphene layer changes its wavelength and intensity based on the RI of the analyte and this phenomenon underpins the sensing principle of the developed graphene based biosensor. The intensity and wavelength shifts recorded for each analyte concentration is illustrated in Fig. 3.23.

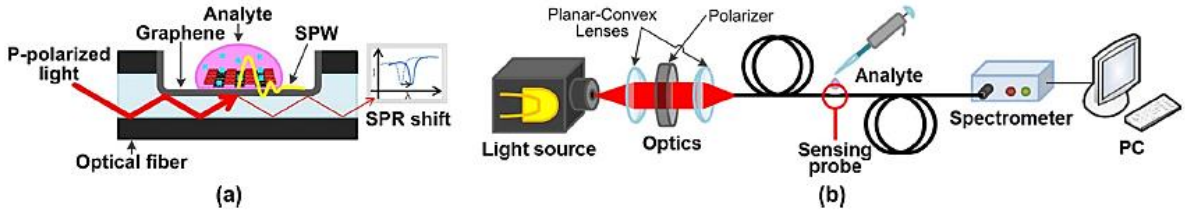

Fig 3. 22 Principle of graphene-based fibre optic SPR biosensor and the experimental setup (a) When the traveling p-polarized incident light heats the graphene–core interface, the surface plasmon wave (SPW) is excited at the graphene–analyte interface. The meaningful signals are obtained due to the interaction between SPW and the propagation constant of analyte (b) There are three main parts; optics part, sensing part, and measurement part. LED light source and sort of optics are involved in the first part. The fabricated sensor with analytes is the second part and lastly, the spectrometer and PC are the measurement part [78].

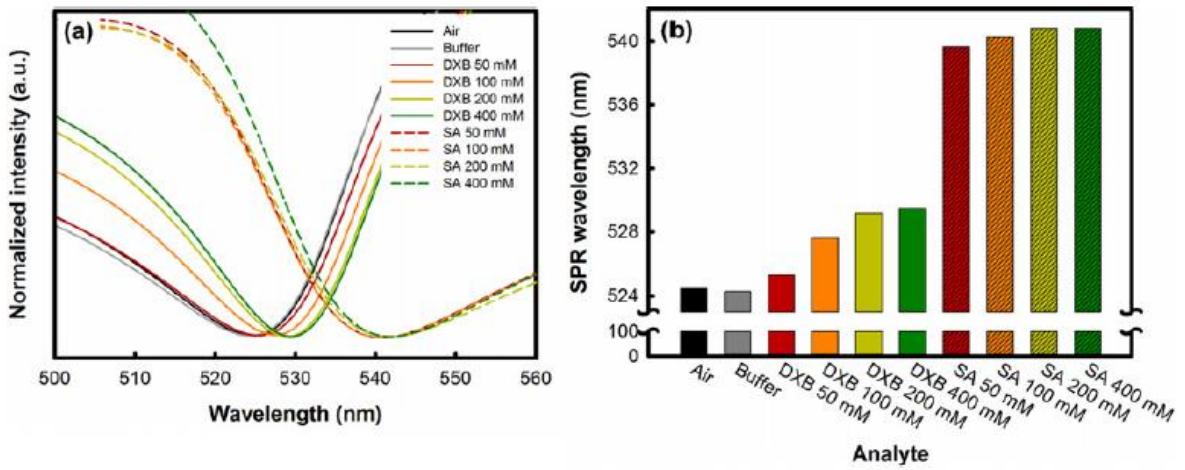

Fig 3. 23 The SPR probe response to without any analyte state (air), buffer, and various concentrations of DXB and SA, viz. 50, 100, 200, and 400 mM. (a) The SPR peak spectra were obtained by data analysis with Lorentzian fitting. Every spectrum was drawn in arbitrary values of normalized intensity but in same scale. There are minute change for the concentrations for DXB and SA respectively, and noticeable difference between the analytes. (b) The bar chart for SPR wavelengths for each analyte. The SPR peaks appeared at around 524 nm for without analyte and buffer cases, 525.3–529.5 nm for DXB samples, and 539.6–540.8 nm for SA samples [78].

Mishra et al. have investigated the performance of a series of graphene nanomaterial coated SPR gas sensors by depositing rGO, CNTs, reduced graphene oxide carbon nanotubes (GCNT) and carbon nanotubes/poly(methyl methacrylate) (GCNT/PMMA) hybrid composite on a

silver-coated unclad core of a fibre [79]. They have tested all four of the graphene nanomaterials based SPR gas sensors against different concentrations of methane, ammonia, hydrogen sulphide, chlorine, carbon dioxide, hydrogen and nitrogen. Among the sensor probes developed, the one with GCNT/PMMA overlay was reported to be highly selective to methane gas. A 30 nm shift in the methane gas concentration range from 10 ppm to 100 ppm has been achieved with a 5 wt.% doping concentration of the GCNT/PMMA hybrid composite coated fibre optic SPR sensor probe.

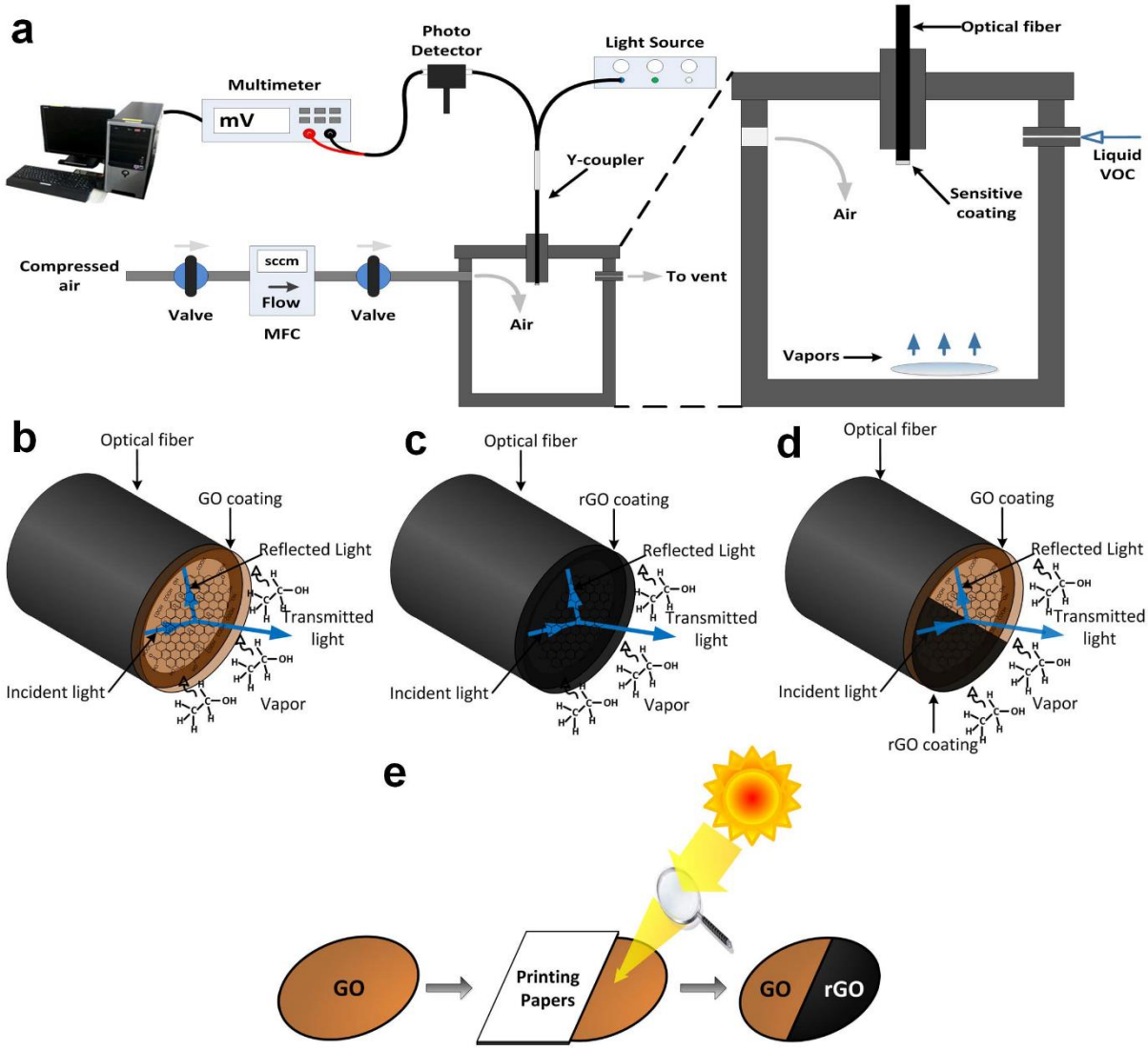

Fig 3. 24 Schematic illustration of the experimental setup used to evaluate the performance of the GO and rGO polymer optical fibre sensors (a) Schematic representation for fabrication of one-headed POF sensor with (b) GO, (c) rGO and (d) GO-rGO (e) Schematic representation for fabrication processes of GO-rGO POF sensor by converting GO into rGO with sunlight [80].

Some et al. have developed an absorption-based GO/rGO coated fibre optic gas sensor to demonstrate the selective high sensitivity of GO under harsh conditions such as high humidity and strong acidic or basic, for volatile organic compounds (VOC) [80]. They have developed

a series of POF based sensors by depositing GO, rGO and GO/rGO coatings on the tip of a POF probe. The experimental setup used, and the fabrication process can be seen in Fig. 3.24.

GO has been converted to rGO by exposing half of the GO thin film to sunlight. The sensor probes developed have been tested against eight different VOCs of very low concentrations (500 ppb). Due to the chemical and physical adsorption of VOC molecules, the RI of the GO and rGO changes, which results in affecting the reflectance of the sensing area that can be detected by recording the sensor output signal via the photodetector. This forms the basis of the GO/rGO coated gas sensor probes developed. They have reported that GO shows a high sensitivity to VOCs due to the oxygen containing groups that is possesses (which contains numerous polar functional groups that can form intermolecular polar interactions with compounds such as nitro and amine), which makes it a better candidate than pristine graphene or rGO when it comes to gas sensing. The response of GO and rGO coated POF sensor probes against different VOCs are shown in Fig. 3.25.

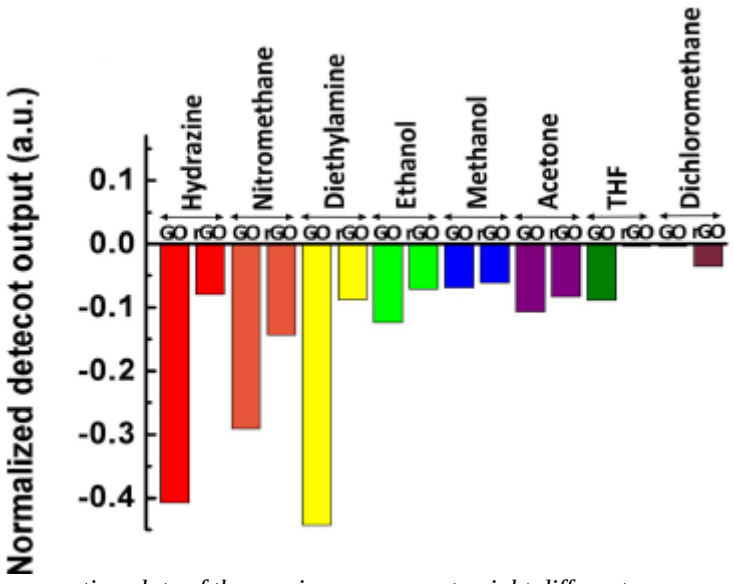

Fig 3. 25 Comparative plots of the sensing responses to eight different vapours at a 500 ppb concentration level [80].

Gao et al have reported an absorption-based GO coated U-bend optical fibre sensor for ethanol detection [81]. GO flakes synthesised by following Hummer's method has been coated on the sensing area of the U-bend probe (fabricated by bending an unclad multimode plastic cladding silica fibre) by use of a dip coating technique. With increasing concentration of ethanol, the RI of the GO thin film increases by effectively capturing ethanol molecules, which leads to changes in the absorbance levels of the input light. This forms the basis of the GO-coated sensor probe developed. It has been reported that the light absorbance with a GO thin layer increased five times compared to a sensor probe without a GO layer in the aqueous ethanol concentration

range of 5% to 100%, which shows the dynamic absorption of ethanol molecules by GO. A schematic diagram showing the experimental setup and the sensing scheme used can be seen in Fig. 3.26.

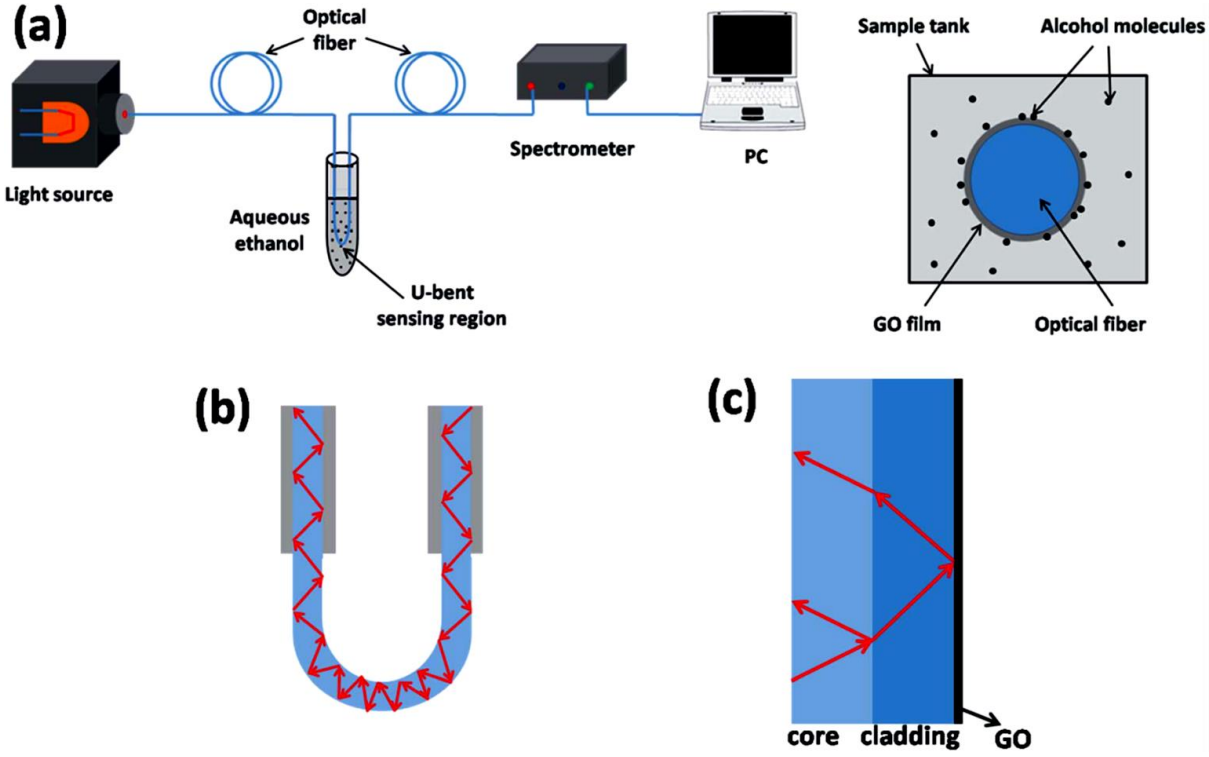

Fig 3. 26 Schematic diagram for (a) the experimental setup and sensing scheme used and (b) the U-bent sensing probe (c) The guiding mechanism of light in the U-bent optical fibre [81].

Another interesting application of GO-coated optical fibres in biomedical detection has been reported by Yao et al. in [82]. A rGO thin film has been deposited on an etched Multi-mode fibre (MMF) to form the fluorescent resonance energy transfer (FRET) on fibre-based detection of Cd^{2+} ions, dopamine and single stranded DNA (ssDNA). Rh6G molecules get adsorbed on the surface of the coated rGO thin film on the fibre. Initially, there is no fluorescence observed due to the fluorescence quenching effect of rGO. However, when analytes are present on the rGO surface, Rh6G molecules get released due to the binding competition and the fluorescence intensity is increased. Furthermore, the effective RI of the rGO thin layer also varies with changing analyte concentration and the phase difference could be measured by exploiting the optical modal interference. This forms the basis of the rGO coated FRET on fibre biomedical sensor developed. LODs of 1.2 nM, 1.3 μM and 1 pM have been reported for Cd^{2+}, dopamine and ssDNA, respectively. A schematic diagram that illustrates the sensing mechanism and the experimental setup is shown in Fig. 3.27.

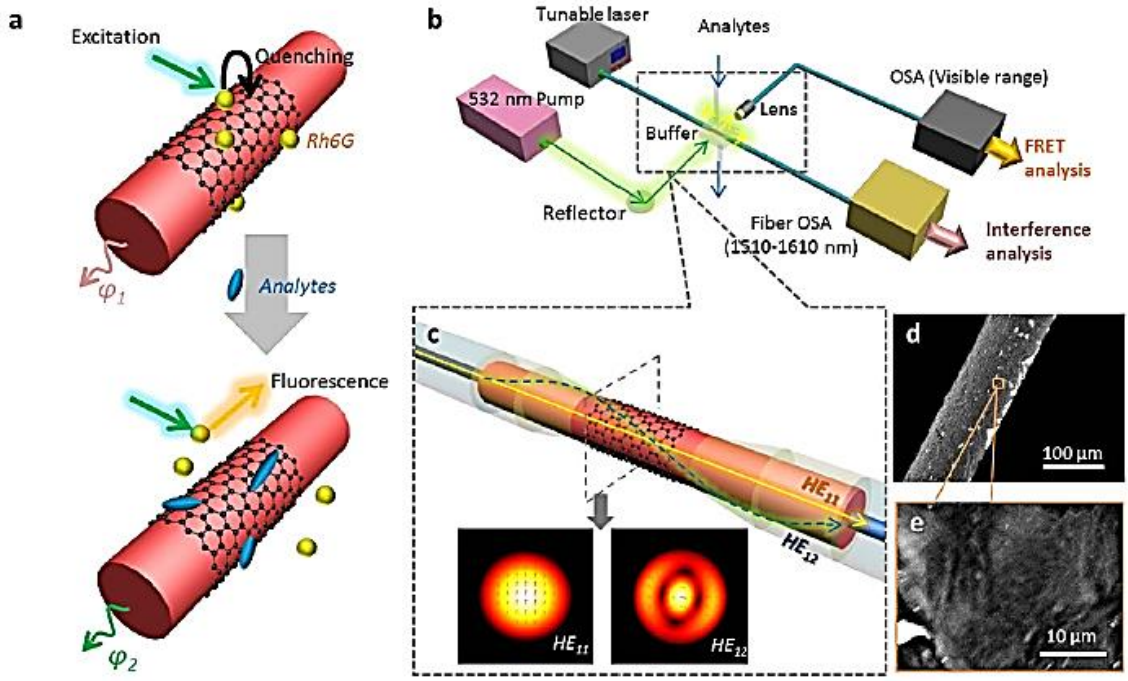

Fig 3. 27 (a) shows the principle of the graphene based 'FRET on fiber' (b) Schematically demonstrates the detection system containing two channels. One is for fluorescence detection, and the other is for all-fibre interference phase measurement (c) Illustrates the probe structure in detail. rGO film (black hexagons) is deposited around the etched MMF section. In the interferometer, interference between HE_{11} and HE_{12} mode occurs, while the HE_{12} mode is enhanced in the rGO-coated area (simulated by FEM method, COMSOL). (d) The SEM image, in which the dark film is the rGO film. (e) The zoom-in of (d) [82].

As established in Chapter 2, grating based sensors are an important part of the family of fibre optic sensors. There is a number of graphene nanomaterials coated in-fibre grating-based sensors which have been reported in the literature in recent years. Wang et al. have developed a humidity sensor based on GO-coated TFBG [83]. The intensity of the transmission spectrum of the GO-coated TFBG changes as a result of water molecule adsorption and desorption process, which is caused by the strong water adsorption characteristics of the GO thin film due to the oxygen containing functional groups present. The RI of the GO overlay changes with varying humidity levels, which is reflected in the transmission spectrum of the GO-coated TFBG, which forms the basis of the sensor probe developed. A drop casting technique has been used to deposit the GO overlay on the surface of the TFBG and a sensitivity of 0.129 dB/RH% has been achieved in the RH range over 10% - 80%. A schematic illustration of the developed sensor probe and its intensity response under varying RH levels are shown in Fig. 3.28.

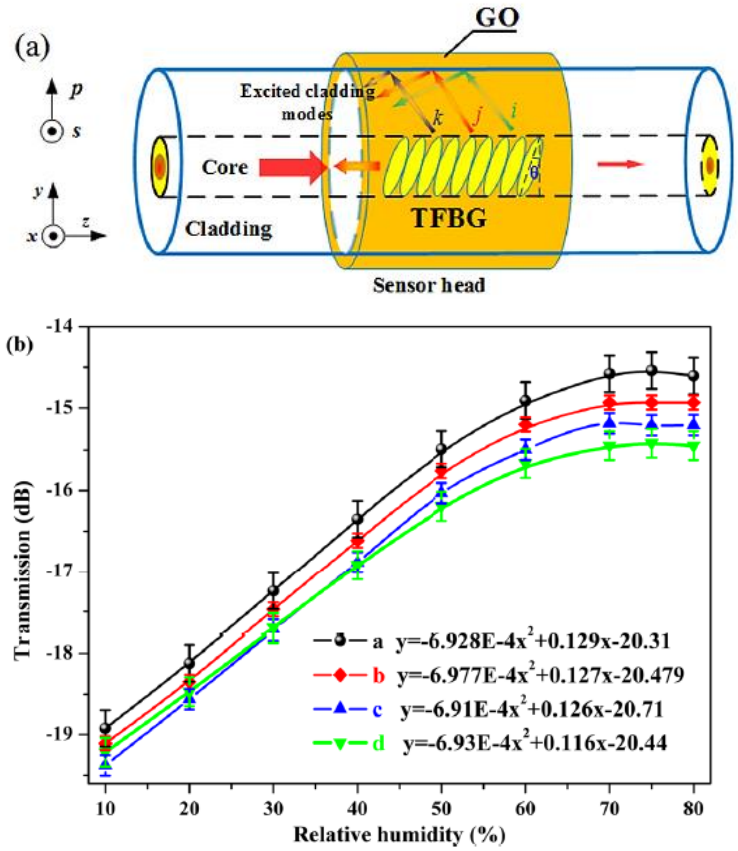

Fig 3. 28 (a) Schematic diagram of GO coated TFBG (b) intensity of four different cladding modes under different RH conditions changing from 10% to 80% [83].

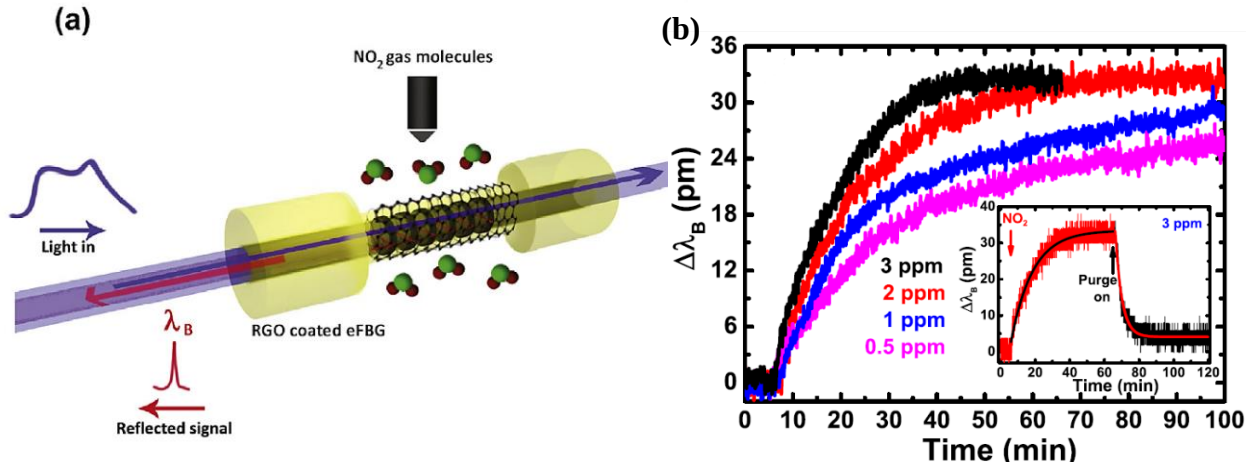

Fig 3. 29 (a) Schematic diagram of the rGO coated eFBG gas sensor (b) Shift in Bragg wavelength as a function of time for different concentrations of NO_2 gas. The inset shows one complete adsorption and desorption cycle for 3 ppm NO_2 gas exposure [84].

Sridevi et al. have reported an ultra-sensitive NO_2 sensor based on a rGO-coated, etched FBG (eFBG) [84]. The rGO thin film deposited on the eFBG surface has been synthesised by the use of the hydrazine reduction method of GO flakes produced by following Hummer's method. A shift in the Bragg wavelength is observed due to the RI change of the rGO thin film by charge transfer during the adsorption process of the NO_2 molecules. This underpins the sensing

principle of the sensor probe developed. A Bragg wavelength shift of 10 pm has been achieved under a NO_2 concentration of 0.5 ppm. A schematic diagram showing the gas sensing mechanism of the rGO coated eFBG and its wavelength response under different NO_2 concentrations are depicted in Fig. 3.29.

Liu et al. have demonstrated a chemical sensor for the measurement of sucrose concentration in water by depositing a GO thin layer on a LPG to develop a GO-coated LPG based external RI sensor [85]. GO has been coated on the LPG using an Electrostatic Self Assembly (ESA) method, which enhances the interaction of light guiding in the LPG and surrounding medium. The RI and the thickness of the deposited GO overlay changes with variations in the surrounding sucrose concentration, which leads to intensity changes of the attenuation loss bands of the GO-coated LPG. This forms the basis of the sensor probe developed. A highest sensitivity of 320.6 dB/RIU in the high index region of 1.42-1.44 has been achieved and the sensitivity of the lower index region of 1.33 - 1.35 has reported to be 99.5 dB/RIU. The transmission spectrum of the GO-coated LPG sensor probe as a function of sucrose concentration is shown in Fig. 3.30.

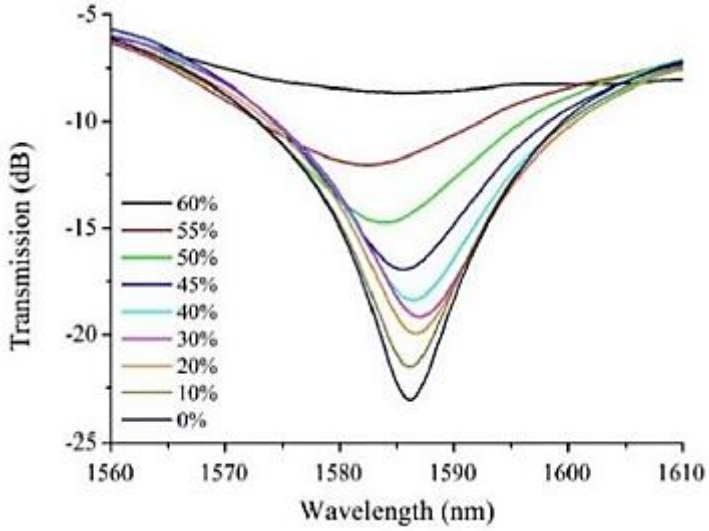

Fig 3. 30 Transmission spectra of the GO coated LGP at different sugar concentration [85].

A summary of the above discussed graphene nanomaterial-based fibre optic sensors is presented in Table 3.1, along with some of the other graphene-based fibre optic sensors reported in the literature.

Table 3. 1 Summary of the properties and characteristics of graphene nanomaterial-based fibre optic sensors

Detection Mechanism	Graphene Nanomaterial	Optical Fibre Configuration	Analyte	Reference
MZI	graphene	Microfibre/graphene waveguide	Ammonia	[76]
MZI	graphene	PCF MZI	RI	[77]
SPR	graphene	Uncladed POF	DXB,SA	[78]
SPR	Ag+, rGO/GCNT/PMMA	Uncladed MMF	Methane	[79]
Absorption	GO/rGO	POF	VOCs	[80]
Absorption	GO	U bent POF	Aqueous alcohol	[81]
Absorption	rGO	Side polished SMF	Temperature	[86]
Fluorescence	rGO	Etched MMF	Cd^{2+}, dopamine, ssDNA	[82]
Bragg power	GO	TFBG	Humidity	[83]
Bragg wavelength	rGO	eFBG	NO_2	[84]
Attenuation band intensity	GO	LPG	RI	[85]
Bragg wavelength	rGO	eFBG	Strain and temperature	[87]

Based on the above discussed graphene nanomaterials-based fibre optic sensor systems, it is evident that graphene-based materials are highly desirable for use in the development of fibre optic sensors due to their particular optical properties. It was also established that GO possesses some highly advantageous characteristics that can be exploited in fabricating fibre optic sensors (in comparison with pristine graphene, for example). Looking at these, first of all, GO consists of a very simple and low-cost method that produces large, high quality yields, compared with complex and less effective (when it comes to the yield) methods used in graphene synthesis. GO also contains oxygen containing groups at its basal plane and its edges, leading the way to highly desirable hydrophilic characteristics that allows it to be dispersed in various organic solvents. This provides for a very effective thin film deposition of GO on fibre surfaces using methods such as spin coating [88], drop casting [87], dip coating [89], electrophoresis [90], ESA [91], LB [92] and Langmuir-Schaefer [93]. This kind of a depositing flexibility is not available with pristine graphene. Moreover, these oxygen containing groups allow GO to interact with other functional groups, which leads to the formation of various composites that can be used in different engineering applications. It was also established that GO exhibits high

sensitivities in gas, humidity and external RI sensing due to these oxygen rich groups that is possess, in comparison with similar rGO or pristine graphene-based sensors. The same is applicable for the development of optical biosensors, where GO is capable of interacting with various molecules and biological agents such as enzymes and protein, which leads to changes in the RI of GO.

Based on these highly desirable and in some cases unique characteristics of GO for the development of thin film-coated fibre optic sensors and tackling the aims and objectives set out in Chapter 1, GO was chosen from among the other graphene nanomaterials as the best candidate to use as a coating and thus to achieve a sensing element, and thus to develop the LPG based external RI, humidity and biosensors which are the objectives of the work in this thesis.

3.6 Summary

A brief introduction to graphene and its derivatives was presented in the beginning of this chapter. Following that, some of the unique and special properties of graphene and GO, present due to their 2D nature, were discussed in some detail. It was shown that graphene nanomaterials have emerged as highly desirable sensing elements to allow the development of novel sensor systems, exploiting these characteristics, such as extremely high surface to volume ratio, low noise characteristics, high charge density and potential under the right circumstances for single molecule detection. A detailed overview of graphene and GO synthesis methods was also presented. This was followed by a comprehensive overview of graphene nanomaterial-based fibre optic sensors, referring to a number of such sensors reported in literature, and thus which has helped to establish some unique and highly desirable properties of GO, in the development of fibre optic sensors (by comparison with the use of pristine graphene as a coating material). Based on the background research conducted and reported in Chapter 2 and Chapter 3, GO-coated on a LPG surface has been identified as a highly desirable sensing mechanism, and thus one that has been chosen to achieving the aims and objectives set out in Chapter 1. The material is one that, considering the experimental facilities available at City, University of London can be effectively exploited to create a series of sensors which could be evaluated and contribute new knowledge to the field. Thus, the next chapter is focused on a detailed consideration of a GO-coated LPG based external RI sensor system and which builds on the above to create an effective sensor system.

3.7 References

[1] Novoselov K S, Geim A K et al., "Electric Field Effect in Atomically Thin Carbon Films," Science, 666-669, 2004.

[2] Novoselov K S, Geim A K, Morozov S V, Jiang D, Katsnelson M I, Grigorieva I V et al., "Two-dimensional gas of massless Dirac fermions in graphene," Nature, 438:197, 2005.

[3] Balandin A A, Ghosh S, Bao W, Calizo I, Teweldebrhan D, Miao F, et al., "Superior thermal conductivity of single-layer graphene," Nano Letters, 8:902, 2008.

[4] Zhu Y W, Murali S, Cai W W, Li X S, Suk J W, Potts J R, et al., "Graphene and graphene oxide: Synthesis, properties, and applications," Advanced Materials, 22, 5226, 2010.

[5] Lee C, Wei X, Kysar J W, Hone J, "Measurement of the elastic properties and intrinsic strength of monolayer graphene," Science, 321:385, 2008.

[6] Choi W, Lahiri I, Seelaboyina R & Kang Y S, "Synthesis of Graphene and Its Applications: A Review," Critical Reviews in Solid State and Materials Sciences, 35:1, 52-71, 2010.

[7] Delhaes P, Graphite and Precursors, CRC Press, 2000.

[8] Hirsch A, "The era of carbon allotropes," Nature Materials, 9 (11), 868870, 2010.

[9] Kroto H W, Health J R, O'Brien S C, Curl R F, Smalley R E, et al., "C60: buckminsterfullerene," Nature, 318 (6042), 162163, 1985.

[10] Iijima S, "Helical microtubules of graphitic carbon," Nature, 354 (6348), 5658, 1991.

[11] Heimann R B, SEvsvukov S E, Koga Y, "Carbon allotropes: a suggested classification scheme based on valence orbital hybridization," Carbon, 35 (1011), 16541658, 1997.

[12] Hoffmann R, Kabanov A A, Golov A A, Proserpio D M, "Homo citans and carbon allotropes," Angewandte Chemie, 55 (37), 1096210976, 2016.

[13] Zhen Z, Zhu H, 1 - Structure and Properties of Graphene, Graphene, Academic Press, 1-12, 2018.

[14] Sood A K, Lund I, Puri Y R, Efstathiadis H, Haldar P, Dhar N K, et al., "Review of graphene technology and its applications for electronic devices." Graphene: New Trends and Developments. London: IntechOpen, 59-89, 2015.

[15] Geim A, Novoselov K, "The rise of graphene," Nature Materials, 6, 183–191, 2007.

[16] Brodie B C, "On the Atomic Weight of Graphite," Philosophical Transactions of the Royal Society of London, 149, 249–259, 1859.

[17] Park S, Ruoff R S, "Chemical methods for the production of graphenes," Nature Nanotechnology, 5:217–24, 2010.

[18] Chen D, Feng H, Li J, "Graphene oxide: preparation, functionalization, and electrochemical applications," Chemical Reviews, 112:6027–53, 2012.

[19] Tang L, Li X, Ji X, Teng K S, Tai G, Ye J, et al., "Bottom-up synthesis of large-scale graphene oxide nanosheets," Journal of Materials Chemistry, 2012.

[20] Liu Y, Chen Y, "Synthesis of large scale graphene oxide using plasma enhanced chemical vapor deposition method and its application in humidity sensing," Journal of Applied Physics, 119:103301, 2016.

[21] Hofmann U and Holst R " Über die Säurenatur und die Methylierung von Graphitoxyd," Berichte der Deutschen Chemischen Gesellschaft A/B, 72: 754-771, 1939.

[22] Ruess G, "Über das Graphitoxyhydroxyd (Graphitoxyd)," Monatshefte für Chemie, 76, 381–417, 1947.

[23] Scholz W and Boehm H P, "Untersuchungen am Graphitoxid. VI. Betrachtungen zur Struktur des Graphitoxids," Zeitschrift für anorganische und allgemeine Chemie, 369, 327–340, 1969.

[24] Nakajima T, Mabuchi A and Hagiwara R, "A new structure model of graphite oxide," Carbon, 26, 357–361, 1988.

[25] Lerf A, He H, Forster M and Klinowski J, "Structure of Graphite Oxide Revisited," Journal of Physical Chemistry B, 102, 4477–4482, 1998.

[26] Dreyer D R, Park S, Bielawski C W and Ruoff R S, "The chemistry of graphene oxide," Chemical Society Reviews, 39, 228-240, 2010.

[27] Berger C, Song Z M, Li T B, Li X B, Ogbazghi A Y, Feng R, Dai Z T, Marchenkov A N, Conrad E H, First P N, et al., "Ultrathin epitaxial graphite: 2d electron gas properties and a route toward graphene-based nanoelectronics," Journal of Physical Chemistry B, 108, 19912–19916, 2004.

[28] De Heer W A, Berger C, Ruan M, Sprinkle M, Li X B, Hu Y K, Zhang B Q, Hankinson J, Conrad E, "Large area and structured epitaxial graphene produced by confinement controlled sublimation of silicon carbide," Proceedings of the National Academy of Sciences of the United States of America, 108, 16900–16905, 2011.

[29] Li X S, Cai W W, An J H, Kim S, Nah J, Yang D X, Piner R, Velamakanni A, Jung I, Tutuc E, et al., "Large-area synthesis of high-quality and uniform graphene films on copper foils," Science, 324, 1312–1314, 2009.

[30] Bae S, Kim H, Lee Y, Xu X F, Park J S, Zheng Y, Balakrishnan J, Lei T, Kim H R, Song Y I, et al., "Roll-to-roll production of 30-inch graphene films for transparent electrodes," Nature Nanotechnology, 5, 574–578, 2010.

[31] Terrones M, "Sharpening the Chemical Scissors to Unzip Carbon Nanotubes: Crystalline Graphene Nanoribbons," ACS Nano, 4, 4, 1775-1781, 2010.

[32] Hernandez Y, Nicolosi V, Lotya M, Blighe F M, Sun Z Y, De S, McGovern I T, Holland B, Byrne M, Gun'ko Y K, et al., "High-yield production of graphene by liquid-phase exfoliation of graphite," Nature Nanotechnology, 3, 563–568, 2008.

[33] Amieva E J, López-Barroso J, Martínez-Hernández A L, "Graphene-Based Materials Functionalization with Natural Polymeric Biomolecules" InTechOpen, 2016.

[34] Hummers W S, Offeman R E, "Preparation of graphitic oxide," Journal of the American Chemical Society, 80, 1339, 1958.

[35] Sturala J, Luxa J, Pumera M, Sofer Z, "Chemistry of Graphene Derivatives: Synthesis, Applications, and Perspectives," Chemistry A European Journal, 24, 5992, 2018.

[36] Kopelevich Y, Esquinazi P, "Graphene physics in graphite," Advanced Materials,19, 4559–4563, 2007.

[37] Yang D, Velamakanni A, Bozoklu G, Park S, Stoller M, Piner R D, Stankovich S, Jung I, Field D A, Ventrice C A, et al., "Chemical analysis of graphene oxide films after heat and chemical treatments by X-ray photoelectron and micro-raman spectroscopy," Carbon, 47, 145–152, 2009.

[38] Pei S F, Cheng H M, "The reduction of graphene oxide," Carbon, 50, 3210–3228, 2012.

[39] Williams G, Seger B, Kamat P V, "TiO2-graphene nanocomposites. UV-assisted photocatalytic reduction of graphene oxide," ACS Nano, 2, 1487–1491, 2008.

[40] Hernaez M, Zamarreño C R, Melendi-Espina S, Bird L R, Mayes A G, Arregui F J, "Optical Fibre Sensors Using Graphene-Based Materials: A Review," Sensors (Basel, Switzerland), 17(1), 155, 2017.

[41] Lakshminarayanan P V, Toghiani H and Jr C U P, "Nitric acid oxidation of vapor grown carbon nanofibers," Carbon, 42, 2433–2442, 2004.

[42] Cotton F A, Wilkinson G, Murillo C A and Bochmann M, Advanced Inorganic Chemistry, Wiley India, Singapore, 2004.

[43] Staudenmaier L, "Verfahren zur Darstellung der Graphitsäure," Ber. Dtsch. Chem. Ges., 31, 1481–1487, 1898.

[44] Adeniji A, Damilola R. "Synthesis and Fabrication of Graphene and Graphene Oxide: A Review," Open Journal of Composite Materials, 09, 207-229. 2019.

[45] Marcano D C, Kosynkin D V, Berlin J M, Sinitskii A, Sun Z, Slesarev A, Alemany L B, Lu W, Tour J M, "Improved synthesis of graphene oxide," ACS Nano, 4, 8, 4806-4814, 2010.

[46] Nair R R, Blake P, Grigorenko A N, et al., "Fine structure constant defines visual transparency of graphene," Science, 320 (5881), 1308, 2008.

[47] Ni Z H, Wang H M, Kasim J, et al., "Graphene thickness determination using reflection and contrast spectroscopy," Nano Letters, 7 (9), 27582763, 2007.

[48] Kim K S, Zhao Y, Jang H, et al., "Large-scale pattern growth of graphene films for stretchable transparent electrodes," Nature, 457 (7230), 706710, 2009.

[49] Weber J W, Calado V E and van de Sanden M C M. "Optical constants of graphene measured by spectroscopic ellipsometry," Applied Physics Letters, 97, 091904, 2010.

[50] Cheon S, Kihm K, Kim H. et al., "How to Reliably Determine the Complex Refractive Index (RI) of Graphene by Using Two Independent Measurement Constraints," Scientific Reports, 4, 6364, 2015.

[51] Sadeghi M M, Pettes M T, Shi L, "Thermal transport in graphene," Solid State Communications, 152 (15), 1321–1330, 2012.

[52] Li L, Feng Z, Qiao X, et al., "Ultrahigh sensitive temperature sensor based on Fabry–Pérot interference assisted by a graphene diaphragm," IEEE Sensors Journal, 15(1), 505–509, 2015.

[53] Leenaerts O, Partoens B, Peeters F M, "Adsorption of H_2O, NH_3, CO, NO_2 and NO on graphene: a first-principles study," Physical Review B, 77 (12), 125416, 2008.

[54] Schedin F, Geim A, Morozov S, et al. "Detection of individual gas molecules adsorbed on graphene," Nature Materials, 6, 652–655, 2007.

[55] Varghese S S, Lonkar S, Singh K K, Swaminathan S, Abdala A, "Recent advances in graphene based gas sensors," Sensors and Actuators B: Chemical, 218, 160-183, 2015.

[56] Singh P, "SPR Biosensors: Historical Perspectives and Current Challenges," Sensors and Actuators B: Chemical, 229, 110-130, 2016.

[57] Wang Y, Liu H, Wang S, Cai M, Ma L, "Optical Transport Properties of Graphene Surface Plasmon Polaritons in Mid-Infrared Band," Crystals, 9, 354, 2019.

[58] Rodrigo D, Limaj O, Janner D, et al. "Mid-infrared plasmonic biosensing with graphene," Science, 349:165–8, 2015.

[59] Huang S, Song C, Zhang G, et al. "Graphene plasmonics: physics and potential applications," Nanophotonics, 6(6), 1191-1204, 2016.

[60] Nemade K R, Waghuley S A, "In situ synthesis of graphene/SnO_2 quantum dots composites for chemiresistive gas sensing," Material Science in Semiconductor Processing, 24, 126–131, 2014.

[61] Wang Z, Zeng H and Su L, "Graphene quantum dots: versatile photoluminescence for energy, biomedical, and environmental application," Journal of Materials Chemistry C, 3, 1157-1165, 2015.

[62] Eda G, and Chhowalla M, "Chemically Derived Graphene Oxide: Towards Large-Area Thin-Film Electronics and Optoelectronics," Advanced Materials, 22: 2392-2415, 2010.

[63] Paredes J I, Villar-Rodil S, Solıs-Fernandez P, Martınez-Alonso A, Tascon J M D, "Atomic Force and Scanning Tunneling Microscopy Imaging of Graphene Nanosheets Derived from Graphite Oxide," Langmuir, 25, 5957-5968, 2009.

[64] Li D, Muller M B, Gilje S, Kaner R B, Wallace G G, "Processable aqueous dispersions of graphene nanosheets," Nature Nanotechnology, 3, 101, 2008.

[65] Robertson J, "Diamond-like amorphous carbon," Mater. Sci. Eng. R, 37, 129, 2002.

[66] Eda G, Lin Y-Y, Mattevi C, Yamaguchi H, Chen H-A, Chen I-S, Chen C-W, Chhowalla M, "Blue photoluminescence from chemically derived graphene oxide.," Advanced Materials, 21, 505-509, 2009.

[67] Luo Z, Vora P M, Mele E J, Johnson A T C, Kikkawa J M, "Photoluminescence and band gap modulation in graphene oxide," Appied Physics Letters, 94, 111909, 2009.

[68] Gao W, Alemany L B, Ci L, Ajayan P M, "New insights into the structure and reduction of graphite oxide," Nature Chemistry,1:403–8, 2009.

[69] Kravets V G, Marshall O P, Nair R R, Thackray B, Zhukov A, Leng J, and Grigorenko A N, "Engineering optical properties of a graphene oxide metamaterial assembled in microfluidic channels," Optics Express, 23, 1265-1275, 2015.

[70] Paredes J I, Villar-Rodil S, Martínez-Alonso A, Tascón J M D "Graphene Oxide Dispersions in Organic Solvents," Langmuir, 24, 19, 10560-10564, 2008.

[71] Dideikin A T, Vul' A Y, "Graphene Oxide and Derivatives: The Place in Graphene Family," Frontiers in Physics, 6, 149, 2019.

[72] Tuinstra F, Koenig J L, "Raman Spectrum of Graphite," J. Chem. Phys., 53, 1126, 1970.

[73] Graf D, Molitor F, Ensslin K, Stampfer C, Jungen A, Hierold C, Wirtz L, "Spatially resolved Raman spectroscopy of single- and few-layer graphene," Nano Letters, 7, 238, 2007.

[74] Jung I, Dikin D A, Piner R D, Ruoff R S, "Tunable Electrical Conductivity of Individual Graphene Oxide Sheets Reduced at "Low" Temperatures," Nano Letters, 8, 4283, 2008.

[75] Zhao Y, Li X, Zhou X, Zhang Y, "Review on the graphene based optical fiber chemical and biological sensors," Sensors and Actuators B: Chemical, 231, 324-340, 2016.

[76] Yao B, Wu Y, Cheng Y, Zhang A, Gong Y, Rao Y-J, Wang Z, Chen Y, "All-optical Mach–Zehnder interferometric NH_3 gas sensor based on graphene/microfiber hybrid waveguide," Sensors and Actuators B: Chemical, 142-148, 2014.

[77] Tan Y C, Tou Z Q, Chow K K, and Chan C C, "Graphene-deposited photonic crystal fibers for continuous refractive index sensing applications," Optics Express, 23, 31286-31294, 2015.

[78] Kim J A, Hwang T, Dugasani A R, Amina R, Kulkarni A, Park S H, Kim T, "Graphene based fiber optic surface plasmon resonance for bio-chemical sensor applications," Sensors and Actuators B: Chemical, 187, 426-433, 2013.

[79] Mishra S K, Tripathi S N, Choudhary V et al., "Surface Plasmon Resonance-Based Fiber Optic Methane Gas Sensor Utilizing Graphene-Carbon Nanotubes-Poly(Methyl Methacrylate) Hybrid Nanocomposite," Plasmonics, 10: 1147, 2015.

[80] Some S, Xu Y, Kim Y et al., "Highly Sensitive and Selective Gas Sensor Using Hydrophilic and Hydrophobic Graphenes," Scientific Reports 3, 1868, 2013.

[81] Gao S S, Qiu H W, Zhang C, Jiang S Z, Z, Liu X Y, Yue W W, Yang C, Huo Y Y, Feng D J and Li H S, "Absorbance response of a graphene oxide coated U-bent optical fiber sensor for aqueous ethanol detection," RSC Advances, 6, 15808, 2016.

[82] Yao B, Wu Y, Yu C et al. "Partially reduced graphene oxide based FRET on fiber-optic interferometer for biochemical detection," Scientific Reports, 6, 23706, 2016.

[83] Wang Y, Shen C, Lou W, Shentu F, Zhong C, Dong X, and Tong L, "Fiber optic relative humidity sensor based on the tilted fiber Bragg grating coated with graphene oxide," Applied Physics Letters, 109, 031107, 2016.

[84] Sridevi S, Vasu K S, Bhat N, Asokan S, Sood A K, "Ultra sensitive NO_2 gas detection using the reduced graphene oxide coated etched fiber Bragg gratings," Sensors and Actuators B: Chemical, 223, 481-486, 2016.

[85] Liu C, Cai Q, Xu B, Zhu W, Zhang L, Zhao J et al., "Fibre optic chemical sensor based on graphene oxide-coated long period grating," Proceedings SPIE 9916, Sixth European Workshop on Optical Fibre Sensors, May. 2016.

[86] Zhang J, Liao G Z, Jin S S, Cao D, Wei Q S, Lu H H, Yu J H, Cai X, Tan S Z, Xiao Y, et al. "All-fiber-optic temperature sensor based on reduced graphene oxide," Laser Physics Letters, 11, 035901, 2014.

[87] Sridevi S, Vasu K S, Bhat N, Asokan S, Sood A K, "Enhanced strain and temperature sensing by reduced graphene oxide coated etched fiber bragg gratings," Optics Letters, 41, 2604–2607, 2016.

[88] Pang S, Tsao H N, Feng X, Mu¨llen K, "Patterned Graphene Electrodes from Solution-Processed Graphite Oxide Films for Organic Field-Effect Transistors," Advanced Materials, 21, 3488-3491, 2009.

[89] Schniepp H C, Li J L, McAllister M J, Sai H, Herrera-Alonso M, Adamson D H, Prud'homme R K, Car R, Saville D A, Aksay I A, "Functionalized single graphene sheets derived from splitting graphite oxide," Journal of Physical Chemistry B, 110, 8535, 2006.

[90] Chen Y, Zhang X, Yu P, Ma Y, "Stable dispersions of graphene and highly conducting graphene films: a new approach to creating colloids of graphene monolayers," Chemical Communications, 4527-4529, 2009.

[91] Liu C, Cai Q, Xu B, Zhu W, Zhang L, Zhao J, Chen X, "Graphene oxide functionalized long period grating for ultrasensitive label-free immunosensing," Biosensors and Bioelectronics, 94, 200-206, 2017.

[92] Cote L J, Kim F, Huang J, "Langmuir−Blodgett Assembly of Graphite Oxide Single Layers," Journal of the American Chemical Society, 131, 1043, 2009.

[93] Gengler R Y N, Veligura A, Enotiadis A, Diamanti E K, Gournis D, Jo´zsa C, Wees B J V, Rudolf P, "Large-Yield Preparation of High-Electronic-Quality Graphene by a Langmuir–Schaefer Approach," Small, 6, 35, 2009.

Chapter 4

Development and Characterisation of a GO coated LPG based External RI Sensor System

4.1 Introduction

Selective chemical detection and measuring the concentration of the associated species is a strongly researched area in the field of sensor development, arising from the many challenges faced when trying to meet specific sensor requirements of industry today. A scenario common to the detection of many chemicals is that their RI changes with changing concentration and this phenomenon offers an opportunity to use external RI sensors as the basis of many chemical and biochemical sensors. In this regard, as discussed in Chapter 1, fibre optic external RI sensors offer some specific advantages over their electronic counterparts and they have been deployed in many different fields such as air quality control [1], haemoglobin testing [2], corrosion detection [3] etc. As established in Chapters 2, LPGs are inherently sensitive to variations in the RI of the medium surrounding the cladding and as such, can be used as the basis of many fibre optic external RI sensor designs.

When it comes to external RI sensing, LPG-based sensors show advantages over other fibre optic sensors due to their simplicity, low fabrication cost and especially due to their enhanced light-matter interaction at the cladding-surrounding medium interface, which can lead to an enhanced RI sensitivity (over that seen for FBG-based devices), for example. Therefore, LPGs were chosen as the basis of the sensor systems developed in this research, preferred over other grating based fibre sensing mechanisms.

This chapter concentrates on a GO-coated LPG based external RI sensor system, exemplified in the form of a NaCl salinity concentration measurement sensor that would potentially serve as a starting platform for many other chemical and biochemical sensors. Based on the theoretical approach of a thin film-coated LPG discussed in Chapter 2, a thin film coating of GO on such a fibre grating is used as the basis of the sensor probes developed and whose performance is analysed in this chapter. A coated GO thin film layer offers two main

advantages over other sensing materials due to the interesting surface chemistry it possess. Firstly, it has the potential to increase the external RI sensitivity of an LPG many-fold [4] and secondly, it enables functionalising of the GO layer to make the sensor selective to the analyte under investigation [5].

Several external RI sensors, based on GO-coated optical fibres and LPGs have been reported in recent years, for example, applied to humidity measurements [6], chemical sensing [7], and detection of haemoglobin [8], IgG [5] and proteins [9], devices that operate through knowing how the external RI sensitivity is affected by the measurand. Thin film coating thickness is one of the most important parameters when it comes to grating-based thin film coated optical fibre sensors, especially if the coating material is a special nanomaterial such as GO. Thus, in this chapter, the thickness-dependent performance of GO-coated, LPG-based external RI sensors has been analysed and their performance optimised through fabricating and assessing four different, representative GO-coated LPG-based sensors for measuring NaCl salinity concentration in water, each with a different GO overlay thickness. Variations in the transmission spectra of the highest order cladding modes of the GO-coated LPGs, monitored in the presence of the different concentrations of NaCl solutions prepared were analysed and the results are discussed in this chapter, as a means to better understand better the effects of increasing GO overlay thickness on the performance and potential of optical fibre sensors of this type.

4.2 Sensing Principle

As discussed in Chapter 2 in some detail, the underpinning principles of the sensors developed and analysed in this chapter are centred around recording and analysing the light propagating in the fibre cladding, as lossy cladding modes, that are affected by the deposited thin film overlay of GO. The RI modulation in the core of the LPG used allows the light propagating in the fibre core as the fundamental core mode to be coupled to the modes in the cladding, on discrete wavelength bands, centred at a wavelength designated here as λ_{res}. This coupling is evident in the LPG transmission spectrum, in creating 'spectral dips' designating a reduction in the minimum intensity of the signal. A typical transmission spectrum of a fabricated LPG is shown in Fig. 4.13 (later in this chapter). As indicated in Chapter 2, when the phase matching conditions are satisfied, the wavelength λ_{res} of a resonance loss band can be written as:

$$\left(n_{core}^{eff}(\lambda_{res}) - n_{clad.m}^{eff}(\lambda_{res})\right)\Lambda_{LPG} - \lambda_{res} = 0 \qquad (4.1)$$

where n_{core}^{eff} and $n_{clad.m}^{eff}$ are the effective refractive indices of the fundamental core mode and the m^{th} order cladding mode, respectively. Λ_{LPG} is the grating period of the LPG used and written into the optical fibre. When a thin film coating, such as GO, is applied to the fibre surface, it can be considered as a double clad waveguide and this approach can be used to analyse its performance. Under these conditions, in a single mode fibre, the light propagating in the core remains insensitive to the RI of the coating, but the effective RI influencing the cladding modes arises from a combination of the cladding RI and the RI of the coated thin layer – in this case, that of the applied GO film.

The influence of the external RI of the material that surrounds the cladding can be expressed as:

$$\frac{d\lambda}{dn_{GO}} = \frac{d\lambda}{dn_{clad,m}^{eff}} \cdot \frac{dn_{clad,m}^{eff}}{dn_{GO}} \tag{4.2}$$

where λ is the wavelength of the attenuation band and n_{GO} is the RI of the surrounding GO overlay. Therefore, based on this relationship, variations in n_{GO} can be detected by monitoring the changes in the transmission spectrum of the resonance loss band of a cladding order mode. This effect enables GO-coated LPGs to be designed and this phenomenon underpins their use as external RI sensors.

When $n_{clad,m}^{eff}$ is smaller than that of the cladding, the phase matching conditions of that particular cladding mode will be satisfied while the effective RI of the core remains the same, thus resulting in a blue shift of the centre wavelength of the resonance band. However, when $n_{clad,m}^{eff}$ is higher than that of the cladding, the cladding-surrounding medium interface will lose its total internal reflection condition, and thus guided modes in the cladding will act as radiation modes or leaky cladding modes. This will result in a reduction of the minimum intensity in the resonance loss band, as well as a red shift of the centre wavelength.

Another important parameter that affects the effective RI of the cladding modes is the thickness of the coated thin film layer, especially noting that the RI of the coated material is higher than that of the glass cladding, as is the case with GO. The thickness of the coated GO layer determines portion of optical power of the cladding modes that is propagated through the coated thin film layer. When the coating is thick enough, the overlay is able to guide one or more of the cladding modes and thus, it starts to act as a waveguide.

The transmission factor of resonance loss bands in a LPG is governed by the following equation,

$$T_i = 1 - sin^2 (K_i L) \quad (4.3)$$

where T_i is the minimum transmission of the i^{th} cladding mode and K_i is the coupling coefficient, which is obtained by an overlap integral of the fibre core fundamental and the i^{th} order cladding mode and by the amplitude of the periodic modulation of the mode propagation constants, as discussed in detail in Chapter 2. The length of the LPG in the probe is represented by L. Changes in the surrounding environment, including the binding of molecules to the GO thin layer, result in variations of the RI of the GO overlay, which eventually affects the evanescent field (the mode field diameters and the mode propagation constants of the cladding modes), and thus the coupling coefficients, which then leads to noticeable (and measurable) changes in the LPG loss bands. This effect underpins the working principle of the GO-coated LPG sensor schemes presented in this work.

4.3 GO Synthesis Process

Among the GO synthesis methods discussed in detail in Chapter 3, Hummer's method is the most commonly GO synthesis method used, due to its simplicity in execution, the shorter time taken to realize a satisfactory yield of GO and low cost overall. Modified versions of the Hummer's method (such as those presented in [10], [11]) are adopted from the original Hummer's method that is presented in [12]. The method is mainly based on oxidation of graphite by introducing oxygen molecules to single layer graphene sheets of the graphite lattice. The reaction occurs between single layer graphene sheets of the graphite lattice and concentrated sulphuric acid, with potassium permanganate acting as a strong oxidation agent and sodium nitrate as a catalyst. Based on the GO synthesis method described in [10], a modified version of the Hummer's method was used to synthesis the GO flakes used in this research. The synthesis process is discussed in detail in the following section.

4.3.1 Materials

The chemicals used in the synthesis process of GO are, graphite flakes (Alfa Aesar), sodium nitrate (98%, Alfa Aesar), potassium permanganate (99%, Sigma Aldrich), hydrogen peroxide (30% wt, Fisher Scientific), sulphuric acid (98%, Sigma Aldrich) and hydrochloric acid (35%, Sigma Aldrich). All the chemicals used were of analytical grade and thus, no further purification was needed.

4.3.2 GO Synthesis – Modified Hummer's Method

As the first step of the used modified version of the Hummer's method, 500 mg of Graphite flakes and 500 mg of $NaNO_3$ were continuously stirred for four hours in 22.5 mL of 99% H_2SO_4 in an ice bath (0-4 ºC). Afterwards, 3 g of $KMnO_4$ was added to the suspension very slowly to keep the reaction temperature below 15 ºC. Then, the mixer was diluted with the addition of 46 mL of DI water and it was stirred for another hour under the same temperature conditions. The ice bath was then removed, and the mixture was stirred for another 2 hours at 35 ºC. Following that, the obtained mixer was kept in a reflux system at 98 ºC for another 15 minutes, which resulted in producing a brown coloured solution after another 10 minutes at 30 ºC. The ice bath and the reflux system used in the above steps, along with the resultant brown coloured solution are shown in Fig. 4.1.

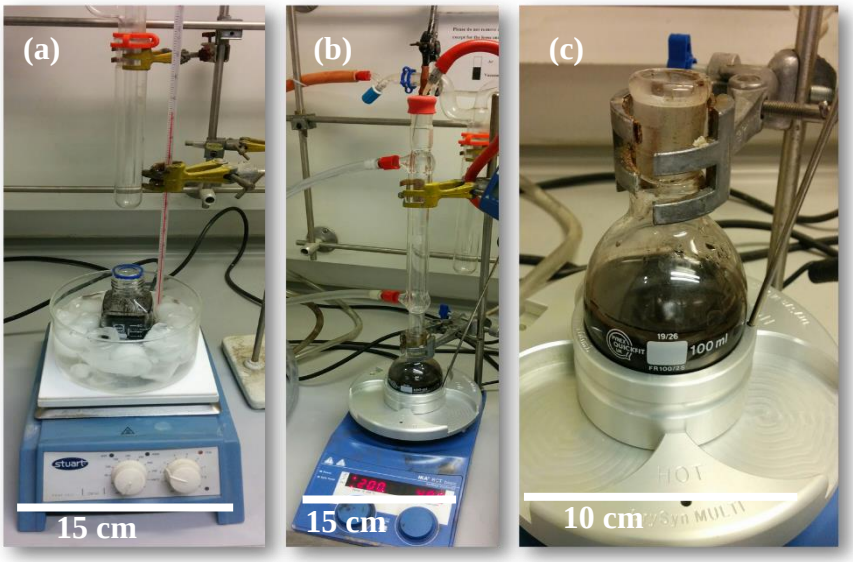

Fig 4. 1 (a) Ice bath used (b) Reflux system used (c) Resultant brown coloured mixture.

Afterwards, the mixture was stirred for another two hours at room temperature. As the next step, 13.3 mL of H_2O_2 was added very slowly (as it reacts very rapidly) and the colour of the mixture turned to bright yellow. At this point, 100 mL of DI water was added to the mixture before keeping it under stirring for another one hour at room temperature. The resultant solution was kept without disturbing for 24 hours until the particles settled at the bottom of the beaker. Following that, using a filter paper, the water was filtered out. The bright yellow coloured solution obtained after the addition of H_2O_2, settled particles after an undisturbed time period of 24 hours and the filtering process can be seen in Fig. 4.2.

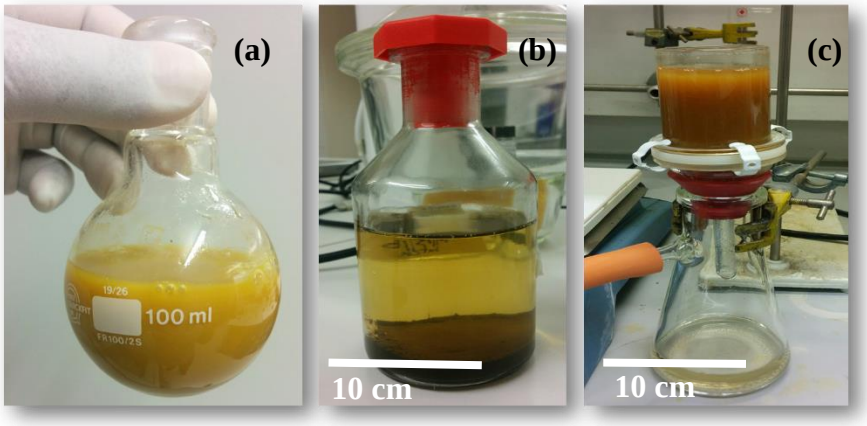

Fig 4. 2 (a) Bright yellow coloured solution obtained (b) Settled particles after a 24-hour undisturbed time period (c) Filtering process used.

Afterwards, the resulting mixture was washed thoroughly by sonication and centrifugation with 10% HCl and then with DI water several times, until a gel like substance was formed. This substance was vacuum dried for 8 hours to obtain the GO flakes used in this research. From the 500 mg of Graphite flakes initially used, a GO yield of 354 mg was obtained. Some images of the systhesised GO flakes, including a scanning electron microscope (SEM) image (by use of a Tescan Vega LMU microscope) is shown in Fig. 4.3.

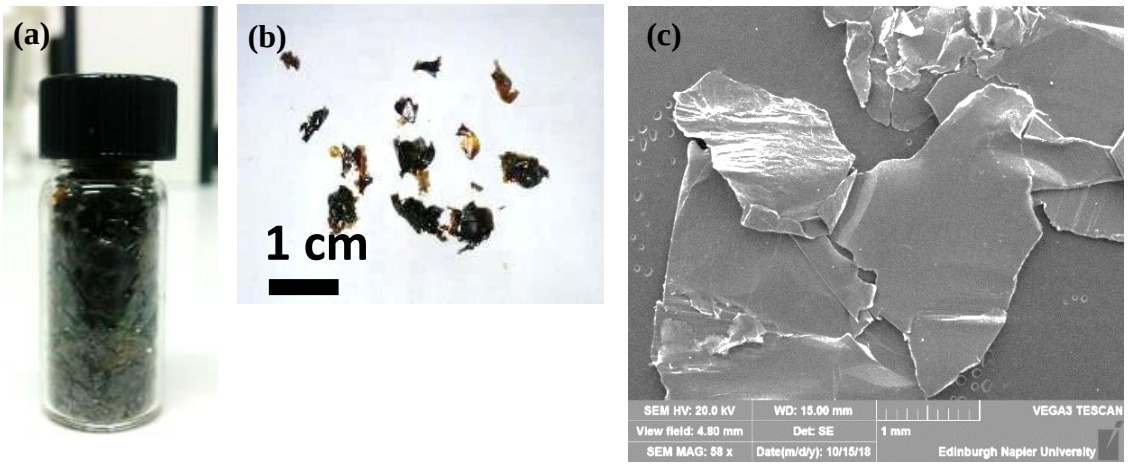

Fig 4. 3 (a),(b) GO flakes synthesised (c) SEM image of the GO flakes synthesised.

For the purposes of material characterisation and thin film coating on optical fibre surface, an aqueous dispersion of these prepared GO flakes is needed. To prepare such an aqueous dispersion, 0.5 mg of the prepared GO flakes were dispersed in 10 mL of deionized water, by performing an ultrasonication process for 2 hours. Ultrasonication also helps to mechanically separate GO sheets from one another by applying an external force.

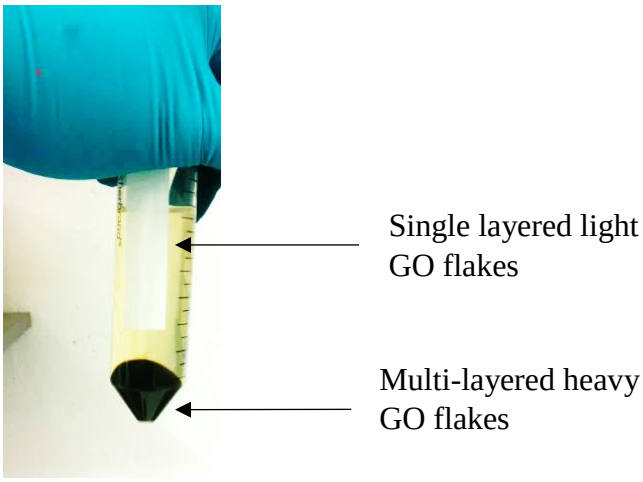

Fig 4. 4 GO aqueous dispersion after centrifugation process.

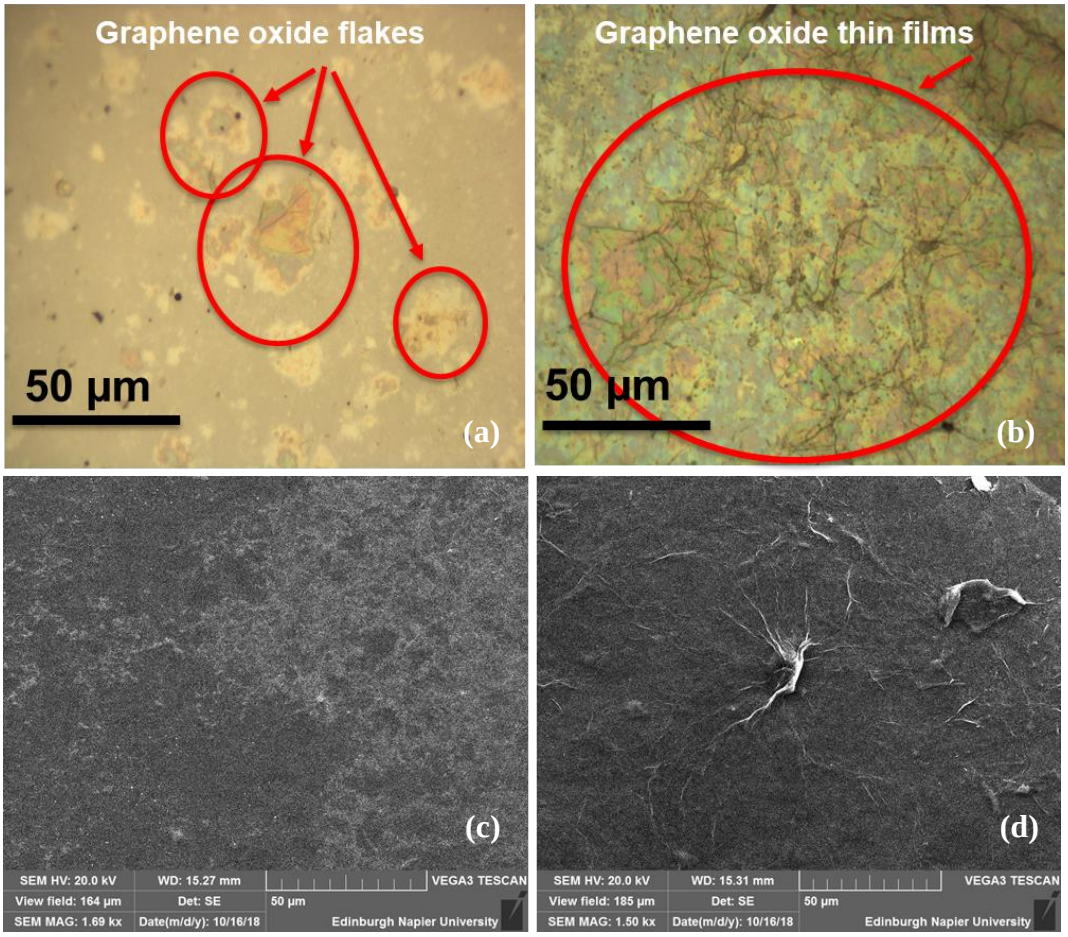

Fig 4. 5 (a) Optical microscopic image of the supernatant (b) Optical microscopic image of the precipitant (c) SEM image of the supernatant (d) SEM image of the precipitant.

Afterwards, the GO dispersion was centrifuged at 3000 rpm for 15 minutes and the supernatant was collected to achieve a high percentage of single-layered GO sheets in the GO aqueous dispersion. The resultant GO solution after the centrifugation process can be seen in Fig. 4.4.

Heavy GO flakes, which settles down at the bottom of the tube contain multilayer graphene sheets and thus, they are of lesser graphene quality. These single layered and multi-layered GO flakes are shown more clearly in Fig. 4.5, in the form of high powered optical microscopic images and SEM images. To achieve these images, 200 µL of GO dispersion from both supernatant and precipitant were drop casted on a thin glass slide by oven drying at 70 ºC for half an hour before putting under a high-power optical microscope and a scanning electron microscope. Multi-coloured GO sites, produced due to the thin film effect of GO flakes can be seen in optical microscope images in both supernatant and precipitant images. The colour of a particular GO site depends on the thin film thickness, as described in [13]. Clearly visible 'wrinkles' created due to many GO layers stacking on top of each other can be observed in the SEM image of the precipitant.

4.4 GO Material Characterisation

Synthesised GO flakes were characterised using Energy Dispersive X-ray Analysis (EDAX) analysis, UV/Vis absorption spectroscopy and Fourier-Transform Infrared (FTIR) spectroscopy. The particle sizes of the obtained supernatant and precipitant of the GO aqueous dispersion and the surface potential of the GO flakes were obtained using a ZetaSizer analysis. These GO material characterisation results obtained are discussed in detail in the following section.

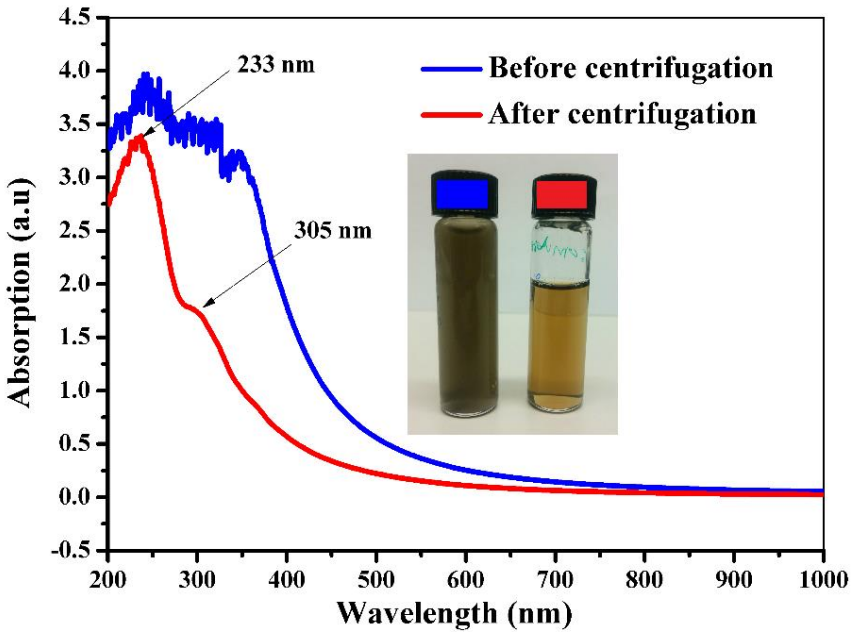

Fig 4. 6 UV/Vis spectrum of the prepared GO aqueous dispersion before and after centrifugation.

4.4.1 UV/Visible Spectrum

The UV/Vis spectrometry is a simple and easy way of measuring the quality of a GO aqueous dispersion. UV/Vis spectrum of the synthesised GO aqueous dispersion was measured using a PerkinElmer Lambda 35 spectrometer, over the range of 200 nm to 1000 nm. Two important characteristics of GO can be observed from the measured UV/Vis spectrum. The first is the 'shoulder' at a wavelength of ~310 nm, which corresponds to the $n-\pi*$ transitions. The other most important feature that can be observed is the peak at ~230 nm, which corresponds to the $\pi-\pi*$ transitions. This particular peak is related to the C-O bonds and number of nanoscale sp^2 clusters appearing on the GO sheets, this being directly related to the amount of single layered GO sheets present in the aqueous dispersion [14]. Therefore, the intensity of this peak at ~230 nm can be used as an indicator of the quality of the prepared GO aqueous dispersion. As is illustrated in Fig. 4.6, a distinctive absorption peak at 233 nm was observed after the GO dispersion was centrifuged, which confirmed that a high number of single-layered GO sheets was obtained, avoiding the creation of multilayers. A very high absorption values were observed at ~ 230 nm peak, before the completion of the centrifugation process (and taking the supernatant) due to high concentration of multi-layered GO flakes present in the GO aqueous dispersion, which resulted in higher absorption values.

As shown in Fig. 4.7, UV/Vis absorption spectrum can also be used to measure the concentration of a GO aqueous dispersion, when calibrated. When the concentration of a GO aqueous dispersion is low, there will be a low absorption peak at ~ 230 nm and similarly, when the GO concentration is high, there will be a readily distinguishable, highly prominent peak shown at ~ 230 nm.

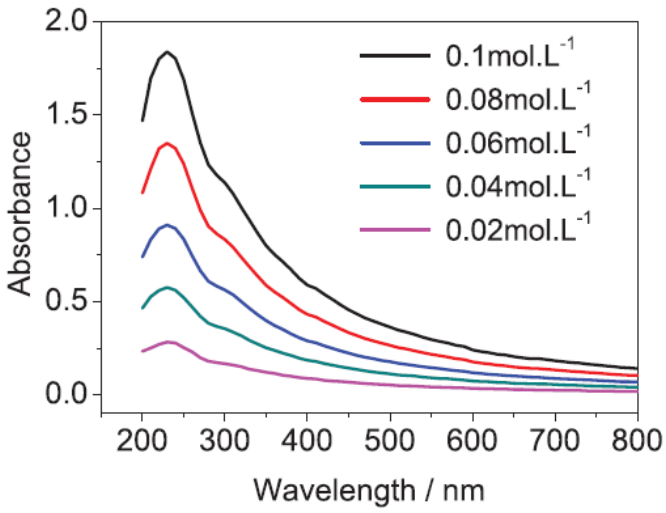

Fig 4. 7 Absorbance of different concentrations of GO [14].

4.4.2 Fourier-Transform Infrared (FTIR) Spectrum

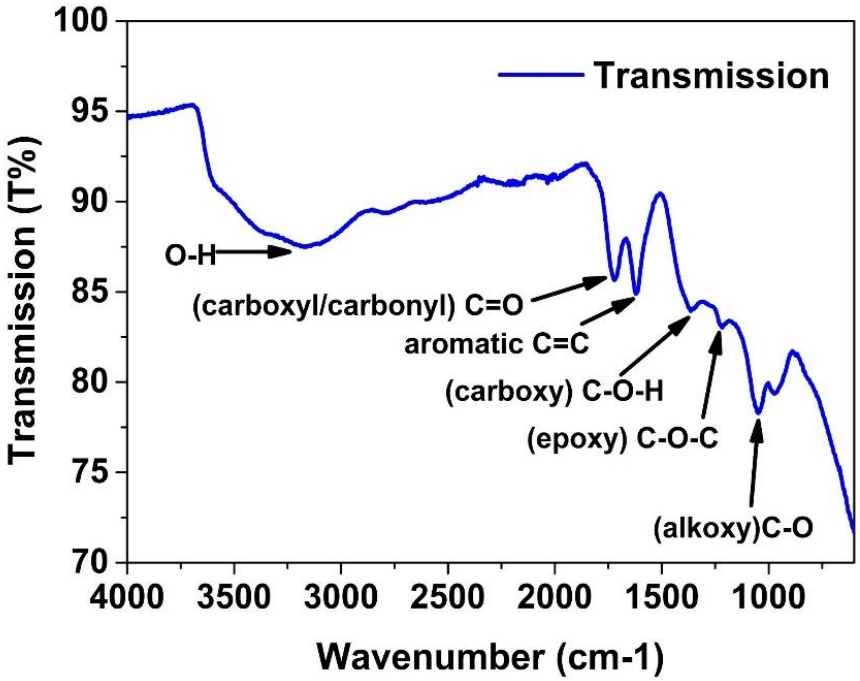

Fig 4. 8 FTIR spectrum of synthesised GO flakes.

FTIR analysis uses the infrared absorption of a certain material to identify the chemical bonds present in the molecule under investigation. The FTIR spectrum of the prepared GO flakes was measured by using a Perkin Elmer Frontier spectrometer. In Chapter 3, it was mentioned that GO contains many oxygen containing groups apart from single layer aromatic carbon sheets, which leads to the rich surface chemistry it possess. These oxygen containing groups present in the synthesised GO flakes can be identified by use of a FTIR spectrum, which is portrayed in Fig. 4.8. The peak at 1619 cm^{-1} represents the aromatic carbon bonds in the two-dimensional GO layers and the remainder of the peaks represent the oxygen containing groups concentrated at the edges and the defects of the single-layer graphene sheets. The wide peak present at around 3170 cm^{-1} represents the water absorption. As shown in the figure, the oxygen containing groups present in the synthesised GO flakes were identified to be carboxyl and carbonyl, epoxy, carboxy and alkoxy groups, based on the respective wavelength peaks observed in the FTIR spectrum. The ratio of the C=O wavelength peak at 1717 cm^{-1} and the C=C wavelength peak at 1615 cm^{-1}, gives an indication as to how much reduction has happened on the GO sample that is been investigated. If C=C wavelength peak is much stronger than the C=O peak, it shows that the sample can be considered as reduced GO, which shows more characteristics similar to graphene than the characteristics of GO. C=C and C=O peaks with somewhat similar strength were observed from the synthesised GO sample, indicating that it

contains a significant amount of oxygen containing groups, which would satisfy the design objectives mentioned in Chapter 3.

4.4.3 Energy Dispersive X-ray Analysis (EDAX) Analysis

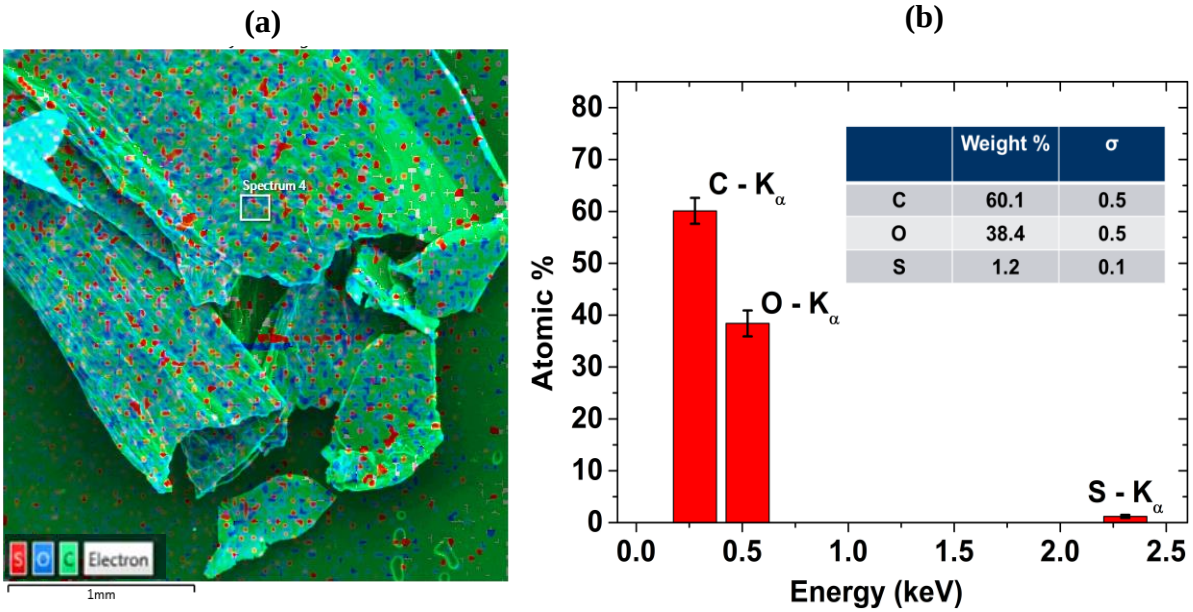

Fig 4. 9 (a) EDAX Image showing C and O sites on GO flakes (b) EDAX spectrum of the squared. Region.

EDAX is an elemental analysis technique that is being used along with the SEM analysis. EDAX uses x-rays emitted from the sample during the electron bombardment of the SEM process to characterise the elemental composition of the analysed volume of the material under investigation. EDAX analysis of the synthesised GO flakes were performed by use of an Oxford Instruments X-Max 20 spectrometer. Fig. 4.9 (a) illustrates an EDAX analysis image showing C and O sites with different colours on the synthesised GO flake and Fig. 4.9 (b) shows the elemental analysis of the white squared region of the GO flake shown in Fig. 4.9 (a). C weight percentage of the volume under analysis was observed to be 60.1% while O recorded a weight percentage of 38.4%. A very low percentage of S shown in the analysis is due to the elemental detection errors of the instrument, which is common in EDAX analysis. These analysis values match very closely with other data reported in [15] and [16].

4.4.4 GO Particle Size

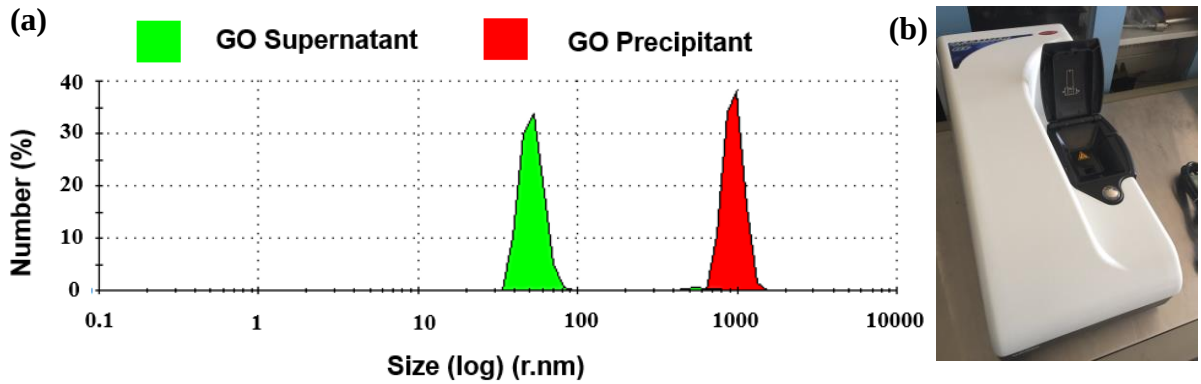

Fig 4. 10 (a) Size distribution of GO supernatant and precipitant (b) Malvern ZetaSizer Nano CS.

The particle size distributions of the GO aqueous dispersions (both the supernatant and the precipitant) were measured using a Malvern ZetaSizer Nano CS, shown in Fig. 4.10 (b). As expected, GO flakes of the supernatant were observed to be much smaller than the particles that were present in the precipitant, as the precipitant contains larger multi-layered GO flakes. In the supernatant, the GO flakes were distributed around a mean particle radius value of 53 nm. In the precipitant, the GO flakes were seen to be distributed around a mean particle radius value of 859 nm. This observation also justifies the use of supernatant in thin film preparation to achieve a higher quality for the GO used.

4.4.5 GO Surface Potential

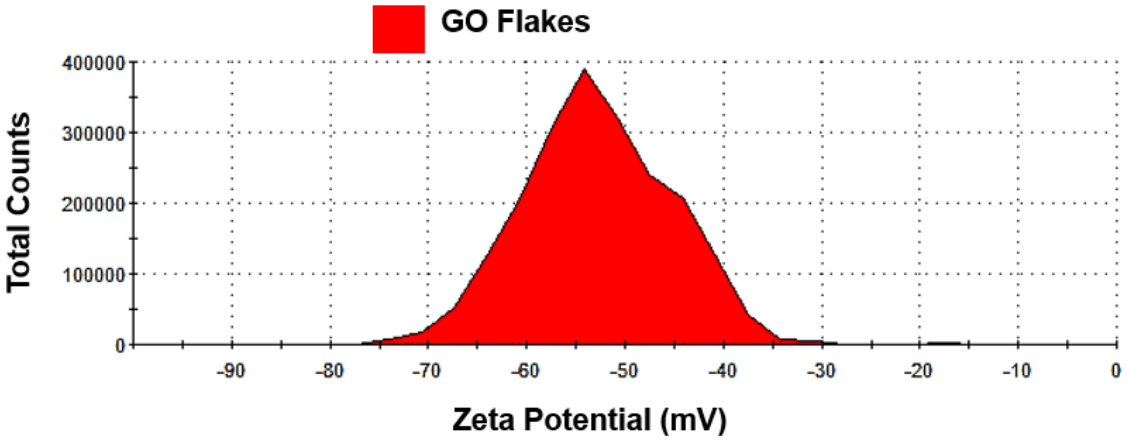

Fig 4. 11 Surface Zeta potential of GO flakes synthesised.

The surface zeta potential of the synthesised GO flakes was also measured using the Malvern ZetaSizer Nano CS instrument. The surface potential is a very important parameter to have knowledge of, if ESA coating technique is used, such is the case in Chapter 5 in the fabrication of the GO-coated LPG based relative humidity sensor. As shown in Fig. 4.11, the surface zeta

potential of the synthesised GO flakes were observed to be centred around a mean zeta potential value of -54 mV, which agrees very well with the reported GO surface potential values reported in [17] and [18].

Based on the GO characterisation results discussed above, the supernatant of a GO aqueous dispersion prepared by taking a 0.5 mg/mL initially concentrated GO dispersion and performing ultrasonication for 2 hours and centrifugation at 3000 rpm for 15 minutes was used in the GO thin film coating process discussed hereafter in this chapter.

4.5 LPG: Theoretical Analysis and Fabrication

A theoretical simulation was performed before the fabrication of the LPGs used in this work to identify the possible resonance loss bands available in the operating wavelength region of 600 nm to 1700 nm: this was important due to the performance limitations of the Optical Spectrum Analyser (OSA) and the broadband light source that were used in this research. In this subsection, firstly, the theoretical simulation results are presented before discussing the LPG fabrication parameters used in the work described in this chapter, in appropriate detail.

4.5.1 Theoretical Analysis

In order to provide a basis for the design of the coated layer on the optical fibre, the FibreCore PS1250/1500 Single Mode Fibre (SMF) used in this work was modelled with COMSOL modal software. First, the relationships underpinning the fibre core and cladding modal dispersion, as a function of the operating wavelengths were obtained (by calculating the effective refractive indices of the core mode and the cladding modes) and then, using equation (1), the wavelength difference ($n_{core}^{eff} - n_{clad.m}^{eff}$) has been calculated for the complete wavelength range from 1000 nm to 1650 nm. The results are illustrated in Fig. 4.12.

It can be noted that the corresponding LPG attenuation bands are present at the zero crossing points. Although many cladding modes are present, only the LP_{01} to LP_{09} modal dispersions are shown here for simplicity. For the 250 μm grating planned in this work, the LP_{01} to LP_{08} attenuation bands are predicted to occur at 1054 nm, 1065 nm, 1080 nm, 1106 nm, 1146 nm, 1202 nm, 1285 nm, and 1445 nm, respectively, due to the mode coupling between core and first consecutive eight cladding modes. It can also be noted that the LP_{09} mode does not cross the zero line over the wide potential operating wavelength range shown here (from 1000 nm to 1650nm). Therefore, the simulation has shown that the LP_{09} mode is not present in this wavelength range.

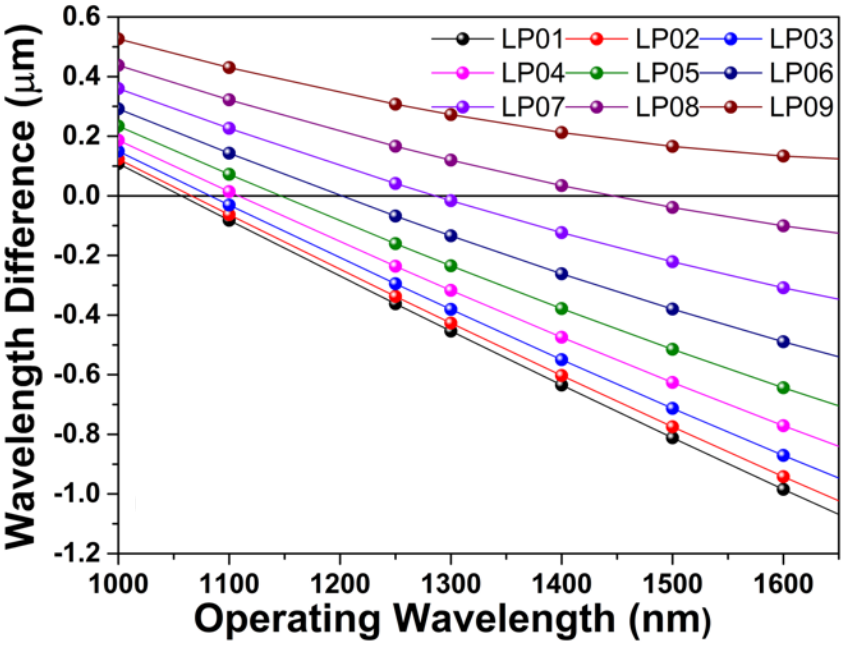

Fig 4. 12 Simulated attenuation bands over the operating wavelength range.

It should be noted that even though the bare LPG was modelled and simulated in this work, it is extremely difficult to model and simulate a LPG with a GO overlay completely as the RI of GO changes with a large number of variables, such as the concentration of GO dispersion, the GO thin film thickness, the bonding between the analyte and the GO overlay, as discussed by Kravets *et al* [19]. This highlights the importance of an experimental investigation, such as was undertaken in this work, using the data from the simulation as a guide to the optimal design, and informing the experimental verification performed.

4.5.2 LPG Fabrication

The LPG fabrication setup described in detail in Chapter 2 was used to inscribe the LPGs used in this work. A 3 cm long Boron-Germanium co-doped photosensitive fibre from FibreCore (PS 1250/1500) was exposed to the light from a 248nm KrF excimer laser through a metal amplitude mask, with a period of 250 μm for 4 minutes and 30 seconds to fabricate the LPGs used in this research. This exposure time was optimised through previous optimisation experiments carried out. The pulse energy of the laser was set at 10 mJ, with a pulse repetition rate of 100 Hz. A 250 μm amplitude mask was chosen so that the resonance peak of the highest cladding order mode, in this case, LP_{08}, was achieved corresponding to a mid-IR wavelength (~1500 nm), near the familiar 'communication bands' and thus facilitating the use of other optical technologies designed for that spectral region. As discussed in detail in Chapter 2, it is noted that the higher order LPG resonance bands provide the high level of sensitivity desired.

At the end of the inscription process, the LPGs were annealed at 100º C for three hours to stabilise their performance when used in sensor applications. The transmission spectrum of the LPG fabricated is shown in Fig. 4.13. A close comparison is seen between the resonance loss bands from the simulated (Fig. 4.12) and the experimentally obtained results (Fig. 4.13), showing that the simulated resonant wavelengths underpinning the system design and obtained from the zero crossing points, agree well with the experimentally obtained LPG spectrum.

4.6 GO Deposition on the Optical Fibre Surface

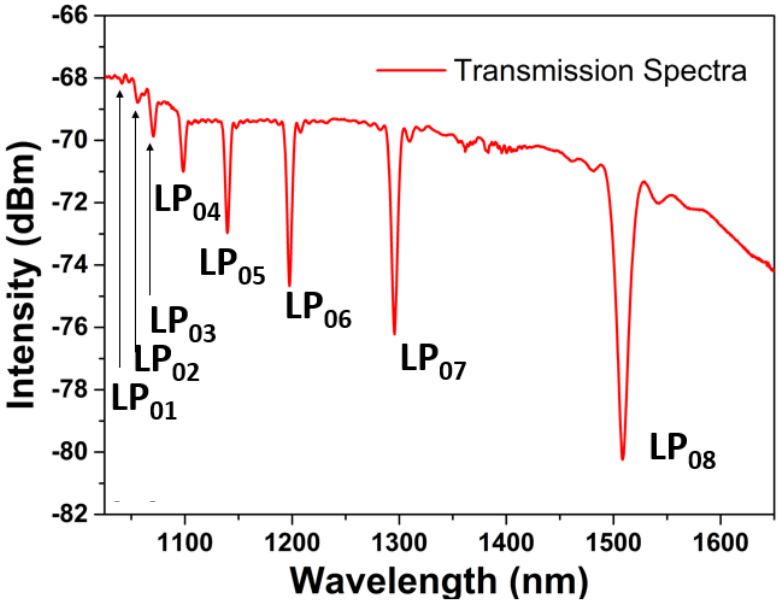

Fig 4. 13 Transmission spectra of the fabricated LPG with an amplitude mask of 250 µm.

Deposition of GO thin film on optical fibre surface is one of the highly important and equally challenging tasks of the research work carried out in this thesis. In the work discussed in this chapter, to investigate a number of external RI sensor designs and thus optimize the performance of the devices, four GO-coated LPG sensors were fabricated, each using a different GO thickness. To provide the most effective coating of the GO, first the LPG fibre surface was cleaned thoroughly with isopropyl alcohol (IPA), following which it was placed in a cleaned metal groove. One of the major objectives of this cleaning process is to clean the fibre surface by remove organic and inorganic dirt and expose the O-H bonds of the Si-O-H groups present on the fibre surface to the outside environment. After that process had been completed, ~200 µL of GO solution (as described above by taking the supernatant of an initial GO aqueous dispersion with a concentration of 0.5 mg/mL) was poured into the groove and the set-up containing the LPG was left at 70 º C for one hour to allow the GO to be deposited on top of the fibre surface, using this drop casting method. One way of controlling the thin film

thickness in using a drop casting technique is to change the GO concentration of the dispersions used to coat the fibre surface. As such, different concentrations of the GO dispersion were used to change the deposited GO thickness of the sensors developed. Sensors are labelled A-D and these are discussed below. For Sensor A, 2 mL of the GO supernatant obtained above was diluted by adding another 8 mL of DI water to achieve a less concentrated GO dispersion. For Sensor B, 2 mL of the same supernatant was diluted by adding 3 mL of DI water to achieve a different concentration of the GO dispersion used. Another way to change the GO thin film thickness is to deposit few layers of the same GO dispersion used. For Sensor C, to observe the difference between these two methods (changing the GO concentration versus adding another layer of the same concentration), two layers of the GO dispersion prepared to be deposited on Sensor A were deposited by repeating the above coating procedure, twice. The GO supernatant mentioned above was deposited (to achieve a higher concentration of the GO dispersion used) on Sensor D without any dilution being used. These GO dispersions used are shown in Fig. 4.14. It can be seen that, as expected, with an increasing concentration of GO, the brownish colour of the dispersions are becoming darker.

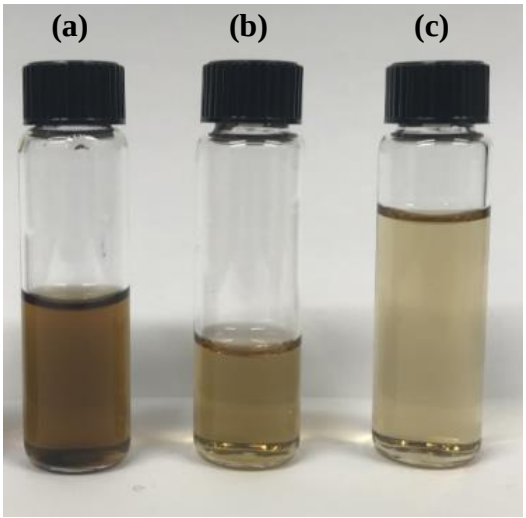

Fig 4. 14 (a) supernatant taken from the GO dispersion (b) 2 mL of the supernatant diluted with 3 mL of DI water (c) 2 mL of the supernatant diluted with 8mL of DI water.

By use of this drop casting method, the GO was deposited directly on the fibre surface, whereas other dip coating methods introduce a linking layer between the GO layer and the fibre surface [7, 8]. Eventually, this linking layer affects the coupling coefficients of the cladding modes of the LPG. The method used here proved to be much more effective, since the objective of this work was to study the effect of the GO thickness (without the combined effect of other linking layers) on the response of the sensors.

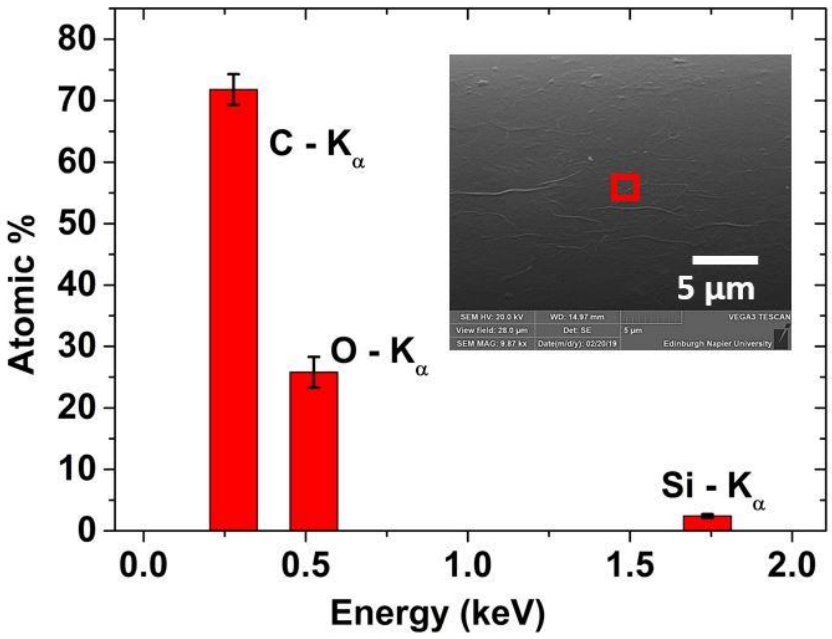

Fig 4. 15 EDAX spectrum of the GO-coated fibre surface of Sensor A. Inset shows the zoomed SEM image of the coated GO layer on Sensor A and the respective red boxed area on the GO coated fibre surface selected to obtain the EDAX analysis.

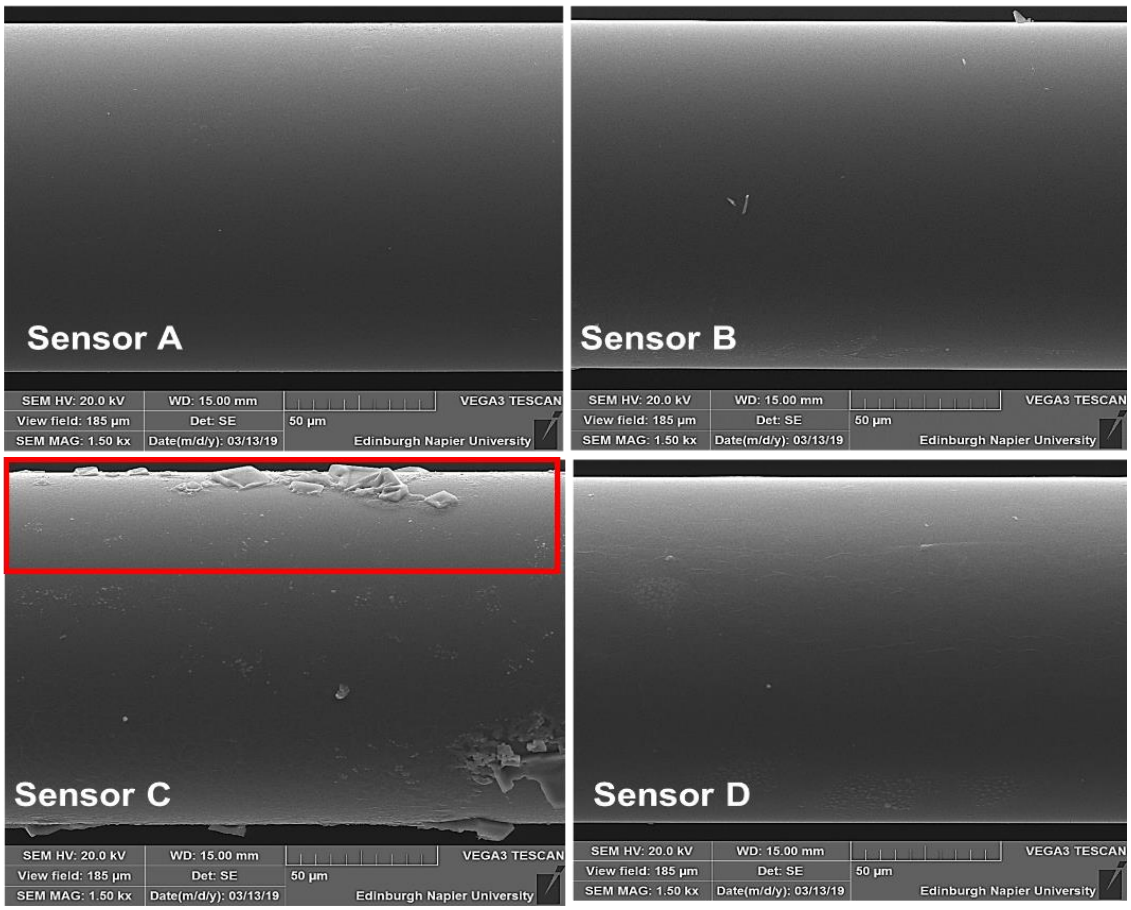

Fig 4. 16 SEM images of GO coated fibre surface of Sensors A (91 nm GO overlay), B (166 nm GO overlay), C (269 nm GO overlay) and D (394 nm GO overlay).

Fig. 4.15 presents a zoomed SEM image of the coated GO layer on Sensor A and the respective EDAX spectrum of the red boxed area on the GO coated fibre surface obtained by use of an Oxford Instruments X-Max 20 spectrometer. Similar types of images taken of the coated GO surface of the other three sensors showed similar results. The atom percentage determined from the pictures matches well with that obtained from other reported GO coatings using similar methods [15]. Further, considering the SEM images shown in Fig. 4.16, it can be concluded that a uniform, high quality GO coating has been achieved on all four sensors.

The thicknesses of the coated GO layers were measured by following another high intensity SEM imaging procedure that includes observing the cross-sections of the GO coated fibres using a calibrated Hitachi S4800 microscope and extracting numerical data from that. An SEM image taken of the cross section of Sensor D for this purpose is shown in Fig. 4.17. This thickness measurement technique used revealed that the coating GO thicknesses of 91 nm, 166 nm, 269 nm and 394 nm had been achieved on Sensor A, Sensor B, Sensor C and Sensor D, respectively. These thickness values lie over the ranges expected from the GO concentrations used. The increase of the surface roughness can be seen in Fig. 4.15 as the thickness increases – visible from the wrinkles appear on the fibre surface due to GO flake deposition, going from Sensor A to Sensor D. The red highlighted area of the SEM image of Sensor C shows the NaCl crystals that were unintentionally deposited on the fibre surface at the end of the experiment.

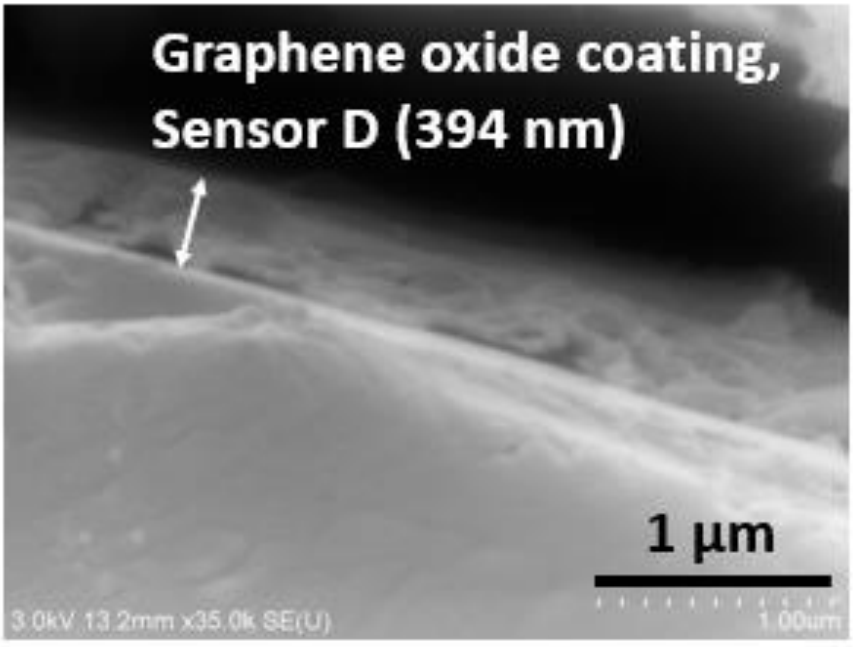

Fig 4. 17 SEM image taken of the cross section of the coated fibre surface of Sensor D to measure the GO coating thickness.

This NaCl deposition occurred since Sensor C was not cleaned with water (before the SEM analysis) after the last RI measurement and the measured spectrum was not affected by this crystallization process.

4.7 Experimental Setup for Evaluating External RI Changes

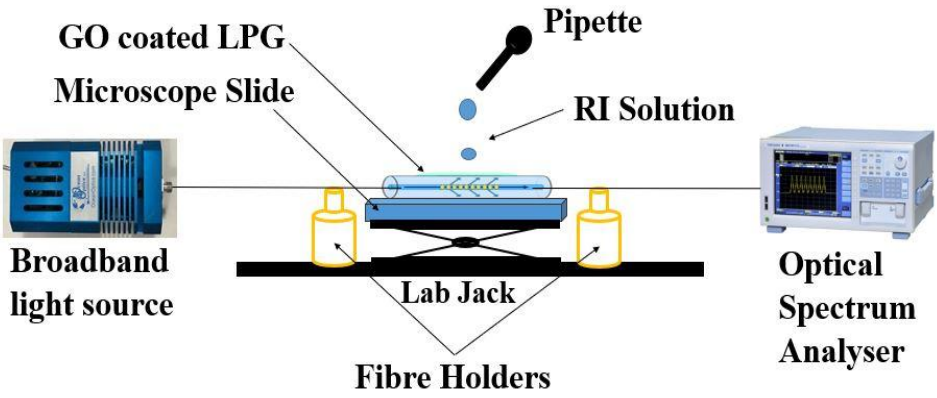

Fig 4. 18 Experimental arrangement used for external RI sensing measurements.

Fig. 4.18 illustrates schematically the experimental setup used to measure and record the transmission spectra of the four different GO-coated LPG sensors, Sensors A-D, whose performance was investigated with changes in the surrounding RI by use of NaCl solutions with different concentrations. One end of the sensor probe was connected to a broadband light source (Ocean Optics LS1) and the other to the input of an Optical Spectrum Analyser (OSA – Yogokawa Model 6370C).

During the experiment, to provide stable and repeatable measurements, the sensor probe was carefully placed on two fibre holders, mounted on an optical bench. A microscope slide was placed on a height-adjustable lab jack, placed directly under the sensing area of the GO coated LPG sensor probe. To measure the transmission spectra at different external RI values, the RI of solutions, beginning with pure distilled water and followed by NaCl solutions of different concentrations (and known values of RI as a result) were obtained. In each case, the different solutions were applied to the microscope slide using a pipette. Following this, the height of the lab jack was increased so that the GO-coated area of the LPG became submerged in the NaCl solution and the transmission spectrum was recorded in each case. At the end of each test, the sensor probe and the microscope slide were thoroughly cleaned properly with lint-free Kimwipe paper before starting the next test, using a different solution. All the measurements were performed at a controlled room temperature of 22 ºC, to avoid any errors in the recording of the wavelength shifts, due to ambient temperature variations.

4.8 Experimental Results and Analysis

To evaluate the external RI performance of the sensors developed (Sensors A, B, C and D), different NaCl solutions, of varying NaCl concentrations, were prepared and the RIs of these solutions were measured by using an Abbe refractometer at a wavelength of 589 nm and at room temperature (22º C), in that way to provide a calibration for the sensor performance. The recorded NaCl calibration graph is shown in Fig. 4.19. The concentrations of NaCl were chosen to create solutions in the lower RI region over the range from 1.330 (pure water) to 1.379 (NaCl saturated in water). This lower RI region is of real importance when it comes to developing biosensors, as most of the bioassays and biochemical interactions are carried out in this range of RI values. Variations in the transmission spectra of the highest order LP_{08} cladding mode of the GO-coated LPGs, monitored in the presence of the different concentrations of NaCl solutions prepared are analysed and presented in this section, seeking therefore to understand the effects of increasing GO overlay thickness on such optical fibre external RI sensors.

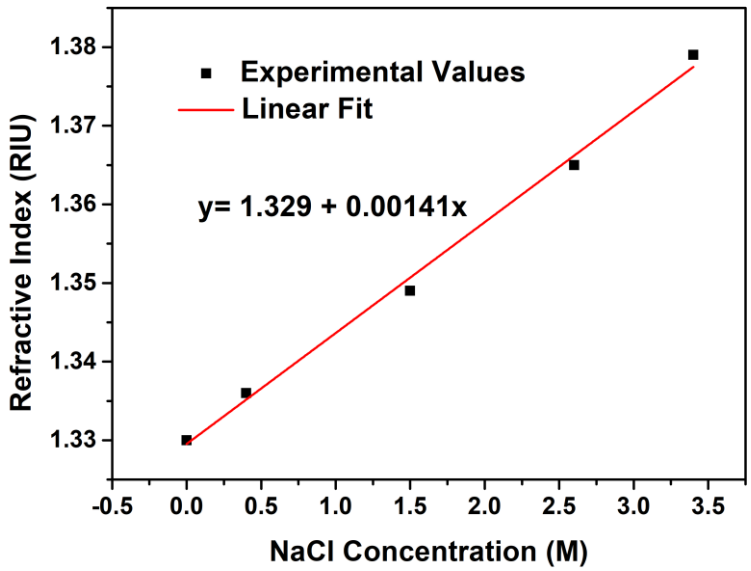

Fig 4. 19 RI of NaCl solutions with varying NaCl concentrations.

By using this reference curve shown in Fig. 4.19, the GO coated external RI sensors (sensors A, B, C and D) can all be used to measure the NaCl salinity concentrations in water. As the chapter mainly concentrates on external RI sensing in general, the performance graphs hereafter are based on the RI values of the prepared NaCl solution, rather than the NaCl concentration, for better clarity in describing external RI response of the prepared sensors.

As discussed in Chapter 2, in a LPG, the resonance loss band corresponding to the highest order cladding mode is most sensitive to the external RI. The highest external RI sensitivity can be achieved by using dual peak resonance LPGs, by tuning the dispersion turning point,

but the focus of this work here is on single peak LPGs for ease of measurement. Sensitivity enhancement by using a dual resonance peak is discussed in Chapter 6. The highest resonance loss band observed in the prepared LPG sensor probes were corresponding to the LP_{08} cladding mode and thus, it was chosen to be interrogated due to its superior sensitivity compared to other resonance loss bands. Table 4.1 depicts the spectral shift of the LP_{08} resonance band of each of the GO-coated LPG sensors, before and after the deposition of GO thin layer. Before coating, the transmission spectra of all the four sensors were obtained and it was noticed that they were broadly similar in their characteristics to the spectrum shown in Fig. 4.13 as the same inscription process was carried out.

Table 4. 1 Spectral shift of the LPG sensors before and after GO coating

Sensor Type	**Measured GO thickness (nm)**	**LP08 resonance loss band centre wavelength (nm) – Before coating**	**LP08 resonance loss band centre wavelength (nm) – After coating**	**Blue shift of LP08 resonance loss band centre wavelength (nm)**	**Minimum Intensity of LP08 resonance loss band- Before coating (dBm)**	**Minimum Intensity of LP08 resonance loss band- After coating (dBm)**	**Minimum Intensity loss of LP08 resonance loss band (dB)**
Sensor A	91 ± 7	1519.94	1516.70	3.24	-87.26	-84.47	2.79
Sensor B	166 ± 12	1510.94	1507.34	3.60	-82.60	-78.87	3.73
Sensor C	269 ± 6	1519.20	1511.30	7.90	-84.34	-77.66	6.68
Sensor D	394 ± 3	1519.58	1514.00	5.58	-89.99	-77.10	12.90

Fig. 4.20 shows the transmission spectra of the LP_{08} resonance band of each of the GO-coated LPG sensors under conditions where varying solutions of different RIs were used, surrounding and then submerging the sensors, with solutions of different NaCl concentrations. Sensor A, with a GO coating of 91 nm, showed a blue shift of 3.24 nm, comparing the situation before and after coating with the GO thin layer – further, the minimum intensity of the resonance band was decreased by 2.79 dB. The centre wavelength of the resonance band, recorded in air after GO deposition, was 1516.70 nm. When Sensor A was fully immersed in water (RI = 1.330), the centre wavelength of the resonance band was recorded at 1506.62 nm. When the external RI was increased from 1.330 to 1.379 by immersing Sensor A in the various NaCl solutions of different concentrations, blue shifts of the centre wavelength were observed, as shown in Fig. 4.20 (a). In addition, the minimum intensities of the resonance bands decreased with the

increasing RI, whilst recording the values of -82.5 dBm and -80.9 dBm for RI values of 1.330 and 1.379, respectively.

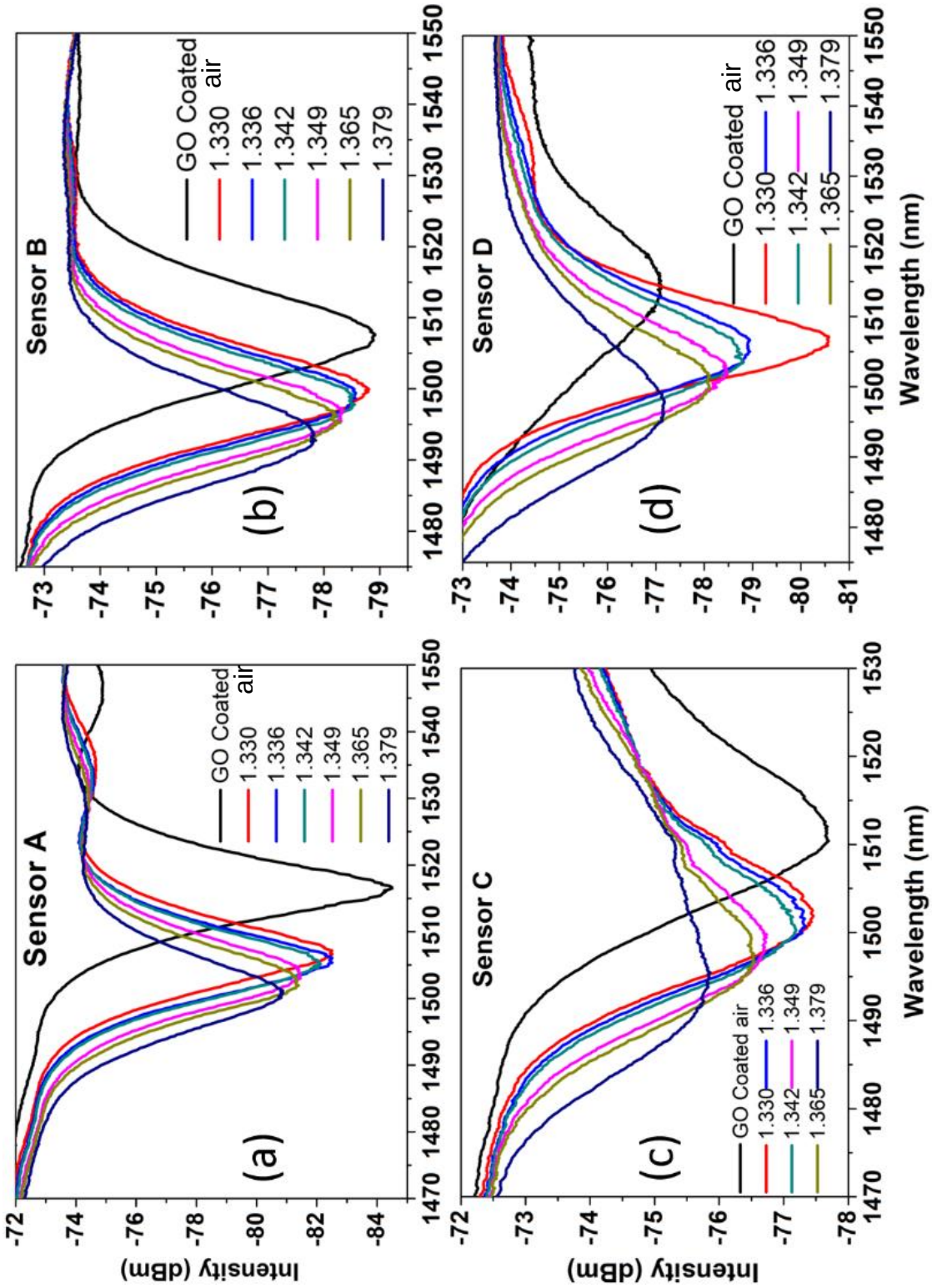

Fig 4. 20 Transmission spectra of Sensor A (a), B (b), C (c) and D (d) with increasing value of the surrounding RI.

The same trends were observed for Sensor B and Sensor C in terms of the centre wavelength and the minimum intensity of the LP_{08} resonance band. Blue shifts of 3.6 nm and 7.9 nm of the centre wavelength were observed after the deposition of the GO thin layers on Sensor B and Sensor C, respectively. The GO thin layer deposition also resulted in a decrease of the minimum intensities of the resonance bands by 3.73 dB and 6.68 dB for Sensor B and Sensor C, in that order. When the liquid surrounding the sensor had a RI value of 1.330 (pure water), Sensor B recorded a centre wavelength value of 1499.96 nm while Sensor C recorded 1502.48 nm under similar conditions. The centre wavelength values of the resonance band were recorded as 1492.94 nm and 1494.92 nm at an external RI of 1.379, with the use of Sensor B and Sensor C, respectively. For Sensor B, the minimum intensities of the resonance band were recorded as -78.87 dBm and -77.82 dBm with the external RI values of 1.330 and 1.379, respectively. The corresponding values of the resonance band minimum intensity were seen to be -77.67 dBm and -75.84 dBm in Sensor C.

As mentioned in sensing principle at the beginning of this chapter, the effective RI of LP_{08} cladding mode ($n_{clad,08}^{eff}$) is affected by the RI of the cladding (n_{clad}), as well as the RI of the medium surrounding the cladding, in this case, GO. GO has a higher RI [19] than that of the cladding. Thus, when a GO thin layer is deposited on the cladding, $n_{clad,08}^{eff}$ increases and according to equation (4.1), a blue shift of the resonance band centre wavelength is observed. With Sensors A, B and C, with increasing layer thickness, the RI of the GO layer also increases, which effectively increases the value of $n_{clad,08}^{eff}$ and there is a consequent increase in the blue shift of the centre wavelength from 3.24 nm to 7.90 nm.

In this region of such values of the GO thickness, even with a GO coating of 269 nm, the $n_{clad,08}^{eff} < n_{clad}$, which is confirmed by the fact that a blue shift of the resonance band centre wavelength is still seen after the GO coating is applied, compared to what is seen using the centre wavelength value of the resonance loss band of the uncoated fibre, in this case, in air.

If $n_{clad,08}^{eff} > n_{clad}$, a red shift of the centre wavelength would be expected after performing the high index GO coating. This phenomenon is discussed extensively in the work of Patrick et al. [20] and also in Chapter 2.

When $n_{clad,08}^{eff}$ is equal to n_{clad}, the coupling between the core and the LP_{08} cladding mode ceases to exist, which results in the complete disappearance of the LP_{08} resonance band, and

this could be considered as an *OFF-resonance* state [20]. Moreover, when $n_{clad,08}^{eff}$ gets very close to the value of n_{clad}, the resonance wavelength blue shift starts to decrease, and finally reaches the *OFF-resonance* state.

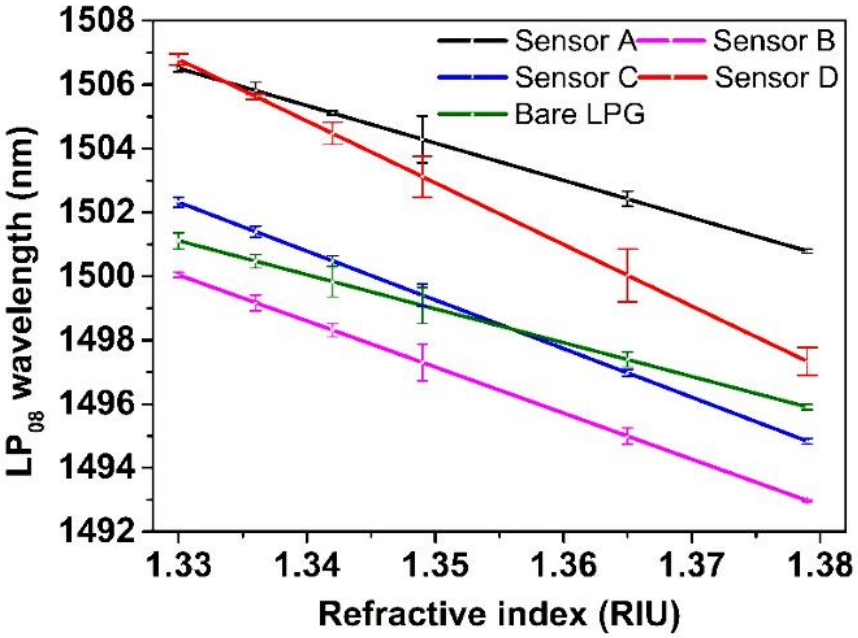

Fig 4. 21 Centre wavelength shift of the LP08 resonance loss band of GO-coated LPG sensors and of a bare, uncoated LPG.

Therefore, it is evident that there is a transition region over the range from $n_{clad,08}^{eff} < n_{clad}$ (which corresponds to a blue shift) to $n_{clad,8}^{eff} > n_{clad}$ (which corresponds to a red shift). It is clear that with a 394 nm GO coating, the $n_{clad,08}^{eff}$ of Sensor D lies in this region. Following the previous trends, Sensor D (with a 394 nm GO coating) was expected to show a further incremental blue shift compared to the 7.90 nm blue shift observed in Sensor C (with a 269 nm GO coating), rather than the much lower blue shift of 5.58 nm actually observed, as shown in Table 4.1. In the case of the Sensor D, with the increasing GO overlay thickness used, the effect of the GO on the RI becomes dominant, which makes the $n_{clad,08}^{eff}$ much closer to n_{clad}. Therefore, as noted above, $n_{clad,08}^{eff}$ gets closer to the *OFF-resonance* state which results in the reduction of blue shift. When Sensor D is immersed in water (RI 1.330), the $n_{clad,08}^{eff}$ value again starts to move away from that for n_{clad}, which results in a blue shift of the centre wavelength, as shown in Fig. 20 (d). These discussed trends related to the centre wavelength shift of the four sensors are shown more clearly in Fig. 4.21. Moreover, it also shows an increase in the minimum intensity of the LP_{08} resonance band, which is opposite to that of

Sensors A, B and C (as shown in Fig. 20 (a), (b), and (c)) that show a decrease of the LP_{08} resonance loss band minimum intensity in the presence of water. In Sensors A, B and C, the coupling between the fibre core mode and the lossy LP_{08} cladding mode was better in air, compared to what is seen in water. However, in Sensor D, the core mode couples better with the lossy cladding mode when the device is immersed in water, rather than in air.

As the thickness of the GO coating is increased, some of the cladding mode power propagates through the high index GO coating layer. This in turn provides a reduced loss in the LPG transmitted spectrum, observed in the reduction of the minimum intensity of the resonance band, from 2.79 dB to 12.89 dB, going from Sensor A to D, with increasing GO layer thickness in each case, as tabulated in Table 4.1.

The blue shift of the centre wavelength observed with increasing surrounding RI introduced by immersing Sensors A, B, C and D in different NaCl solutions, whose RI values range from 1.330 to 1.379, can be explained as follows. When the GO layer is in contact with water or a NaCl solution, the GO changes its optical properties, influencing its RI, which results in changing the coupling coefficients between the fibre core and LP_{08} cladding mode. Also, as shown in the work of Zheng et al. [21], the d-spacing between two single layered GO sheets also changes when the GO is in contact with the NaCl solutions (and water). These changes in the GO layer thickness are illustrated in Fig. 4.22.

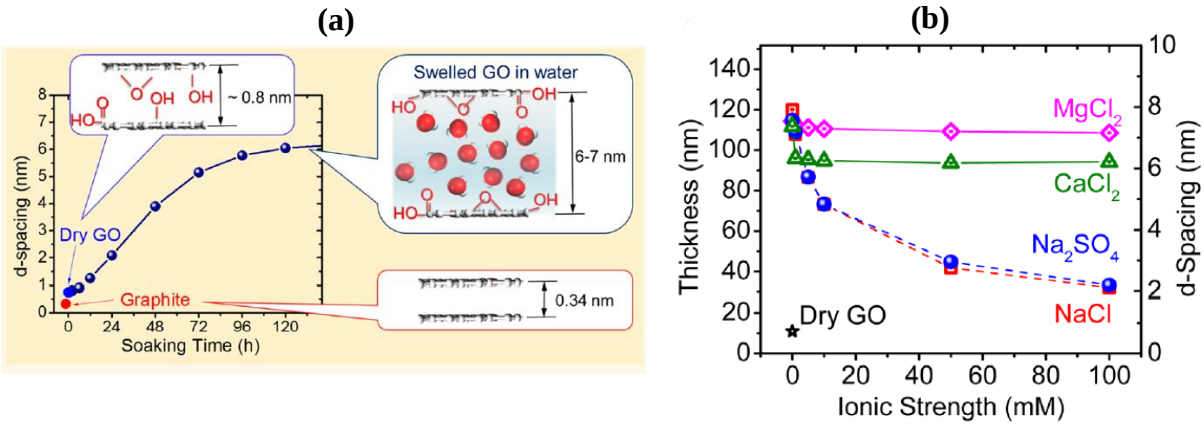

Fig 4. 22 (a) Swelling of GO in the presence of water molecules (b) Change of d-spacing in GO in the presence of NaCl [21].

It can be seen that when a dry GO flake is soaked in water for some time, the d-spacing between two single layered GO sheets expand to 6-7 nm from the initial value of 0.34 nm. When Na^+ and Cl^- ions come into contact with a GO flake, the d-spacing between two single layered GO sheets depends on the ionic strength of the NaCl solution used.

Both these phenomena contribute to the change of the optical properties of the GO thin layer when it is immersed in a solution. This change of the optical properties results in a change of the value of $n_{clad,08}^{eff}$ and thus, a change in the centre wavelength of the resonance band is observed. As shown in [22], when GO thickness increases, Na^+ and Cl^- ions find it hard to penetrate the GO layers and as a consequence, there are changes noted to the GO RI and its other optical properties. It is difficult to determine the exact value of the RI of the GO layer when it is in contact with NaCl solution (or water) but based on the blue shift of the resonance band centre wavelength observed, it can be concluded that the change in GO RI results in an increasing value of $n_{clad,08}^{eff}$. Considering these results in detail, in Sensor D, (as mentioned by Bandyopadhyay *et al.* in the literature [23]), the LP_{08} mode must be reaching its mode transition point: this can be achieved by depositing a high index thin film, where the superior RI sensitivity of Sensor D can also be explained by this phenomenon.

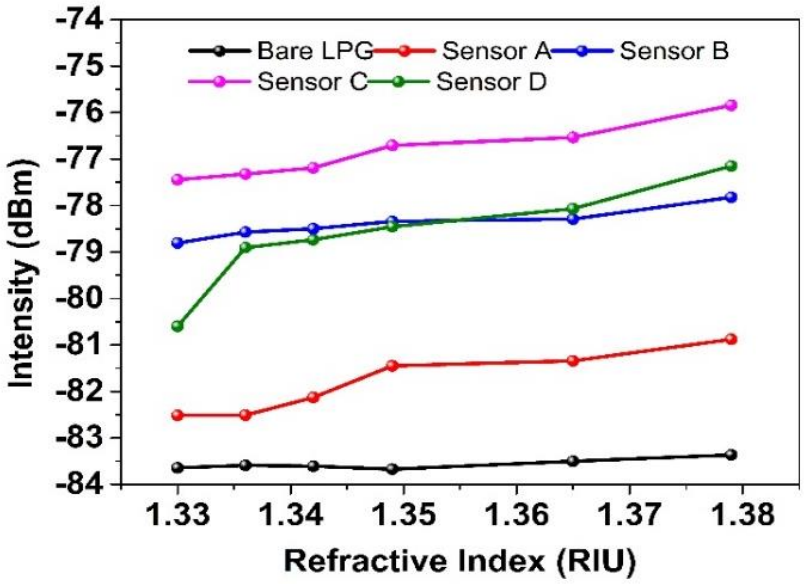

Fig 4. 23 Minimum intensity change of the LP08 resonance loss band of GO coated LPG sensors and of a bare, uncoated LPG.

Fig. 4.23 illustrates the changes in the minimum intensity of LP_{08} resonance loss band of the four sensors in the NaCl solutions used, of different concentrations, compared to those of a bare, uncoated LPG. A minimal change (0.28 dB) in the minimum intensity was observed when the external RI was increased from 1.330 to 1.379 with an uncoated LPG. In Sensors A, B, C and D, the GO overlay changes its optical properties in the presence of NaCl solution to affect the $n_{clad,08}^{eff}$ and thus the coupling coefficient and causing a reduction of the resonance band's minimum intensity is observed with the increasing external RI values. When the external RI was increased from 1.330 to 1.379, the change of the minimum intensity was recorded to be

1.64 dB, 0.98 dB and 1.60 dB for Sensors A, B and C, respectively. Sensor D however did show a considerable, but nonlinear change of 3.45 dB with the same external RI variation. However, there was no noticeable trend observed in the minimum intensity of the resonance loss band with the increased thickness of the GO overlay. Considering this and the nonlinear change of minimum intensity response suggests that the best way to develop the most effective RI sensors in the lower RI region (of 1.330 to 1.379) with a GO-coated LPGs is to consider the wavelength shift of the resonance loss bands, rather than the minimum intensity response.

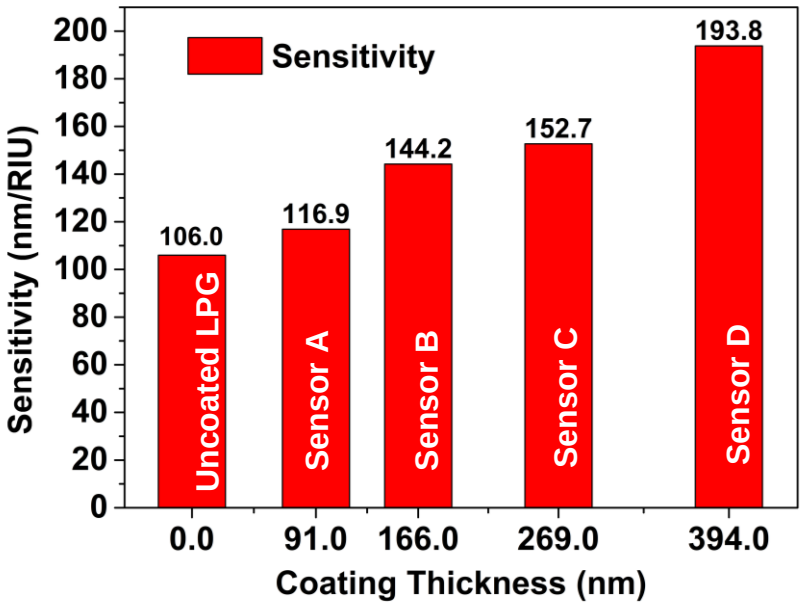

Fig 4. 24 Centre wavelength shift sensitivity of the LP08 resonance loss band of GO- coated LPG sensors and of a bare, uncoated LPG.

Fig. 4.21 illustrates the centre wavelength shift of the LP_{08} resonance loss band and Fig. 4.24 its sensitivity, for the four sensors, with increasing external RI from 1.330 to 1.379 (and compared to that of a bare LPG). The linear correlation coefficients calculated for the fitted graphs shown in Fig. 4.21 are 0.965, 0.982, 0.993, and 0.973 for the performance of Sensors A, B, C and D, respectively. Here, Sensor C showed a much better linear response compared to the other three sensors, with less deviations from the linear curve fitting. As described in the sensor fabrication section, the GO layer thickness of Sensors A, B and D was controlled by changing the concentration of the GO dispersion used to coat the fibre surface while, by contrast, Sensor C was fabricated by depositing two layers of the same GO dispersion. Based on this observation, it is evident that a more linear, and desirable response can be achieved by introducing many layers of the same GO dispersion, rather than using a high concentration of GO dispersion to increase the GO overlay thickness.

The sensitivities of the GO-coated sensors were calculated by taking the slope of the curves shown in Fig. 4.21. The wavelength shift sensitivity of an uncoated LPG was recorded to be 106 nm/RIU in the low RI region (from 1.330 to 1.379). As shown in Fig. 4.24, with increasing GO overlay thickness, the wavelength shift sensitivities of 116.9 nm/RIU, 144.2 nm/RIU, 152.7 nm/RIU and 193.8 nm/RIU were recorded for Sensors A, B, C and D, respectively. These increased sensitivities correspond to a 10.3 %, 36.1 %, 44.1 % and 82.8% increase over the resonance wavelength shift sensitivity in the external RI region of 1.330 to 1.379, for the GO thicknesses of 91 nm, 166 nm, 269 nm and 394nm (in that order). Some previous work has been reported on GO-coated external RI sensors based on dual-peak LPGs [5,8] but data on an investigation of the resonance band wavelength shift of a GO-coated single peak LPG based external RI sensor do not seem to be evident from the literature. Based on the improvement of the sensitivity achieved in the external RI region (of 1.330 to 1.379) by introducing a GO overlay, it is clear that the GO-coated LPG based external RI sensor design considered in this work has the potential not only to be used as a NaCl salinity concentration measurement sensor *per se* but as the basis for some designs of fibre optic biosensors, as discussed in [8].

4.9 Summary

An insight into the thickness-dependent performance of a GO-coated LPG-based external RI sensor approach has been considered in this chapter, through a detailed analysis of the coating characteristics and performance, in light of its use in sensor applications. In so doing, four sensors (Sensors A to D) with different GO overlay thicknesses were fabricated and their performance characteristics examined. The external RI responses of these four sensors were investigated in the lower RI region, from 1.330 to 1.339, as this region is potentially attractive in biosensing, as bioassays and biochemical investigations are frequently carried out in this region. The sensors operate by exploiting the tuneable RI of a GO layer with surrounding solutions having different values of RI. The performance depended on the unique characteristics seen from the two-dimensional nature of GO coating layers used. A drop casting method was used to deposit a few hundred nanometres of GO as a layer on the fibre surface. Given the sensor performance reported, a satisfactory linear response of the LP_{08} resonance band wavelength shift was obtained over the external RI region, from 1.330 to 1.379, for all four sensors considered, with increasing GO overlay thicknesses. The highest external RI sensitivity of 193.8 nm/RIU was achieved with a GO layer thickness of 394 nm, this showing an 83% increment in the sensitivity achieved, compared to an uncoated LPG. The work discussed in the chapter showed that there is an optimal GO thickness that should be deposited

to achieve the maximum wavelength shift of the resonance band, without reaching the *OFF-resonance* state.

Two of the objectives set out were realised, based on the results obtained in the work and described in this chapter. First, to vary the external RI, solutions with different concentrations of NaCl were used and based on the RI calibration curve discussed, it is evident that the GO coated external RI sensors developed can be used for NaCl salinity concentration measurements in water. Secondly, due to its unique surface chemistry (oxygen functional groups present on graphene layers), GO enables the functionalisation of its surface to develop more selective biosensors and as such, the developed GO coated LPG based external RI sensors lays a platform to develop various other more selective and more efficient chemical sensors. In the next chapter, building on the results reported in this chapter, the design and development of another GO-coated LPG based sensor will be discussed in the field of relative humidity measurements.

4.10 References

[1] Hromadka J, Korposh S, Partridge M C, James S W, Davis F, Crump D, Tatam R P, "Multi-parameter measurements using optical fibre long period gratings for indoor air quality monitoring," Sensors and Actuators B: Chemical, 244, 217-225, 2017.

[2] G. D. Jay et al., "Point-of-Care Noninvasive Hemoglobin Determination Using Fiber Optic Reflectance Spectroscopy," 2007 29th Annual International Conference of the IEEE Engineering in Medicine and Biology Society, Lyon, 2932-2935, 2007.

[3] Liu H, Liang D, Zeng J, Jin J, Wu J, Geng J, "Design of a long-period fiber grating sensor for reinforcing bar corrosion in concrete," Journal of Intelligent Material Systems and Structures, 23, 45–51, 2011.

[4] Yu Z, Yan B, Li Z, Ruan X, Zhang Y, and Dai Y, "Graphene induced sensitivity enhancement of thin-film coated long period fiber grating," Journal of Applied Physics, 124, 184503, 2018.

[5] Liu C, Cai Q, Xu B, Zhu W, Zhang L, Zhao J, Chen X, "Graphene oxide functionalized long period grating for ultrasensitive label-free immunosensing," Biosensors and Bioelectronics, 94, 200-206, 2017.

[6] Dissanayake K P W, Wu W, Nguyen H, Sun T and Grattan K T V, "Graphene oxide coated long period grating based fibre optic humidity sensor," 2017 25th Optical Fiber Sensors Conference (OFS), 1-4, 2017.

[7] Liu C, Cai Q, Xu B, Zhu W, Zhang L, Zhao J et al., "Fibre optic chemical sensor based on graphene oxide-coated long period grating," Proceedings of SPIE 9916, Sixth European Workshop on Optical Fibre Sensors, May. 2016.

[8] Liu C, Xu B J, Zhou L, et al., "Graphene oxide functionalized long period fiber grating for highly sensitive hemoglobin detection," Sensors and Actuators B: Chemical, 261, 91–96, 2018.

[9] Qi W, Bo-Tao W, "Surface plasmon resonance biosensor based on graphene oxide/silver coated polymer cladding silica fiber," Sensors and Actuators B. Chemical, 275, 332-338, 2018.

[10] Paulchamy B, Arthi G and Lignesh B D, "A Simple Approach to Stepwise Synthesis of Graphene Oxide Nanomaterial," Journal of Nanomedicine and Nanotechnology, 2015.

[11] Marcano D C, Kosynkin D V, Berlin J M, Sinitskii A, Sun Z, Slesarev A, Alemany L B, Lu W, Tour J M, "Improved synthesis of graphene oxide," ACS Nano, 4, 8, 4806-4814, 2010.

[12] Hummers W S, Offeman R E, "Preparation of graphitic oxide," Journal of American Chemical Society, 80, 1339, 1958.y

[13] Chi H, Liu Y J, Wang F, He C, "Highly Sensitive and Fast Response Colorimetric Humidity Sensors Based on Graphene Oxides Film," ACS Applied Materials Interfaces, 7, 36, 19882-19886, 2015.

[14] Lai Q, Zhu S, Luo X, Zou M and Huang S, "Ultraviolet-visible spectroscopy of graphene oxides," AIP Advances, 2, 3, 032146, 2012.

[15] Sridevi S, Vasu K S, Bhat N, Asokan S, Sood A K, "Ultra sensitive NO_2 gas detection using the reduced graphene oxide coated etched fiber Bragg gratings," Sensors and Actuators B: Chemical, 223, 481-486, 2016.

[16] Haitham K, Shaimaa M, Tiyash B, Bayachou M, " Manganese Oxide/Hemin-Functionalized Graphene as a Platform for Peroxynitrite Sensing," Journal of The Electrochemical Society, 165, G3133-G3140, 2018.

[17] Mingjie L, Chenming L, Hong C, Yi Z, "Surface Charge Research of Graphene Oxide, Chemically Reduced Graphene Oxide and Thermally Exfoliated Graphene Oxide," Advanced Materials Research, 716, 127-131, 2013.

[18] Li M, Liu C, Xie Y, Cao H, Zhao H, Zhang Y, "The evolution of surface charge on graphene oxide during the reduction and its application in electroanalysis," Carbon, 66, 302-311, 2014.

[19] Kravets V G, Marshall O P, Nair R R, Thackray B, Zhukov A, Leng J, and Grigorenko A N, "Engineering optical properties of a graphene oxide metamaterial assembled in microfluidic channels," Optics Express, 23, 1265-1275, 2015.

[20] Patrick H J, Kersey A D, and Bucholtz F, "Analysis of the Response of Long Period Fiber Gratings to External Index of Refraction," J. Lightwave Technol, 16, 1606-1612, 1998.

[21] Zheng S, Tu Q, Urban J J, Jeffrey, Li S, and Mi B, "Swelling of Graphene Oxide Membranes in Aqueous Solution: Characterization of Interlayer Spacing and Insight into Water Transport Mechanisms," ACS Nano, 11, 6440-6450, 2017.

[22] Morelos A et al, "Effective NaCl and dye rejection of hybrid graphene oxide/graphene layered membranes," Nature Nanotechnology, 12, 1083–1088, 2017.

[23] Bandyopadhyay S, Biswas P, Chiavaioli F, Dey T K, Basumallick N, Trono C, Giannetti A, Tombelli S, Baldini F, and Bandyopadhyay S, "Long-period fiber grating: a specific design for biosensing applications," Applied Optics, 56, 9846-9853, 2017.

Chapter 5

Graphene oxide-coated LPG-based Relative Humidity Sensor

5.1 Introduction

In the previous chapter, the design and development of a GO-coated LPG-based external RI sensor system has been discussed and its characteristics reported in detail. In this Chapter, building on the proven external RI sensitivity of GO when coated on a LPG surface, the design and development of a fibre optic Relative Humidity (RH) sensor is discussed along with its temperature response. RH, in a way that is similar to both temperature and pressure, is a very common measurement that is being used by industry in a wide range of applications. These applications vary across a number of sectors: from automotive to health and medical, the semiconductor industry, food processing, meteorological measurements, measurements linked to air conditioning systems and to structural health monitoring. While good quality humidity monitoring is of significant importance in each of these applications, there are issues where better humidity monitoring could permit major savings in industry e.g. RH is directly related to the corrosion levels of steel bars in structures in the building and construction industry. Further, humidity sensors must be able to meet the different requirements that arise from the wide range of different applications and the variety of situations in which the measurement of RH is needed. In this regard, fibre optic sensors show a significant advantage over their electrical counterparts due to their small size, immunity to electromagnetic interference, biocompatibility, easy multiplexing capability and their ability to be used in very hazardous and corrosive environments. Among the various humidity sensing materials in use, such as polymers (polyamide and PVA) [1-2], metal oxides [3], porous materials [4] and nano-materials [5], GO has emerged as a very interesting and thus potentially suitable material for better humidity measurement. This is mainly due to its super-permeability to water molecules [6] which reduces the response time and increases the sensitivity of potential GO-based humidity sensors when compared to other materials. By exploiting the advantages of optical fibre sensors and the interesting humidity sensing characteristics of GO as a new material for

this application, in this chapter, a fibre optic sensor scheme that comprises a GO-coated LPG, which lies at the core of the essential sensing principle discussed in this thesis, is considered in detail. Achieving a stable coating was critically important to a successful sensor design and so GO flakes were immobilized on the silica fibre surface by functionalising the LPG surface area with polymerizable acrylate groups using 3-(trimethoxysilyl)propyl methacrylate, before coating the GO onto the fibre surface. The transmission spectra of this GO-coated LPG was examined, and this can then be used as the basis of the sensor scheme that was planned and is discussed. It is known that it is necessary to provide a correction for temperature excursions in the use of this probe for the measurement of RH, and thus, the temperature dependency of the coating on the LPG was also investigated and its performance analysed so that correction mechanisms can be used in a practical sensor design.

5.2 GO based Humidity Sensors

The term *humidity* is associated with water in the gaseous state, but it is usually associated with water vapour characteristics in the field of measurement. Moreover, *moisture* is a term that is often get interchanged with *humidity*, even though *moisture* refers to water in its liquid form (although it should be noted that water vapour often rapidly condenses to the liquid state, giving moisture in the form of water droplets, a phenomenon seen often in the natural world). When the actual definition of humidity is considered, which means water in a gaseous state: water vapour found in a mixture of gases behaves in accordance with the familiar gas laws. Therefore, according to Dalton's law [7], amount of pressure the water vapour exerts equates to the partial pressure of the water vapour components in the gas mixture considered. Moreover, saturated water pressure in a gaseous environment is a function of temperature. Based on this, Relative Humidity (RH) is defined as the ratio of actual water pressure to the saturated water pressure at a specific temperature and RH is a measurement of the amount of water vapour present in the environment. In the form of an equation, RH can be defined as follows.

$$Relative\ Humidity\ (RH) = \frac{P_w}{P_{ws}} \times 100\%$$

where P_w is the partial pressure of the water vapour and P_{ws} is the saturated water vapour pressure at that particular temperature. The sensor developed in this work has been designed to measure the value of RH in the environment, while compensating for the variations caused by the temperature excursions that may occur.

In recent times, graphene and GO have been researched and extensively studied as components of sensor systems, this arising from their extraordinarily high surface area to volume ratios and high surface chemistry, present due to their unique 2D nature. These very high surface to volume ratios provide a platform for the development of highly sensitive sensors for different engineering applications. When it comes to gas sensing, GO has advantages to consider over graphene itself, mainly due to the oxygen containing groups (the hydroxyl, epoxy and carboxylic groups) that it possess. Due to these oxygen containing groups, GO has *hydrophilic* properties in contrast to graphene, which is *hydrophobic* [8]. The hydrophilic properties of GO then allows it to be used for the detection of polar gases, such as water (vapour) molecules. Moreover, GO can be realised using low cost, simple procedures, such as Hummer's method, described in Chapter 4. Along with these favourable qualities mentioned above, GO further proves to be an excellent candidate for humidity sensing in particular due to its super-permeability (that arises due to the oxygen containing groups that it contains) to water molecules. Based on these excellent and desirable qualities of GO for applications in humidity sensing, many GO-based humidity sensors have been reported in literature. These are discussed briefly below in light of this work to create a new design of sensor.

5.2.1 GO based Electrical Humidity Sensors

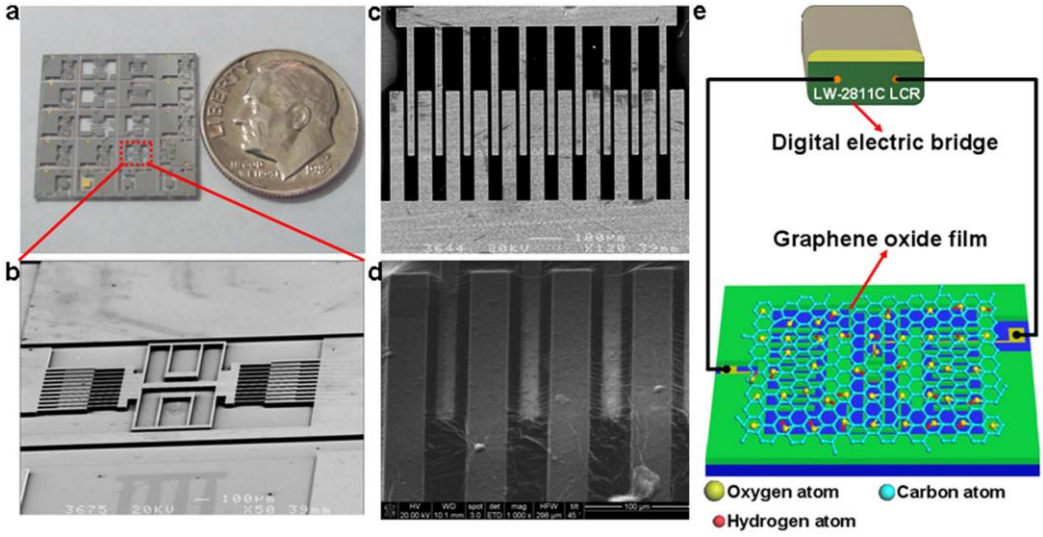

Fig 5. 1 Characterization of the sensor and humidity testing system (a) Digital photographs of the device (Reference is a 1 Dime US coin) (b) SEM image of the area set off by a red dashed line (c) SEM image of the interdigitated electrodes without GO (d) SEM image of interdigitated electrodes covered with G-O films. (e)Schematic diagram of the humidity testing system [9].

Bi et al. reported a capacitive based humidity sensor [9] based on a GO thin film, reporting a x10 times higher sensitivity and faster response time (less than 1/4 of that of the time reported) and a rapid recovery time (less than 1/2 of that of the time reported) when compared to other,

conventional capacitive-based humidity sensors. The authors used a drop casting method to deposit the thin GO layer on top of the electrodes that act as the capacitors.

Chemical groups present in the GO single layer sheets make the GO electrically insulating and they have used this quality of the GO layer to develop the GO based humidity sensor, shown in Fig. 5.1.Variations in the capacitance and the sensitivity of the GO based humidity sensor reported is shown in Fig. 5.2, operating in the RH range from 15% to 95%. The adsorption of water molecules on the GO surface caused the capacitance of the sensing electrodes to increase and this phenomenon acts as the sensing principle of this sensor scheme.

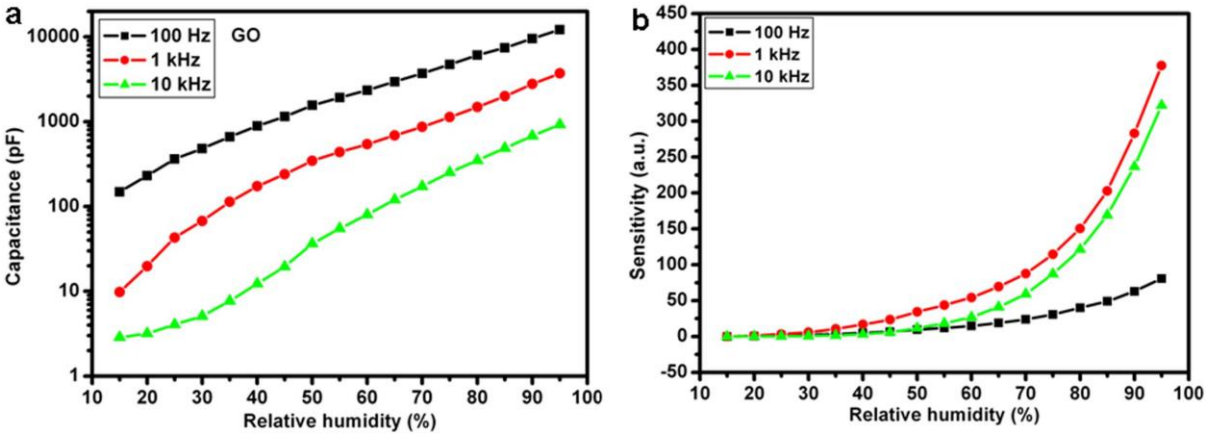

Fig 5. 2 Capacitance and sensitivity versus RH at 100 Hz, 1 kHz, and 10 kHz (a) Output capacitances of sensors as a function of RH (b) Defined sensitivity as a function of RH [9].

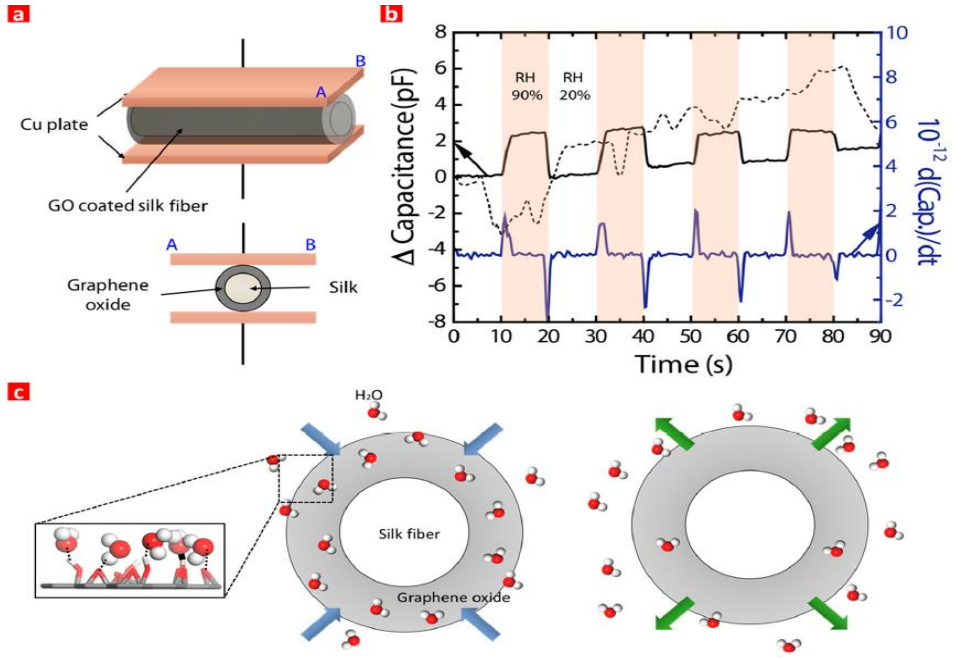

Fig 5. 3 (a) Schematic image of capacitive humidity sensor where GO coated SF has been implemented. The average diameter of SF is 0.17 cm (b) The capacitance and its derivative curve of the sensor when the humidity changed between 20% RH and 90% RH. The dot represents the intact silk between the two Cu plates (c) Schematic image of H_2O absorption (RH 90%) and desorption (RH 20%) characteristics on GO coated SF [10].

Han et al. also reported a cylindrical silk fibre (SF)-based GO capacitive humidity sensor in the literature [10]. They used an electrostatic self-assembly of GO sheets (negatively charged GO in the solution get attracted to the positively charged SF surface via electrostatic force without any help from adhesive intermediates) to coat a GO thin film on the SF surface. However, the calibration data were sparse as they only reported on the performance with two humidity levels, 20% RH and 90%RH to demonstrate the sensor performance. The design and implementation of the sensor is illustrated in Fig. 5.3.

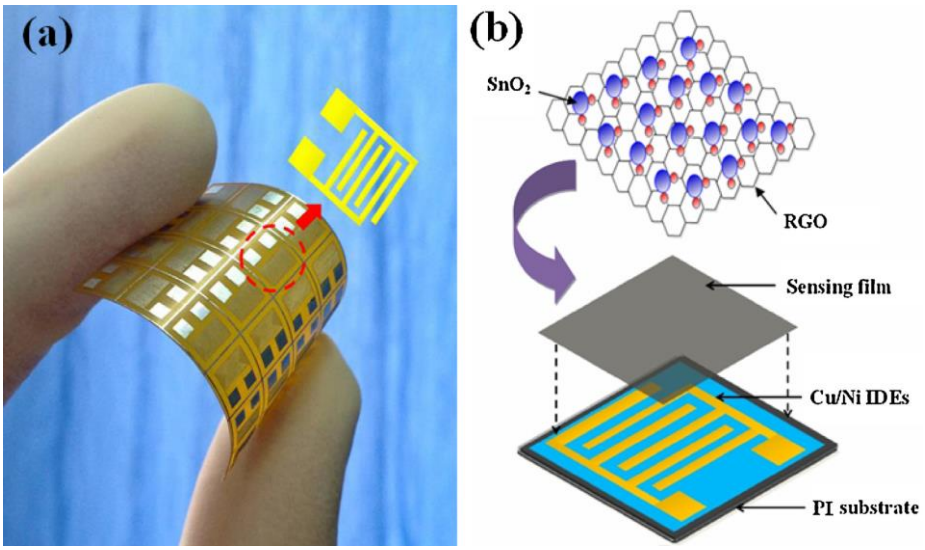

Fig 5. 4 (a) Optical image of sensor array on a flexible PI substrate. (b) Schematic illustration of as-fabricated sensor prototype [11].

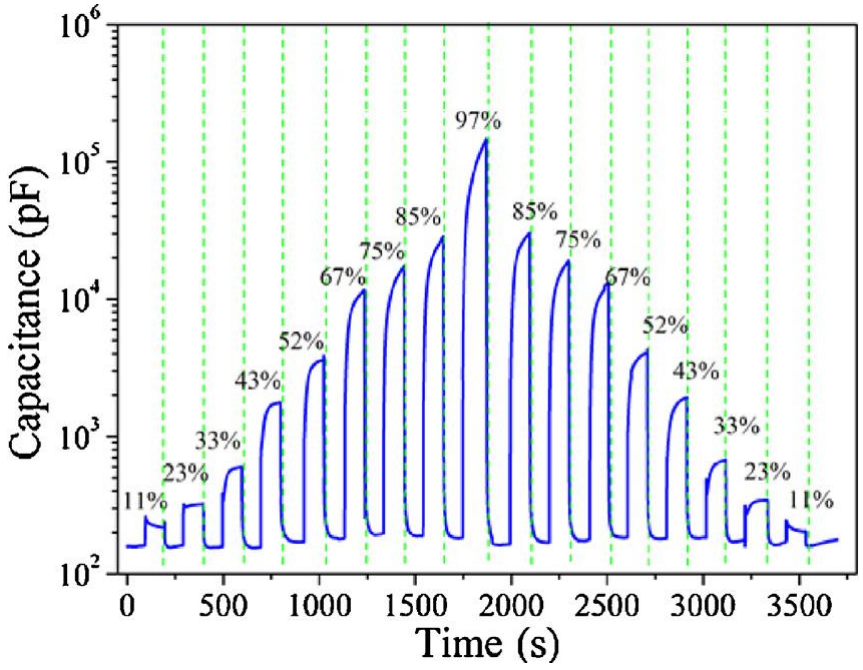

Fig 5. 5 Capacitance response of the SnO_2/RGO hybrid composite sensor under switching RH at 10 kHz [11].

Another type of GO-based humidity sensor has been reported by Zhang et al. in the literature [11] where their sensor is based on tin oxide (SnO_2)/rGO nanocomposite film. The humidity sensor has been fabricated on a polyamide (PI) substrate with microelectrodes by using a facile one-step hydrothermal route. Sensor prototype can be seen in Fig. 5.4. They have investigated the capacitive response of the flexible SnO_2 decorated rGO nano-hybrid film under different humidity conditions at room temperature and the performance of the sensor developed as a result is illustrated in Fig. 5.4. The capacitive response of the SnO_2/rGO based humidity sensor reported is shown in Fig. 5.5 over the RH range from 11% RH to 97%RH.

There are a number of other GO-based humidity sensors reported in the literature, e.g. [12] and [13], based on a similar capactive and resistance based approach. All these sensors exploit the high adsoprtion of water molecules by GO thin films and the intrinsic insulation of GO, especially from the adsorption of water molecules, to reflect in the eletronic parameters of capacitance and resistance a viable approach to develop a suite of GO-based humidity sensors.

5.2.3 GO based Optical Humidity Sensors

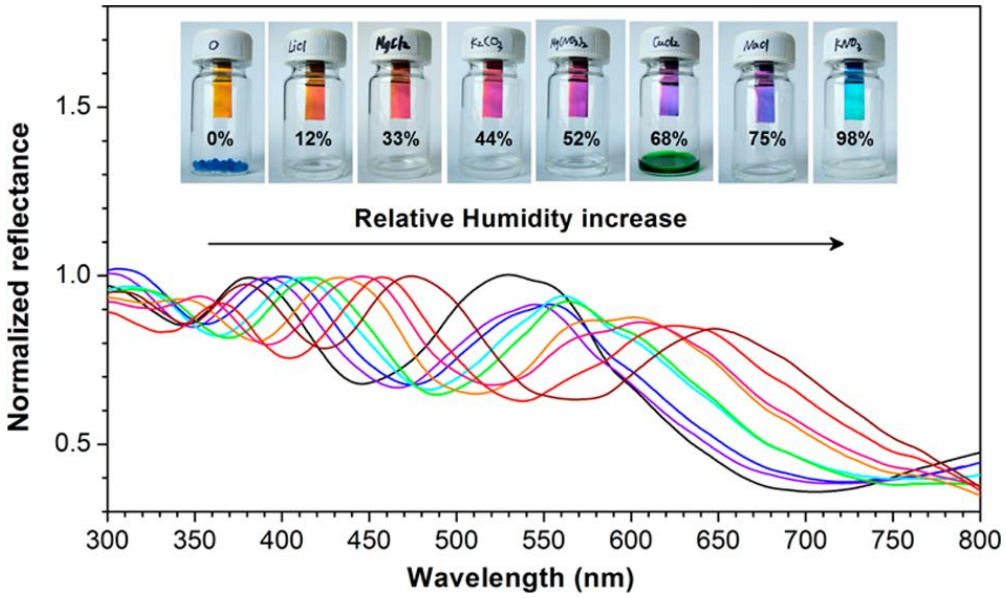

Fig 5. 6 Colorimetric GO based humidity sensor [6].

Apart from the above discussed resistance and capacitance based approach, there are several other GO-based humidity sensors reported, taking advantage of the optical properties of GO thin films.

A GO thin film-based colorimetric humidity sensor has been reported by Chi et al. [6]. They have shown that different thin film thicknesses of GO reflect different wavelengths of the visible spectrum, this changing with the relative humidity present. A dip coating technique has

been used to fabricate the GO thin film probes reported and the results of this study can be seen in Fig. 5.6, illustrating the performance over the RH range from 0%RH to 98%RH. They have also reported that the GO thin films exhibit 'ultrafast' sensing to moisture (a response within 250 ms) because of the unique atomic-level thickness and the super-permeability of GO sheets used.

Another all-optical GO-based humidity sensor has been reported by Lim et al. [14]. They have drop-cast a GO thin film on a SU8 polymer channel waveguide to develop the sensor shown in Fig. 5.7. The developed sensor is based on the changes in the TE-mode absorption of GO with varying RH levels. The transmission of the sensor shows a linear response, with a calibration factor of 0.553 dB/%RH, measured over the range 60%RH to 100%RH.

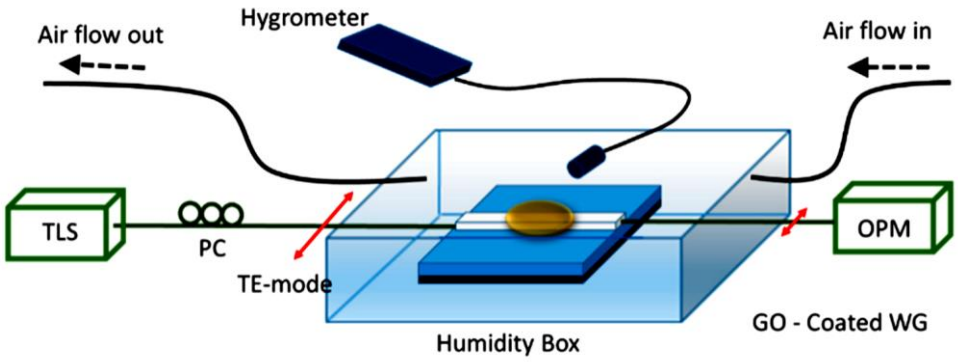

Fig 5. 7 GO coated SU8 polymer waveguide in a humidity measurement setup [14].

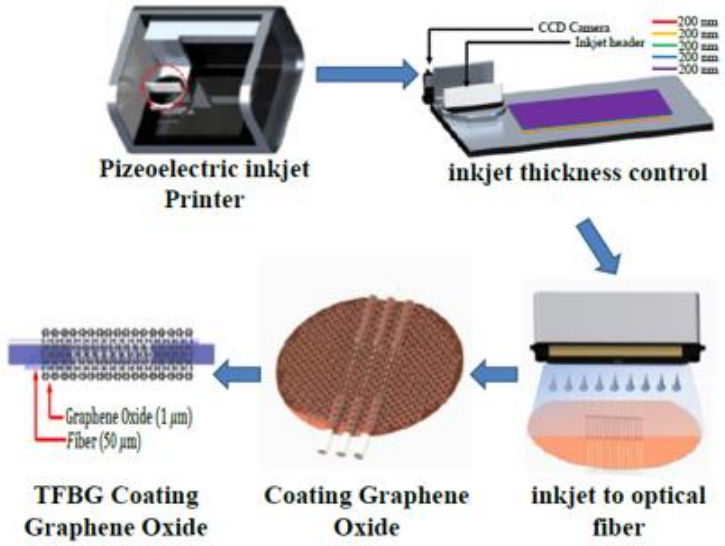

Fig 5. 8 Piezoelectric inkjet technology used to coat the fibre with GO [15].

Chiu et al. developed a GO-fibre grating based humidity sensor [15] by depositing a GO thin layer on top of a Tilted Fibre Bragg Grating (TFBG) by the use of a piezoelectric inkjet

technology. They have used in this work the tuneability of the RI of GO under varying humidity conditions (which leads to TFBG spectrum changes), as the basis of the sensor developed. The reported sensitivity is 0.01 nm/%RH with a linearity of 0.996. A schematic of the piezoelectric inkjet technology used to fabricate the sensor is illustrated in Fig. 5.8.

A fibre optic-based humidity sensor has been reported by Wang et al. [16]. Here, a GO/PVA (polyvinyl alcohol) composite film has been coated on a fibre surface to form the basis of this in-fibre MZI based fibre optic humidity sensor.

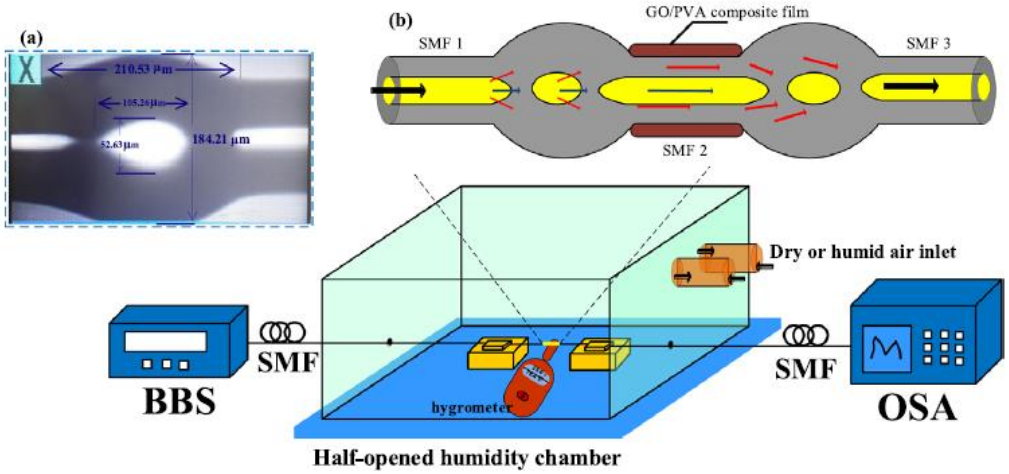

Fig 5. 9 Schematic diagram of the experimental setup (a) structure of the waist-enlarged taper, and (b) the partially enlarged drawing of the sensing head [16].

The MZI comprises two waist-enlarged tapers with the length between two tapers, at 20 mm. The GO/PVA composite film absorbs water molecules to change the effective RI of the higher order cladding modes, which results in changes of the interference pattern of the MZI sensor probe developed and illustrated in Fig. 5.9. A sensitivity of 0.193 dB/%RH has been achieved with a linear correlation coefficient of 99%, over the humidity range 25%RH to 80%RH, by the use of this GO/PVA-composite based fibre optic humidity sensor scheme.

Based on these GO-based humidity sensors reported, it is evident that GO shows excellent potential and characteristics when it comes to the development of humidity sensors. Most of the humidity sensors reported so far are based on electronic techniques and they have shown important performance features, such as a reduced response time and increased sensitivity. However, in applications like structural health monitoring, where it is required to have the sensors in very harsh environments (for example in sewers to monitor the humidity level, as RH is directly related to corrosion levels and thus affects the potential integrity of the structure), these electronic sensors will not have the capability to have a long operational lifetime, as was shown by Alwis et al. [1]. Optical fibre sensors were suggested in that work as an important

way to solve this problem of achieving a long operational use under harsh conditions and arising from that need, a key driver of this work has been to develop a GO-based optical fibre sensor scheme with good performance which can be compared with fibre optic humidity sensors using other humidity responsive materials. The approach taken has been to exploit the excellent humidity sensing characteristics of GO and the advantages of optical fibres shown in structural health monitoring as the basis of an optical fibre RH sensor scheme. As shown above, several GO-based humidity sensors designs have been reported, taking advantage of the optical properties of GO but the number of reported designs is very limited, compared to the much wider range of GO-based electronic sensors reported. As such, in an attempt to bridge this gap and exploit the positive characteristics of the GO material, a thin film-coated LPG-based fibre optic humidity sensor has been developed in this work. The sensing principle, followed by the fabrication steps and a review of the performance characteristics of the sensor probe developed are discussed in detail in the next part of this chapter.

5.3 Sensing Principle

As mentioned in the introduction, the GO-coated LPG based RH sensor discussed in this chapter is based on the broad sensing principle discussed in Chapter 4 for the development of an external RI monitoring system but applied to RH sensing using the approach discussed. Due to the RI modulations present in LPGs, light propagating in the core interferes with some of the co-propagating cladding modes and the associated resonance bands can be seen in the transmission spectra. These resonance bands depend on (and change with) the effective RI of the propagating medium, which comprises the known RI of the cladding, as well as the RI of the material coated on the fibre that surrounds the cladding, which is GO. In the specific RH sensor discussed in this chapter, due to the unique quality of super-permeability to water molecules and water adsorption due to oxygen containing groups, the GO layer that forms the basis of the sensor changes its optical properties (such as propagating constants of cladding order modes and the RI) when the GO thin layer coated on the fibre is in contact with moisture and these effects are reflected in the transmission spectra of the GO-coated LPG sensor probe created. The equations which relate these changes in the transmission spectra (centre wavelength of the resonance loss bands and the minimum intensity) of a GO-coated LPG were discussed in detail in Chapter 4 and provide the theoretical background to the work discussed here.

5.4 Fabrication of the Sensor Probe

A B/Ge co-doped photosensitive fibre (purchased from Fibrecore, UK) was exposed to the light from a 248-nm KrF excimer laser with a pulse energy of 10 mJ and a pulse frequency of 175 Hz through a metal amplitude mask with a period of 400 µm to create the 25 mm long LPG that forms the basis of the sensor. After the inscription process, the LPG was annealed at 100℃ for 2.5 hours to stabilize its optical properties. The transmission spectrum of the LPG thus fabricated is illustrated in Fig. 5.10.

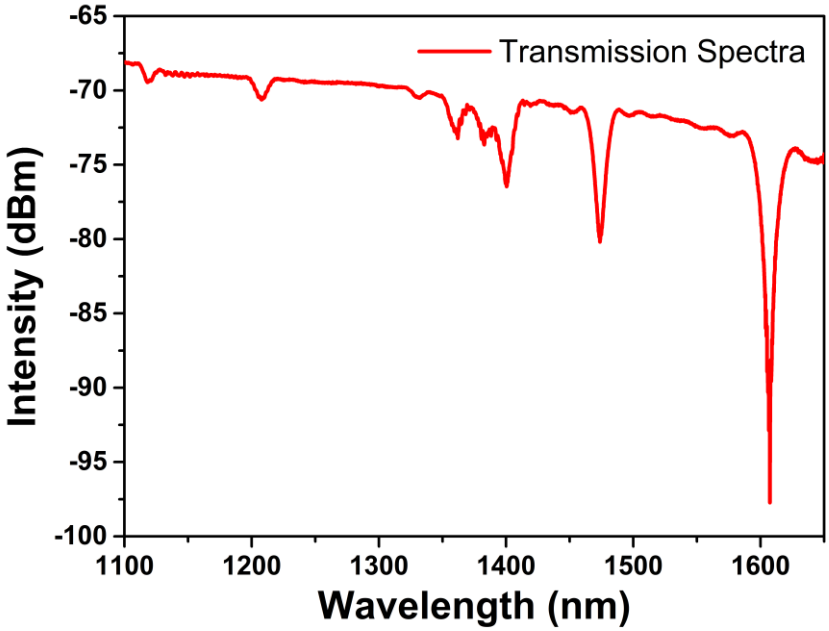

Fig 5. 10 Transmission spectrum of the LPG inscribed with an amplitude mask of 400 µm

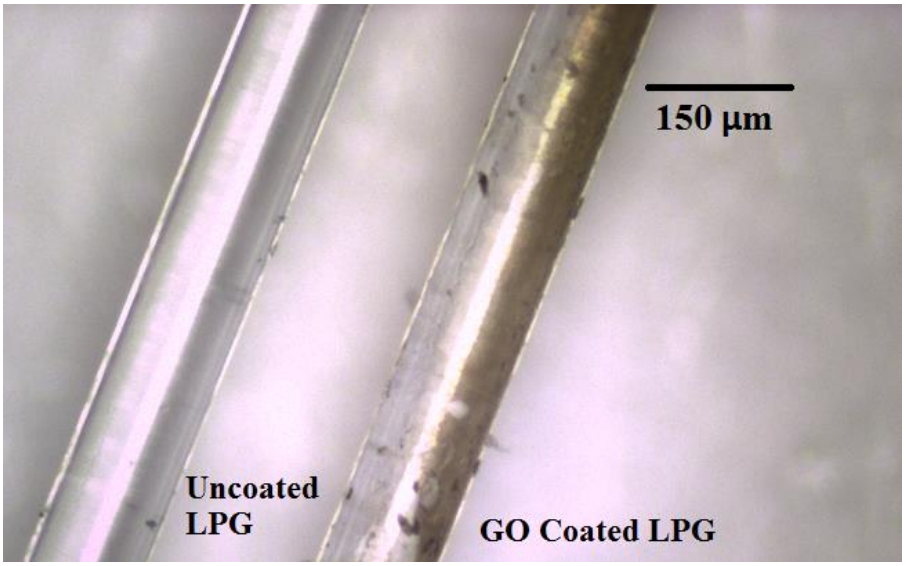

Fig 5. 11 Microscopic image of GO-coated LPG (right) and a bare, uncoated LPG (left).

0.5 mg of GO flakes, synthesised as described in Chapter 4, was dissolved in 10 mL of deionized (DI) water to prepare the GO aqueous dispersion. After stirring for 12 hours, the GO

aqueous dispersion was sonicated for 1 hour before being centrifuged for another 20 minutes at 3000 rpm. This centrifugation process was carried out three times and the supernatant was taken to achieve a high percentage of single layered GO flakes in the solution.

Before coating the fibre, the LPG was immersed in a H_2SO_4:H_2O_2 (7:3) solution at room temperature for 1 hour, followed by being washed thoroughly in an ultrasonic bath with distilled water and dried at 100 ℃ for half- an-hour to clean the bare coating surface and leave it with exposed hydroxyl groups, which facilitate bonding of a silane agent. Afterwards, the LPG surface was functionalized by immersing in a 3-(trimethoxysilyl)propyl methacrylate solution for 30 minutes, followed by drying at 70 ℃ for half an hour to stabilize the immobilized silane layer. GO was then coated on the functionalized LPG surface by immersing it in 200 µL of prepared GO aqueous dispersion and drying at 45 ℃. Deposition of GO sheets on the LPG surface occurs due to the π-π non-covalent interactions that take place between the π bonds present at the end of 3-(trimethoxysilyl)propyl methacrylate groups and those of the GO sheets. Immersing in the GO aqueous dispersion was repeated three times to achieve a brownish black coloured coating, which is clearly visible in the microscopic image (together with a bare LPG for cross-comparison) shown in Fig. 5.11. By comparing the microscopic images taken, an approximation of the coating thickness was made, estimated to be ~1.5 µm. The increase in coating thickness compared to that of the sensors fabricated in Chapter 4 can be attributed to the additional silane layer present (methacrylate layer). The transmission spectrum of the LPG, obtained both before and after coating, is illustrated in Fig. 5.12.

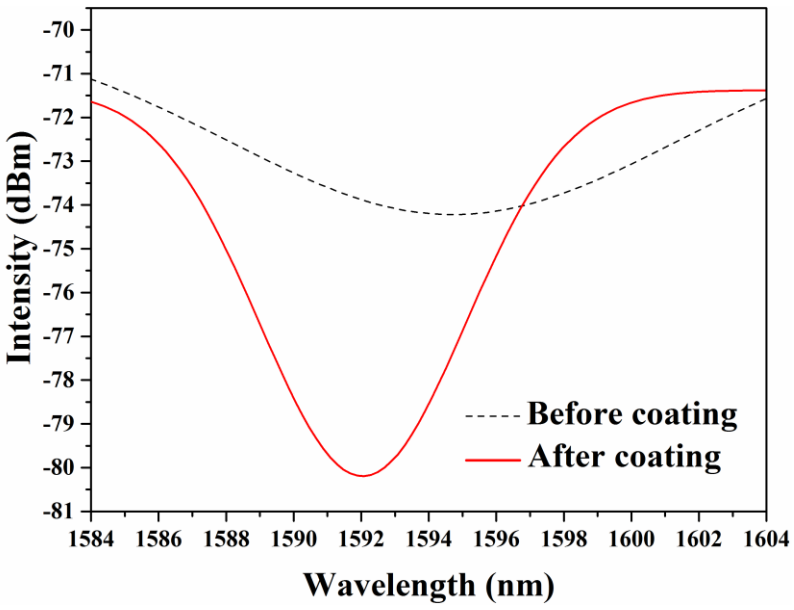

Fig 5. 12 Transmission spectra of the LPG before and after coating, in the wavelength region 1584 nm to 1604 nm.

These results indicated that the GO sheets prepared were successfully coated on the LPG surface in this key fabrication step for the probe.

5.5 Experimental Setup for Evaluating the Humidity Sensitivity

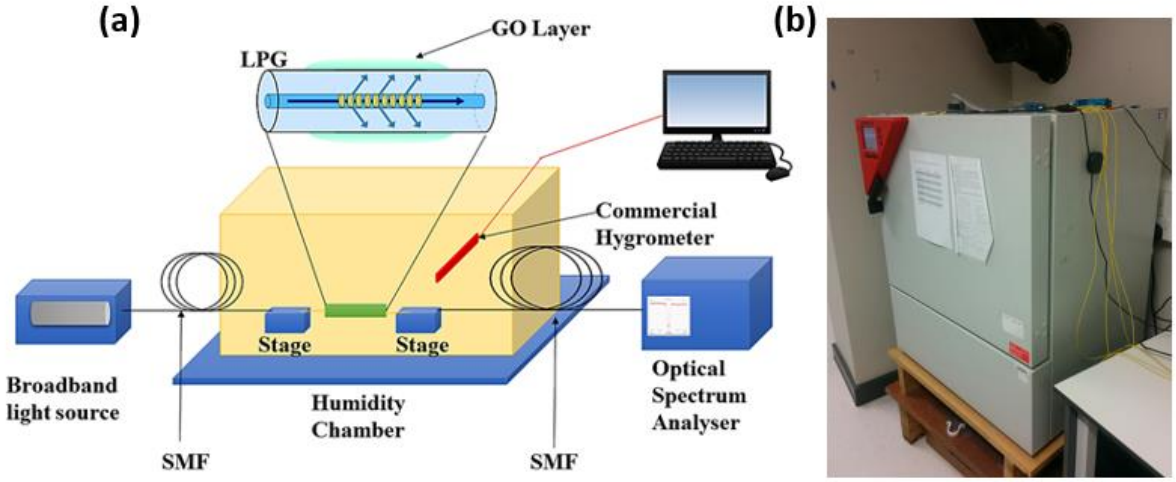

Fig 5. 13 (a) Experimental setup used for humidity sensing (b) Humidity Chamber.

Fig. 5.13 illustrates the experimental setup used for evaluation of the sensor performance as a function of humidity (40%RH to 95%RH) and temperature (25 ℃ to 70 ℃) changes. To do so, one end of the GO-coated LPG was connected (via SMF-Single Mode Fibre) to a broadband light source (OceanOptics LS1) and the other connected to an Optical Spectrum Analyzer (Yogokawa AQ6370C) to record the transmission spectra.

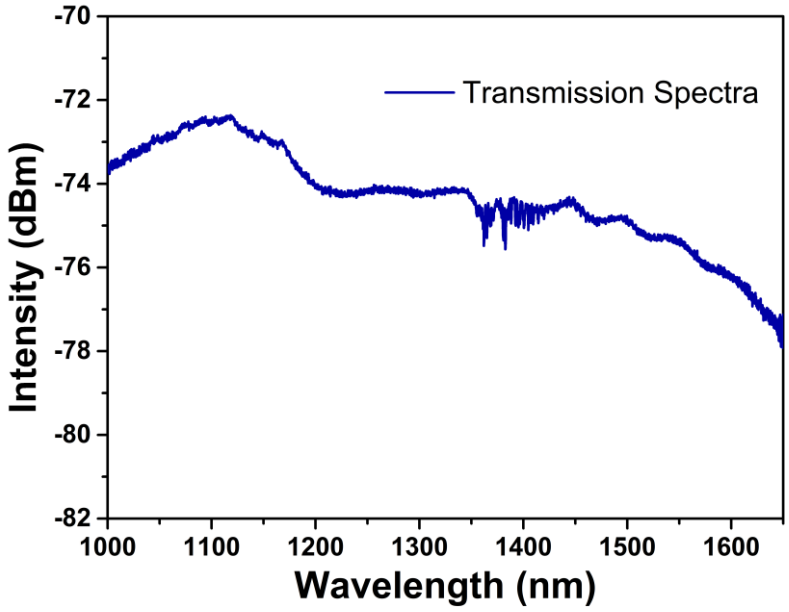

Fig 5. 14 Spectrum of the LS1 Ocean Optics broadband light source.

The spectrum of the OceanOptics LS1 halogen broadband source in the wavelength region of 1000 nm to 1650 nm is shown in Fig. 5.14.

The spectrometer offers a wavelength measurement range from 600 nm to 1700 nm and a spectral resolution of 0.5 nm. The GO-coated LPG was mounted on two stages (as illustrated in Fig. 5.13 (a)) inside the humidity chamber (Binder KBF 115, shown in Fig. 5.13 (b)) to minimize the errors caused by external strain and bending effects. The humidity chamber was used as it was capable of accurate control of the relative humidity over the range from 5%RH to 95%RH, at a particular (and known) temperature value (25 ℃ to 100 ℃). The system was allowed to stabilize before each transmission spectrum was recorded at each particular humidity level chosen. A commercial hygrometer was used to cross-calibrate the sensors to shown performance, in terms of temperature and relative humidity.

5.6 Experimental Results and Analysis

5.6.1 Humidity Response

Before monitoring the humidity-sensitive response of the GO-coated LPG sensor probe, the humidity response of a bare LPG was recorded for cross-comparison purposes. The RH response of a bare LPG, fabricated using the same process mentioned above, is illustrated in Fig. 5.15.

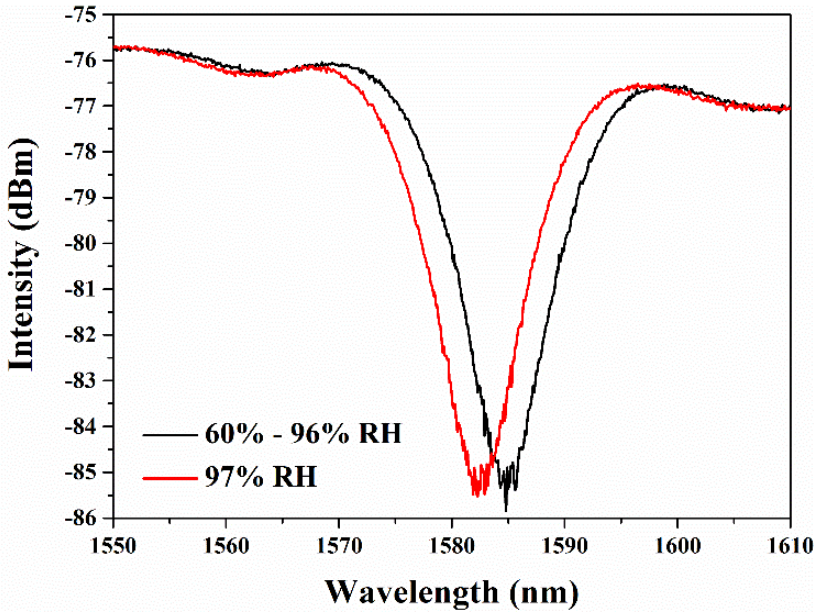

Fig 5. 15 Humidity response of a bare LPG used for cross-comparison.

For this experiment, the same laboratory setup was used (as illustrated in Fig. 5.13), but this time, replacing the GO-coated LPG with a bare LPG. Initially, the temperature was fixed at 25℃. There was not any noticeable change observed in the transmission spectrum until the RH

level reached ~97%, at which point, a slight change in the resonance band intensity and wavelength was seen, as shown in Fig. 5.15. At very high humidity levels (>97% RH), water droplets can become deposited on the fibre surface, which leads to a measurement error due to slight strain being applied to the LPG. The wavelength shift observed in this test can therefore be explained by this effect.

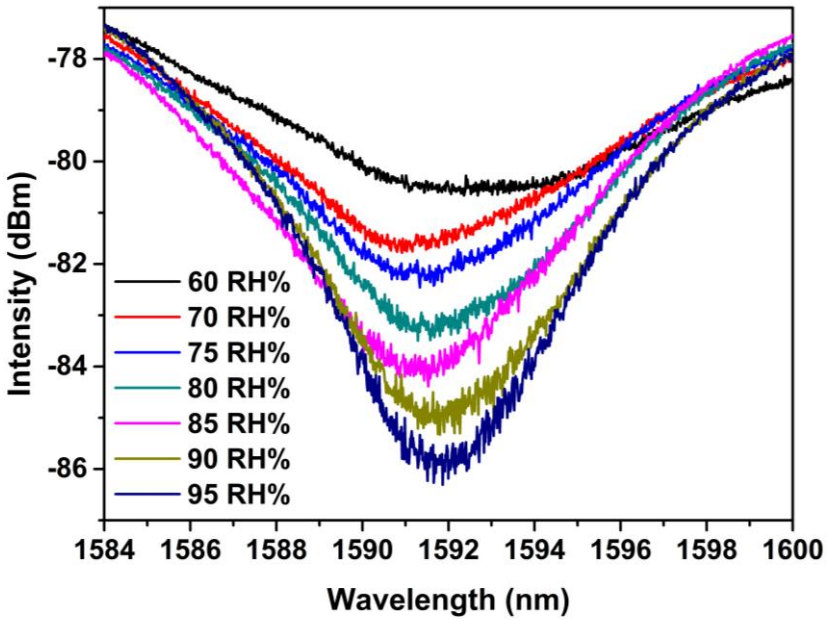

Fig 5. 16 Transmission spectra of GO coated LPG at different relative humidity levels.

To observe the humidity response of the GO-coated LPG sensor, the temperature of the humidity chamber was initially fixed at 25 ℃ and the relative humidity level was changed over the range from 20%RH to 95%RH. Fig. 5.16 illustrates the transmission spectra of the resonance band of the GO-coated LPG, monitored at a centre wavelength of 1592 nm, for various different levels of humidity in the test chamber. A minimal intensity or centre wavelength shift was observed for humidity levels lower than 60%, but beyond that, it was clearly observed that with increasing humidity, the intensity of the resonance band increased, with an accompanying slight shift of the centre wavelength. This observed active response range of 60%RH to 95%RH corresponds well with the performance of other carbon nanomaterials-based humidity sensors, reported in the literature [14, 21, 23-25]. The unique characteristic of the GO used in this work is however, that by contrast, it is super-permeable to water molecules as discussed in the first part of this chapter. When moisture molecules are present inside the GO material, a change in the optical properties of the GO layer (such as is reflected in the RI and coupling coefficient changes) is induced, and hence the change of centre

wavelength and the intensity of the resonance loss band. The adsorption of moisture on GO thin films can be characterised by two processes [9]. These two processes are illustrated in Fig. 5.17.

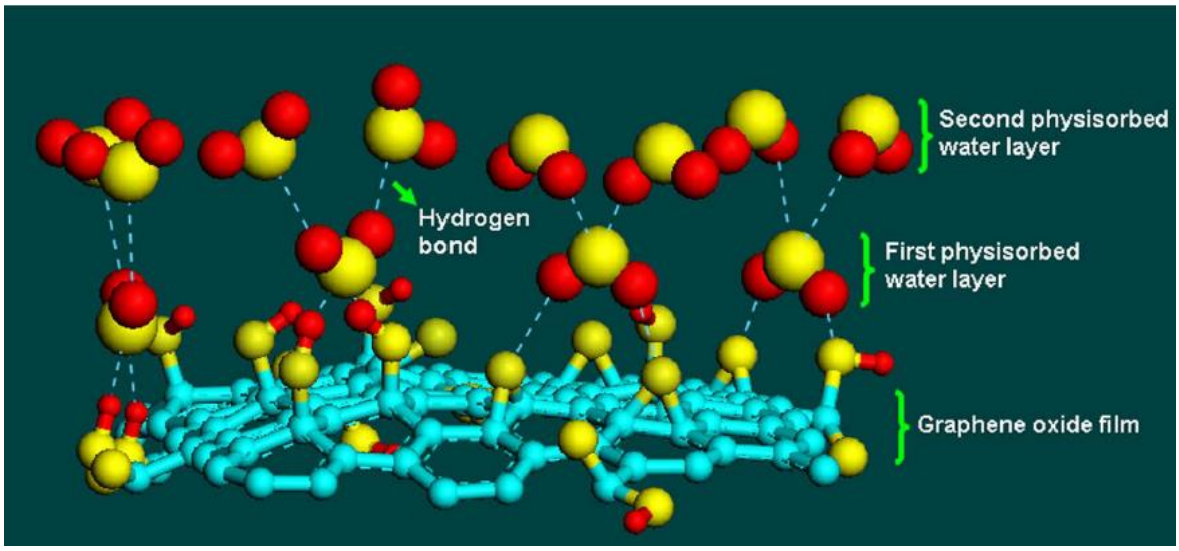

Fig 5. 17 Schematic of humidity sensing at GO thin films [9].

At lower RH values, water molecules get physiosorbed to the available sites on the GO surface, which are created by the oxygen containing groups that it possess, by use of double hydrogen bonds. In this region, water molecules get attached to the GO surface very strongly and requires more energy to break these double hydrogen bonds to move around freely. Arguably, the minimal response of the fabricated GO coated LPG sensor seen until the 60%RH could be a result of this first process of water adsorption on GO thin films, as a smaller number of water molecules get attached to the GO surface compared with the second GO adsorption process described below. When the RH level increases, water molecules are physiosorbed via single hydrogen bonds to the hydroxyl groups now present on the GO surface as a result of the first layer of water molecules. In this region, water molecules are more mobile and behave much like bulk liquid. The rapid response seen in the developed sensor at high RH values above 60% may be a result of this second physisorption process.

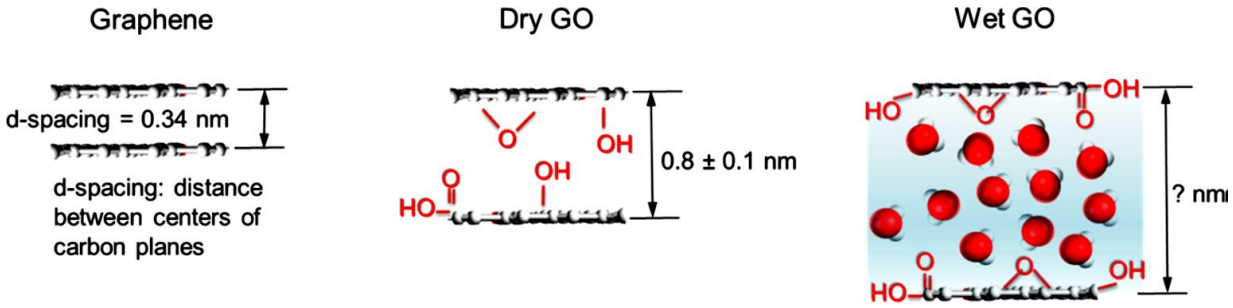

Fig 5. 18 Swelling of GO thin film layers in the presence of water molecules [17].

This adsorption process causes GO to change its optical properties such as its RI and propagation constants of higher order cladding modes.

Another phenomenon that causes GO to change its optical properties is, change in its layer thickness in the presence of water, as shown by Zheng et al. in [17]. As can be seen in Fig. 5.18, they have shown that d-spacing between two GO planes increases when a GO thin film is in contact with water and this is caused by the super-permeability of GO as discussed in the first part of this chapter. It is extremely difficult to determine which of these phenomena causes the optical response (with the available facilities) recorded with the GO coated LPG based humidity sensor discussed in this work but it can be concluded that the results obtained have been influenced by a combination of these effects.

Fig. 5.19 depicts the intensity change of the resonance band centred at 1592 nm, for varying RH levels. The minimum intensities of -80.5 dBm and -85.7 dBm were recorded at 60%RH and 95%RH, respectively. A good linear correlation between the RH level and the resonance band intensity was observed with a linear correlation coefficient of 0.980. This leads to a RH sensitivity of 0.15 dB/%RH over the range of 60%RH to 95%RH at 25 ℃.

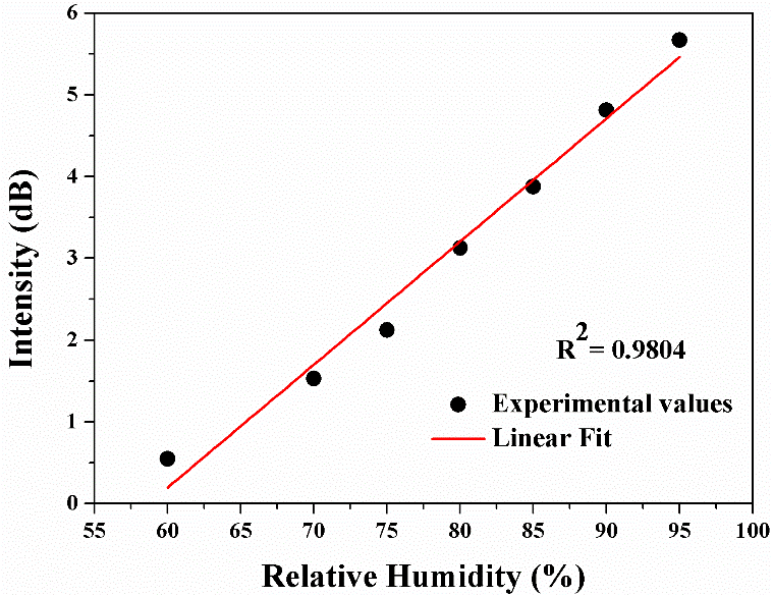

Fig 5. 19 Intensity variations of the resonance band centred at 1592 nm at different RH levels.

Comparing the response of the bare LPG (illustrated in Fig. 5.15, which recorded a negligible intensity variation over a relative humidity range of 60% to 97%), with the response of the GO-coated LPG, tested over the humidity range recorded in Fig. 5.16, it is evident that the use of the GO coating has considerably improved the sensitivity of the LPG-based probe in these tests performed under varying RH conditions.

5.5.2 Temperature Response

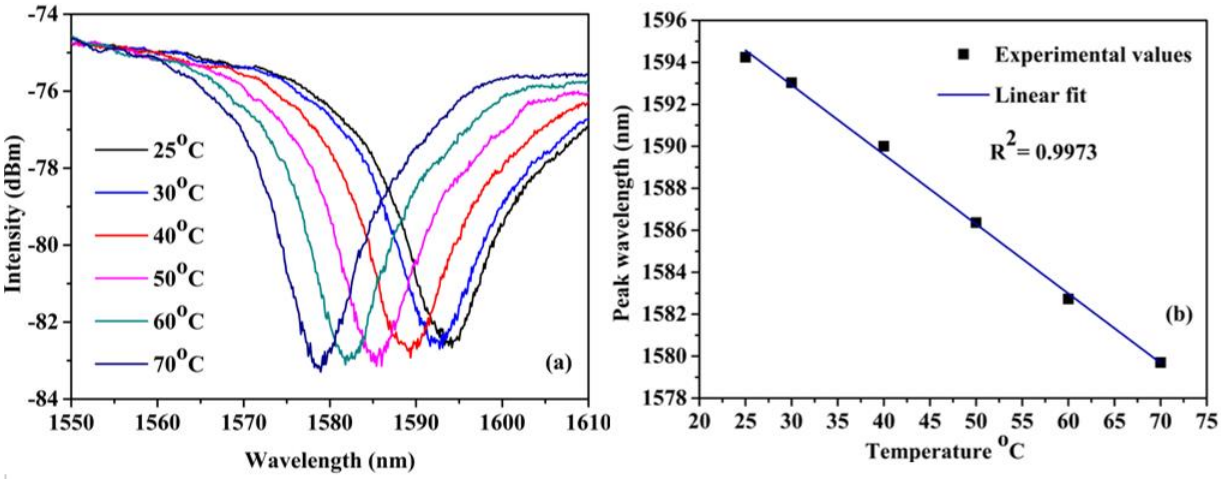

Fig 5. 20 (a) Transmission spectra of GO coated LPG at different temperatures (b) Centre wavelength of the resonance band as a function of temperature.

It is well known that temperature will have an effect on the response of the LPGs in the fibre (as discussed in detail in Chapter 2) and this combines with the effect due to humidity on the coating. Thus, it is necessary to obtain a profile of the temperature effect alone, undertaken at constant relative humidity, to allow for any cross-sensitivity to be removed. Therefore, the effect of temperature on the sensor probe further was investigated (as a correction for thermal changes may be needed in practical applications of the sensor) by fixing the relative humidity level at 45%RH and changing the temperature from 25 ℃ to 70 ℃ Fig. 5.20 (a) illustrates the transmission spectra, showing the resonance band change at various discrete temperatures, while Fig.5.20 (b) depicts the centre wavelength shift of the same resonance band over the same temperature range from 25 ℃ to 70 ℃. Centre wavelengths of 1594.2 nm and 1579.7 nm were recorded at 25 ℃ and 70 ℃, respectively, showing the spectral range of the device. A very good linear correlation between the temperature change and the centre wavelength shift was observed, with a temperature sensitivity of 0.32 nm/℃ and a linear correlation coefficient of 0.997. A slight change of the resonance band intensity (0.6 dB) was observed when the temperature was increased from 25 ℃ to 70 ℃.

By comparison, when an uncoated LPG, fabricated using the same setup (and the same amplitude mask), was exposed to increasing temperature from 25 ℃ to 70 ℃, a similar wavelength shift was observed (but without the small change in the resonance band intensity seen). The temperature change induces a variation in the grating period (by changing its length), and thus creating a shift in the resonance wavelength. The material, in this case GO, also contributes to the resonance band characteristics by changing its effective RI as a result of the temperature changes. The change in the resonance band intensity, which was observed for

the GO-coated LPG (but not in the uncoated LPG), can thus be noted. The centre wavelength shift, recorded as a function of temperature changes, can be used for effective temperature measurement and, as needed, for temperature compensation of the humidity sensor, where humidity is measured under varying temperature conditions. The ability to measure both parameters (humidity and temperature) configured this way in the same sensor probe is an advantage of this approach over fibre optic humidity sensors that require two gratings [1] – in that way to compensate for the error caused by varying temperature conditions.

Based on the obtained results, the performance of the sensor developed can be compared with the performance of other sensors using similar carbon nanomaterials. A wide variety of optical humidity sensor designs that use a variety of sensing materials have been reported and Table 5.1 summarizes the characteristics of these sensors reported for ease of cross comparison.

Table 5. 1 Comparison between the responses of optical RH sensors coated with different material

Structure	Sensing Material	RH range	Sensitivity	Reference and Remarks
Carbon nanomaterial-based optical humidity sensors				
TFBG	GO	10 – 80%	0.129 dB/%RH	[18]
In Fibre - MZI	GO/PVA composite	25 – 80%	0.193dB/%RH	[16]
Etched FBG	Carbon Nanotubes	20 – 90%	~31 pm/%RH	[19]
Side Polished Fibre	GO	58.2 – 92.5%	0.427 dB/%RH	[20] Temperature response recorded
TFBG	GO	20 – 80%	0.01 nm/%RH	[15] Temperature response recorded
SU8 Waveguide	rGO and TiO2	35 – 95%	~0.47dB/%RH	[21]
SU8 Waveguide	GO	60 - 100%	0.553 dB/% RH	[14]
Side Polished Fibre	rGO	70 – 95%	0.31 dB/%RH	[22]
Hollow Core Fibre	rGO	60 – 90%	0.22 dB/%RH	[23]
In Fibre – MZI	GO	60 – 77%	0.349 dB/%RH	[24]
LPG	GO	60 – 95%	0.15 dB /%RH	This work - temperature response recorded
Other sensing materials based optical fibre humidity sensors				
No core fibre	HEC/PVDF Hydrogel	40 – 90%	0.196 dB/RH%	[25]
Nonadiabatic Tapered Fibre	PDDA/Poly R-478	75 – 100%	0.52 dB/RH%	[26]
Side Polished Fibre	WS2	35%–85%	0.121 dB/RH%	[27]
U-Shaped PCS Fibre	Phenol red Doped PMMA	20%–80%	0.15 dB/RH%	[28]
Tapered Fibre	Agarose Gel	30%–80%	0.13 dB/RH%	[29]
FBG	PI	15 – 95%	6 pm/%RH	[1]
LPG	PI	20 – 85%	100 pm/%RH	[30]
LPG	Hydrogel	38.9 - 100%	0.2 nm/%RH	[31]
LPG	Gelatin	90-99%RH	0.833%RH/dB	[32]

As can be seen from Table 5.1, most of the GO and other carbon nanomaterial-based humidity sensors have shown their best sensitivity in the higher RH range above 60% RH. This agrees well with the recorded results of the GO-coated LPG based sensor developed. As discussed above, the RH level of the environment is a function of temperature and as such, one major requirement of any humidity sensor is to have the ability of temperature compensation. However, from the sensor data recorded in Table 5.1, only two carbon nanomaterial-based humidity sensors have presented the temperature response required to compensate for temperature excursions in the environment, along with the GO-coated LPG-based humidity sensor developed in this work. However, it should be noted that comprehensive treatment of temperature compensation of the developed GO coated LPG based RH sensor would require a much more detailed temperature response analysis in the RH sensitive range of above 60% RH. Moreover, the LPG is the simplest and most cost-effective optical structure recorded, among the various GO-based optical humidity sensors. One of the aims and objectives of this research has been to develop a humidity sensor that can be applied in structural health monitoring and this objective has been achieved by developing the GO-coated LPG based humidity sensor discussed, showing a performance which compares well with the other GO-based humidity sensors reported.

The sensor proposed can be developed further to achieve a better performance by optimizing the coating thickness, and thus to achieve the highest sensitivity. In the previous chapter it was shown that there is an optimal thickness for a coating material that has a greater RI than that of cladding and especially, carbon nanomaterials, as shown also in the literature [33]. Thus, with an optimization of coating thickness, important changes in the wavelength shift can also be achieved along with the intensity shift of the resonance bands, allowing for the development of dual parameter sensors. Further refinement can come from the variation of the period of the grating, to achieve a higher sensitivity, as higher order modes are bound to be more sensitive to the external RI. This approach will be discussed further in the next chapter, which considers the development of a GO-coated dual peak resonance LPG-based BSA concentration measurement sensor, in which a higher sensitivity has been achieved by exploiting the dispersion turning point of the LPGs, so as to exploit the increased sensitivities of higher order cladding modes. Furthermore, knowing that GO could be reduced to achieve the characteristics of graphene by applying a chemical or thermal reduction process, in that way the use of reduced GO could add another dimension to this GO-coated LPG-based optical fibre sensor design discussed.

5.6 Summary

A novel approach to the design of several humidity sensor probes has been presented, these being based on a GO-coated LPG. The sensor probe operates by exploiting the super-permeability of the GO used to water molecules, and its dependency on the thermo-optic properties in the presence of such water molecules. The fabrication of such probes has been made convenient by using an improved Hummer's method for the GO synthesis. 3-(trimethoxysilyl)propyl methacrylate was coated on the LPG surface to immobilize coated GO flakes to achieve a stable sensor performance. A satisfactory linear response for the humidity sensor was recorded over the 60%RH to 95%RH range, with a sensitivity of 0.15 dB / %RH at 25 ℃. A good linear correlation between temperature and the centre wavelength shift was also observed for a temperature range of 25 ℃ to 70 ℃. The sensor performed with a consistent repeatability and stability. A cross comparison was also made with other graphene nanomaterials based optical humidity sensors reported.

In conclusion, based on the promising results obtained, the work shown has indicated that GO is a promising sensing material. The research has shown that GO is a very attractive sensing material for use in optical fibre humidity sensors. In the next chapter, a method for improving the sensitivity of GO-coated LPG-based optical fibre sensors will be discussed, illustrating a GO-coated dual resonance peak LPG-based BSA concentration measurement sensor.

5.7 References

[1] Alwis L S M, Bustamante H, Roth B, Bremer K, Sun T and Grattan K T V, "Evaluation of the Durability and Performance of FBG-Based Sensors for Monitoring Moisture in an Aggressive Gaseous Waste Sewer Environment," Journal of Lightwave Technology, 35, 16, 3380-3386, 2017.

[2] Alwis L, Sun T and Grattan K T V, "Design and performance evaluation of polyvinyl alcohol/polyimide coated optical fibre grating-based humidity sensors," Review of Scientific Instruments, 84, 2013.

[3] John S, Michael T, Michael B, "Nanostructured Metal Oxide Thin Films for Humidity Sensors," Sensors Journal, IEEE, 8, 1422 – 1429, 2008.

[4] Jalkanen T, Määttänen A, Mäkilä E, et al., "Fabrication of Porous Silicon Based Humidity Sensing Elements on Paper," Journal of Sensors, 2015, 927396, 10, 2015.

[5] Huda A, Sarah A, Hadi A, "Efficient humidity sensor based on an etched no-core fiber coated with copper oxide nanoparticles," Journal of Nanophotonics, 12, 1, 2018.

[6] Chi H, Liu Y J, Wang F, He C, "Highly Sensitive and Fast Response Colorimetric Humidity Sensors Based on Graphene Oxides Film," ACS Applied Materials and Interfaces, 7, 36, 19882-19886, 2015.

[7] Yeo T L, Sun T, and Grattan K T V, "Fibre-optic sensor technologies for humidity and moisture measurement," Sensors and Actuators A: Physical, 144, 1, 280-295, 2008.

[8] Eda G, and Chhowalla, M. "Chemically Derived Graphene Oxide: Towards Large-Area Thin-Film Electronics and Optoelectronics," Advanced Materials, 22, 2392-2415, 2010.

[9] Bi H, Yin K, Xie X et al., "Ultrahigh humidity sensitivity of graphene oxide," Scientific Reports 3, 2714, 2013.

[10] Han K I, Kim S, Lee I G, Kim J P, Kim J.-H, Hong S,W, Cho B J, Hwang W S, "Compliment Graphene Oxide Coating on Silk Fiber Surface via Electrostatic Force for Capacitive Humidity Sensor Applications," Sensors, 17, 407, 2017.

[11] Zhang D, Chang H, Li P, Liu R, Xue Q, "Fabrication and characterization of an ultrasensitive humidity sensor based on metal oxide/graphene hybrid nanocomposite," Sensors and Actuators B: Chemical, 225, 233-240, 2016.

[12] Wee B-H, Khoh W-H, Sarker A K, Lee C-H and Hong J-D, "A high-performance moisture sensor based on ultralarge graphene oxide," Nanoscale, 7, 17805-17811, 2015.

[13] Zhao C, Qin M and Huang Q, "Humidity sensing properties of the sensor based on graphene oxide films with different dispersion concentrations," Sensors, *2011 IEEE,* Limerick, 129-132, 2011.

[14] Lim W H, Yap Y K, Chong W Y and Ahmad H, "All-Optical Graphene Oxide Humidity Sensors," Sensors, 14, 24329-24337, 2014.

[15] Chiu Y-D, Wu C-W, Chiang C C, "Tilted Fiber Bragg Grating Sensor with Graphene Oxide Coating for Humidity Sensing," Sensors, 17, 2129, 2017.

[16] Wang Y, Shen C, Lou W, Shentu F, "Fiber optic humidity sensor based on the graphene oxide/PVA composite film," Optics Communications, 372, 229-234, 2016.

[17] Zheng S, Tu Q, Urban J J, Jeffrey, Li S, and Mi B, "Swelling of Graphene Oxide Membranes in Aqueous Solution: Characterization of Interlayer Spacing and Insight into Water Transport Mechanisms," ACS Nano, 11, 6440-6450, 2017.

[18] Wang Y, Shen C, Lou W, Shentu F, Zhong C, Dong X, and Tong L, "Fiber optic relative humidity sensor based on the tilted fiber Bragg grating coated with graphene oxide," Applied Physics Letters, 109, 031107, 2016.

[19] Shivananju B N et al., "Highly Sensitive Carbon Nanotubes Coated Etched Fiber Bragg Grating Sensor for Humidity Sensing," IEEE Sensors Journal, 14, 8, 2615-2619, 2014.

[20] Huang Y, Zhu W, Li Z, Chen G, Chen L, Zhou J et al., "High-performance fibre-optic humidity sensor based on a side-polished fibre wavelength selectively coupled with graphene oxide film," Sensors and Actuators B: Chemical, 255, 1, 2018,

[21] Ghadiry M, Gholami M, Lai C K, Ahmad H, Chong W Y, "Ultra-Sensitive Humidity Sensor Based on Optical Properties of Graphene Oxide and Nano-Anatase TiO_2," PLoS ONE 11(4): e0153949, 2016.

[22] Yi X, Jun Z, Xiang C, Shaozao T, Jianhui Y, Huihui L, Yunhan L, Guozhen L, Shiping L, Jieyuan T, Zhe C, "Reduced graphene oxide for fiber-optic humidity sensing," Optics Express, 22, 2014.

[23] Gao R, Lu D F, Cheng J, Jiang L, Qi Z M, "Humidity sensor based on power leakage at resonance wavelengths of a hollow core fiber coated with reduced graphene oxide," Sensors and Actuators B: Chemical, 222, 618–624, 2016.

[24] Wang Y Q, Shen C Y, Lou W M, Shentu F Y, "Polarization-dependent humidity sensor based on an in-fiber Mach-Zehnder interferometer coated with graphene oxide," Sensors and Actuators B: Chemical. 234, 503–509, 2016.

[25] Xia L, Li L H, Li W, Tian K, Liu D M, "Novel optical fiber humidity sensor based on a no-core fiber structure," Sensors and Actuators A: Physical, 190 (1), 1–5, 2013.

[26] Corres J M, Bravo J, Matias I R, Arregui F J, "Nonadiabatic tapered sing-mode fiber coated with humidity sensitive nanofilms," IEEE Photonics Technology Letters, 18(8), 935–937, 2006.

[27] Luo Y, Chen C, Xia K, Peng S, Guan H, Tang J, Lu H, Yu J, Zhang J, Xiao Y, Chen Z, "Tungsten disulfide(WS2) based all-fiber-optic humidity sensor," Optics Express, 24 (8), 8956–8966, 2016.

[28] Gupta B D, "A novel probe for a fiber optic humidity sensor," Sensors and Actuators B: Chemical, 80, 132–135, 2001.

[29] Bariain C, Matias I R, Arregui F I, Lopez-Amo M, "Optical fiber humidity sensor based on a tapered fiber coated with agarose gel," Sensors and Actuators B: Chemical, 69, 127–131, 2000.

[30] Alwis S, "Optimization of Polymer Coated Long Period Grating-based Sensors," PhD Thesis, City University London, London, UK, 2013.

[31] Liu Y, Wang L, Zhang M, Tu D, Mao X, and Liao Y, "Long-period grating relative humidity sensor with hydrogel coating," Photonics Technology Letters, IEEE, 19, 880–882, 2007.

[32] Tan K M, Tay C M, Tjin S C, Chan C C, and Rahardjo H, "High relative humidity measurements using gelatin coated long-period grating sensors," Sensors and Actuators B: Chemical, 110, 335–341, 2005.

[33] Bock W J, Eftimov T, Smietana M, Mikulic P, "Efficient distributed moisture-ingress sensing using diamond-like carbon-nanocoated long-period gratings," Optics Communications, 284, 19, 4470-4472, 2011.

Chapter 6

GO Functionalised LPG for Label-Free Measurement of Bovine Serum Albumin (BSA) Concentration

6.1 Introduction

The detection of biological species and the accurate measurement of their concentration is an extremely important process in applications such as those in healthcare, microbiology, drug discovery in the pharmaceutical sector, environmental monitoring and clinical analysis [1]. This chapter is focused on the fabrication and development of a suite of label-free fibre optic biosensors that has been developed to measure the BSA concentrations in an aqueous solution, by using a GO-coated LPG as the basis of a sensor probe approach discussed in this work. The first part of this chapter is focused on highlighting the importance of GO coatings on LPGs in biosensing by discussing the advantages of fibre optic and GO-based biosensors, with reference to the recent literature. The second part of this chapter builds on that review and the opportunities for new research by focusing on work done to enhance the sensitivity of the BSA biosensor developed by use of a GO-coated dual-peak resonance LPG (DLPG), to exploit the increased intrinsic external RI sensitivity of higher order cladding modes of the used LPG grating structure. GO has been coated on these sensor probes by use of a drop casting technique as discussed earlier in Chapter 4. The variations in the transmission spectra of the highest order cladding modes of the GO-coated LPGs, monitored in the presence of different concentrations of sucrose solutions prepared, were also analysed and the results are presented in this chapter, seeking therefore to provide external RI calibration for the biosensors developed. The chapter concludes with a cross-comparison of the sensitivities of before and after the GO coating on the LPG and DLPG probes, to highlight the protein biosensor sensitivity enhancement achieved by use of a GO overlay on a DLPG grating structure.

6.2 Importance of GO and Optical Fibre Sensors in Biosensing

To cater to the ever-increasing demand for highly sensitive and more effective biosensors that arises with the rapid advancements of the industries mentioned in the Introduction to this chapter, there is a need to overcome the challenges and drawbacks arising from conventional biosensing procedures. Usually, conventional biosensing platforms are associated with time consuming procedures that often require the use of complex and expensive instrumentation and analysis by experienced professionals in the field. More often, such biosensing samples need to go through a long preparation processes and large quantities of samples are required to obtain the detection sensitivity and the measurement of the analyte concentration in the sample. Another disadvantage of conventional biosensing mechanisms is that they require a labelling process in the detection and measurement of the target molecules. However, in a label-free biosensor, the molecular interaction can be converted into an electrical or optical signal and as such, it can be detected, and the concentrations can be measured conveniently without the need of any labelling process. Therefore, label-free detection leads to faster results and higher sensitivity [2]. When it comes to label-free biosensing, optical fibre sensors have shown considerable advantage over conventional biosensing techniques such as SPR or interferometry, due to their small size, high compatibility with already available commercial optoelectronic devices, biocompatibility, multiplexing and long-distance monitoring capability. A few different types of optical fibre-based biosensors have been reported based on FBGs, TFBGs and LPGs [3] while different types of techniques such as fibre tapering [4], side polishing [5] and cladding etching [6], have been used to increase the sensitivity of those optical fibre-based biosensors that have been developed. These biosensors have been used in a number of biomedical applications such as detection of antibody antigen [7], protein [8], cellular behaviour [9], DNA [10] and bacteria [11]. Among these, LPGs are preferred over other fibre optic techniques, mainly due to their enhanced sensitivity to external RI and ease of fabrication. As discussed in detail in Chapter 4, the intrinsic external RI sensitivity of LPGs can be enhanced by depositing a thin film coating that has a higher RI than that of the cladding, such as GO. Moreover, as reported by Shu et al. in [12], DLPGs that operates near the dispersion turning point (DTP) have shown increased sensitivity to external RI variations by exploiting the increased cladding-surrounding light interaction of higher order cladding modes. Thus, the development of highly sensitive label-free biosensors by depositing a GO thin layers on DLPG fibre grating structures represents an opportunity for new and useful sensor designs. Among the sensing materials that have been used in biosensing, the suitability of GO as a sensing

material has been discussed extensively in the previous three chapters, by describing the positive sensing characteristics that it possess, such as high surface to volume ratio and rich surface chemistry that is present, due to its unique 2D nature. Moreover, due to the oxygen-containing groups that it contains, GO is biocompatible and becomes water dispersible, characteristics which are highly desirable in biosensing applications. Sharma et al. have summarised the various types of biosensors that have been developed based on biosensing characteristics of GO in a recent paper in the literature [13] in detecting various biomolecules such as Vitamin E, protein, Thrombin, Human IgG, Hepatitis C virus etc. Some of these applications are illustrated in Fig. 6.1.

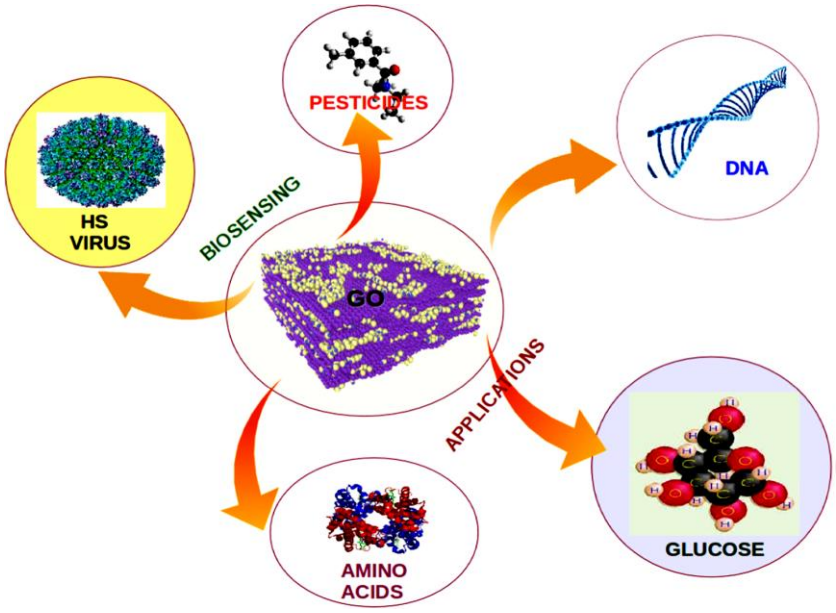

Fig 6. 1 Sensing applications of GO [13].

A limited number of fibre optic biosensors have been reported using sensor designs that exploit the favourable characteristics of fibre gratings and GO as a sensing material. For example, Sridevi et al. have reported an etched FBG based biosensor [14] for the detection of protein concanavalin A (Con A). The etched FBG surface has been functionalised with GO and single wall carbon nanotubes (SWCNT) to attach mannose-functionalized poly(propyl ether imine) (PETIM) dendrimers (DMs) to the GO surface that acts as multivalent ligands, having specificity to detect lectin Con A. When Con A molecules gets attached to the GO/SWCNT functionalised etched FBG surface, the effective RI of the core mode gets affected and these optical changes are reflected in the Bragg wavelength shift. They have reported a LOD of 500 pM for the GO coated etched FBG with an affinity constant of 3.4×10^8. A schematic diagram that explains the sensing principle of the developed sensor, along with a graph of sensor performance with different concentrations of Con A is illustrated in Fig. 6.2.

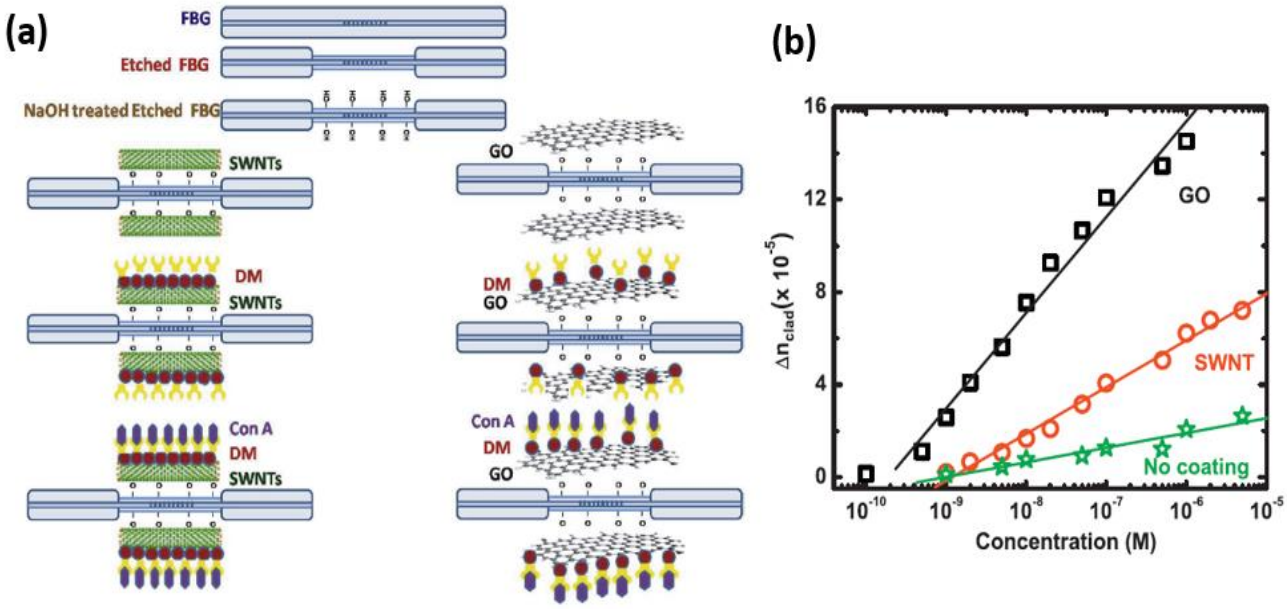

Fig 6. 2 (a) Sensing principle of the GO/SWCNT coated etched FBG based biosensor (b) Change in the surrounding medium which acts as cladding of the etched FBG as a function of concentration of Con A solution [14].

Another etched FBG based biosensor for the detection of D-glucose and glycated haemoglobin (HbA1c) has been reported by the same research group in the literature in [15]. In this, they have coated an etched FBG surface with amino phenyl boronic acid (APBA)-functionalized rGO to trap glucose molecules on the FBG surface. The sensing mechanism used is similar to that described in the previous example, and has a reported LOD of 1 nM by the use of this APBA–RGO complex coated etched FBG biosensor.

A schematic diagram of the developed glucose sensing mechanism is illustrated in Fig. 6.3.

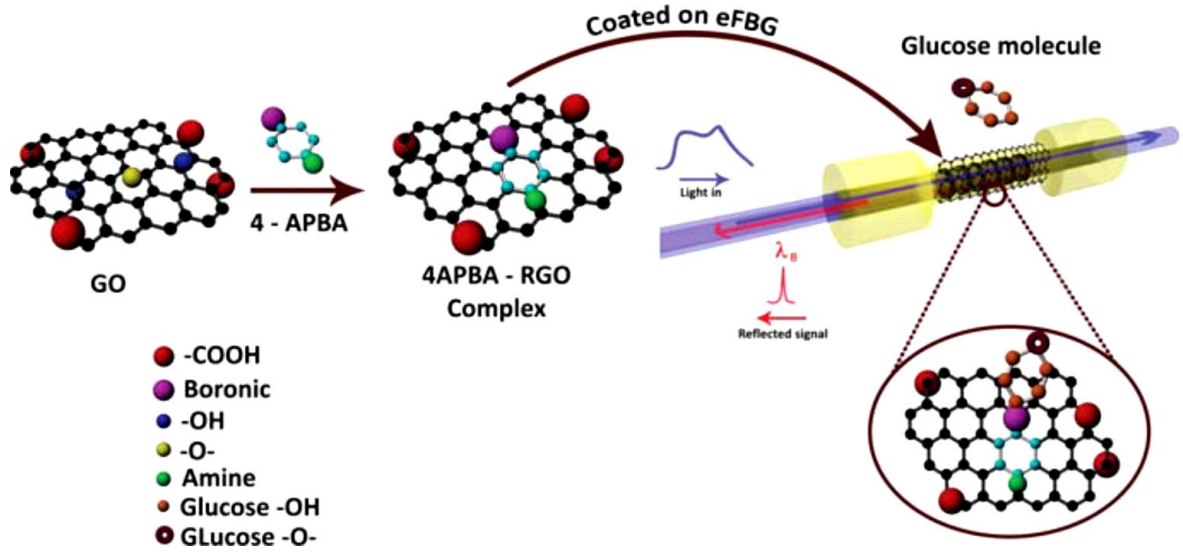

Fig 6. 3 Schematic of the glucose sensing mechanism for etched FBG sensor coated with the APBA-RGO complex [15].

The same group has reported that C-reactive protein (CRP) can be detected by functionalising an etched FBG surface with an anti-CRP antibody (aCRP)-graphene oxide (GO) complex [16]. A LOD value of 10 µg/L has been achieved by use of this particular GO – aCRP functionalised eFBG sensor. A cladding etching process has been performed on these sensors as the mechanism used to increase the external RI sensitivity of the FBG structures employed. Even though high sensitivities have been realised using this technique, etching of the cladding involves hydrofluoric acid (HF) (extremely harmful to humans and the environment and thus alternatives are sought). To overcome this materials problem, LPGs can be used as a low cost and easy to implement alternative due to their intrinsic high external RI sensitivities, as illustrated in Chapter 4. However, there has been a very limited number of GO coated LPG based biosensors reported in literature in spite of their obvious advantages. Liu et al. have reported two GO-coated DLPG based biosensors that can be used to detect haemoglobin [17] and antibody-antigen effects [18]. Higher indexed cladding modes of a LPG exhibits parabolic properties (which will be discussed in detail in the next subsection of this chapter) and as such, there is a group of DTPs that exits in the phase matching curves of these particular higher order modes. Due to this, two resonance peaks of the same mode can be realised that portray wavelength shifts of different signs under the same external RI perturbation. These twin resonance peaks are extremely sensitive to external RI variations compared with a normal resonance peak associated with lower order modes of a LPG. The GO-coated DLPG based biosensors reported in [17] and [18] have exploited this intrinsic high external RI sensitivity of DLPG structures, further enhanced by a thin layer coated of GO to form the basis of the GO coated biosensors reported. Based on the results, LODs of 7 ng/mL and 0.05mg/mL for IgG and haemoglobin, respectively, have been achieved. A schematic diagram of the GO-coated DLPG based IgG biosensor fabrication approach is illustrated in Fig. 6.4, followed by an

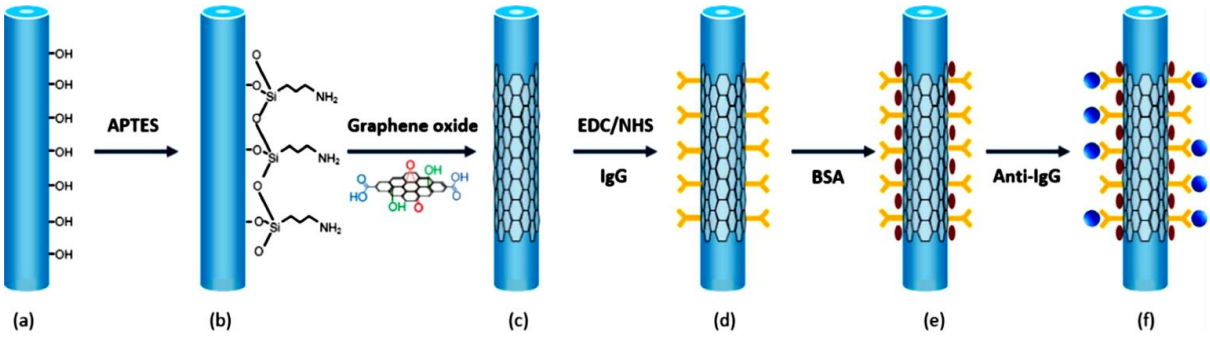

Fig 6. 4 Schematic illustration of fibre optic biosensor based on GO-coated DLPG: (a) DLPG silica fibre surface with alkaline treatment (b) Silanization by APTES (c) GO deposition (d) IgG immobilization via EDC/NHS (e) Passivation of unreacted sites by BSA blocking solution (f) Binding interaction between probe bioreceptor (IgG) and target analyte (anti-IgG) [17].

illustration of the dependence of wavelength shift against anti-IgG concentrations shown in Fig. 6.5.

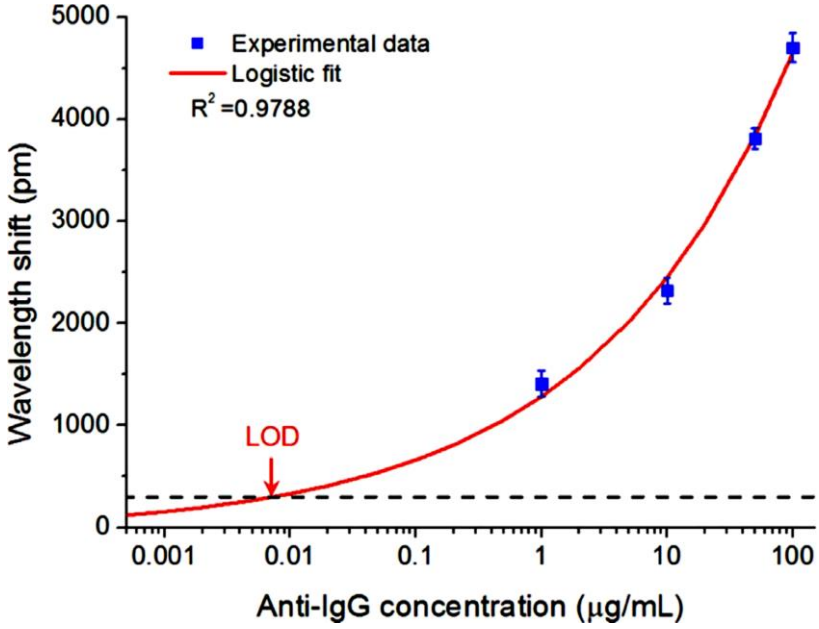

Fig 6. 5 Dependence of wavelength shift against anti-IgG concentrations. The red line is the best logistic fitting curve [17].

Among all the proteins available, BSA plays an important role in the fields of biomedical and diagnostics. It is also used as a protein concentration standard in various laboratory experiments. BSA is also a part of number of biochemical applications such as enzyme-linked immunosorbent assay, immunoblots and immunohistochemistry [19]. Target drug delivery is another important biomedical application that is associated with BSA, as shown by An et al. in [19]. BSA also acts as a biomarker for the bovine disease, mastitis [20], which is one of the most common diseases in dairy cattle worldwide that causes significant losses in the dairy industry. In this respect, detection and quantification of BSA is very crucial in all of the biomedical applications discussed above. There are a few fibre optic based biosensors reported in the field of protein detection in literature. Guo et al. have used a TFBG to detect urinary protein variations with a protein sensitivity of 5.5 dB/(mg/mL) with a LOD of 1.5×10^{-3} mg/mL [21]. As discussed above, Sridevi et al. used a GO-antibody complex coated etched FBG to detect CRP in blood. Urrutia et al. have used a tapered optical fibre with an Au-nanocoating to detect proteins with a lowest detection concentration of 2.5 nM [22]. Zhengyong Li et al. have demonstrated that a detection sensitivity of −38.9 nm/(mg/mL) with a detection limit of $2.57 \times 10-4$ mg/mL can be achieved in BSA detection by use of an in-fibre MZI based optical fibre biosensor [23]. However, to the best of the author's knowledge, there is only one GO-based fibre optic biosensor reported on the detection of BSA proteins to date, which has been

reported by Esposito et al. in the recent literature [24]. A multilayer system consisting of a polycarbonate (PC) film and a much thinner layer of GO coated on a single ended LPG forms the basis of this fibre optic biosensor, developed to detect biotinylated BSA. An extremely low LOD of 0.2 aM has been achieved, which is one of the lowest reached so far with this sensing technology. A schematic diagram of the GO-coated LPG based biotinylated BSA sensor developed is illustrated in Fig. 6.6, followed by the variations of the transmission spectra of the resonance loss band with varying BSA concentrations, shown in Fig. 6.7.

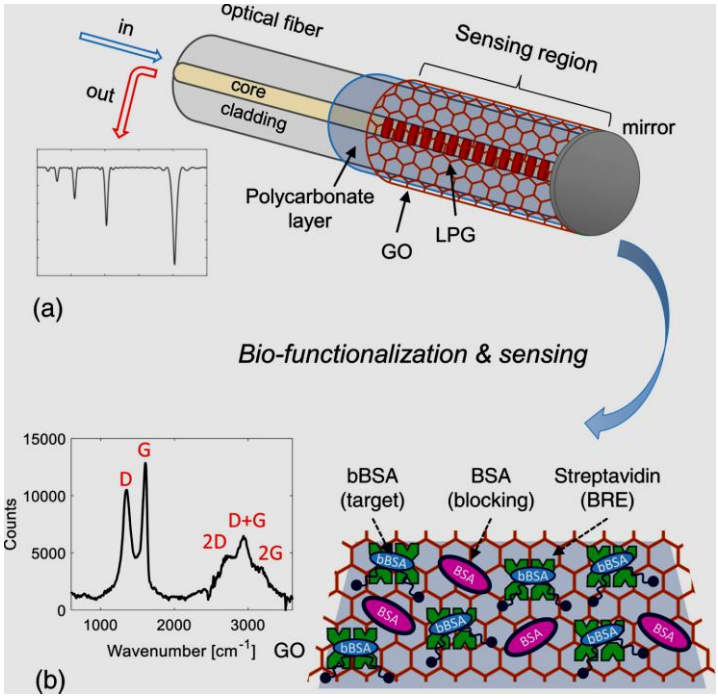

Fig 6. 6 Schematic (not at scale) of: (a) single-ended LPG sensor; (b) Sensor surface bio-functionalization and sensing mechanism (in inset the Raman spectrum of GO) [24].

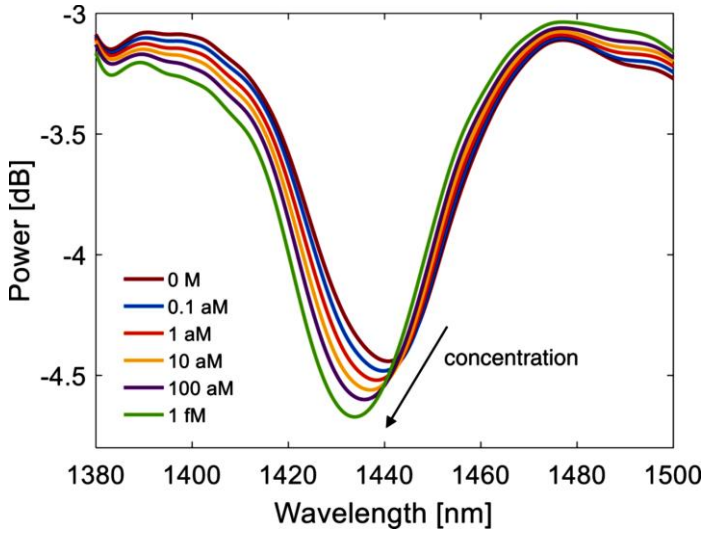

Fig 6. 7 Spectrum of LP07 band of sample LPG1 acquired in PBS after the incubation of each concentration of bBSA [24].

Based on the GO-based biosensors reported in the discussion above, it is evident that GO shows excellent RI sensitivity characteristics when it comes to the development of external RI-based biosensors. It is also evident that optical fibre biosensors provide a greater level of simplicity compared to conventional biosensing processes, especially when it comes to label-free detection of biomolecules. Thus, there is a research opportunity and a 'market gap' to address that can be exploited by developing optical fibre biosensors that use GO as the sensing element. Therefore, a GO-coated DLPG based fibre optic biosensor approach has been developed in this work to detect and measure the concentrations of BSA protein, in a label-free way. The next part of this chapter focuses on the sensing mechanism and sensor fabrication steps of the GO-coated DLPG based BSA sensor developed, followed by an analysis of its performance when used in the measurement of different concentrations of BSA.

6.3 Dual Peak Resonance of LPGs

Most of the LPG-based external RI sensors developed make use of the relatively lower order cladding modes fabricated with relatively large grating periods. However, it has been shown by Shu et al. [12] that higher order cladding modes are capable of producing dual resonance peaks by coupling the cladding mode with a phase matching condition that is closer to the DTP, and these dual resonance of higher order modes have been exploited in external RI sensing due to its significantly superior external RI sensitivity. This enhanced sensitivity of dual peak resonance has been used in the GO-coated DLPG-based BSA concentration measurement sensor developed in this work. The dual peak resonance produced by higher order cladding modes of a LPG will be explained further in the discussion below.

As discussed in detail in Chapter 2, a LPG couples the light from the fundamental core mode to co-propagating cladding modes at a resonance wavelength defined by the phase-matching condition, $\lambda_{res} = \Delta n_{eff} \Lambda$ [25], where Λ is the grating period and Δn_{eff} is the core-cladding mode-index difference. Shu et al. have calculated the relationship between resonance wavelength and the grating periods for the first 30 cladding modes for a B/Ge co-doped photosensitive fibre, which has been depicted in Fig. 6.8 below [25]. It has to be noticed that a similar B/Ge co-doped photosensitive fibre has been used to fabricate the LPGs used in this work.

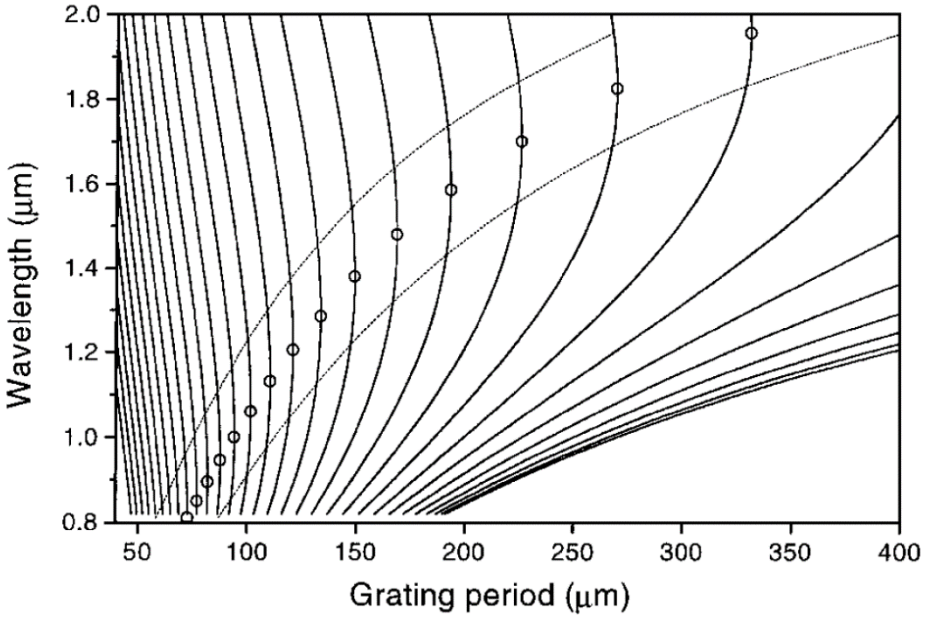

Fig 6. 8 Calculated relationship between resonant wavelengths and grating periods for the first 30 cladding modes in B/Ge co-doped fibre. Open circles, dispersion turning points of the phase curves [25].

DTPs of the phase matching curves have been depicted by open circles. It can be noticed that the slope direction of the phase curves changes from low to higher order modes, turning at these DTPs, at which $(d\lambda_{res}/d\Lambda) \rightarrow \infty$. The phase curve in the region below these points have positive dispersion with $(d\lambda_{res}/d\Lambda) > 0$ and in contrast, the phase curve in the region above these points have negative dispersion with $(d\lambda_{res}/d\Lambda) < 0$. As the slopes near these DTPs are very steep, the cladding order modes coupled near this region are extremely sensitive to any external perturbation that would cause changes in the grating period or the effective RI of these coupled modes. Extremely high external RI sensitivities of LPGs that operate near DTPs can be explained by this phenomenon.

It is evident from Fig. 6.8 that the higher order modes shows a clear parabolic nature. In fact, if the wavelength range is increased, all the phase matching curves will show a parabolic nature. This means that, for a given grating period, a cladding mode will satisfy the phase-matching conditions at two separate wavelengths and this is defined as the dual resonance. For higher order cladding modes, the described dual resonance could be realised in the operating wavelength region of 600 nm to 1750 nm.

One way to realise dual resonance from a particular B/Ge co-doped photosensitive fibre is to change the grating period. Shu et al. demonstrated this in [25] and the dual resonance peaks achieved for different grating periods are depicted in Fig. 6.9.

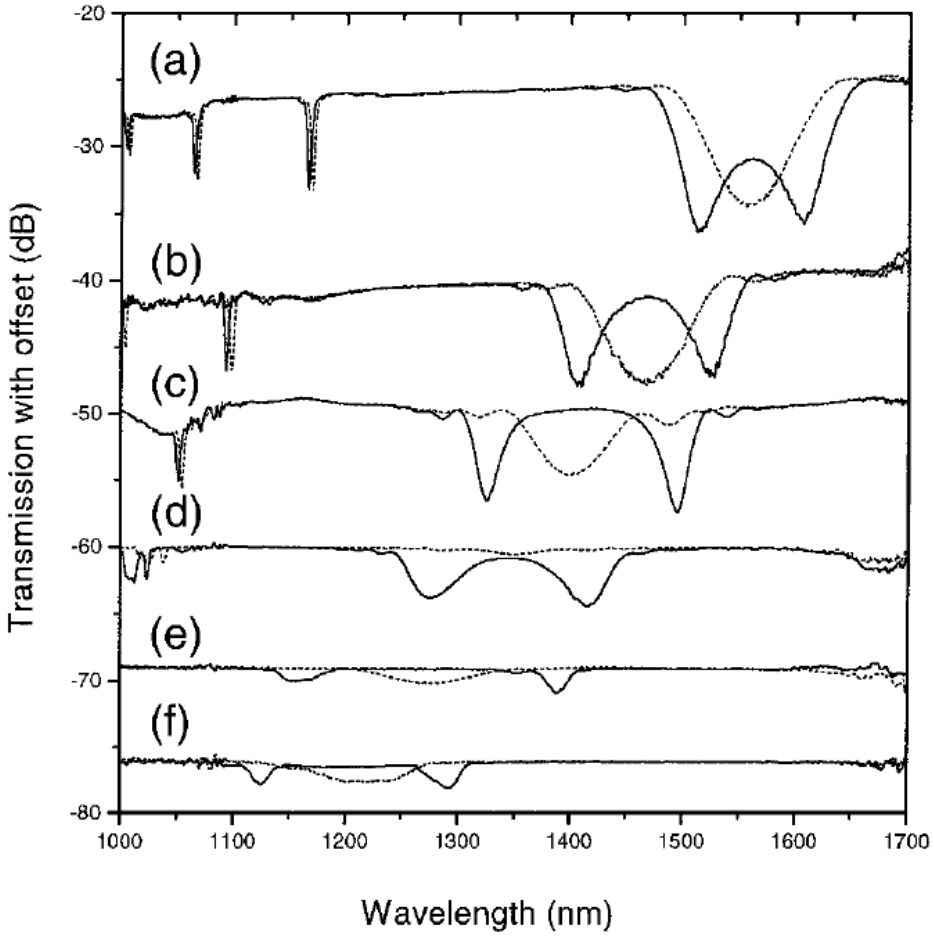

Fig 6. 9 Measured transmission spectra before and after the transition from the dual-resonance state (solid curves) to the dispersion turning point (dotted curves) (a) Λ = 202.5 μm (b) Λ= 175 μm (c) Λ= 153 μm (d) Λ= 133 μm (e) Λ= 120 μm (f) Λ= 109 μm [25].

Dual resonance of LPGs can also be achieved by etching the cladding, which results in mode transitions of the LPGs. This method has been demonstrated by Chen et al. in [26], where they simulated the phase matching curves of higher order cladding modes with varying cladding radii. The results of this simulation are presented in Fig. 6.10 (a). It was also demonstrated that the dual peak resonance will decrease and will eventually cease to exist with an increased UV exposure in the inscription process. These characteristics of the dual resonance with increased UV exposure can be seen in Fig. 6.10 (b).

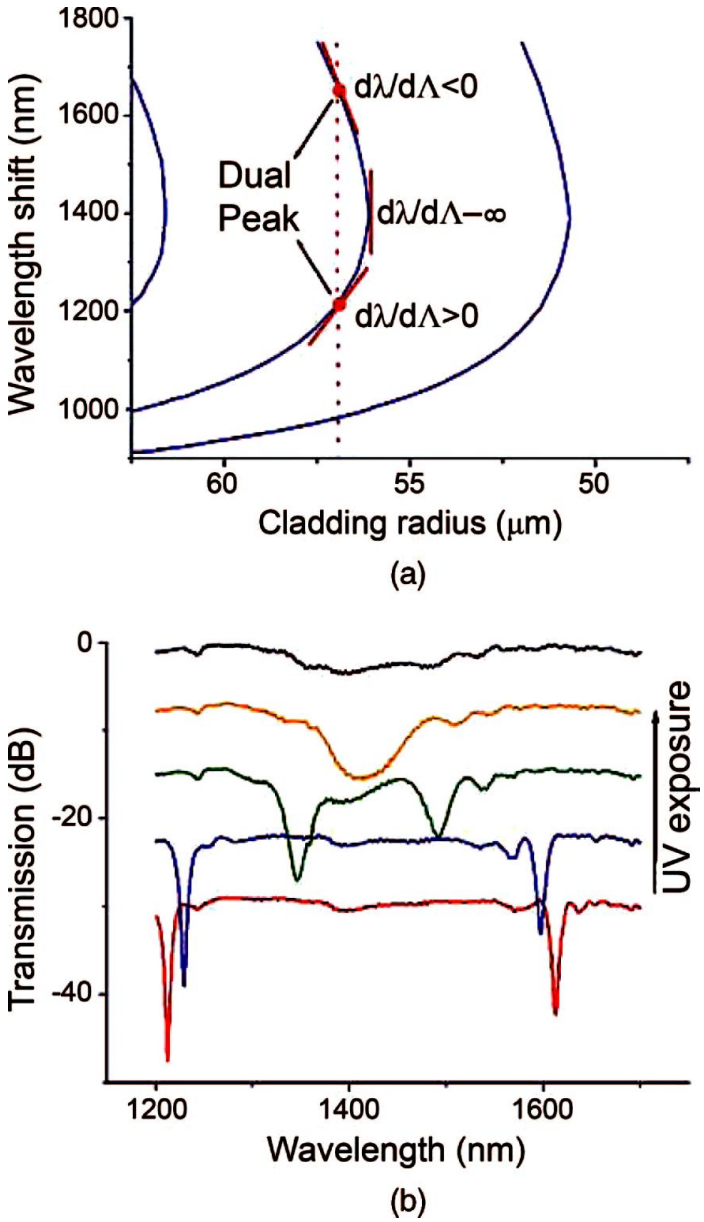

Fig 6. 10 (a) Simulated phase curves of a dual-peak LPG of 160 μm period for reduced cladding radii from 62.5 to 51.5 μm (b) Spectral evolution of a dual-peak LPG with a period of 158 μm under increased (arrow direction) UV exposure [26].

The external RI response of a DLPG was demonstrated by Shu et al. in [12]. Changes in the transmission spectra of a DLPG that has been produced with a grating of period 153 μm and with varying external RI, are shown in Fig. 6.11. The figure shows that the 12th order resonance peak (at ~ 1050 nm) indicates a blue shift of just 13.1 nm, when the surrounding RI changed from 1 to 1.44. Compared with that, the dual resonance peaks of the 13th order recorded a significant increment in sensitivity by more than an order of magnitude. This experiment illustrates the significantly enhanced external RI sensitivity of DLPGs, compared with LPGs that operate in comparatively lower order modes.

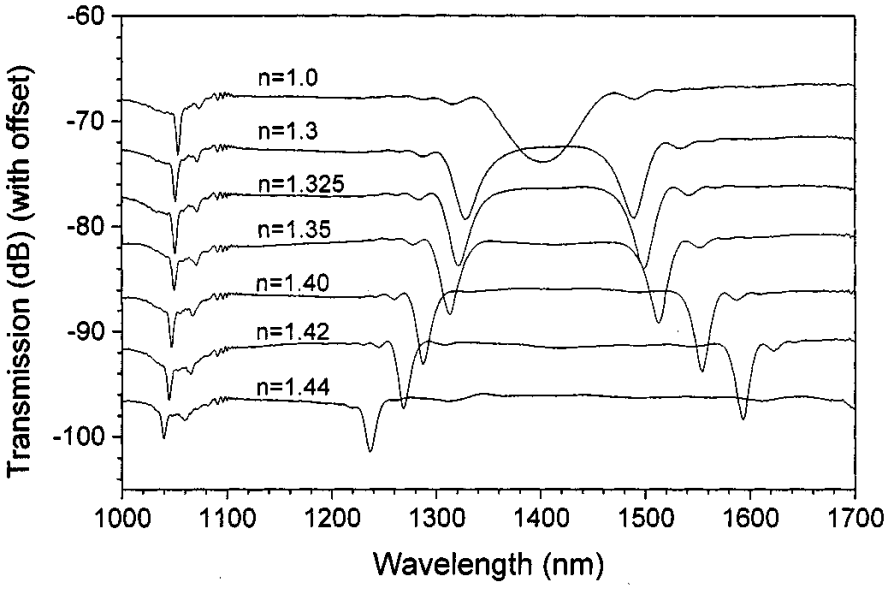

Fig 6. 11 Transmission spectrum of the Λ = 153 µm grating for different values of the SRI [12].

Recently, Smietana et al. [27] demonstrated that thin film deposition of a high indexed material can enhance the external RI sensitivity of a DLPG considerably. To do so, they applied a thin aluminium oxide (Al_2O_3) layer onto a LPG to achieve a RI sensitivity that exceeded 9000 nm/RIU. It was also demonstrated in Chapter 4 that the external RI sensitivity of a LPG can be increased significantly by depositing a thin film layer of GO. Therefore, considering the advantages of using DLPGs and GO in achieving high sensitivities in external RI sensing, a GO-coated DLPG-based BSA concentration measurement sensor has been developed in this work. Moreover, the enhanced performance of this sensor probe has been illustrated by comparison with the performance of a bare DLPG and a LP_{08} resonance peak of a GO-coated LPG using the same variations of the BSA concentrations and the surrounding RI values mentioned. The fabrication steps of these sensor probes are discussed in detail in the next subsection, followed by a discussion of the experimental results obtained.

6.4 Fabrication of the Sensor Probes

The LPG and DLPG structures used in this chapter were fabricated using the same grating fabrication facility described in Chapter 2. A B/Ge co-doped single mode photosensitive fibre purchased from Fibrecore, UK (PS 1250/1500), with a cut-off wavelength of 1250 µm, was exposed to the light from a 248-nm KrF excimer laser with a pulse energy of 10 mJ and a pulse frequency of 100 Hz through a metal amplitude mask with a period of 250 µm to create the 30 mm long LPG used to fabricated the GO coated LPG sensor probe discussed in this work. 4 minutes and 30 seconds of UV light exposure time was chosen after an optimisation process

carried out previously and applied here. After the inscription process, the LPG was annealed at 100 ℃ for 3 hours to stabilize its optical properties.

The DLPG with a grating period of 150 µm and 30 mm length was inscribed on a B/Ge co-doped single mode photosensitive fibre from Fibrecore, UK (PS 980 nm), with a cut-off wavelength of 850 nm , by exposing to the UV light from the same KrF excimer laser through a 150 µm metal amplitude mask. This specific fibre and the amplitude mask was chosen to realise the DLPG resonance of the higher order cladding modes within the operating wavelength region of the OSA (this being from 700 nm to 1650 nm). The pulse energy was set at 10 mJ and a pulse frequency of 100 Hz was used in this DLPG inscription process that was optimised to allow a UV light exposure time of 6 minutes after the previous optimisation process was carried out. After the inscription process, the fabricated DLPG was annealed at 100 ℃ for 3 hours to stabilize its optical properties. It should be noted that, by using these DLPG fabrication specifications, dual resonance has been achieved without any cladding etching being required.

A drop casting technique was used to deposit GO thin film layers on the surface of the LPG and the DLPG, as fabricated above, to create the GO-coated fibre optic biosensor probes used in this work. To do so, 5 mg of GO flakes, synthesised as described in Chapter 4, was dissolved in 10 mL of DI water to prepare the GO aqueous dispersion with a concentration of 0.5 mg/mL. Then the GO aqueous dispersion was sonicated for 1.5 hours before being centrifuged for another 20 minutes at 3000 rpm. After this centrifugation process, the supernatant was used to achieve a high percentage of single layered GO flakes in the solution. Afterwards, 1 mL of the supernatant was diluted with 5 mL of DI water to achieve the concentration required to realise an optimum thickness of the GO overlay on LPG structures, without the peaks of the resonance loss bands required to monitor the optical changes reflected in the resonance loss band characteristics caused by variations in external RI values disappearing.

To start off the GO deposition process, first the LPG and DLPG fibre surfaces were cleaned thoroughly with IPA and DI water-soaked Kimwipe papers in that order, to remove any organic or inorganic dirt that must have rested on the optical fibre surface. By doing so, O-H groups of the Si – O – H groups that are present on the fibre surface get exposed to the outward environment, which is an important step in forming the hydrogen bonds with oxygen containing groups of the GO sheets, when using this drop casting technique. Then the cleaned fibre was rested on a Teflon groove, following which 200 µL of the prepared GO solution was

poured into the groove and the setup containing the fibre grating submerged in GO was oven dried at 70 ℃ for one hour to complete this GO thin film deposition process. Fig. 6. 12 (below) illustrates the setup containing the optical fibre on a Teflon groove that was used to deposit the GO on the fibre surface using this drop casting technique. In comparison with the metal groove used in Chapter 4 experiments, Teflon is an extremely inert substance, which significantly reduces the likelihood of GO sample getting contaminated during the deposition process. Therefore, to increase the quality of the GO coated LPG based biosensors developed in this chapter, a Teflon groove was used instead of a metal groove.

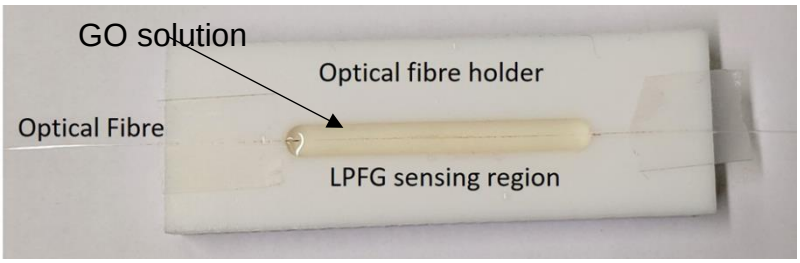

Fig 6. 12 Setup used for the deposition of GO on the fibre surface.

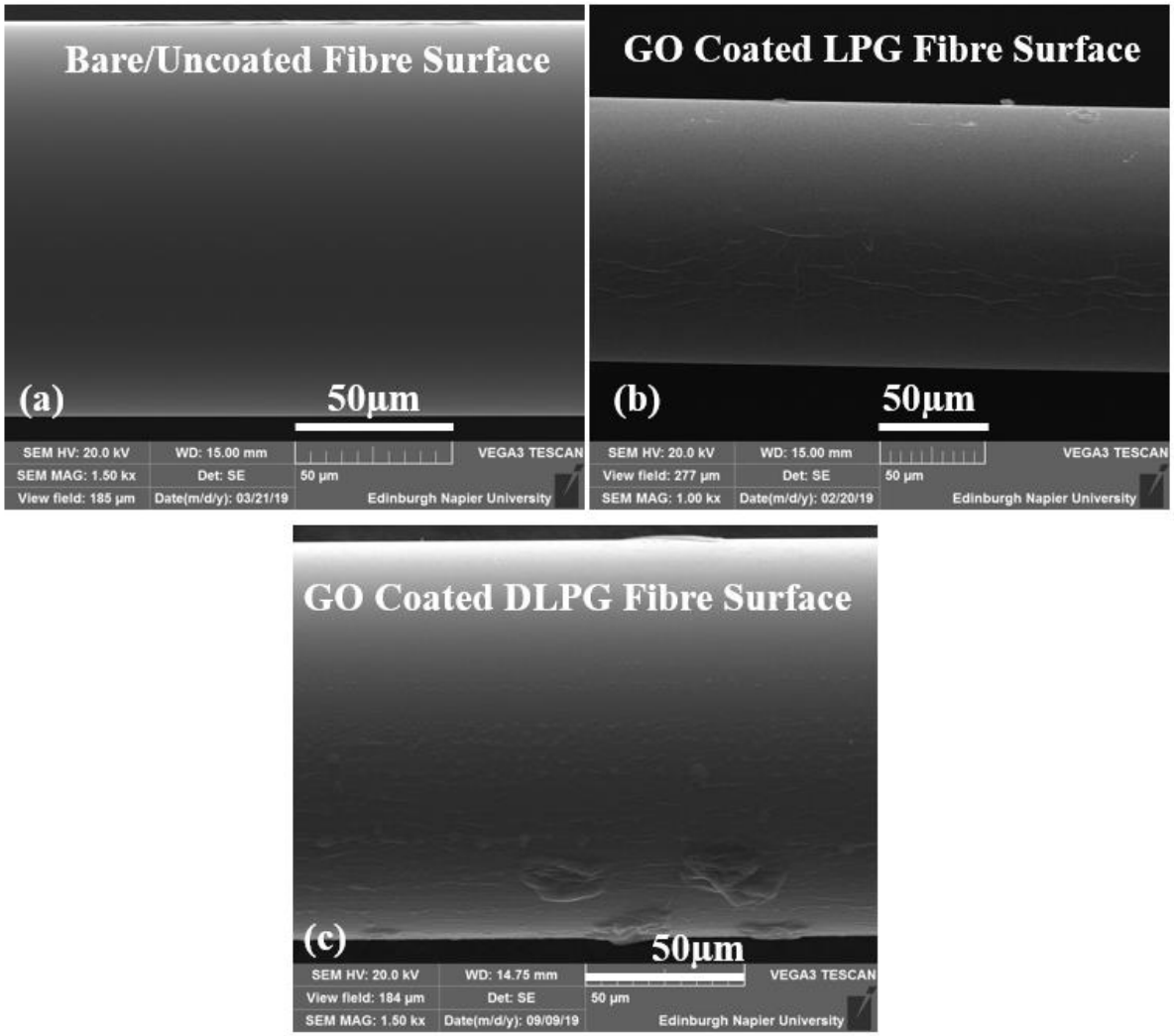

Fig 6. 13 SEM images of the fibre surface of (a) bare fibre (b) LPG (c) DLPG.

Zoomed SEM images of the bare fibre surface, the GO-coated LPG fibre surface and the GO-coated DLPG surface, taken using an Oxford Instruments X-Max 20 spectrometer are presented in Fig. 6.13 for the purpose of comaprison. The surface roughness introduced by the GO thin layer deposition on the LPG and DLPG surfaces is clearly visible, compared with the smooth surface of the bare, uncoated fibre. To characterise the GO coating on the LPG and DLPG surface, EDAX anylsis of the coated fibre surfaces was also performed with the help of the same spectrometer. EDAX analysis results of the GO-coated DLPG surface are presented in Fig. 6.14 and a similar result was also obtained for the GO coated LPG. A high percentage of carbon (72%) and oxygen (16%) atoms were noticed in the EDAX analysis of the red squared region of the GO-coated DLPG surface, shown in the inset of Fig. 6.14, along with the fairly homogeneous and uniform GO coating noticable in the SEM images which suggested that an effective and efficient GO thin fim coating has been achieved on the fibre surface using the drop casting technique discussed above. The thickness of the GO coating achieved was measured using a similar SEM technique to that described in section 4.6 by taking the cross section SEM images of the GO coated LPG and DLPG, which showed that a GO thin layer thickness of ~ 410 nm (± 20 nm) had been achieved on both LPG and DLPG grating structures.

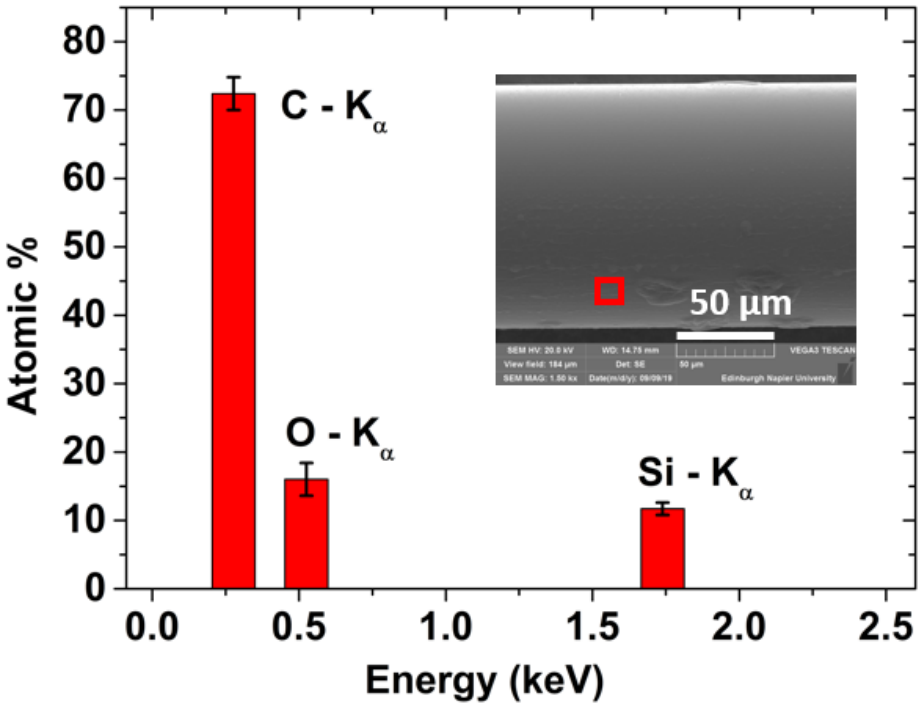

Fig 6. 14 EDAX spectrum of the GO coated fibre surface of the DLPG. Inset shows the zoomed SEM image of the coated GO layer on DLPG and the respective red boxed area selected to obtain the EDAX analysis.

The high indexed GO coating achieved on the LPG and DLPG surface resulted in a centre wavelength and minimum intensity changes in the resonance loss bands of both the LPG and DLPG sensor probes. These changes were monitored by recording the transmission spectra of the GO-coated LPG (GO-LPG) and GO-coated DLPG (GO-DLPG), before and after the GO thin film deposition. The optical changes noted in the transmission spectra can be seen in Fig. 6.15 and Fig. 6.16 for GO coated LPG and GO coated DLPG, respectively.

As can be seen in Fig. 6.15, the centre wavelength of the LP_{08} mode (the highest order resonance loss band achieved with the 250 µm amplitude mask used) of the uncoated LPG was recorded at 1508 nm with an intensity value of –85.13 dBm. After the deposition of the GO thin film overlay, the centre wavelength of the LP_{08} band performed a slight blue shift (~1 nm) while recording a centre wavelength value of 1507.04 nm. The minimum intensity of this resonance loss band was noted to be reduced by 7.41 dB to record an intensity value of –77.72 dBm. These optical changes are caused by the changes in the effective RI of the LP_{08} cladding mode, introduced by the high indexed GO layer that has been deposited on the LPG surface.

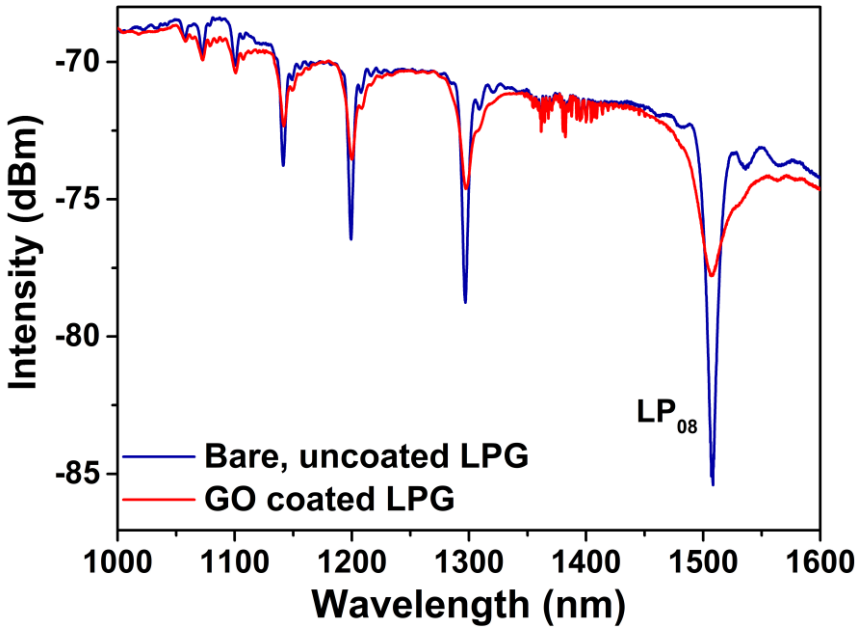

Fig 6. 15 Transmission spectra of uncoated and GO coated LPG.

As shown in Fig. 6.16, LP_{013}^{blue} peak of the uncoated DLPG recorded a centre wavelength value of 1100.2 nm with an intensity of -82.6 dBm. A centre wavelength value of 1411.2 nm with an intensity of -89.5 dBm was recorded for the LP_{013}^{red} peak of the uncoated DLPG. After the deposition of the GO thin layer, these dual peaks shift in opposite directions, in which the LP_{013}^{blue} peak performed a blue shift while the LP_{013}^{red} peak performed a red shift. After the blue shift, LP_{013}^{blue} peak recorded a centre wavelength value of 1091.2 nm with an intensity value of -

73.74 dBm, which amounted to 9 nm of wavelength shift and 6.9 dB of minimum intensity loss. Compared with that, LP_{013}^{red} peak performed a red wavelength shift of 21.2 nm with a minimum intensity loss of 15.77 dB while recording a centre wavelength value of 1432.4 nm and an intensity of -73.77 dBm.

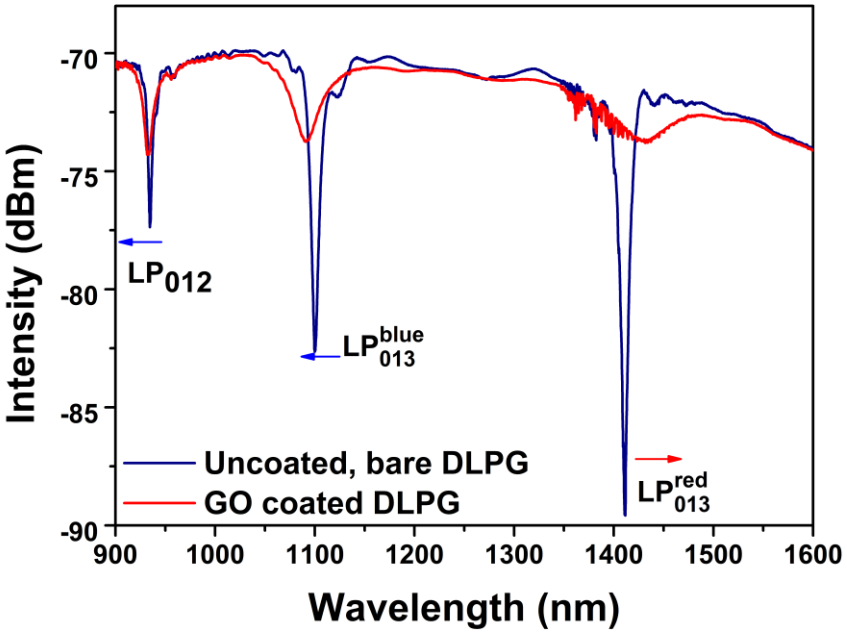

Fig 6. 16 Transmission spectra of uncoated and GO coated DLPG.

Based on this analysis of the transmission spectra of GO-LPG and GO-DLPG, before and after the GO thin film deposition, it is evident that the DLPG has shown an increased sensitivity to the optical changes caused by the GO thin film overlay in the centre wavelength shift of the resonance loss bands.

6.5 Experimental Setup

After completion of the GO deposition process, a similar experimental setup that was described in Fig. 4.18 in Section 4.7 was used to measure and record the external RI response and the BSA concentration measurement results of the GO-LPG and GO-DLPG sensor probes that were fabricated. To do so, one end of the sensor probe was connected to a broadband light source (OceanOptics LS1) and the other end to an OSA to record the transmission spectra of the GO-coated LPG based sensor probe under investigation. Throughout the experiments, the room temperature was maintained at a constant value of 22 ±1 °C, to eliminate the temperature dependent spectrum changes that could affect the external RI and thus the biosensor performance of the GO-LPG and GO-DLPG sensor probes that were fabricated.

6.6 Performance Analysis of GO-DLPG Biosensor

Before analysing the biosensor performance of the GO-DLPG structure, it was calibrated by measuring and recording its external RI response. To do so, the transmission spectrum of the GO-DLPG sensor probe was recorded after immersing it different RI solutions, prepared by dissolving different quantities of sucrose in distilled water. These aqueous sucrose solutions were prepared with measured RI values of 1.345, 1.355, 1.362, 1.372, 1.390, 1.412 and 1.449, measured by an Abbe refractometer at a wavelength of 589 nm and at room temperature (22º C). Fig. 6.17 and Fig. 6.18 depicts the transmission spectra of a bare DLPG and GO-DLPG against these sucrose solutions with different values of RI used.

It can be seen that the dual peaks move in opposite directions with increasing external RI values, where the LP_{013}^{blue} peak moves to the shorter wavelength region, while the LP_{013}^{red} peak moves the longer wavelength region. In contrast, the LP_{012} peak exhibits a blue shift. As illustrated by Fig. 6.17, in the GO-DLPG, the minimum intensities of the dual peaks reduce significantly with the increasing external RI values. This is consistent with the other reported DLPG external RI sensors published in the literature in [17-18] and [12]. When a high index thin layer is deposited on a LPG surface, such as GO, modes propagating in the cladding are partially radiated to the overlay, behaving as leaky modes. The coupling coefficient between these guided modes is dependent on the external RI. As explained by Erdogan et al. [28], the intensity of the resonance peaks decrease as the increasing external RI reduces the overlap integral between the core and the cladding modes. When the effective external RI approaches that of the cladding, the core mode will be coupled to the broadband radiation mode, with no distinct resonance loss bands noticed. Based on the significantly decreased resonance loss band intensities recorded, it can be noticed in Fig. 6.17 that the transmission spectra of the GO-coated LPG with a surrounding RI value of 1.449 seems to be approaching this off-resonance state.

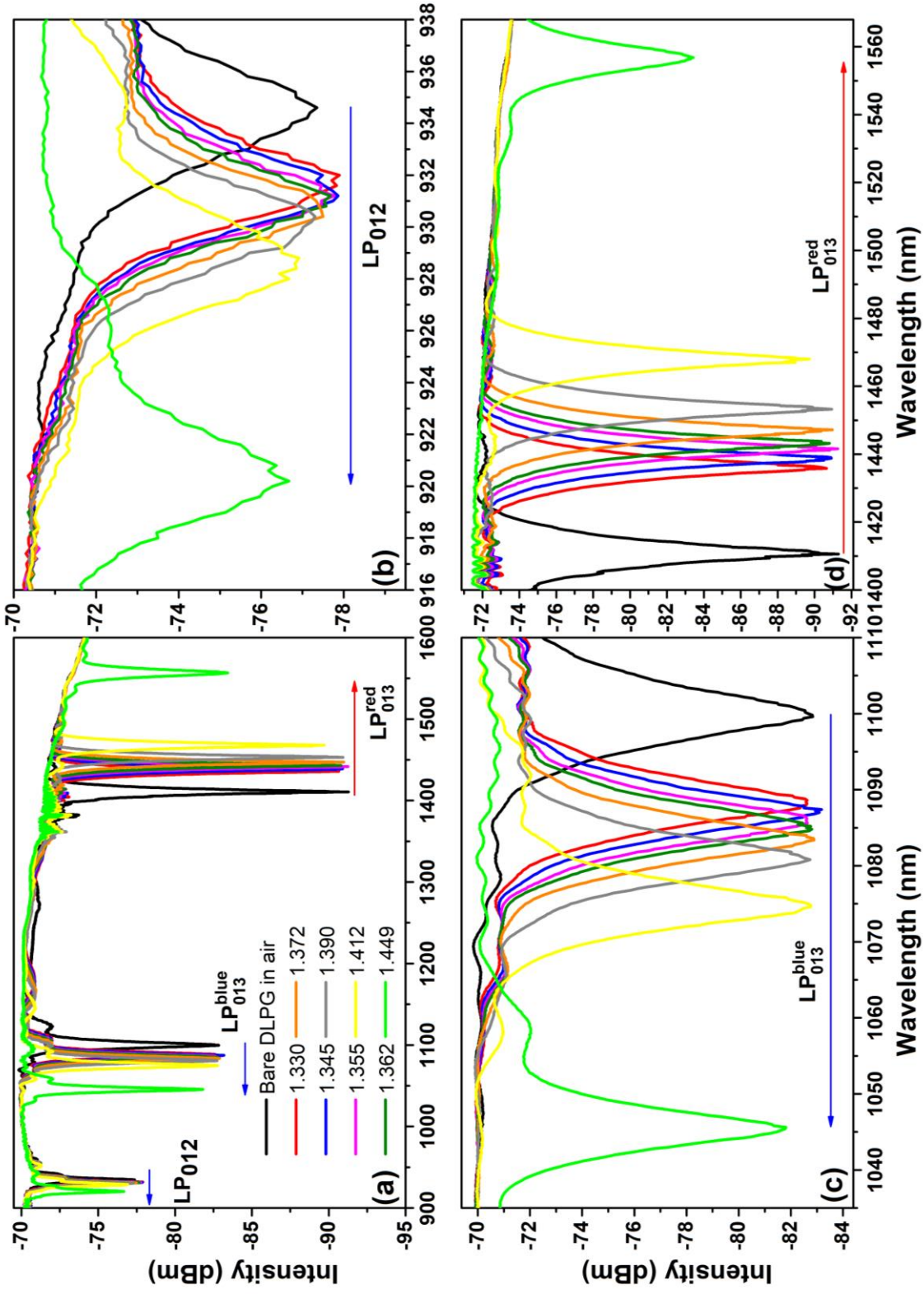

Fig 6. 17 (a) Transmission spectra of bare DLPG measured in different sucrose concentrations (b) Zoomed evolution of LP_{012} mode (c) Zoomed evolution of LP_{013}^{blue} peak (d) Zoomed evolution of LP_{013}^{red} peak.

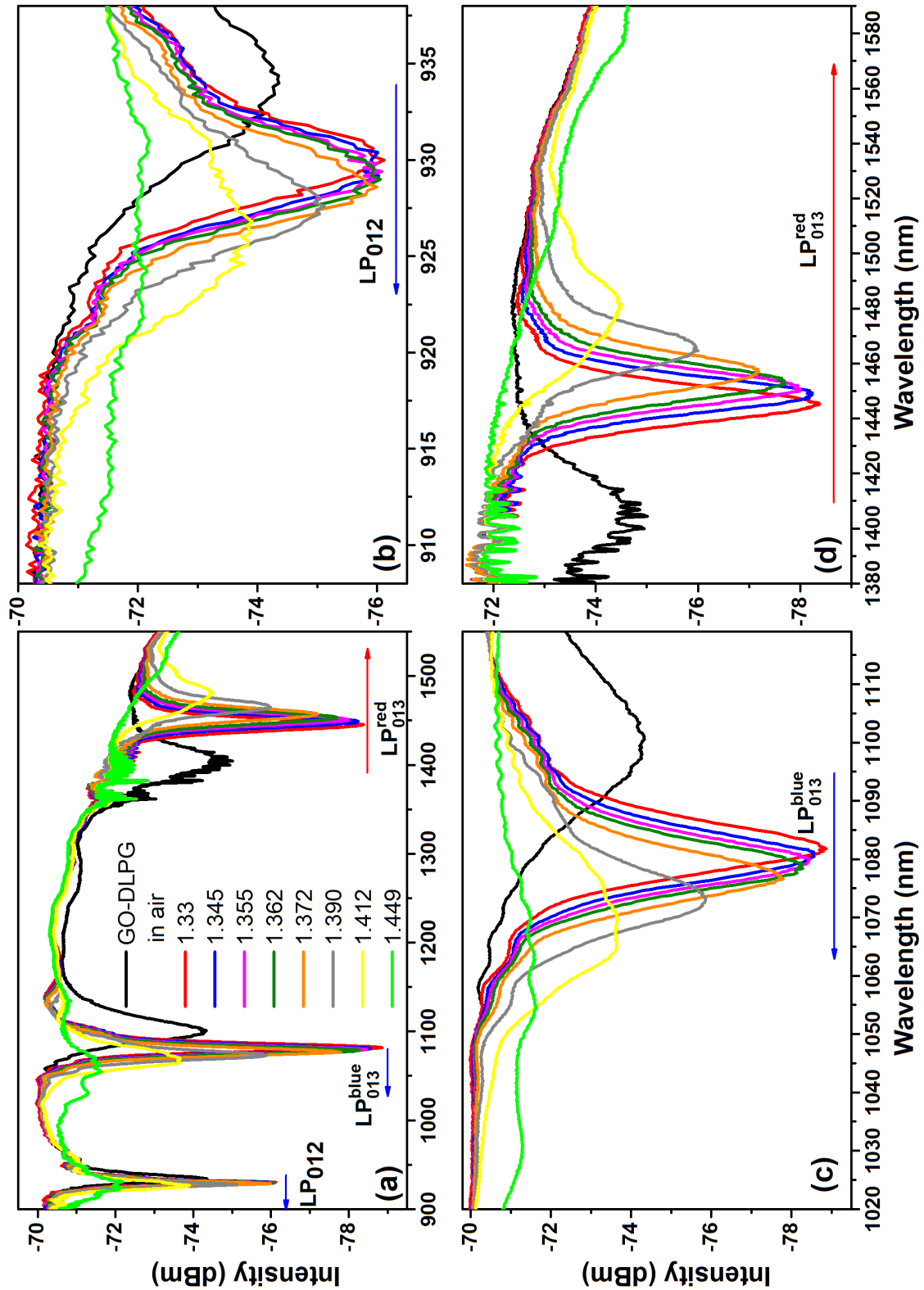

Fig 6. 18 (a) Transmission spectra of GO- DLPG measured in different sucrose concentrations (b) Zoomed evolution of LP_{012} mode (c) Zoomed evolution of LP^{blue}_{013} peak (d) Zoomed evolution of LP^{red}_{013} peak.

To compare the external RI sensitivities of the GO- LPG and GO-DLPG, LP_{08} the wavelength shift and the dual peak separation of these two sensor probes are presented in Fig. 6.19.

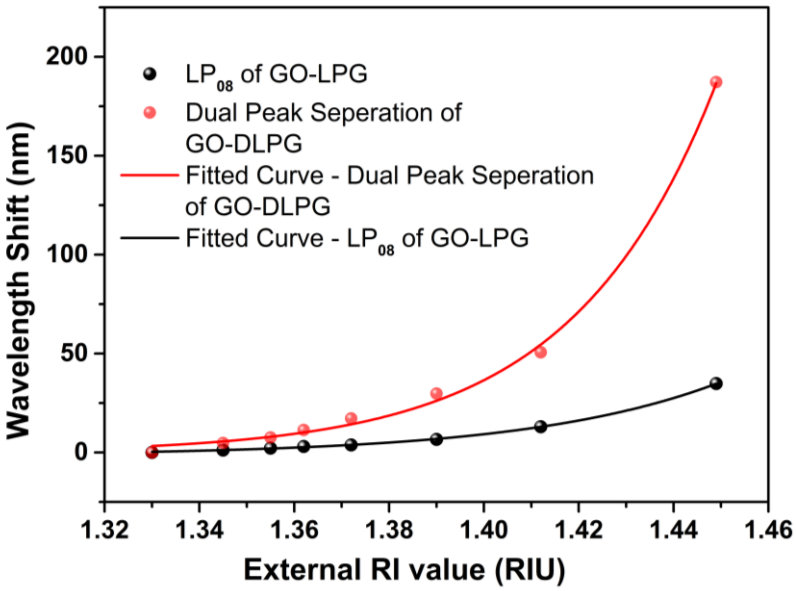

Fig 6. 19 Dual peak separation of GO-DLPG and LP_{08} wavelength shift of GO-LPG under varying external RI values.

Both the GO-LPG and GO-DLPG are observed to be demonstrating a nonlinear relationship with increasing external RI values from 1.330 to 1.449. The red symbols representing the dual peak separation of the GO-DLPG represent sensitivity values of 399 nm/RIU and 3692 nm/RIU in the lower RI region of 1.330-1.372 and higher RI region of 1.412-1.449, respectively. By contrast, the LP_{08} mode of the GO-LPG recorded sensitivity values of 92 nm/RIU and 589 nm/RIU for the corresponding RI regions. The external RI sensitivity of these GO coated sensor probes depends on the changing characteristics of the GO thin film overlay, such as the RI and the thickness, as described in detail in Chapter 4. Based on these results, it is evident that the external RI sensitivity of a GO-coated DLPG can be improved by 333% and 526% in the low and high RI regions, respectively, when compared with the sensitivities of a GO-coated LPG with the roughly the same GO overlay thickness.

To study the performance of the GO-LPG and GO-DLPG biosensor probes in measuring BSA concentrations, the sensing area of these probes were incubated in aqueous solutions of five different BSA concentrations of 0.2 g/mL, 0.5 g/mL, 0.8 g/mL, 1.0 g/mL, 1.2 g/mL and 1.5 g/mL. The optical response of the GO coated biosensor probes were analysed by recording the transmission spectra using the same experimental setup described in section 6.5. The variations

in the transmission spectrum of the GO-LPG, uncoated DLPG and the GO-DLPG sensor probes are depicted in Fig. 6.20, Fig. 6.21 and Fig. 6.22, respectively.

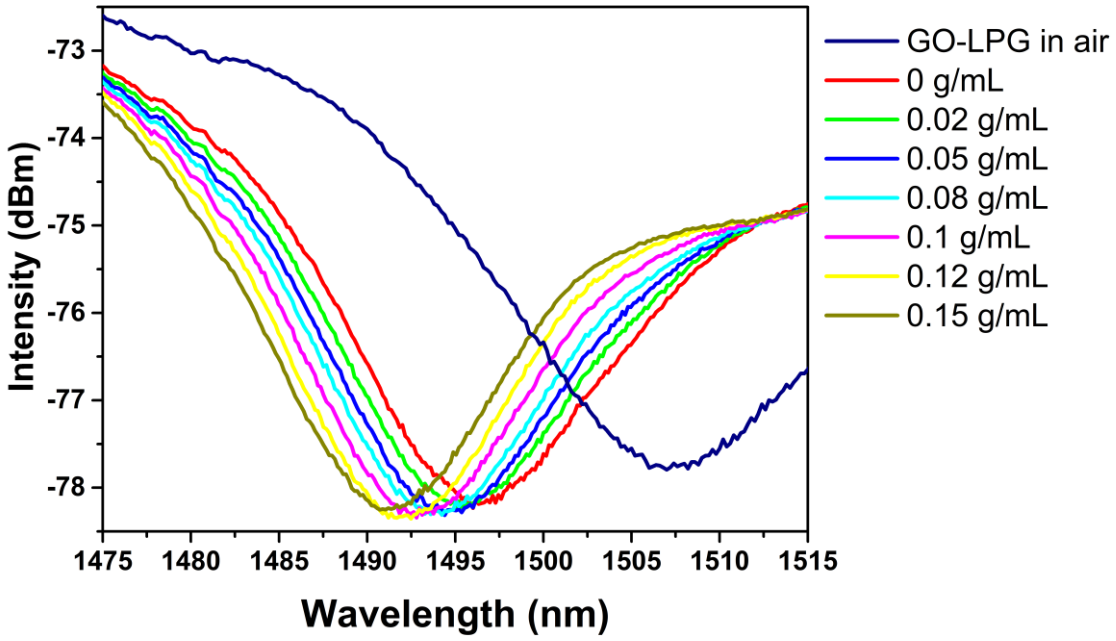

Fig 6. 20 Transmission spectra of GO-LPG biosensor probe under different BSA concentrations.

As can be seen from Fig. 6.20, the centre wavelength of LP_{08} resonance loss band of the GO-coated LPG sensor probe showed a blue shift of 5.44 nm when the BSA concentration was increased from 0 g/mL to 1.5 g/mL, with a negligible change in the resonance loss band intensity. In the bare DLPG sensor probe response presented in Fig. 6.21, the blue shift of the LP_{012} resonance peak was noticed to be less than 1 nm in contrast with a blue shift of 2.4 nm and a red shift of 5.4 nm recorded by the LP_{013}^{blue} and LP_{013}^{red} peaks, respectively, in the same region of increasing BSA concentrations. When it comes to the DLPG-based sensor probes, it can be noticed that the red shift of the LP_{013}^{red} peak is much more prominent than the blue shift of the LP_{013}^{blue} peak, with increasing BSA concentration values. The resonance wavelength shift of the GO-DLPG sensor probe was recorded to be significantly higher than both the GO-LPG and uncoated DLPG sensor probes, while recording a blue shift of 7.4 nm and a red shift of 17.4 nm by the LP_{013}^{blue} and LP_{013}^{red} peaks, respectively. These observed trends of the resonance wavelength can be seen more clearly in Fig. 6.23. Another major difference noticed in the dual resonance peaks of the GO-DLPG sensor probe, in comparison with GO-LPG and uncoated DLPG sensor probes, is the significant enhancement of peak intensity of the dual resonance peaks.

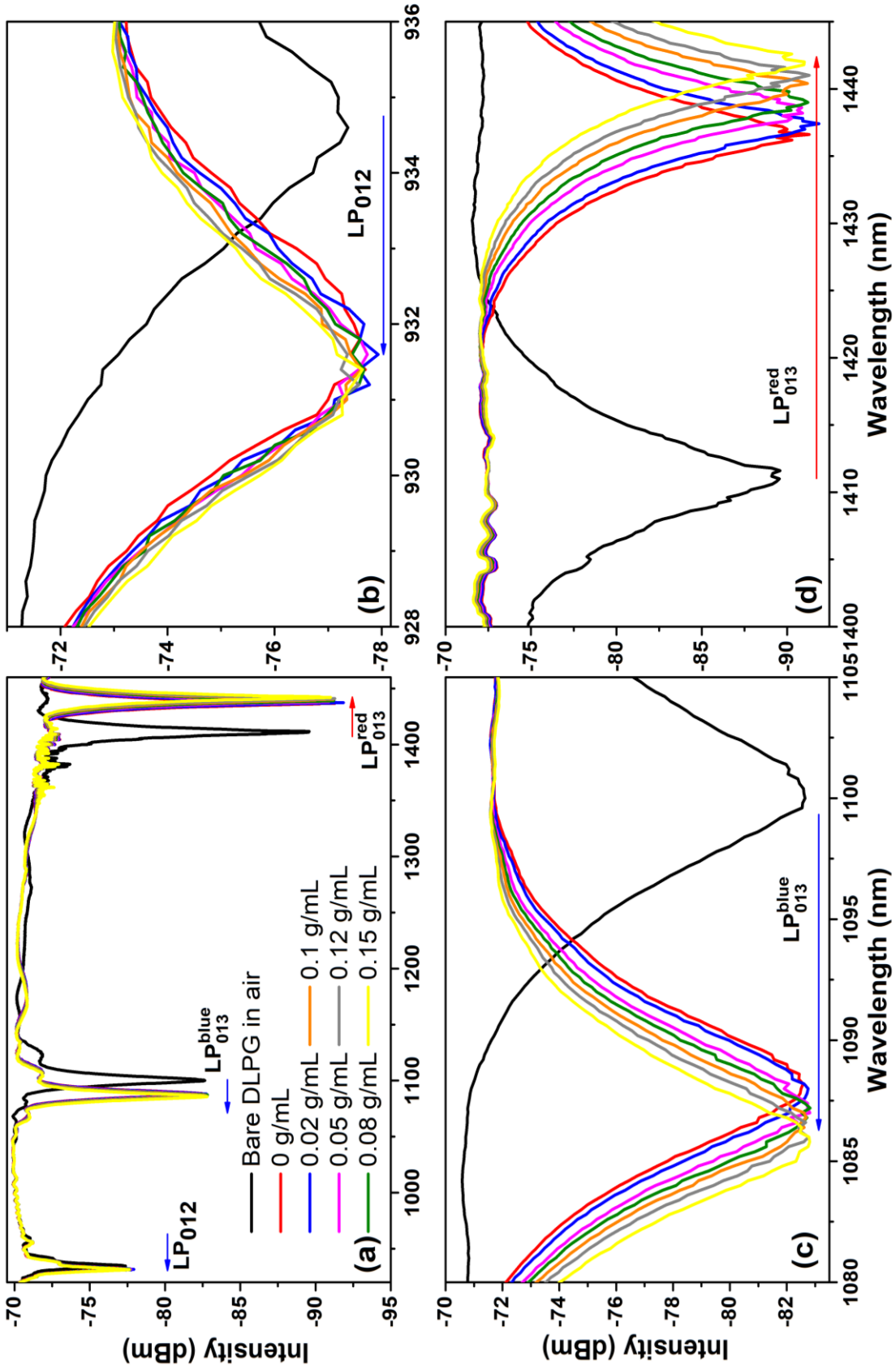

Fig 6. 21 (a) Transmission spectra of bare DLPG measured in different BSA concentrations (b) Zoomed evolution of LP_{012} mode (c) Zoomed evolution of LP_{013}^{blue} peak (d) Zoomed evolution of LP_{013}^{red} peak.

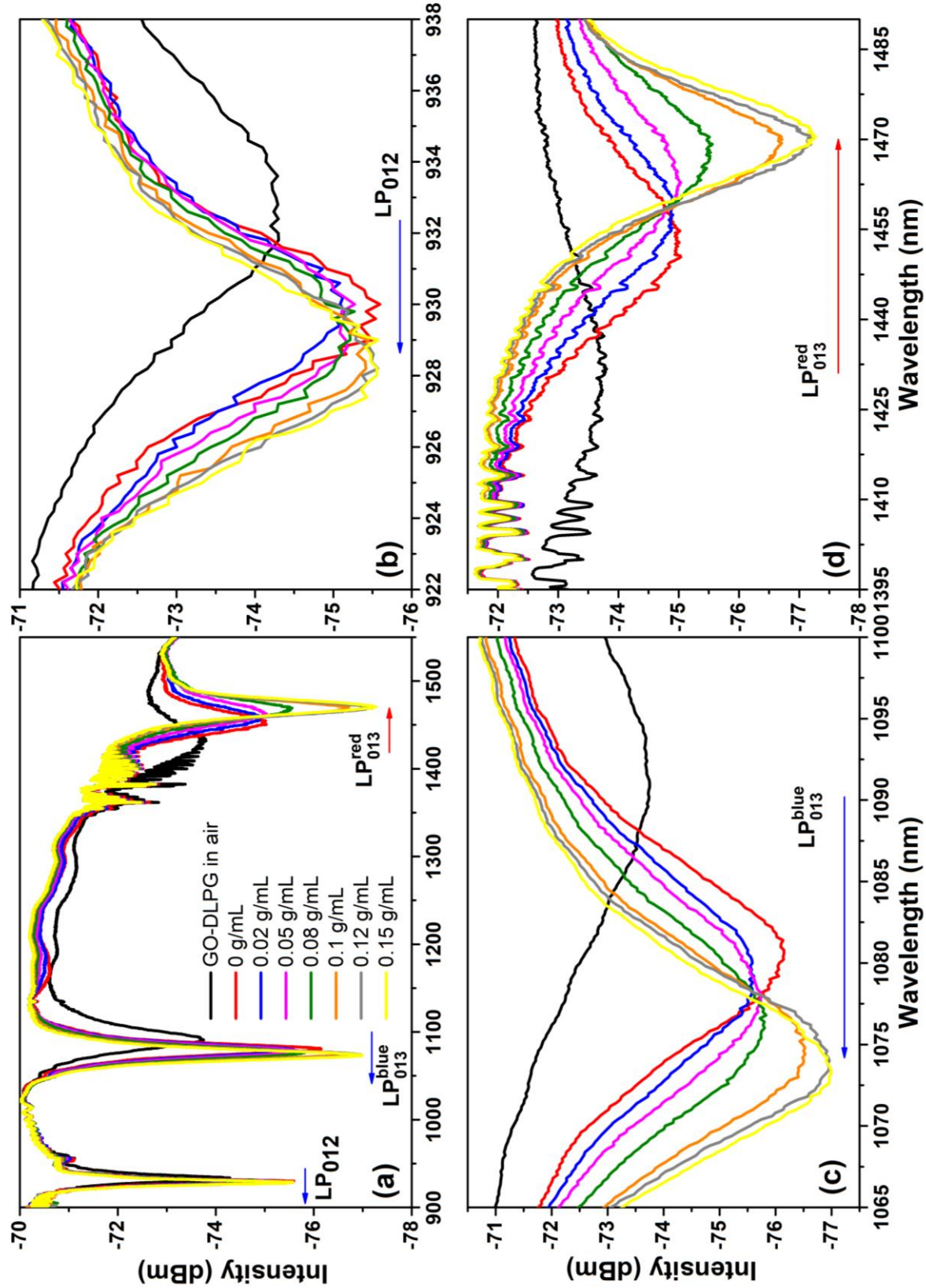

Fig 6. 22 (a) Transmission spectra of GO coated DLPG measured in different BSA concentrations (b) Zoomed evolution of LP_{012} mode (c) Zoomed evolution of LP^{blue}_{013} peak (d) Zoomed evolution of LP^{red}_{013} peak.

Fig. 6.23 illustrates the sensitivity curves of GO-LPG, uncoated DLPG and GO-DLPG in the form of resonance wavelength shift with increasing BSA concentrations from 0.2 g/mL to 1.5 g/mL.

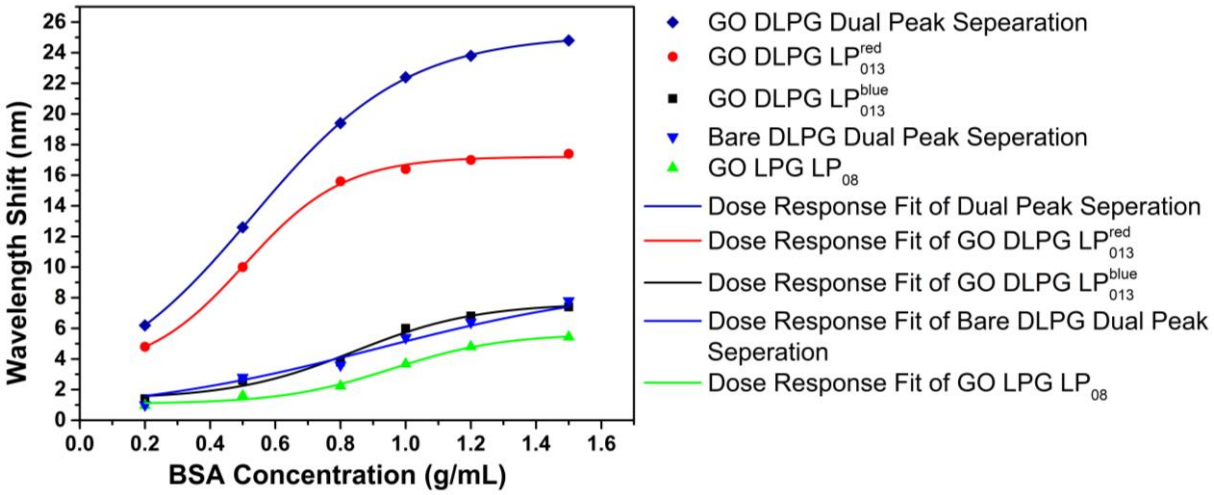

Fig 6. 23 Wavelength shift of the sensor probes with varying BSA concentrations.

Two sections of the wavelength shift curve can be noticed for all the resonance loss bands of the GO-coated sensor probes, except for the bare DLPG dual peak separation curve. A linear increment in wavelength shift can be observed for BSA concentration values from 0.2 g/mL to 0.8 g/mL, whereas at higher BSA concentrations (above 1.0 g/mL), the wavelength shift curves of these GO-coated sensors appeared to be reaching a saturation point, showing a parabolic nature. At lower BSA concentrations, there is high number of available binding sites on the GO surface for BSA molecules to interact with GO but when the BSA concentration is increased, the covalent and non-covalent interactions reach a saturation point due to these available binding sites already being populated with BSA molecules. However, this doesn't apply to the uncoated DLPG, in which the wavelength shift is solely based on the external RI change.

The enhanced sensitivities of the resonance loss band centre wavelength and minimum intensity, with variations in the BSA concentration values, are caused by the enhanced light matter interaction of dual peak resonance appear in higher order cladding modes in the interface of cladding-GO thin film overlay, which results in the optical perturbations of the LP_{013} cladding mode. These perturbations are caused by the GO-BSA interactions that take place when the sensor probe is immersed in BSA solutions, which will be discussed in more detail below.

Interactions between the GO and proteins such as BSA can be categorised into two major processes, as explained in [29] by Simsikova et al. First, proteins are physically adsorbed to the GO surface non-covalently. BSA molecules become attached to the GO surface through this physisorption process by weak Van der Waals forces, electrostatic bonding and π-π interactions. Jeyachandran et al. have demonstrated that BSA molecules become adsorbed to hydrophilic surfaces, such as GO, with a higher interaction strength than to the hydrophobic surfaces [30]. In addition, oxygen containing groups that possess O-H groups of GO also support hydrogen bonding between GO surface and BSA molecules and this phenomenon also supports non-covalent bonding of BSA to the GO thin film overlay. Secondly, BSA molecules become attached to the GO surface via covalent bonds. This means of interaction is mainly facilitated by the reactive oxygen containing groups present in GO basal plane. This type of covalent bonding predominantly happens due to the reaction between amino acid residues present on the protein surface and the oxygen containing groups present on the GO surface. In general, covalent immobilization of BSA on the GO surface ensures the highest binding strength between GO and the protein molecules, which increases the operational stability towards heat and pH. Yang et al. have explained the covalent bonding between the GO and BSA [31] by comparing the FTIR spectra of GO, BSA and GO-BSA, which are depicted in Fig. 6.24 (below).

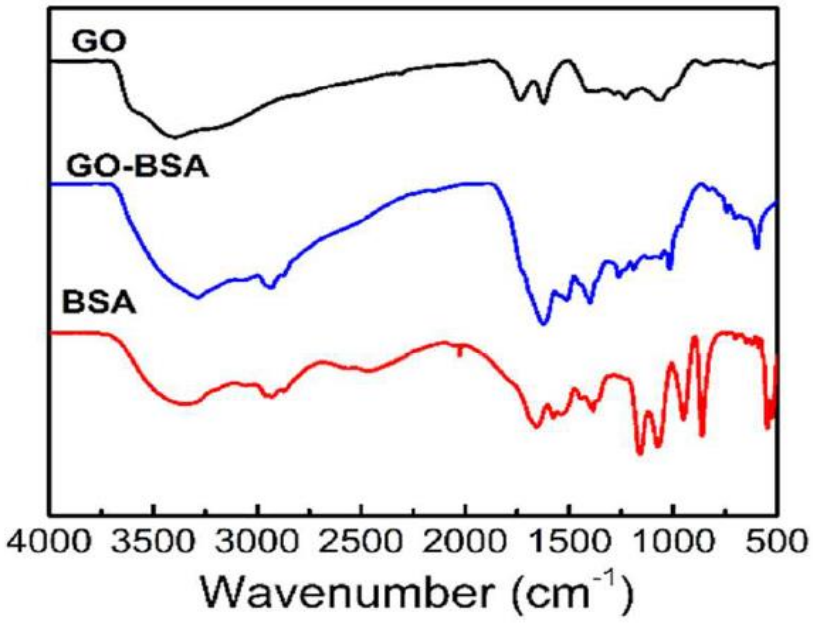

Fig 6. 24 FTIR spectra of GO, BSA and GO-BSA [31].

As can be seen from Fig. 6.24, the chemical bond of GO-BSA composite relates to the O=C-NH in-plane bending vibration at 630 cm^{-1}, compared with the FTIR spectra of GO. The new

peak at 1650 cm^{-1} explains the disappearance of the carboxyl peak at 1750 cm^{-1} in the FTIR spectrum of the GO-BSA and this is due to the cross-linking of O=C-OH with amide groups, which indicated that the amine groups of BSA have been successfully grafted onto the GO surface. The new peak present at 2850 cm^{-1} in the GO-BSA FTIR spectrum can be explained by the C-H stretching vibrations of the methane groups of BSA. In summary, the appearance of the significant peaks at 2850 cm^{-1} and 630 cm^{-1} in the GO-BSA FTIR spectrum, in contrast with the FTIR spectrum of GO, suggests the successful formation of GO-BSA covalent bonding.

Based on the analysed results shown in Fig. 6.23, it is evident that the developed GO-DLPG sensor is suitable for the measurement of BSA concentrations of less than 1.0 g/mL. In the region of BSA concentrations from 0.2 g/mL to 0.8 g/mL, the LP_{08} resonance loss band of the GO-LPG recorded a sensitivity of 2.1 nm/(g/mL), whereas sensitivity of the dual peak separation (considering both blue and the red shift of the two-resonance peaks) of an uncoated DLPG was noted to be 4.3 nm/(g/mL). When it comes to the GO-DLPG sensor probe, sensitivity values of 4 nm/(g/mL) and 18 nm/(g/mL) have been calculated for the LP_{013}^{blue} and LP_{013}^{red} peaks, respectively, in the same BSA concentration range. By considering the wavelength shift of both dual resonance peaks, the sensitivity of the GO-coated DLPG was calculated to be 22 nm/(g/mL), which showed that the sensitivity of BSA concentration measurement can be increased 11 fold when compared with a GO-coated LPG and 5 fold when compared with an uncoated DLPG, by using this GO coated DLPG sensor probe. The LOD of the developed GO-DLPG was calculated to be 0.9 µg/mL, based on the resolution of the OSA used in this experiment.

The sensing mechanism of the GO coated biosensor probes developed arises as the non-covalent and covalent interactions between the GO surface and the BSA molecules change the local RI at the GO-analyte (BSA) interface where the evanescent wave penetrates, to induce an optical signal change that is reflected in the wavelength shift, shown in Fig. 6.23. The sensitivity, S, of the biosensors developed can be defined by the ratio of the optical signal change (resonance wavelength shift) to the variations in the measurement quantity, which can be defined as follows [18].

$$S = \frac{\Delta\lambda}{\Delta C} = \frac{\Delta\lambda}{\Delta n}\frac{\Delta n}{\Delta C} = S_{RI}E$$

where S is the sensitivity, $\Delta\lambda$ is the resonance wavelength shift, ΔC is the local change in BSA concentration and Δn is the corresponding RI change. The interactions between BSA molecules and GO surface changes the local analyte concentration (ΔC), which changes the local effective RI (Δn), which results in an optical change reflected in the resonance wavelength shift ($\Delta\lambda$). Based on this, it can be concluded that the sensitivity of the sensor developed depends on two factors; the sensitivity to the external RI change (S_{RI}) and the effectiveness (E) of the interaction between GO and the analyte, in this case BSA.

It has to be noticed that the developed GO coated LPG based biosensor platform is not specific to the detection of BSA molecules. The optical response observed is predominantly caused by the RI change introduced to the LPG waveguide system by BSA molecules present in the testing sample. However, as GO is capable of interacting with a wide range of biomolecules (as a result of its rich surface chemistry), the optical response observed could also be affected by any interactions between GO and non-BSA biomolecules, if such biomolecules capable of interacting with GO are present in the sample. GO itself is not selective to any specific biomolecule and thus, comprehensive steps should be taken during the design process to ensure the selectivity of the biosensors that use GO as the sensing material. Selectivity of such biosensors can be realised by functionalising the deposited GO overlay with species specific bio receptors. One such technique is to exploit the specific interaction between streptavidin and biotin, as shown in [24] by Esposito et al. Streptavidin is a protein that shows an extraordinary high affinity towards biotin and as such, GO overlay can be functionalised with streptavidin to specifically detect biotinylated biomolecules present in the sample. Antibodies produced by white blood cells during immune reactions show an extremely high affinity towards its respective antigens. As shown by Liu et al. in [18], this specific interaction between antibodies and antigen can be exploited to develop GO based biosensors with very high selectivity towards the targeted biomolecule. Deposited GO overlay can be functionalised with a chosen antibody and thus, only the antigens specific to that particular antibody will be captured by the developed sensor. By this way, only the targeted biomolecule will influence the optical response observed by the GO based biosensors under consideration.

Nevertheless, the atomic flat surface, high surface to volume ratio, tuneable RI based on the surrounding medium, biocompatibility and high number of surface functional oxygen containing groups make GO an ideal sensing material for immobilisation of biomolecules, which results in a significant enhancement of the effectiveness of the interaction between the

GO surface and the analyte that makes GO-based biosensors a more desirable approach when compared to conventional biosensing platforms.

6.7 Summary

A label-free sensor designed to measure BSA concentrations using a GO-coated DLPG has been presented in this chapter, at the same time discussing the sensor fabrication steps and the system performance (BSA concentration measurement and external RI sensing) in some detail. Moreover, its external RI and biosensor performance were compared with an uncoated DLPG and the LP_{08} resonance loss band of a GO-coated LPG. A drop casting technique was used to deposit the GO thin film overlays of ~ 400 nm on the GO-coated sensor probes discussed in this chapter. The external RI sensitivity values of 399 nm/RIU and 3692 nm/RIU were achieved using the GO-coated DLPG in the low (1.330 – 1.372) and high (1.412 – 1.449) external RI regions respectively, which were shown to be 4 and 6 times higher than the sensitivity of LP_{08} resonance mode of a GO-coated LPG in the same RI region. When approaching the BSA concentration measurement, the highest sensitivity of 22 nm/(g/mL) was achieved by the dual peak separation of the GO-coated DLPG sensor probe in the BSA concentration region from 0.2 g/mL to 0.8 g/mL, which led to a LOD of 0.9 µg/mL based on the highest resolution of the OSA used to conduct the experiment. It was also noted that the achievable LOD is 11 times better than that of a GO-coated LPG sensor probe and 5 times better than that of an uncoated DLPG sensor probe. These promising results indicated that GO is an excellent sensing material for biosensor development due the rich surface chemistry that it possess. While being highly sensitive to the varying BSA concentrations, the GO-coated DLPG sensor probe developed also provides a platform for other potential applications, such as uranium (VI) absorption from aqueous solutions (as shown by Yang et al in [31]). This is made possible as the incorporation of proteins turns GO into a very versatile general platform that enables self-assembly of various nanoparticles of different shapes, compositions and properties [29].

6.8 References

[1] Marks R S, Lowe C R, Cullen D C, Weetall H H, Karube I, Handbook of Biosensors and Biochips, Wiley, Weinheim, 2007.

[2] Sansone L, Macchia E, Taddei C, Torsi L, Giordano M, “Label-free optical biosensing at femtomolar detection limit,” Sensors and Actuators B: Chemical, 255, 1097–1104, 2018.

[3] Stephen J & Ralph T, “Optical fibre long-period grating sensors: characteristics and application,” Measurement Science & Technology, 14(5), R49-R61, 2003.

[4] Ding J, Zhang A, Shao L-Y, Yan J-H, He S, "BFiber-taper seeded long-period grating pair as a highly sensitive refractive-index sensor," IEEE Photonics Technology Letters, 17, 1247–1249, 2005.

[5] Zhao D, Zhou K, Chen X, Zhang L, Bennion I, "Implementation of vectorial bend sensors using long-period gratings UV-inscribed in special shape fibres," Measurement of Science and Technology. 15, 1647–1650, 2004.

[6] Jang H S, Park, K N, Kim J P, Sim S J, Kwon, O J, Han, Y G, Lee K S, "Sensitive DNA biosensor based on a long-period grating formed on the side-polished fiber surface," Optics Express 17, 3855–3860, 2009.

[7] DeLisa M P, Zhang Z, Shiloach M, Pilevar S, Davis C C, Sirkis J S, Bentley W E, "Evanescent Wave Long-Period Fiber Bragg Grating as an Immobilized Antibody Biosensor," Analytical Chemistry, 72, 2895–2900, 2000.

[8] Lepinay S, Staff A, Ianoul A, Albert J, "Improved detection limits of protein optical fiber biosensors coated with gold nanoparticles," Biosensors and Bioelectronics, 52, 337–344, 2014.

[9] Shevchenko Y, Camci-Unal G, Cuttica D, Dokmeci M, Albert J, Khademhosseini A, "Surface plasmon resonance fiber sensor for real-time and label-free monitoring of cellular behavior," Biosensors and Bioelectronics, 56, 359–367, 2014.

[10] Chen X, Zhang L, Zhou K, Davies E, Sugden K, Bennion I, Hughes M, Hine A, "Real-time detection of DNA interactions with long-period fiber-grating-based biosensor," Optics Letters, 32, 2541–2543, 2007.

[11] Brzozowska E, Smietana M, Koba M, Gorska S, Pawlik K, Gamian A, Bock W J, "Recognition of bacterial lipopolysaccharide using bacteriophage-adhesin-coated long-period gratings," Biosensors and Bioelectronics, 67, 93–99, 2015.

[12] Shu X, Zhang L, Bennion I, "Sensitivity Characteristics of Long-Period Fiber Gratings," Journal of Lightwave Technology, 20, 255–266, 2002.

[13] Sharma D, Kanchi S, Sabela M I, Bisetty K, "Insight into the biosensing of graphene oxide: Present and future prospects," Arabian Journal of Chemistry, 9, 2, 238-261, 2016.

[14] Sridevi S, Vasu K S, Jayaraman N, Asokan S, Sood A K, "Optical bio-sensing devices based on etched fiber Bragg gratings coated with carbon nanotubes and graphene oxide along with a specific dendrimer," Sensors and Actuators B: Chemical, 195 150-155, 2014.

[15] Sridevi S, Vasu K S, Jayaraman N, Asokan S, Sood A K, "Optical detection of glucose and glycated hemoglobin using etched fiber Bragg gratings coated with functionalized reduced graphene oxide," Journal of Biophotonics, 9: 760-769, 2016.

[16] Sridevi S, Vasu K S, Jayaraman N, Asokan S, Sood A K, "Sensitive detection of C-reactive protein using optical fiber Bragg gratings," Biosensors and Bioelectronics, 65, 251-256, 2015.

[17] Liu C, Xu B J, Zhou L, et al., "Graphene oxide functionalized long period fiber grating for highly sensitive hemoglobin detection," Sensors and Actuators B: Chemical, 261, 91–96, 2018.

[18] Liu C, Cai Q, Xu B, Zhu W, Zhang L, Zhao J, Chen X, "Graphene oxide functionalized long period grating for ultrasensitive label-free immunosensing," Biosensors and Bioelectronics, 94, 200-206, 2017.

[19] An F F, Zhang X H, "Strategies for preparing albumin-based nanoparticles for multifunctional bioimaging and drug delivery," Theranostics, 7, 3667–3689, 2017.

[20] Verhoeff J, Smit J A H "Bovine serum albumin and cell counts in the diagnosis of subclinical udder infection," Veterinary Quarterly, 3:1, 38-45, 1981.

[21] Guo T, Guan B O, and Albert J, "Tilted fiber grating mechanical and biochemical sensors," Optics and Laser Technology, 78, 19–33, 2016.

[22] Urrutia A, Bojan K, Marques L, Mullaney K, Goicoechea J, James S, Clark M, Tatam R, and Korposh S, "Novel Highly Sensitive Protein Sensors Based on Tapered Optical Fibres Modified with Au-Based Nanocoatings," Journal of Sensors, 2016, 1–11, 2016.

[23] Li Z, Liao C, Chen D, Song J, Jin W, Peng G-D, Zhu F, Wang Y, He J, and Wang Y, "Label-free detection of bovine serum albumin based on an in-fiber Mach-Zehnder interferometric biosensor," Optics Express, 25, 17105-17113, 2017.

[24] Esposito F, Sansone L, Taddei C, Campopiano S, Giordano M, Iadicicco A, "Ultrasensitive biosensor based on long period grating coated with polycarbonate-graphene oxide multilayer," Sensors and Actuators B: Chemical, 274, 517-526, 2018.

[25] Shu X, Lin L, and Bennion I, "Sensitivity characteristics near the dispersion turning points of long-period fiber gratings in B/Ge codoped fiber," Optics Letters, 26, 1755-1757, 2001.

[26] Chen X, Zhou K, Zhang L, and Bennion I, "Dual-peak long-period fiber gratings with enhanced refractive index sensitivity by finely tailored mode dispersion that uses the light cladding etching technique," Applied Optics, 46, 451-455, 2007.

[27] Śmietana M, Koba M, Mikulic P, and Bock W J, "Towards refractive index sensitivity of long-period gratings at level of tens of μm per refractive index unit: fiber cladding etching and nano-coating deposition," Optics Express, 24, 11897-11904, 2016.

[28] Erdogan T, "Cladding-mode resonances in short- and long-period fiber grating filters," Journal of Optical Society of America. A, 14, 1760–1773, 1997.

[29] Simsikova M, Sikola T, "Interaction of Graphene Oxide with Proteins and Applications of their Conjugates," Journal of Nanomedicine Research, 5(2), 2017.

[30] Jeyachandran Y L, Mielczarski E, Rai B, Mielczarski J A, "Quantitative and Qualitative Evaluation of Adsorption/Desorption of Bovine Serum Albumin on Hydrophilic and Hydrophobic Surfaces," Langmuir, 25, 19, 11614-11620, 2009.

[31] Yang P, Liu Q, Liu J, Zhang H, Li Z, Li R, Liu L, and Wang J, "Bovine Serum Albumin-Coated Graphene Oxide for Effective Adsorption of Uranium(VI) from Aqueous Solutions," Industrial & Engineering Chemistry Research, 56 (13), 3588-3598, 2017.

Chapter 7

Conclusions and Future Work

7.1 Conclusions of the work carried out

The primary objective of the research work carried out in this research programme has been to exploit the unique characteristics of recently discovered 2D graphene nanomaterials linked to the highly sought-after properties of optical fibre sensors, for use in applications such as structural health monitoring, external RI sensing, chemical concentration measurement and biosensing. This has been exemplified in the development of a series of GO-coated LPG-based external RI sensors to measure NaCl salinity in water, with the simultaneous measurement of RH and temperature, and in a specific application to BSA concentration measurement, all of which illustrate the versatility of the sensor approach. The field of graphene nanomaterials-based fibre optic sensors is a very novel area of research and thus, the results presented in this thesis and the achievements attained are put forward to illustrate a further contribution to this new area of research and thus to contribute to the broader evaluation of the effectiveness of using graphene nanomaterials with fibre optic sensors.

The research work carried out in this thesis has reported a number of key features which have been published in open international literature and the conclusions and achievements, recognised in light of the aims and objectives set out in Chapter 1 can be set out as follows.

<u>Background Research</u>

- A comprehensive overview of the characteristics of FBGs and LPGs for use in sensors was given, by focusing on the key features which include mode guiding fundamentals, operating principles, fabrication methods and sensing characteristics of fibre gratings. By analysing a number of coated LPG external RI sensors reported in literature, the use of LPGs was introduced as the basis of the chosen fibre optic sensing mechanism in the development of several graphene nanomaterial-coated sensors realised in this work based on the advantages shown by LPGs in external RI sensing.

- Based on the comprehensive overview presented on graphene nanomaterials, it was established that GO showed desirable properties and characteristics over other graphene derivatives (pristine graphene and rGO) for the development of fibre optic based external RI sensors/biosensors outlined in the aims and objectives due to the rich surface chemistry that it possesses, hydrophilic characteristics and simple and low cost synthesis process.

GO Synthesis

- An improved version of the Hummer's method was successfully deployed to produce high quality and consistent GO thin films. The quality of the prepared GO thin films was proven by UV/Vis, FTIR, EDAX and SEM analysis to validate the success of the synthesis process carried out.

External RI Sensor System

- An external RI sensor system which contained GO coated LPG as the basis was successfully developed by the use of a drop casting technique to deposit a few hundred nanometres thick GO thin films on the optical fibre surface.
- The NaCl salinity measuring capability of the developed GO coated LPG sensor probes was proven by the successful detection of variations in the surrounding RI using of NaCl solutions with varying concentrations.
- The enhanced RI sensitivity achieved by the use of GO overlays on fibre gratings was quantified with a measured increase in the external RI sensitivity of 83% for the GO coated LPG sensor compared to an uncoated LPG sensor and a highest external RI sensitivity of 193.8 nm/RIU in the RI region of 1.330 to 1.379.

Humidity Sensor Probe

- Multi-parameter sensing capability of the developed GO-coated LPG based humidity sensor probe was proven by the successful measurement of RH levels and temperature values, simultaneously.
- The enhanced RH sensitivity realised by the use of GO overlays on LPG fibre surfaces was quantified with a satisfactory linear response of the humidity response achieved in the RH region of 60%RH - 95%RH, reporting a sensitivity of 0.15 dB/%RH at room temperature.

- Performance of the sensor probe thus realised was successfully cross compared with good agreement with other graphene nanomaterial-based and polymer coated fibre optic RH sensors reported in literature.

Label-Free Detection of Protein Concentrations

- The label-free detection capability of the developed GO coated DLPG based biosensor probe was proven by the successful detection of variations in protein concentration using of BSA solutions with varying concentrations.
- Strong binding affinity of GO with protein molecules was successfully established by comparing the BSA detection performance of a GO coated DLPG and a bare DLPG.
- The superior protein sensitivity achieved by combining DLPGs with GO overlays was quantified with a measured LOD of 0.9 μg/mL of the GO coated DLPG biosensor probe that is 11 times higher than that of a GO-coated LPG sensor probe.
- These promising results indicated that the GO coated DLPG sensor probe developed in this work has the ability to be used as highly sensitive, label-free biosensing platform, which could also be made species-specific by modifying the GO surface with other species-specific functional groups.

Contribution to the Community

- The positive research outcomes achieved in this work have been widely disseminated (via two peer reviewed journal publications and four international conference papers) and continue to be reported (one journal publication is under review and another one is in progress by the time of writing) in the peer reviewed international literature.

Thus, it is evident that the aims and objectives set out in Chapter 1 have been addressed to a large extent and results respirated from the work carried out in this research programme.

7.2 Proposal for Future Work

The successful and extensive research work conducted in this programme has highlighted the potential applications of the fusion of the unique sensing characteristics of graphene nanomaterials and the advantages of fibre optic sensors, in this recently-established field of graphene nanomaterial-based fibre optic sensors. The direction of the future research discussed below has the potential to address a number of different industrial applications. Examples include:

- A vital issue that delays the involvement of graphene nanomaterials in real world applications is their potential instability over time. All the experiments performed in this thesis have been conducted under laboratory conditions and it is essential to investigate the long-term stability of the developed sensors, especially of the GO-coated LPG based RH sensor, so that it has the potential of being used for structural health monitoring in the long term – to have stability over a period of years for example. Future research can be carried out to develop GO-polymer composites (such as GO/PVA composites), which have the potential of solving the stability issue of graphene nanomaterials, while increasing the humidity sensitivity, due to porous nature of the polymers.
- Graphene nanomaterials have exhibited enhanced sensitivity to a wide range of analytes due to their single atom thickness and the high surface area of they possess. This leads to a very practical concern from potential cross sensitivity, when these materials are used as sensing elements in the development of fibre optic sensors. Therefore, techniques for increasing the selectivity and specificity of the developed GO- coated LPG sensors could be investigated further by functionalising the coated GO overlay with analyte-specific nanomaterials or by development of nanocomposites as mentioned above.
- It was established in this thesis that GO coated DLPG can be used as the basis of other highly sensitive, label-free biosensing platforms. The proposed sensor design can be explored further by functionalising the coated GO layer with various species-specific bio-materials to develop more selective fibre optic biosensor systems.
- External RI sensor performance of the GO coated LPG can be investigated further by varying the GO overlay thickness to increase the sensitivity. However, the effect of the coating thickness could be explored further to achieve the optimum coating thickness that makes the LPG operating closer to the DTP, which increases the sensitivity of the developed sensor probes significantly.
- It was established that DLPGs exhibit extremely high external RI sensitivities compared to LPGs as they have the ability to access higher order cladding modes with energy fields that extend beyond the cladding. The DLPGs fabricated in the work carried out in this thesis used an amplitude mask of 150 μm period due to the limitations of the availability. If the grating period is reduced further, resonance loss bands

corresponding to even higher cladding modes can be accessed by the DLPG structure, which could improve the external RI sensitivity even higher than the reported values.

That above suggests that this will be a fruitful area of research for some years to come.

List of Publications

Journal Papers

1. **K. P. W. Dissanayake**, W. Wu, H. Nguyen, T. Sun and K. T. V. Grattan, "Graphene-Oxide-Coated Long-Period Grating-Based Fiber Optic Sensor for Relative Humidity and External Refractive Index," Journal of Lightwave Technology, vol. 36, no. 4, pp. 1145-1151, 15 Feb.15, 2018. doi: 10.1109/JLT.2017.2756097

2. **Kasun Dissanayake**, Papiya Dhara, Rahul Kumar, Souvik Ghosh, Hien T. Nguyen, Tong Sun, and Kenneth T V Grattan, "Fibre optic chemical sensors for environmental monitoring using sensitive nano-material coatings", Asian Journal of Physics, 28 (7-9), 567-578, 2019.

3. **Kasun Dissanayake**, Souvik Ghosh, Leonardo Binetti, Lourdes Alwis, B.M. Azizur Rahman, Tong Sun and Kenneth Grattan, "Thickness Dependent Performance Analysis of Graphene oxide-coated Long Period Grating-based Low Refractive Index Sensor System",– under review.

4. **Kasun Dissanayake**, Souvik Ghosh, Leonardo Binetti, Tong Sun and Kenneth Grattan, "Measuring Bovine Serum Albumin (BSA) Concentration by Graphene oxide-coated Dual Resonance Long Period Grating" – in progress.

Conference Papers

1. **Kasun Prabuddha Wasantha Dissanayake** , Miodrag Vidakovic, Fabian Matthias, Tong Sun and Kenneth T.V. Grattan, "Graphene oxide coated Long Period Grating for Optical Sensing Purposes", Journal of Physics, Conference Series, vol. 1151, pages. 012022. 2019 doi: 10.1088/1742-6596/1151/1/012022

2. **Kasun Dissanayake**, Souvik Ghosh, Leonardo Binetti, Bruno Rente, Lourdes Alwis, Tong Sun and Kenneth Grattan, "External Refractive Index Sensitivity Enhancement of a Long Period Grating by Graphene Oxide Overlay", Second Latin American Workshop on Optical Fiber Sensors- LAWOFS 2019, 17-19.07.2019, Rio De Janeiro, Brazil.

3. **Kasun Prabuddha Wasantha Dissanayake**, Rahul Kumar, Hien Nguyen, Weiping Wu, Tong Sun and Kenneth T.V. Grattan, "Stability of Graphene Oxide encapsulated Gold Nanorods for optical sensing purposes", Journal of Physics, Conference Series, vol. 1065, pages. 032021. 2018 doi:10.1088/1742-6596/1065/3/032021

4. **K. P. W. Dissanayake**, W. Wu, H. Nguyen, T. Sun and K. T. V. Grattan, “Graphene oxide coated long period grating based fibre optic humidity sensor”, 2017 25th Optical Fiber Sensors Conference (OFS), Jeju, 2017, pp. 1-4. doi: 10.1117/12.2265465